

**FABRICATION AND CHARACTERIZATION  
OF ADVANCED MATERIALS AND  
COMPOSITES FOR ELECTROCHEMICAL  
SUPERCAPACITORS**

By Mustafa Sami Ata, B.S, M.Sc

A Thesis Submitted to the School of Graduate Studies in Partial Fulfillment  
of the Requirements for the Degree Doctor of Philosophy

McMaster University © Copyright by Mustafa Sami Ata, August 2017

DOCTOR OF PHILOSOPHY (2017)

McMaster University

Department of Materials Science and Engineering)

Hamilton, Ontario

TITLE: Fabrication and Characterization of Advanced Materials and Composites for Electrochemical Supercapacitors

AUTHOR: Mustafa Sami Ata, MSc. (McMaster University, Canada), B.S. (Kırıkkale University, Turkey)

SUPERVISOR: Dr. Igor Zhitomirsky, Distinguished Engineering Professor, Ph.D., P.Eng.

NUMBER OF PAGES: XXIX, 236

*Dedicated to my beloved wife,  
son and daughter*

## Abstract

Electrochemical supercapacitors (ESs) have attracted great attention due to the advantages of long cycle life, high charge/discharge rate and high power density compared to batteries. Significant improvement in ES performance has been achieved via development of advanced nanostructured materials, such as  $\text{MnO}_2$  and composite  $\text{MnO}_2$ -MWCNT and PPy-MWCNT electrodes.

In this dissertation, advanced dispersants were developed and investigated for the dispersion, surface modification and electrophoretic deposition (EPD) of metal oxides, multiwalled carbon nanotubes (MWCNT) and polypyrrole (PPy) in different solvents.

Nature-inspired strategies have been developed for the fabrication of MWCNT films and composites. The outstanding colloidal stability of MWCNT, dispersed using anionic bile acids, allowed the EPD of MWCNT. Composite  $\text{MnO}_2$ -MWCNT films were obtained by anodic EPD on Ni plaque and Ni foam substrates. Good dispersion of MWCNT during Py polymerization was achieved and allowed the formation of PPy coated MWCNT. The film and bulk electrodes, prepared by EPD and slurry impregnation methods, respectively, showed high capacitance and good capacitance retention at high charge-discharge rates.

The mechanisms of dispersion and deposition were investigated. Cathodic and anodic EPD of MWCNT,  $\text{MnO}_2$ ,  $\text{Mn}_3\text{O}_4$  was achieved using positively and negatively charged dispersants. Co-deposition of MWCNT and  $\text{MnO}_2$  was performed using a co-dispersant, which dispersed both MWCNT and  $\text{MnO}_2$  in ethanol. Composite films were tested for ES applications.

The efficient dispersion was achieved at relatively low dispersant concentrations due to strong adsorption of the dispersants on the particle surface, which involved the polydentate bonding. We found the possibility of efficient dispersion of MWCNT in ethanol using efficient anionic dispersants. The electrostatic assembly method has been developed, which offers the benefit of improved mixing of  $\text{MnO}_2$  and MWCNT. The use of different anionic and cationic dispersants allowed the fabrication of electrodes with enhanced capacitance and improved capacitance retention at high charge–discharge rates and high active mass loadings. The asymmetric devices, containing positive  $\text{MnO}_2$ –MWCNT and negative AC–CB electrodes showed promising performance in a voltage window of 1.6 V.

We proposed another novel concept based on electrostatic heterocoagulation of  $\text{Mn}_3\text{O}_4$ –MWCNT composites in aqueous environment. In this case, various dispersants were selected for adsorption and dispersion of MWCNT and  $\text{Mn}_3\text{O}_4$  and this allowed the formation of stable aqueous suspensions of positively charged MWCNT and negatively charged  $\text{Mn}_3\text{O}_4$ , which facilitated the formation of advanced composites with improved mixing of the components. Testing results showed promising performance of  $\text{Mn}_3\text{O}_4$ –MWCNT composites for applications in electrodes of electrochemical supercapacitors.

Key words: colloid, dispersion, manganese dioxide, hausmannite, carbon nanotubes, polypyrrole, electrophoretic deposition, heterocoagulation, supercapacitor, asymmetric

## **Acknowledgement**

First of all, I would like to express my deepest gratitude to my supervisor Professor Igor Zhitomirsky for constant support, kind guidance, patience and valuable suggestions to both my research and my life. It is an honor working with you.

I would also like to thank all my committee members, Dr. Hatem Zurob and Dr. Gu Xu, for their valuable time in evaluating my research work and provide useful suggestions and comments. I would also like to thank Dr. Shiping Zhu, Dr. Neslihan Dogan and Dr. Dmitri Malakhov participating my proposal exam, comprehensive exam. I pass over my sincere gratutes to Dr. Alex Adronov, Dr. Younggy Kim and Dr. John Wen for their participations and suggestions to my PhD dissertation exam. I hereby also sincerely thank the graduate course teachers Dr. Igor Zhitomirsky, Dr. Gu Xu, Dr. James Britten, Dr. Hatem Zurob and Xiaoang Li. I obtained more than I thought from these courses.

Many technicians have helped me testing samples and analyzing results. I am thankful to Megan Fair, Victoria Jarvis, Chris Butcher, Steve Koprach and Frank Gibbs for their assistance and support.

It was truly my pleasure to work at Department of Materials Science and Engineering, McMaster University. I enjoy the time with my wonderful groupmates and friends. I would like to express my appreciation to Yisong Su, Yangshuai Liu, Yeling Zhu, Cameron Wallar, Parick Wojtal, Dan Luo, Tianshi Zhang, Shilei Chen, Yanchao Sun, Jieming Li, Kaiyuan Shi, Ryan Poon, Jordan Milen, Ri Chen, Aseeb Syed, Fan Haoyu, Xinya Zhao, Amanda

Clifford, Ali Goger, Mehmet Filiz for their generous help in course work, research projects and daily life.

I am very thankful for the financial support from the National Education of Republic of Turkey.

I owe a special thanks to my family who supported me and helped me throughout my life and during this study. I dedicate this work to you all. Dear mom, dad I have no idea how to thank you enough for providing me with the opportunity to be where I am today. I love you so much.

I also dedicate this Ph.D. thesis to my two lovely children, Salih and Elif who are the pride and joy of my life. I love you more than anything and I appreciate all your patience and support during my Ph.D. studies.

At last I do not know how to begin with saying thank you to my soul mate, my dearest wife and my best friend, Hilal. I love you for your patience, for being so understanding and for putting up with me through the toughest moments of my life. I thank Allah (God) for enlightening my life with your presence. You are the best thing that has ever happened to me.

## Declaration of Academic Achievements

This dissertation was used to fulfill the requirements of Ph.D. degree. The major research project was undertaken from September 2012 to August 2017.

The author of this dissertation and the supervisor are the major contributor to the presented materials. As the primary author, contributions included but not limited to literature review, proposal and approaches, experiments setup, materials synthesis, film preparation, electrochemical tests, materials characterization, data analysis, and journal article writing.

The results of this dissertation were published in 9 papers in peer-reviewed journals, which were listed below:

1. **Mustafa S Ata** and Igor Zhitomirsky, *Colloidal methods for the fabrication of  $Mn_3O_4$ -MWCNT electrodes with high areal capacitance*, **Journal of Colloid and Interface Science**, submitted
2. **Mustafa S Ata**, Sohan Ghosh, Igor Zhitomirsky, *Electrostatic assembly of composite supercapacitor electrodes, triggered by charged dispersants*, **Journal of Materials Chemistry A**, 2016, 4(45), 17857-17865
3. **Mustafa S Ata**, Patrick Wojtal, Igor Zhitomirsky, *Electrophoretic deposition of materials using humic acid as a dispersant and film forming agent*, **Colloids and Surfaces A: Physicochemical and Engineering Aspects**, 2016, 493, 74-82

4. **Mustafa S Ata** and Igor Zhitomirsky, *Electrochemical Deposition of Composites Using Deoxycholic Acid Dispersant*, **Materials and Manufacturing Processes**, 2016, 31(1), 67-73
5. **Mustafa S Ata**, Patrick Wojtal, Igor Zhitomirsky, *Surface modification and electrophoretic deposition of materials using carboxyalkylphosphonic acids*, **Materials Letter**, 2016, 184, 320-323
6. **Mustafa S Ata** and Igor Zhitomirsky, *Colloidal methods for the fabrication of carbon nanotube–manganese dioxide and carbon nanotube–polypyrrole composites using bile acids*, **Journal of Colloid and Interface Science**, 2015, 454, 27-34
7. **Mustafa S Ata**, Guo-zhen Zhu, Gianluigi Botton, Igor Zhitomirsky, *Electrophoretic deposition of manganese dioxide films using new dispersing agents*, **Advances in Applied Ceramics**, 2014, 113(1), 22-27
8. **Mustafa S Ata**, Yangshuai Liu, Igor Zhitomirsky, *A review of new methods of surface chemical modification, dispersion and electrophoretic deposition of metal oxide particles*, **RSC Advances**, 2014, 4, 22716-22732.

In addition to the work presented at here, I was the co-first author or co-author of 3 papers relevant to my thesis study.

9. Yangshuai Liu, Dan Luo, **Mustafa S. Ata**, Tianshi Zhang, Cameron J. Wallar, Igor Zhitomirsky, *Universal dispersing agent for electrophoretic deposition of inorganic materials with improved adsorption, triggered by chelating monomers*, **Journal of Colloid and Interface Science**, 2016, 462, 1-8
10. Yangshuai Liu, **Mustafa S. Ata**, Kaiyuan Shi, Guo-zhen Zhu, Gianluigi Botton, I. Zhitomirsky, *Surface modification and cathodic electrophoretic deposition of ceramic materials and composites using Celestine blue dye*, **RSC advances**, 2014, 4(56), 29652-29659

11. Yanchou Sun, **Mustafa S. Ata**, Igor Zhitomirsky, *Electrophoretic deposition of linear polyethylenimine and composite films*, **Surface Engineering**, 29(7), 495-499

## Table of Contents

|  |               |
|--|---------------|
| <b>Abstract.....</b>                               | <b>IV</b>     |
| <b>Acknowledgement.....</b>                        | <b>VI</b>     |
| <b>Declaration of Academic Achievements.....</b>   | <b>VIII</b>   |
| <b>Table of Contents.....</b>                      | <b>X</b>      |
| <b>List of Figures.....</b>                        | <b>XIV</b>    |
| <b>List of Tables.....</b>                         | <b>XXVI</b>   |
| <b>List of Abbreviations and Symbols.....</b>      | <b>XXVIII</b> |
| <b>Chapter 1 Introduction.....</b>                 | <b>1</b>      |
| References:.....                                   | 4             |
| <b>Chapter 2 Literature Review.....</b>            | <b>5</b>      |
| 2.1 History of supercapacitors technology.....     | 5             |
| 2.2 Principles of energy storage.....              | 6             |
| 2.2.1 Electrochemical double-layer capacitors..... | 6             |
| 2.2.2 Pseudocapacitors.....                        | 7             |
| 2.2.3 Hybrid systems.....                          | 10            |
| 2.2.4 Supercapacitor parameters.....               | 12            |
| 2.2.5 Comparison of energy storage mechanisms..... | 13            |
| 2.2.6 Applications of supercapacitors.....         | 15            |
| 2.3 Electrode materials.....                       | 16            |
| 2.3.1 Carbon supercapacitors.....                  | 17            |
| 2.3.1.1 Activated carbons.....                     | 18            |
| 2.3.1.2 Carbon Aerogels.....                       | 19            |
| 2.3.1.3 Carbon nanotubes.....                      | 20            |
| 2.3.1.4 Graphene.....                              | 21            |
| 2.3.2 Metal oxides.....                            | 23            |
| 2.3.2.1 Ruthenium oxide.....                       | 24            |
| 2.3.2.2 Nickel Oxide.....                          | 25            |
| 2.3.2.3 Cobalt oxide.....                          | 26            |

|   |   |           |
|---|---|-----------|
| 2.3.2.4   | Iron oxide .....  | 26        |
| 2.3.2.5   | Vanadium oxide .....  | 27        |
| 2.3.2.6   | Manganese oxide .....   | 27        |
| 2.3.2.7   | Other metal oxides .....  | 29        |
| 2.3.3   | Conducting polymers .....   | 30        |
| 2.3.4   | Summary of Electrode Materials .....  | 33        |
| 2.4   | Electrolytes .....  | 34        |
| 2.4.1   | Aqueous electrolyte .....   | 35        |
| 2.4.2   | Organic electrolytes .....  | 37        |
| 2.4.3   | Ionic liquids .....   | 37        |
| 2.5   | Fundamentals of electrode fabrication .....                                     | 39        |
| 2.5.1   | Thin film electrodes .....  | 40        |
| 2.5.2   | Composite electrodes .....  | 47        |
|   | References: .....   | 49        |
| <b>Chapter 3 Objectives .....</b>   |   | <b>62</b> |
| <b>Chapter 4 Experimental procedures .....</b>  |   | <b>63</b> |
| 4.1   | Starting materials .....  | 63        |
| 4.2   | Materials synthesis .....   | 65        |
| 4.3   | Electrophoretic deposition procedure .....                                      | 66        |
| 4.4   | Electrode and ES device fabrication using slurry impregnation .....             | 70        |
| 4.5   | Fabrication of negative electrodes for ES devices .....                         | 71        |
| 4.6   | Materials characterization .....  | 71        |
| 4.7   | Electrochemical characterization .....  | 73        |
| 4.7.1   | Cyclic voltammetry .....  | 73        |
| 4.7.2   | Electrochemical impedance spectroscopy .....                                    | 74        |
| 4.7.3   | Cyclic charge-discharge .....   | 75        |
|   | References: .....   | 75        |
| <b>Chapter 5 Colloidal methods for the fabrication of MnO<sub>2</sub>-MWCNT and PPy-MWCNT composites using bile acids .....</b> |   | <b>76</b> |
| 5.1   | Fundamental aspects of bile acids .....   | 76        |
| 5.2   | Dispersion and deposition mechanism of ChNa and TChNa .....                     | 78        |
| 5.3   | Mechanism of ChNa film formation by using QCM and EPD methods .....             | 79        |
| 5.4   | Adsorption and methodology study of ChNa .....                                  | 82        |
| 5.5   | EPD and characterization of MWCNT dispersed by ChNa and TChNa dispersants ..... | 84        |
| 5.6   | EPD of MnO <sub>2</sub> in the presence of ChNa .....                           | 87        |

|  |  |            |
|--|--|------------|
| 5.7  | Morphology and electrochemical characterization of MnO <sub>2</sub> -MWCNT composite electrodes prepared using ChNa..... | 88         |
| 5.8  | Morphology and electrochemical characterization of PPy-MWCNT composite electrodes with TChNa .....                       | 90         |
| 5.9  | Conclusions.....   | 93         |
|  | References;.....   | 94         |
| <b>Chapter 6 EPD of Composites Using Deoxycholic Acid Dispersant....</b>         |  | <b>97</b>  |
| 6.1  | Mechanism of DCH electrodeposition.....  | 97         |
| 6.2  | Morphology and adsorption study of DCNa.....   | 100        |
| 6.3  | The advantages of using DCNa as a dispersant for MWCNT .....   | 102        |
| 6.4  | EPD of MWCNT using DCNa as a dispersant .....  | 104        |
| 6.5  | Morphology study of MnO <sub>2</sub> and MnO <sub>2</sub> -MWCNT composites.....   | 107        |
| 6.6  | Capacitive performance of MnO <sub>2</sub> -MWCNT composite film .....   | 108        |
| 6.7  | Conclusions.....   | 110        |
|  | Reference .....  | 110        |
| <b>Chapter 7 EPD of MnO<sub>2</sub>-CNT composites using new dispersants ...</b> |  | <b>113</b> |
| 7.1  | Introduction.....  | 113        |
| 7.2  | Structures of PEI, FA, PAH and HA .....  | 114        |
| 7.3  | EPD of PEI and composite film.....   | 115        |
| 7.3.1  | Advantages of using polyethylenimine.....  | 115        |
| 7.3.2  | Preparation, kinetics and morphology of LPEI.....  | 117        |
| 7.3.3  | Morphology study of MnO <sub>2</sub> , deposited using PEI.....  | 119        |
| 7.4  | Properties and applications of FA.....   | 122        |
| 7.4.1  | EPD of MnO <sub>2</sub> using FA .....   | 122        |
| 7.4.2  | FTIR characterization of FA adsorption.....  | 125        |
| 7.5  | Pamoic acid as a film forming dispersant.....  | 126        |
| 7.5.1  | Deposition kinetics and morphology study of PAH .....  | 128        |
| 7.6  | Humic acid as a dispersant and film forming agent.....   | 129        |
| 7.6.1  | Mechanism of electrodeposition of HA .....   | 131        |
| 7.6.2  | EPD of different materials using HA as a dispersant .....  | 136        |
| 7.6.3  | Co-deposition of MnO <sub>2</sub> and MWCNT nanoparticles .....  | 140        |
| 7.6.4  | Capacitive performance of MnO <sub>2</sub> -MWCNT composite film .....   | 141        |
| 7.7  | Conclusions.....   | 144        |
| 7.8  | Acknowledgement .....  | 146        |
|  | References:.....   | 146        |

|  |            |
|--|------------|
| <b>Chapter 8 Surface modification and EPD of materials using carboxyalkylphosphonic acids .....</b>                                      | <b>156</b> |
| 8.1 Fundamental aspects and adsorption mechanisms of phosphonic acids.....   | 156        |
| 8.2 EPD of MnO <sub>2</sub> in presence of 3PHA and 16PHA.....   | 158        |
| 8.3 Adsorption and morphology study of 3PHA and 16PHA .....  | 159        |
| 8.4 Electrochemical characterization of MnO <sub>2</sub> -MWCNT composite electrodes in presence of 3PHA and 16PHA .....                 | 161        |
| 8.5 Conclusions.....   | 164        |
| References;.....   | 165        |
| <b>Chapter 9 Electrostatic assembly of composite supercapacitor electrodes, triggered by charged dispersants .....</b>                   | <b>166</b> |
| 9.1 Electrostatic heterocoagulation in non-aqueous solvent.....  | 166        |
| 9.2 EPD of MnO <sub>2</sub> using PHA, PGR and PCA as dispersants.....   | 170        |
| 9.3 Electrochemical characterization of deposited films .....  | 174        |
| 9.4 Morphology of composite electrodes before and after cycling tests .....  | 181        |
| 9.5 Electrochemical characterization of asymmetric device.....   | 184        |
| 9.6 Conclusion .....   | 188        |
| Reference: .....   | 189        |
| <b>Chapter 10 EPD of Mn<sub>3</sub>O<sub>4</sub> using CA and CIB.....</b>   | <b>193</b> |
| 10.1 Introduction.....   | 193        |
| 10.2 EPD of Mn <sub>3</sub> O <sub>4</sub> using CA .....  | 195        |
| 10.3 EPD of Mn <sub>3</sub> O <sub>4</sub> using CIB .....   | 198        |
| 10.4 Electrochemical characterization of Mn <sub>3</sub> O <sub>4</sub> -MWCNT composite electrodes prepared using CIB .....             | 203        |
| 10.5 Conclusion .....  | 205        |
| References:.....   | 205        |
| <b>Chapter 11 Colloidal methods for the fabrication of Mn<sub>3</sub>O<sub>4</sub>-MWCNT electrodes with high areal capacitance.....</b> | <b>209</b> |
| 11.1 Introduction.....   | 209        |
| 11.2 Morphology study of Mn <sub>3</sub> O <sub>4</sub> using P(SSA-MA).....   | 212        |
| 11.3 Electrochemical capacitive performance of Mn <sub>3</sub> O <sub>4</sub> using EV.....  | 218        |
| 11.4 Electrochemical capacitive performance of Mn <sub>3</sub> O <sub>4</sub> using PY .....   | 222        |
| 11.5 Conclusion .....  | 226        |
| References:.....   | 227        |
| <b>Chapter 12 Conclusions .....</b>  | <b>232</b> |

**Future works ..... 236**

## **List of Figures**

Figure 2-1 Schematic representation of EDCL type ESs [9]..... 7

Figure 2-2 Schematic illustration of pseudocapacitor type ESs[9]..... 8

Figure 2-3 Different types of pseudocapacitive behavior from B.E. Conway: (a) underpotential deposition, (b) redox pseudocapacitance, and (c) intercalation pseudocapacitance[15]..... 9

Figure 2-4 Schematic illustration of hybrid type ESs[9] ..... 11

Figure 2-5 Sketch of Ragone plot for various energy storage and conversion devices. The cross line is the time constants of the devices[12]..... 14

Figure 2-6 Taxonomy of the supercapacitor materials[24]..... 17

Figure 2-7 Carbon properties and their role in supercapacitors[34]..... 19

Figure 2-8 Conceptual diagram of single-walled carbon nanotube (SWCNT) (A) and multiwalled carbon nanotube (MWCNT) (B) delivery systems showing typical dimensions of length, width, and the separation distance between graphene layers in MWCNTs[45].  
..... 21

Figure 2-9 Schematic depiction of (a) the stacked geometry (b) the operating principle in case of the in-plane supercapacitor device[51]..... 22

Figure 2-10 The maximum specific capacitance values reported from the addition of different pseudocapacitive functionalizing materials[77]..... 30

|  |    |
|--|----|
| Figure 2-11 Schematic diagram of charging-discharging state for (a) p-type and (b) n-type CP electrodes[8].  | 32 |
| Figure 2-12 The reported specific capacitances for both EDLCs and pseudocapacitors including metal oxides and conducting polymers in single or composite electrode materials[129]. | 33 |
| Figure 2-13 Effects of the electrolyte on the ES performance[130].   | 35 |
| Figure 2-14 The working potential windows of various electrode materials in aqueous electrolyte[135].  | 36 |
| Figure 2-15 Basic types of ionic liquids: aprotic, protic and zwitterionic types.  | 38 |
| Figure 2-16 Schematic of cathodic EPD and ELD[143].  | 41 |
| Figure 2-17 Schematic illustration of interaction between two particles in suspension....  | 41 |
| Figure 2-18 Schematic of the interaction energy as a function of separation between two particles in suspension[143].  | 44 |
| Figure 2-19 Schematic aggregation process from stable suspension to sedimentation[146].  | 44 |
| Figure 4-1 Schematic illustration of MnO <sub>2</sub> synthesizing process.  | 65 |
| Figure 4-2 Schematic procedure of EPD  | 67 |
| Figure 4-3 Schematic representation of material impregnation into Ni foam collector ....   | 71 |
| Figure 4-4 Princeton PARSTAT 2273 potentiostat and scheme of three-electrode setup.  | 73 |
| Figure 5-1 Chemical structures of (A) ChNa and (B) TChNa.  | 79 |
| Figure 5-2 Deposit mass versus time measured by QCM for 0.1 g L <sup>-1</sup> ChNa solution at a deposition voltage 3 V.   | 80 |

Figure 5-3 Deposit mass versus ChNa concentration in solutions at deposit voltage of 10 V and deposition time of 5 min. .... 81

Figure 5-4 CVs for stainless steel electrode in 2g L<sup>-1</sup> ChNa solution at a scan rate of 20 mV s<sup>-1</sup>, arrow shows increasing cycle number. .... 82

Figure 5-5 FTIR spectra for (a) as received ChNa and (b) deposit, prepared from 1 g L<sup>-1</sup> ChNa solution at a deposition voltage of 10 V. .... 83

Figure 5-6 (A and B) SEM images at different magnifications for deposit, prepared from 2 g L<sup>-1</sup> ChNa solution at a deposition voltage of 10 V. .... 84

Figure 5-7 Deposit mass for deposits prepared from 1 g L<sup>-1</sup> MWCNT suspensions at a deposition voltage of 10 V versus (A) ChNa concentration at a deposition time of 5 min, (B) time at ChNa concentration of 1 g L<sup>-1</sup>, (C) TChNa concentration at a deposition time of 5 min, and (D) time at TChNa concentration of 1 g L<sup>-1</sup>. .... 86

Figure 5-8 SEM images of deposits prepared at a deposition voltage of 10 V for 1 g L<sup>-1</sup> MWCNT suspension containing (A) 1 g L<sup>-1</sup> ChNa and (B) 1 g L<sup>-1</sup> TChNa. .... 87

Figure 5-9 Deposit mass versus time for 4 g L<sup>-1</sup> MnO<sub>2</sub> suspensions, containing 0.5 g L<sup>-1</sup> ChNa at a deposition voltage of 10 V. .... 88

Figure 5-10 SEM images of deposit obtained from a suspension, containing 4 g L<sup>-1</sup> MnO<sub>2</sub>, 1 g L<sup>-1</sup> MWCNT and 1 g L<sup>-1</sup> ChNa. .... 89

Figure 5-11 (A) CV at a scan rate at 5 mV s<sup>-1</sup>, (B) specific capacitance versus scan rate, (C) real part C' and (D) imaginary part C'' of capacitance, calculated from the impedance data for MnO<sub>2</sub>-MWCNT composite, prepared by EPD using ChNa as a dispersant. .... 90

Figure 5-12 SEM image of PPy coated MWCNT prepared using TChNa as a dispersant 92

Figure 5-13 (A) CV at a scan rate at  $5 \text{ mV s}^{-1}$ , (B) specific capacitance versus scan rate, (C) real part  $C'$  and (D) imaginary part  $C''$  of capacitance, calculated from the impedance data for PPy coated MWCNT, prepared using TChNa as a dispersant. .... 92

Figure 6-1 Structure of DCNa..... 98

Figure 6-2 CVs for a SS electrode in  $1 \text{ g L}^{-1}$  DCNa solution at  $0.02 \text{ V s}^{-1}$  for different cycle numbers from 1 to 10, obtained using a standard SCE reference electrode. .... 99

Figure 6-3 QCM in-situ measurements data for deposition yield in  $0.1 \text{ g L}^{-1}$  DCNa solution at a voltage of 3V..... 100

Figure 6-4 Film mass as a function of DCNa concentration in solutions at a constant cell voltage of 10 V and deposition duration of 5 min. .... 100

Figure 6-5 (A, B) SEM images at different magnifications of a DCH film, deposited using  $2 \text{ g L}^{-1}$  DCNa solution at a constant cell voltage of 10 V..... 101

Figure 6-6 FTIR for (a) DCNa and (b) DCH film material, obtained from  $1 \text{ g L}^{-1}$  DCNa solution at a constant cell voltage of 10 V..... 102

Figure 6-7 Deposit mass as a function of DCNa concentrations in  $1 \text{ g L}^{-1}$  MWCNT suspension at a deposition voltage of 10 V and deposition duration of 5 min. .... 105

Figure 6-8 SEM images of a MWCNT film at different magnifications..... 106

Figure 6-9 FTIR for (a) as-received MWCNT and (b) deposited MWCNT ..... 107

Figure 6-10 SEM images of (A)  $\text{MnO}_2$  and (B)  $\text{MnO}_2$ -MWCNT composite film. .... 108

Figure 6-11 (A) CV at  $5 \text{ mV s}^{-1}$  obtained using a standard SCE reference electrode (B) capacitance as a function of scan rate, (C, D) frequency dependencies of  $C_s^*$  components for  $\text{MnO}_2$ -MWCNT composite electrode in  $0.5 \text{ M Na}_2\text{SO}_4$  solutions..... 109

|  |     |
|--|-----|
| Figure 7-1 Chemical structures of (A) PEI, (B) FA, (C) PAH and (D) HA .....  | 115 |
| Figure 7-2 Film mass versus deposition time, measured using QCM for 0.1g L <sup>-1</sup> LPEI-H <sup>+</sup> solutions at deposition voltages of (a) 4 V, (b) 7 V and (c) 10 V. ....   | 118 |
| Figure 7-3 SEM images of cross-sections of LPEI films obtained from 1 g L <sup>-1</sup> LPEI-H <sup>+</sup> solutions at deposition voltage of 10 V and deposition times of (a) 3 min and (b) 10 min [arrows show film (F) and conductive Pt layer deposited on silicon substrate (S)] ..... | 118 |
| Figure 7-4 SEM images of (A) surface and (B) cross-section of film deposited from 1 g L <sup>-1</sup> LPEI-H <sup>+</sup> solution, containing 10 g L <sup>-1</sup> MnO <sub>2</sub> at a deposition voltage of 20 V during 5 min. ....  | 120 |
| Figure 7-5 TGA data for (A) pure-LPEI and (B) a–pure-MnO <sub>2</sub> and b–composite deposits prepared from 1 g L <sup>-1</sup> LPEI-H <sup>+</sup> solution, containing 10 g L <sup>-1</sup> MnO <sub>2</sub> .....  | 121 |
| Figure 7-6 Adsorption mechanism of FA .....  | 123 |
| Figure 7-7 Deposit mass versus FA concentration in 4 g L <sup>-1</sup> MnO <sub>2</sub> suspension at a deposition voltage 20 V and a deposition time 5min.....  | 124 |
| Figure 7-8 Deposit mass versus deposition time for 4 g L <sup>-1</sup> MnO <sub>2</sub> suspension, containing 0.5 g L <sup>-1</sup> FA at a deposition voltage 20V.....   | 124 |
| Figure 7-9 FTIR spectra of (a) pure FA powder and (b) 4 g L <sup>-1</sup> MnO <sub>2</sub> suspensions containing 0.5 g L <sup>-1</sup> FA.....  | 126 |
| Figure 7-10 Adsorption mechanisms of PAH (A) bis-bidentate and (B) bis-monodentate (C) bidentate chelatin and (D) bidentate bridging bonding. ....   | 127 |

Figure 7-11 Film mass measured using QCM for PAH film on a gold coated quartz electrode with area of  $0.2 \text{ cm}^2$  at a deposition voltage of 3 V (distance between electrodes 10 mm), deposited from  $0.1 \text{ g L}^{-1}$  PANa solution in water. .... 129

Figure 7-12 (A and B) SEM images of PAH film at different magnifications. .... 129

Figure 7-13 Schematic of the chemical structure of HA, showing chelating groups (a-catechol ligand, b-salicylate ligand). .... 132

Figure 7-14 Deposit mass versus time obtained using QCM from  $0.1 \text{ g L}^{-1}$  HA solutions in (A) water and (B) mixed ethanol–water (50% water) solvent at deposition voltages of (a) 3 V and (b) 5 V. .... 134

Figure 7-15 Deposit mass versus HA concentration in a mixed water-ethanol solvent (50%water) at a deposition voltage of 100 V and deposition time of 5 min. .... 135

Figure 7-16 SEM image of HA film prepared from  $1 \text{ g L}^{-1}$  HA solution in a mixed water–ethanol solvent (50% water). .... 136

Figure 7-17 (A and B) SEM images at different magnifications of a deposit obtained from  $0.5 \text{ g L}^{-1}$  HA solutions in a mixed water-ethanol solvent (50% water), containing  $4 \text{ g L}^{-1} \text{ MnO}_2$ . .... 138

Figure 7-18 (A and B) SEM images at different magnifications of a deposit, prepared from  $0.5 \text{ g L}^{-1}$  HA solutions in a mixed water-ethanol solvent (50% water), containing  $4 \text{ g L}^{-1}$  MWCNT. .... 138

Figure 7-19 SEM images at different magnifications of deposits, prepared from  $0.5 \text{ g L}^{-1}$  HA solutions in a mixed water–ethanol solvent (50% water), containing  $4 \text{ g L}^{-1}$  (A, B) Pd and (C, D) Ni nanoparticles. .... 139

Figure 7-20 SEM images of composites, deposited from  $0.5 \text{ g L}^{-1}$  HA solutions in a mixed water–ethanol solvent (50% water), containing  $4 \text{ g L}^{-1}$   $\text{MnO}_2$  and (A)  $0.25$ , (B)  $0.5 \text{ g L}^{-1}$  MWCNT. .... 141

Figure 7-21 (A) CV at a scan rate of  $2 \text{ mV s}^{-1}$ , (B) specific capacitance versus scan rate, (C) real  $C'$  and (D) imaginary  $C''$  parts of capacitance, derived from the impedance data, versus frequency for  $\text{MnO}_2$ –MWCNT electrodes, prepared from  $0.5 \text{ g L}^{-1}$  HA solutions in a mixed water–ethanol solvent (50% water), containing  $4 \text{ g L}^{-1}$   $\text{MnO}_2$  and  $0.5 \text{ g L}^{-1}$  MWCNT. .... 143

Figure 7-22 Capacitance retention versus cycle number for the composite  $\text{MnO}_2$ –MWCNT electrodes, prepared from  $0.5 \text{ g L}^{-1}$  HA solutions in a mixed water-ethanol solvent (50% water), containing  $4 \text{ g L}^{-1}$   $\text{MnO}_2$  and  $0.5 \text{ g L}^{-1}$  MWCNT. .... 144

Figure 8-1 Bonding modes (A) of phosphonic acids to metal atoms (M) on inorganic surfaces: (a) chelating bidentate, (b) bridging bidentate, (c) bridging tridentate and (d) chelating tridentate; chemical structures of (B) 3PHA, (C) 16PHA and (D) octaPHA... 157

Figure 8-2 Deposit mass versus deposition time at a deposition voltage of  $20 \text{ V}$  for (A)  $4 \text{ g L}^{-1}$   $\text{MnO}_2$  suspensions, containing  $0.3 \text{ g L}^{-1}$  of (a) 3PHA and (b) 16PHA. .... 159

Figure 8-3 FTIR spectra of  $\text{MnO}_2$  deposits prepared using (a) 3PHA and (b) 16PHA. ... 160

Figure 8-4 SEM images of  $\text{MnO}_2$  films, deposited from  $4 \text{ g L}^{-1}$   $\text{MnO}_2$  suspensions, containing  $0.3 \text{ g L}^{-1}$  of (A) 3PHA and (B) 16PHA at a deposition voltage of  $20 \text{ V}$ . ..... 161

Figure 8-5 (A) Cyclic voltammetry (CV) data at a scan rate of  $2 \text{ mV s}^{-1}$  (B) capacitance, calculated from the CV data versus scan rate, (C) real part  $C'_s$  and (D) imaginary part  $C''_s$  of complex areal capacitance  $C^*_s = C'_s - iC''_s$  versus frequency, calculated from the

XX

impedance data for the MnO<sub>2</sub> electrodes, prepared using 3PHA as a dispersant and multiwalled carbon nanotubes (20 mass %) as a conductive additive, using 0.5 M Na<sub>2</sub>SO<sub>4</sub> electrolyte..... 162

Figure 8-6 (A) Cyclic voltammetry (CV) data at a scan rate of 2 mV s<sup>-1</sup> (B) capacitance, calculated from the CV data versus scan rate, (C) real part C'<sub>s</sub> and (D) imaginary part C''<sub>s</sub> of complex areal capacitance C\*<sub>s</sub> = C'<sub>s</sub> - iC''<sub>s</sub> versus frequency, calculated from the impedance data for the MnO<sub>2</sub> electrodes, prepared using 16PHA as a dispersant and multiwalled carbon nanotubes (20 mass %) as a conductive additive, using 0.5 M Na<sub>2</sub>SO<sub>4</sub> electrolyte..... 163

Figure 9-1 Chemical structures of (A) PHA, (B) PGR, (C) PCA, (D) AZA and (E) NB 167

Figure 9-2 Bonding mechanisms of (A-D) PHA, (E, D) PGR, and (G) PCA, involving Mn atoms (M) on the particle surface. .... 169

Figure 9-3 Comparison of suspension stability of (a) without dispersant, (b) PHA, (c) PGR, and (d) PCA in 4 g L<sup>-1</sup> MnO<sub>2</sub> suspension with 0.2 g L<sup>-1</sup> additive concentration after 3 days. .... 170

Figure 9-4 Deposit mass as a function of the concentration of (A) PHA and (C) PCA in 4 g L<sup>-1</sup> MnO<sub>2</sub> at a deposition voltage of 20 V and (B) PGR 10 g L<sup>-1</sup> MnO<sub>2</sub> suspension at a deposition voltage of 50 V and deposition time of 5 min. .... 172

Figure 9-5 FTIR spectra for MnO<sub>2</sub> particles, deposited by EPD using (a) PHA, (b) PGR and (c) PCA..... 174

Figure 9-6 (A,B,C) CVs for MnO<sub>2</sub>-MWCNT electrodes prepared (A) without dispersant, (B) using PGR and AZA, (C) using PGR and NB at scan rates of (a) 2, (b) 5 and (c) 10 mV

$s^{-1}$  and (D) SC versus scan rate for electrodes prepared using (a) PGR and AZA, (b) PGR and NB ..... 177

Figure 9-7 (A) Nyquist plot for complex impedance and frequency dependences of (B)  $C_s'$  and (C)  $C_s''$  for  $MnO_2$ -MWCNT electrodes prepared using (a) PGR and AZA, (b) PGR and NB and (c) without dispersants ..... 178

Figure 9-8 (A,B,D,E) CVs at scan rates of (a) 2, (b) 5 and (c)  $10\text{ mV s}^{-1}$  and (C,F)  $C_s$  versus scan rate dependences for  $MnO_2$ -MWCNT electrodes prepared using (A), (C(a)) PCA and AZA, (B), (C(b)) PCA and NB; (D), (F(a)) PHA and AZA and (E), (F(b)) PHA and NB. .... 179

Figure 9-9 (A,D) Nyquist plots of complex impedance; frequency dependences of (B,E)  $C_s'$  and (C,F)  $C_s''$  for  $MnO_2$ -MWCNT electrodes, prepared using (A(a)), (B(a)) and (C(a)) PCA and AZA, (A(b)), (B(b)) and (C(b)) PCA and NB, (D(a)), (E(a)) and (F(a)) PHA and AZA, (D(b)), (E(b)) and (F(b)) PHA and NB. .... 180

Figure 9-10 SEM images of (A)  $MnO_2$  powder, (B)  $MnO_2$ -MWCNT composite prepared without dispersants, (C)  $MnO_2$ -MWCNT composite prepared using PHA and NB dispersants before electrochemical cycling, (C)  $MnO_2$ -MWCNT composite prepared using PHA and NB dispersants after 1000 cycles ..... 182

Figure 9-11 Capacitance retention versus cycle number at a scan rate of  $50\text{ mV s}^{-1}$  for  $MnO_2$ -MWCNT electrodes, prepared using PHA and NB dispersants. .... 183

Figure 9-12 X-ray diffraction patterns of (a) as-prepared  $MnO_2$  powder and (b)  $MnO_2$ -MWCNT electrode, prepared using PHA and NB dispersants and Ni current collector, after 1000 cycles..... 183

Figure 9-13 (A) CVs at scan rates of (a) 2, (b) 5 and (c) 10  $\text{mV s}^{-1}$ , (B) capacitance versus scan rate and (C) galvanostatic charge-discharge curves at currents at (a) 3, (b) 5, (c) 7.5 and (d) 10 mA for asymmetric coin cell capacitors, containing  $\text{MnO}_2$ -MWCNT positive and AC-CB negative electrodes..... 185

Figure 9-14 (A) Nyquist plot of complex impedance and (B,C) frequency dependences of components of complex capacitance: (B)  $C_s'$  and (C)  $C_s''$  for asymmetric coin cell capacitors, containing  $\text{MnO}_2$ -MWCNT positive and AC-CB negative electrodes..... 186

Figure 9-15 Capacitance retention versus cycle number at a scan rate of 50  $\text{mV s}^{-1}$  for asymmetric capacitor cell containing  $\text{MnO}_2$ -MWCNT positive and AC-CB negative electrode..... 187

Figure 9-17 LED bulbs powered by supercapacitor devices. .... 187

Figure 10-1 (A) XRD (B) TEM images of  $\text{Mn}_3\text{O}_4$  prepared at 60°C. .... 194

Figure 10-2 Chemical structure of (A) CA and (B) ClB ..... 195

Figure 10-3 Possible adsorption mechanisms of CA: (a) bidentate chelating bonding, (b) bidentate bridging bonding (inner sphere), (c) bidentate bridging bonding (outer sphere) of catechol group, (d) adsorption, involving a carboxylic group. .... 196

Figure 10-4 Deposit mass versus CA concentration in 10  $\text{g L}^{-1}$   $\text{Mn}_3\text{O}_4$  suspension at a deposition voltage 20 V and a deposition time 5 min..... 198

Figure 10-5 Deposit mass versus deposition time for 10  $\text{g L}^{-1}$   $\text{Mn}_3\text{O}_4$  suspension, containing 0.5  $\text{g L}^{-1}$  CA at a deposition voltage of 20 V..... 198

Figure 10-6 Suggested adsorption mechanism of ClB, involving metal atoms M on a particle surface: (A) bidentate bridging bonding and (B) bidentate chelating bonding. .200

Figure 10-7 Deposit mass versus ClB concentration in  $4 \text{ g L}^{-1} \text{ Mn}_3\text{O}_4$  suspension at a deposition voltage 20 V and a deposition time 5 min.....201

Figure 10-8 Deposit mass versus deposition time for  $4 \text{ g L}^{-1} \text{ Mn}_3\text{O}_4$  suspension, containing  $0.5 \text{ g L}^{-1}$  ClB at a deposition voltage of 20 V. ....201

Figure 10-9 SEM images of films, prepared from  $4 \text{ g L}^{-1}$  suspensions of (A)  $\text{Mn}_3\text{O}_4$ , containing  $0.5 \text{ g L}^{-1}$  ClB at a deposition voltage of 20 V.....202

Figure 10-10 (a) FTIR and (b)UV-vis data for deposits, prepared from  $4 \text{ g L}^{-1}$  suspensions of  $\text{Mn}_3\text{O}_4$ , containing  $0.5 \text{ g L}^{-1}$  ClB at a deposition voltage of 20 V. ....203

Figure 10-11 (A) CVs at scan rate (a) 2 (b) 5 and (c)  $10 \text{ mV s}^{-1}$ , (B) specific capacitance versus scan rate, (C) real part  $C'_s$  and (D) imaginary part  $C''_s$  of complex areal capacitance  $C^*_s = C'_s - iC''_s$  versus frequency, calculated from the impedance data for the  $\text{MnO}_2$  electrodes, prepared using ClB as a dispersant and MWCNT (20 mass %) as conductive additive, using  $0.5 \text{ M Na}_2\text{SO}_4$  electrolyte.....204

Figure 11-1 (A) Chemical structure of P(SSA-MA) and (B-D) adsorption of P(SSA-MA) on  $\text{Mn}_3\text{O}_4$ , involving (B) complexation, (C) outer-sphere bonding and (D) inner-sphere bonding of Mn atoms on the particle surface by MA monomers. ....213

Figure 11-2 X-ray diffraction pattern of  $\text{Mn}_3\text{O}_4$ . ....215

Figure 11-3 SEM images of  $\text{Mn}_3\text{O}_4$  powder at different magnifications. ....216

Figure 11-4 Chemical structure of (A) EV and (B) PY. ....218

Figure 11-5 CVs at a scan rate of  $10 \text{ mV s}^{-1}$  for as-prepared (A) composite 1 and (B) composite 2. ....219

Figure 11-6 Specific capacitance versus scan rate for composite 1 for TPs: (a) 1, (b) 2, (c) 3, (d) 4.....220

Figure 11-7 Nyquist plot of complex impedance for composite 1: (A) as prepared and (B) after TPs (a) 1, (b) 2, (c) 3 and (d) 4. ....220

Figure 11-8 Frequency dependences of real ( $C'_s$ ) and imaginary ( $C''_s$ ) components of complex capacitance for composite 1, calculated from the impedance data, obtained after TPs (a) 1, (b) 2, (c) 3 and (d) 4. ....221

Figure 11-9 (A) Capacitance variation with the cycle number at a scan rate of  $50 \text{ mV s}^{-1}$  for composite 1 after TP4 and (B) corresponding CV for cycles 1, 500 and 1000. The data in (A) is normalized by the capacitance calculated from the CV cycle 1.....222

Figure 11-10 Specific capacitance versus scan rate for composite 2 for TPs: (a) 1, (b) 2, (c) 3, (d) 4.....223

Figure 11-11 Nyquist plot of complex impedance for composite 2: (A) as prepared and (B) after TPs (a) 1, (b) 2, (c) 3 and (d) 4. ....223

Figure 11-12 Frequency dependences of real ( $C'_s$ ) and imaginary ( $C''_s$ ) components of complex capacitance for composite 2, calculated from the impedance data, obtained after TPs (a) 1, (b) 2, (c) 3 and (d) 4. ....224

Figure 11-13 A) Capacitance variation with the cycle number at a scan rate of  $50 \text{ mV s}^{-1}$  for composite 2 after TP4 and (B) corresponding CV for cycles 1, 500 and 1000. The data in (A) is normalized by the capacitance calculated from the CV cycle 1.....224

## List of Tables

|  |     |
|--|-----|
| Table 2-1 Correlations of types of systems giving rise to pseudocapacitance with application to electrochemical capacitors <sup>a</sup> [22] ..... | 10  |
| Table 2-2 Comparison between electrochemical double layer capacitors (EDLC) and pseudocapacitors[23] .....   | 10  |
| Table 2-3 Summary of different types of hybrid supercapacitor devices[25] .....  | 12  |
| Table 2-4 Comparison table among selected electrochemical energy storage technologies[26].....   | 15  |
| Table 2-5 Comparison between batteries and ESs[27] .....   | 15  |
| Table 2-6 Comparison of different carbon materials and their properties in EDLC electrodes[52].....  | 23  |
| Table 2-7 Properties and characteristics of various carbon and carbon-based materials as ESs electrode materials[41] .....                         | 23  |
| Table 2-8 Pseudocapacitance and conductivity of selected metal oxides[25] .....  | 24  |
| Table 2-9 Theoretical and experimental specific capacitances of conducting polymers[125].<br>.....   | 31  |
| Table 2-10 Different electrode synthesis methods in terms of materials, advantages, disadvantages[141] .....                                       | 39  |
| Table 2-11 Electrophoretic and Electrolytic Deposition of Ceramic Materials[143].....  | 45  |
| Table 7-1 Band assignments for pure FA and MnO <sub>2</sub> deposits obtained using FA dispersant.<br>.....  | 125 |

Table 9-1 Band Assignments for MnO<sub>2</sub> deposits obtained using PHA, PGR and PCA..173

Table 9-2 Capacitances, calculated from CV data at scan rates of 2 and 100 mV s<sup>-1</sup> and capacitance retention in the scan rate range of 2-100 mV s<sup>-1</sup> for MnO<sub>2</sub> –MWCNT electrodes, prepared without and with different dispersants..... 176

## List of Abbreviations and Symbols

|           |  |
|-----------|--|
| A (unit)  | Ampere   |
| AC        | Activated Carbon                               |
| aq.       | Aqueous  |
| C         | Capacitor                                      |
| C (unit)  | Coulomb  |
| Cdl       | Double-layer capacitance                       |
| Cm        | Mass normalized specific capacitance           |
| cm (unit) | Centimeter                                     |
| CNT       | Carbon Nanotubes                               |
| Cs        | Areal normalized specific capacitance          |
| CV        | Cyclic Voltammetry                             |
| C $\phi$  | Pseudocapacitance                              |
| DTA       | Differential Thermal Analysis                  |
| Ed        | Energy density                                 |
| EDLC      | Electrochemical Double Layer Capacitor         |
| EIS       | Electrochemical Impedance Spectroscopy         |
| ELD       | Electrolytic Deposition                        |
| EPD       | Electrophoretic Deposition                     |
| ES        | Electrochemical Supercapacitors                |
| ESR       | Equivalent Series Resistance                   |
| F         | Faraday constant (96 485 F mol <sup>-1</sup> ) |
| F (unit)  | Farad  |

|            |   |
|------------|---|
| FTIR       | Fourier transform infrared Spectroscopy |
| g (unit)   | Gram                                    |
| h (unit)   | Hour                                    |
| IHP        | Inner Helmholtz Plane (IHP)             |
| kg (unit)  | Kilogram                                |
| L (unit)   | Liter                                   |
| M (unit)   | Mole per liter                          |
| mM (unit)  | Millimole per liter                     |
| m (unit)   | Meter                                   |
| mg (unit)  | Milligram                               |
| min (unit) | Minute                                  |
| mL (unit)  | Millilitre                              |
| mV (unit)  | Millivoltage                            |
| MWCNT      | Multi-walled Carbon Nanotubes           |
| nm (unit)  | Nanometer                               |
| OHP        | Outer Helmholtz Plane (OHP)             |
| Pd         | Power density                           |
| TGA        | Thermogravimetric analysis              |

## Chapter 1 Introduction

Economic development, climate change and limitation of fossil fuels, awareness for CO pollution generate a need in alternative energy sources and methods of energy storage become increasingly important[1]. Batteries and electrochemical supercapacitors (ESs) play a crucial role, especially for the development of electric and hybrid vehicles. ESs have attracted wide attention for energy storage due to their unique characteristics in term of high power density, excellent reversibility and longer cyclic life than conventional batteries[2]. ESs are used in buses, aircrafts, portable electronic devices such as cellular phones, portable drills, camera flash lights, etc.

ESs are categorized into two types, based on charge-storage mechanism[2]: (1) the electrochemical double layer capacitors (EDLC) and (2) pseudocapacitors. EDLC mechanism is based on the separation of charges at the interface between a solid electrode and an electrolyte[3], whereas pseudocapacitance involves fast, reversible Faradaic reactions which occur in the bulk of the electrode materials or at electrode surface over an appropriate range of potentials[4]. The capacitance of ESs varied in range of microfarads ( $\mu\text{F}$ ) to thousands of farads (kF), at least 1,000 times larger than the capacitance of a typical electrolytic capacitor. ESs are also characterized by lower internal resistance compared to batteries. Active electrode materials such as carbon (carbon nanotubes (CNT), carbon fibers (CF), graphene, activated carbon (AC), carbon black(CB) etc.), conducting polymers (polyaniline, polypyrrole, etc.), and metal oxides (oxides of manganese, ruthenium, nickel, etc.) have received the most interest.

Many transition-metal oxides have been shown to be excellent electrode materials for ESs. Recently, high SC of a hydrous form of  $\text{RuO}_2$  has been reported (above  $600 \text{ F g}^{-1}$  [5]), which is associated with pseudocapacitance. Although  $\text{RuO}_2$  system gives very high SC, it is quite expensive. To bring down the cost, oxides of iron, vanadium, nickel and cobalt in aqueous electrolytes have been explored. Of all the cheap metal oxides,  $\text{MnO}_2$  is the most promising. Low cost, environmentally friendly, long cyclic life, high capacitance (the theoretical SC  $\sim 1370 \text{ F g}^{-1}$ ) [6], and natural abundance of  $\text{MnO}_2$  are its main features. Its potential application as an electrode material for ESs is being extensively studied. The main drawback of  $\text{MnO}_2$  is poor electronic and ionic conductivity which results in low utilization of high theoretical SC in devices. The SC of  $\text{MnO}_2$  reported in literature [7,8] is in the range of  $100\text{-}300 \text{ F g}^{-1}$ , which is quite low compared to its theoretical value.

Carbon materials have advantages of high specific surface area and high conductivity, whereas pseudocapacitive materials have high specific capacitance (SC). It is beneficial to utilize both high surface area and conductivity of carbon materials and high SC of pseudocapacitive materials by combining them together to form composite materials.

It is important to note that dispersing carbon materials and pseudocapacitive materials homogeneously is very critical to achieve composite materials. Dispersant selection plays a crucial role in processing of individual materials. The important task is to find advanced dispersants, suitable for co-dispersion of materials of different types and fabrication of advanced composites.

The typical ES device consists of both anode and cathode immersed in electrolyte and separated by a membrane separator. Based on the materials choice, two different designs,

symmetric and asymmetric, can be developed. For symmetric ES device both anode and cathode electrode materials are same; otherwise, it is named as asymmetric ES device. To achieve the best capacitive performance, the capacitance of cathode and anode must be matched to equal each other.

This work was focused on the fabrication of thin film and bulk ESs using advanced processing techniques. Advanced dispersants were discovered and used for dispersing CNT, graphene, AC, CB, polypyrrole (PPy), and  $\text{MnO}_2$  in water and ethanol solvents. Advanced dispersants were developed for co-dispersion of different materials, such as  $\text{MnO}_x$ , CNT and graphene. Electrophoretic deposition (EPD) method has been utilized for the deposition of oxide particles and carbon nanotubes using advanced dispersants and film forming agents. In the synthesis of electrochemically active materials, dispersants also played roles of capping agents in synthesis of  $\text{MnO}_2$  and dopants for PPy to improve its capacitive performance. The morphologies obtained at different conditions were analyzed and optimized in order to achieve the best electrochemical performance.  $\text{MnO}_x$  nanoparticles and CNT were mixed together on the nanoscale using co-dispersants and the films prepared by EPD method from the mixed suspensions showed good capacitive performance. PPy was coated on the surface of CNT using additives which could disperse CNT in ethanol and work as dopants for PPy. AC/CB composites were developed for negative electrode for the fabrication of  $\text{MnO}_2$ /AC-CB asymmetric ES devices. The capacitance of both anode and cathode and capacitance retention in whole charge/discharge rates range were fitted very well and allowed for the fabrication of advanced devices.

## References:

- [1] Wang, G., Zhang, L., and Zhang, J., 2012, "A Review of Electrode Materials for Electrochemical Supercapacitors," *Chem. Soc. Rev.*, **41**(2), pp. 797–828.
- [2] Conway, B. E., *Electrochemical Supercapacitors - Scientific Fundamentals and Technological Applications*, Springer.
- [3] Sarangapani, S., Tilak, B. V., and Chen, C.-P., 1996, "Materials for Electrochemical Capacitors Theoretical and Experimental Constraints," *J. Electrochem. Soc.*, **143**(11), pp. 3791–3799.
- [4] Zheng, J. P., and Jow, T. R., 1995, "A New Charge Storage Mechanism for Electrochemical Capacitors," *J. Electrochem. Soc.*, **142**(1), pp. L6–L8.
- [5] Simon, P., and Gogotsi, Y., 2008, "Materials for Electrochemical Capacitors," *Nat Mater*, **7**(11), pp. 845–854.
- [6] Devaraj, S., and Munichandraiah, N., 2005, "High Capacitance of Electrodeposited MnO<sub>2</sub> by the Effect of a Surface-Active Agent," *Electrochem. Solid-State Lett.*, **8**(7), pp. A373–A377.
- [7] Toupin, M., Brousse, T., and Bélanger, D., 2002, "Influence of Microstructure on the Charge Storage Properties of Chemically Synthesized Manganese Dioxide," *Chem. Mater.*, **14**(9), pp. 3946–3952.
- [8] Reddy, R. N., and Reddy, R. G., 2003, "Sol–gel MnO<sub>2</sub> as an Electrode Material for Electrochemical Capacitors," *J. Power Sources*, **124**(1), pp. 330–337.

## **Chapter 2 Literature Review**

### **2.1 History of supercapacitors technology**

H.I. Becker[1] from General Electric patented in 1957 the first supercapacitor device, based on the double-layer charge storage mechanism. He used porous carbon electrodes in an aqueous electrolyte. Electrochemical supercapacitors, also called ultracapacitors, or supercapacitors, have been known from the 1800s. First commercial devices developed in 1966 by Standard Oil of Ohio's (SOHIO)[2] researchers utilized the double-layer capacitance of high area carbon in a non-aqueous electrolyte,. The term of "Supercapacitor" was introduced by NEC in 1978 and it was used for computer memory back-up power device[3]. Since then, supercapacitors have generated great interest for a wide and growing range of applications, including load cranes, forklifts, electric vehicles, electric utilities, factory power backup and other applications.

Between 1975 and 1981 a different principle, called pseudocapacitance, was developed by B. Conway. Ruthenium oxide was the first material to prepare electrodes of pseudocapacitors[4,5]. However, the Ru materials are very expensive. Therefore, researchers investigated other metal oxides, such as manganese oxides and nickel oxides. With the technology evaluations, ES devices are ranging from small milli-farad to several kilo-farad devices, which have exceptional power performance[6].

Based on the market search[7], the supercapacitor market was valued at USD ~725 million in 2014. Today several companies such as Maxwell Technologies, NEC/TOKIN, ELNA, Panasonic, and several others invest in electrochemical capacitor development.

## **2.2 Principles of energy storage**

Based on energy storage mechanism, electrical energy can be classified into two different categories[8]: (1) electrochemical double-layer capacitors (EDCLs) and (2) pseudocapacitors. Additionally, the hybrid systems were developed, which combined Faradic and non-Faradic process to store charge.

### **2.2.1 Electrochemical double-layer capacitors**

In EDCLs, the accumulation and release mechanism of electrostatic charge is based on nanoscale charge separation at the electrochemical interface is formed between an electrode and an electrolyte[9]. The principle behind the capacitor is demonstrated in Figure 2-1. When the voltage is applied, the positive and negative charges are distributed close to each other over an extremely short distance. Such a charge distribution is known as an electrical double-layer. Specific surface area required to be increased and distance between charges in the double layer must be decreased to achieve higher energy density [3,10].

Due to EDCLs storage mechanism is a non-faradaic process, there is no chemical reaction occurs, and as a result this type of process eliminates active material swelling which conventional batteries demonstrate during charging and discharging[3].

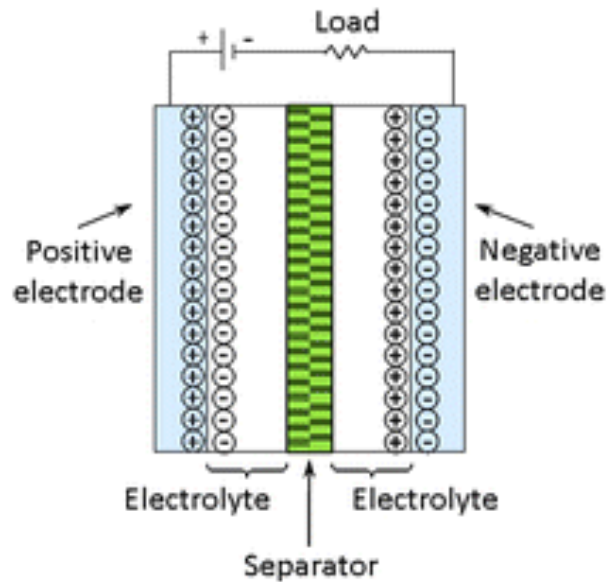


**Figure 2-1 Schematic representation of EDCL type ESs [9].**

Due to the use of high surface area active materials, EDLC has considerably more energy than the traditional capacitor. The surface area  $A$  of EDLC is much larger than the conventional capacitor's electrode surface area. The thickness of double-layer charge separation is very small. Other benefits of EDLCs are: environmentally friendly, very high reversibility in repetitive charge/discharge and long cyclic life ( $>10^5$  cycles)[11].

### **2.2.2 Pseudocapacitors**

Another type of ESs, called pseudocapacitors, is much more complicated than the EDLC. Pseudocapacitors or redox ESs have a Faradaic charge storage mechanism based on fast and reversible surface reactions (Figure 2-2)[12]. Particle sizes, surface area, porosity, the conductivity of the active material, nature of the electrolyte and cell design are important factors, controlling the capacitive behavior of the electrode materials. With the comparison to the capacitance of EDLC, the capacitance of pseudocapacitors is 10-100 times higher

because the ions and cations actually diffuse into the electrode material rather than forming a double layer on the surface[13]. On the other hand, pseudocapacitors' power performance generally lower than EDCLs' because of the slower faradaic process involved[14].

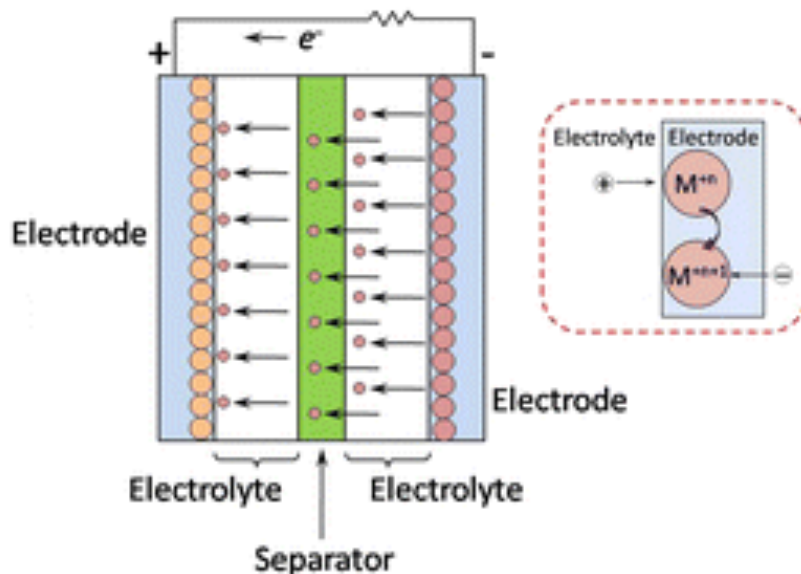


**Figure 2-2 Schematic illustration of pseudocapacitor type ESs[9]**

Pseudocapacitive electrochemical features were categorized in three faradaic mechanisms by B.E. Conway: (1) underpotential deposition, (2) redox pseudocapacitance, and (3) intercalation pseudocapacitance (Figure 2-3)[8,15]. In underpotential deposition (UPD) process, the cation of the different surface ad-atom is reduced and deposited on the monolayer at the bulk metal layers. As an example, in order to overcome the poisoning effect of organic adsorbates like CO, tin UPD process is generally used in the literature[16,17]. Redox pseudocapacitive behavior occurs when ions are electrochemically adsorbed onto the surface or near the surface of a material with a concomitant faradaic charge-transfer. Metal oxides, such as  $\text{RuO}_2$ ,  $\text{Fe}_3\text{O}_4$ ,  $\text{MnO}_2$  and  $\text{NiO}$ [18–20], as well as

electronically conducting polymers[21], are classic examples of redox pseudocapacitive materials, which are currently under extensive research. Intercalation pseudocapacitance is a result of ion intercalation into tunnels or layers of a redox-active material, accompanied with faradaic charge transfer process but with no crystallographic phase change[22].

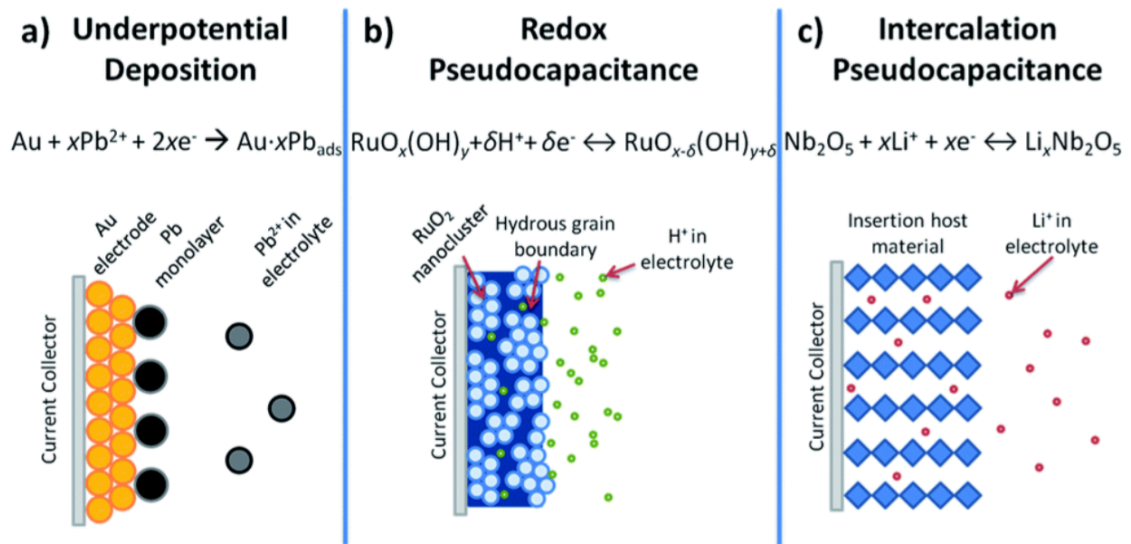


**Figure 2-3 Different types of pseudocapacitive behavior from B.E. Conway: (a) underpotential deposition, (b) redox pseudocapacitance, and (c) intercalation pseudocapacitance[15]**

Table 2-1 demonstrates the thermodynamic equations for dependence of electrode potential on logarithmic activity functions for a redox reaction, an intercalation process and a surface process. The differentiated equations in this table lead to respective pseudocapacitance relations having similar mathematical forms[22].

**Table 2-1 Correlations of types of systems giving rise to pseudocapacitance with application to electrochemical capacitors<sup>a</sup>[22]**

| System type   | Essential relations  |
|---|--|
| (a) Redox system:<br>$Ox + ze^- \rightleftharpoons Red$ and $O^{2-} + H^+ \rightleftharpoons$ in lattice  | $E = E^\circ + \frac{RT}{zF} \ln \frac{R}{1-R}$<br>$R = [Ox]/([Ox] + [Red]); R/(1-R) = [Ox]/[Red]$                               |
| (b) Intercalation system:<br>$Li^+$ into "MA <sub>2</sub> "   | $E = E^\circ + \frac{RT}{zF} \ln \frac{X}{1-X}$<br>$X =$ occupancy fraction of layer lattice sites (e.g. for $Li^+$ in $TiS_2$ ) |
| (c) Underpotential deposition of metal adatoms,<br>$M^{z+} + S + ze^- \rightleftharpoons SM$ (S = surface lattice sites) or $H^+ e^- + S \rightleftharpoons SH$ . | $E = E^\circ + \frac{RT}{zF} \ln \frac{\theta}{1-\theta}$<br>$\theta =$ two-dimensional site occupancy fraction                  |

<sup>a</sup>Note that (b) and (c) can be regarded as mixing of occupied ( $X$  or  $\theta$ ) sites with unoccupied sites,  $(1-\theta)$  or  $(1-X)$

Table 2-2 illustrates comparison the essential parameters of EDLC and pseudocapacitor. EDCLs have relatively lower capacitance but with better cycling ability, while pseudocapacitors have higher capacitance but with lower rate capability and hybrid capacitor compromises between EDCLs and pseudocapacitors with moderate power and energy density. Generally, one of the storage mechanism is a dominating mechanism[22]

**Table 2-2 Comparison between electrochemical double layer capacitors (EDLC) and pseudocapacitors[23]**

| EDLC   | Pseudocapacitor   |
|--|---|
| 1. Non-Faradaic  | Involves Faradic process(es) $2000 \mu F cm^{-2}$ for single-state process; $200-500 \mu F cm^{-2}$ for multi-state, overlapping process                                    |
| 2. $20-50 \mu F cm^{-2}$   | $C$ fairly constant with potential for $RuO_2$ ; for single-state process; exhibits marked maximum  |
| 3. $C$ fairly constant with potential, except through the potential of zero charge     | Can exhibit several maxima for overlapping; multi-state processes, as for H at Pt, Quite reversible but has intrinsic electrode-kinetic rate limitation determined by $R_f$ |
| 4. Highly reversible charging/discharging  | Has restricted voltage range  |
| 5. Has restricted voltage range (contrast Non-electrochemical electrostatic capacitor) | Exhibits mirror-image voltammograms   |
| 6. Exhibits mirror-image voltammograms   |   |

### 2.2.3 Hybrid systems

Hybrid supercapacitors suggest an alternative way which has many advantages and minimizes disadvantages of EDLCs and redox capacitors. Moreover, hybrid capacitors show better capacitive behavior[24]. Basically, hybrid capacitors are the combination of Faradaic and non-Faradaic processes to store charge. Figure 2-4 illustrates the construction

of a hybrid supercapacitor, which consists of two current collectors, two electrodes, electrolyte, and separator. Their energy and power density are much higher than corresponding parameters of EDLCs. On the other hand, their cycling stability is much better than that of pseudocapacitors. The hybrid system is classified into three different categories based on electrode combination; asymmetric, composite and battery type electrodes[24]. Asymmetric hybrids combine an EDLC electrode with a pseudocapacitor electrode. The composite electrode integrates carbon-based materials with conducting metal oxide or polymer in a single electrode with different charge storage mechanisms. Battery type hybrids are as same as asymmetric hybrids, but they combine ES electrodes with battery electrodes. Table 2-3 gives a summary of different types of the hybrid supercapacitor.

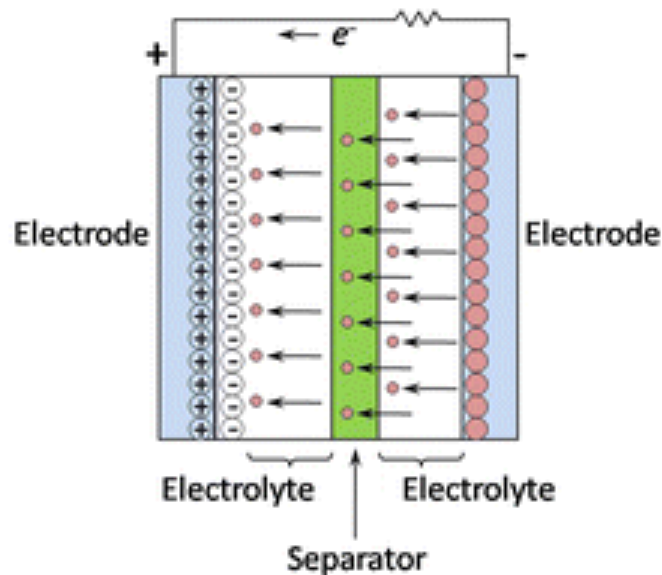


Figure 2-4 Schematic illustration of hybrid type ESs[9]

**Table 2-3 Summary of different types of hybrid supercapacitor devices[25]**

| Type of supercapacitor             | Electrode material |                                | Dominant charge storage mechanism | Advantages/disadvantages  |
|------------------------------------|--------------------|--------------------------------|-----------------------------------|---|
| Asymmetric hybrid supercapacitor   | Anode:             | Pseudocapacitive materials     | Pseudocapacitance                 | High energy and power density, good cyclability                               |
|                                    | Cathode:           | Carbon                         | Double-Layer capacitance          |   |
| Composite supercapacitor           | Anode:             | Redox metal oxide or polymer   | Pseudocapacitance                 | High energy density, moderate costs and stability                             |
|                                    | Cathode:           | Redox metal oxide or polymer   | Pseudocapacitance                 |   |
| Battery-like hybrid supercapacitor | Anode:             | Li-ion intercalation materials | Lithiation/delithiation           | High energy density, high cost and requires electrode material capacity match |
|                                    | Cathode:           | Carbon                         | Double-layer capacitance          |   |

#### 2.2.4 Supercapacitor parameters

The double-layer capacitance can be estimated by the formula, similar to the conventional capacitors.

$$C_{dl} = \epsilon_r \epsilon_0 A/d \quad (2-1)$$

where  $\epsilon_r$  is the dielectric constant of the double-layer region,  $\epsilon_0$  is the permittivity of free space,  $A$  is the surface area of the electrode and  $d$  is the thickness of the double layer, which depends on the concentration of the electrolyte and on the size of the ions.

Energy density and power density are two major parameters for energy storage devices.

Energy density represents the amount of energy stored per unit mass, while power density

describes how fast the energy is released. The energy density (E) and power density (P) are calculated by:

$$E = \frac{1}{2} (CV^2) \quad (2-2)$$

$$P = V^2 / 4R \quad (2-3)$$

where capacitance, voltage, and equivalent series resistance (ESR) are C, V, and R, respectively. The equations indicate that capacitance, voltage window must be high and ESR must be small for an ideal energy storage system. The capacitance (C), calculated from the following equation as well;

$$C = Q_{\text{tot}}/V_{\text{tot}} \quad (2-4)$$

where  $Q_{\text{tot}}$  is the total charge, and  $V_{\text{tot}}$  is the voltage change for charge/discharge of the electrode. The interfacial specific capacitance,  $Sc_i$  and gravimetric specific capacitance,  $Sc_m$  are given by equations;

$$Sc_i = C / A \quad (2-5)$$

$$Sc_m = C / W \quad (2-6)$$

where A is the area of active material dipped in the electrolyte and W is the weight of the active material on the substrate.

### **2.2.5 Comparison of energy storage mechanisms**

The power-energy characteristic of conventional capacitors, ES, battery, and fuel cell are shown in the Ragone plot in Figure 2-5.

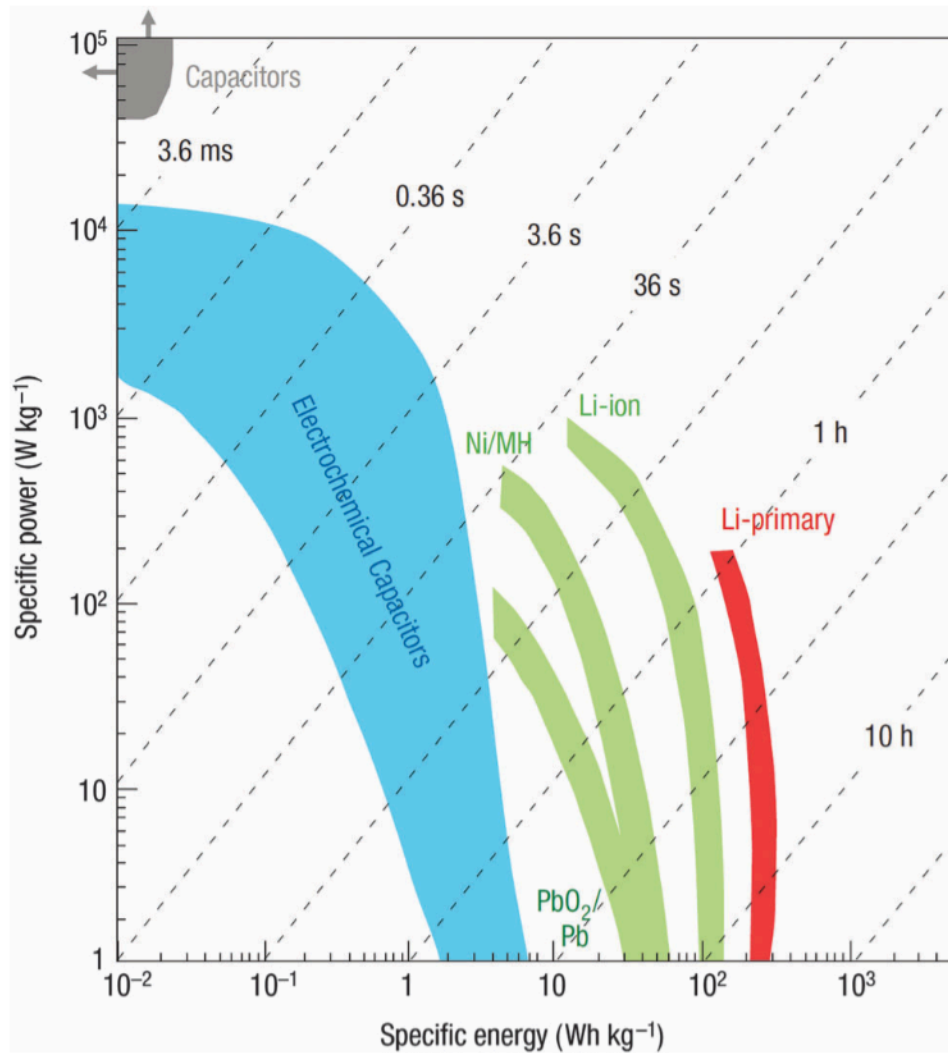


**Figure 2-5 Sketch of Ragone plot for various energy storage and conversion devices. The cross line is the time constants of the devices[12].**

As graphically explained in the Figure 2-5, batteries and fuel cells have greater energy density than conventional capacitors and ESs; on the other hand, they possess lower power density. Even though conventional capacitors process high power density, they have low energy density and cannot be used for long duration application. Meanwhile, ES fills the gap between batteries, fuel cell, and conventional capacitors. ESs have lower energy

density than batteries and fuel cells; however, they have the advantages of higher power density, higher cyclic life, and reversibility (Table 2-4). Nevertheless, the Ragone plot does not cover all other performance parameters such as safety, cycle life, more importantly cost.

Table 2-5 reflects the fundamental comparison between batteries and ESs.

**Table 2-4 Comparison table among selected electrochemical energy storage technologies[26]**

| Characteristics                          | Capacitor              | Supercapacitor | Battery    |
|--|------------------------|----------------|------------|
| Specific energy ( $\text{W h kg}^{-1}$ ) | < 0.1                  | 1–10           | 10–100     |
| Specific power ( $\text{W kg}^{-1}$ )    | $\gg 10,000$           | 500–10,000     | < 1000     |
| Discharge time                           | $10^{-6}$ to $10^{-3}$ | s to min       | 0.3–3 h    |
| Charge time                              | $10^{-6}$ to $10^{-3}$ | s to min       | 1–5 h      |
| Coulombic efficiency (%)                 | About 100              | 85–98          | 70–85      |
| Cycle-life                               | Almost infinite        | > 500,000      | about 1000 |

**Table 2-5 Comparison between batteries and ESs[27]**

| Comparison parameter   | Battery                                      | Supercapacitor           |
|------------------------|--|--------------------------|
| Storage mechanism      | Chemical                                     | Physical                 |
| Power limitation       | Reaction kinetics, mass transport            | Electrolyte conductivity |
| Energy storage         | High (bulk)                                  | Limited (surface area)   |
| Charge rate            | Kinetically limited                          | High, same as discharge  |
| Cycle life limitations | Mechanical stability, chemical reversibility | Side reactions           |

### 2.2.6 Applications of supercapacitors

Due to limited energy and power density, ESs were mostly used for memory back-up in early years. As for the back-up source, the ESs are mostly served for memories, system

boards, clocks, microcomputers. The increasing research helped to enhance their energy and power density.

As the main power source, the ESs can deliver large current pulses in milliseconds. ES can support fuel cells and batteries in automotive applications. Although because of high energy density, fuel cells and batteries are promising energy storage devices for electric vehicles, but high power requirement is the biggest problem which can be addressed by ESs. As ES have fast charge rate, the regenerative braking is possible[28]

Finally, ESs may not be a primary energy source yet; recent developments help ESs to save 40% of energy usage at industrial equipment like a seaport rubber-tired gantry crane[27].

### **2.3 Electrode materials**

As discussed earlier, ES can be divided into three types. Selection of electrode materials plays an essential role in specifying the ESs' electrical behavior. As Figure 2-6 shows, ESs can be classified into three different materials, carbon based, metal oxides, and conducting polymers.

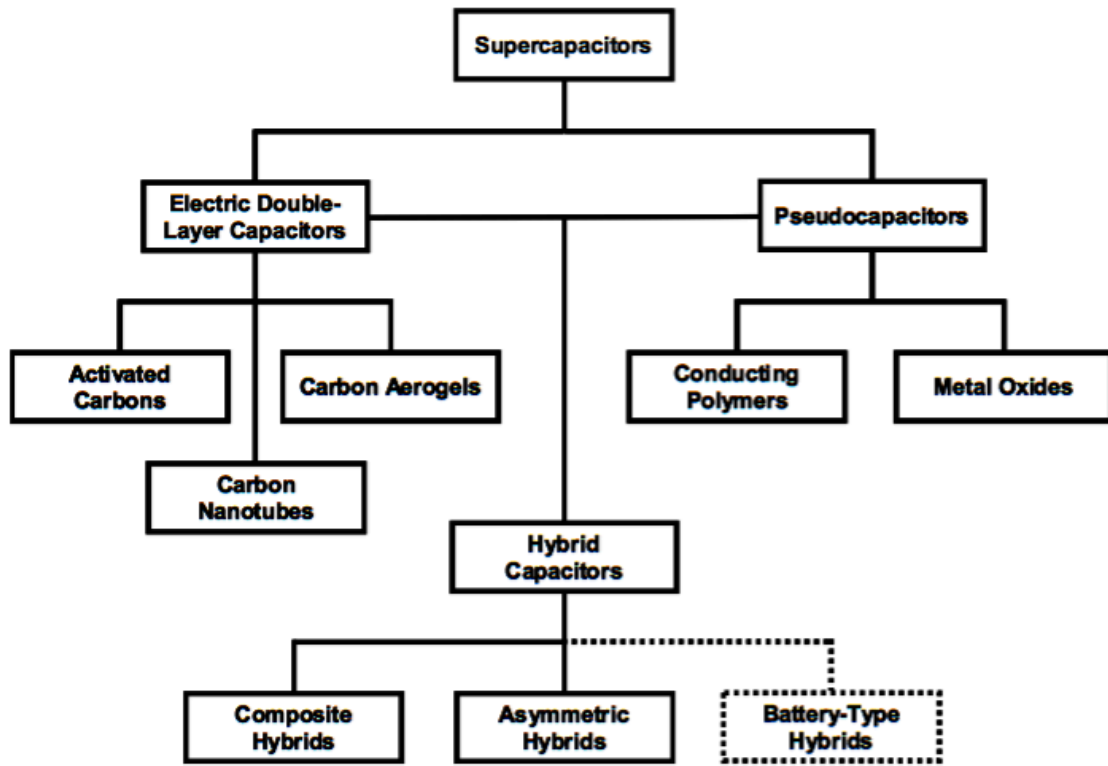


Figure 2-6 Taxonomy of the supercapacitor materials[24]

### 2.3.1 Carbon supercapacitors

The advantages of carbon materials are high conductivity, high surface area, corrosion resistance, abundance, high-temperature stability, controlled pore structure, easy processing and compatibility in composite materials[29]. The relatively low cost makes carbon materials especially attractive for ES applications. Besides two properties, high conductivity and high surface area, pore size has a distinguishable role. Recent studies show that specific capacitance (SC) does not increase linearly with surface area due to accessible contact limit between electrode materials and electrolytes[30–32]. Activated carbons (AC), carbon aerogels, carbon fibers and carbon nanotubes (CNT) are different forms of carbon materials, commonly used as electrode materials for ESs.

### 2.3.1.1 Activated carbons

Due to high surface area and low cost, AC is one of the most used materials for ES electrodes. Besides to most used material, Dr. Cooney reported that AC is the oldest material which used in Egypt around 1500 B.C[33]. Natural renewable resources such as coconut shells wood, corn grain and beer leafs, fossil fuels and coal or coke, also synthetic precursors like polymers are carbon-rich precursors[34,35]. After carbonization and activation process from carbon-rich organic precursors, ACs can be obtained with porosity formation. Depending on the activation technique, the specific surface is (SSA) in the range of 500 to 3000  $\text{m}^2 \text{g}^{-1}$ ; however, the useable SSA reported in the range of 1000-2000  $\text{m}^2 \text{g}^{-1}$ [34,36]. The process of increasing electrode surface area consists of thermal and chemical treatment of the carbonaceous material. There are mainly three classes of pores, shown in Figure 2-7; (1) micropores (diameter < 2nm), (2) mesopores (diameter < 2 - 50 nm) and (3) macropores (diameter > 50nm)[34].

Unfortunately, not all pores are electrochemically accessible. The larger size of electrolyte ions causes the restriction of the movement of the electrolyte. Additionally, the high surface area and porosity can result in a poor conductivity, which is affecting power density[37]. Due to pore size is controlled by the activation process, it is very difficult to achieve optimum particle size distribution. Consequently, high surface area of AC materials cannot be usable fully. The result is that the high surface area of the carbon cannot be fully exploited to form the double-layer. Because of the smaller size of solvent ions and a higher dielectric constant of aqueous electrolyte, it provides higher capacitance value (in the range from 100 to 300  $\text{F g}^{-1}$ )[12] than in organic electrolyte (in the range of 50 to 150  $\text{F g}^{-1}$ )[37].

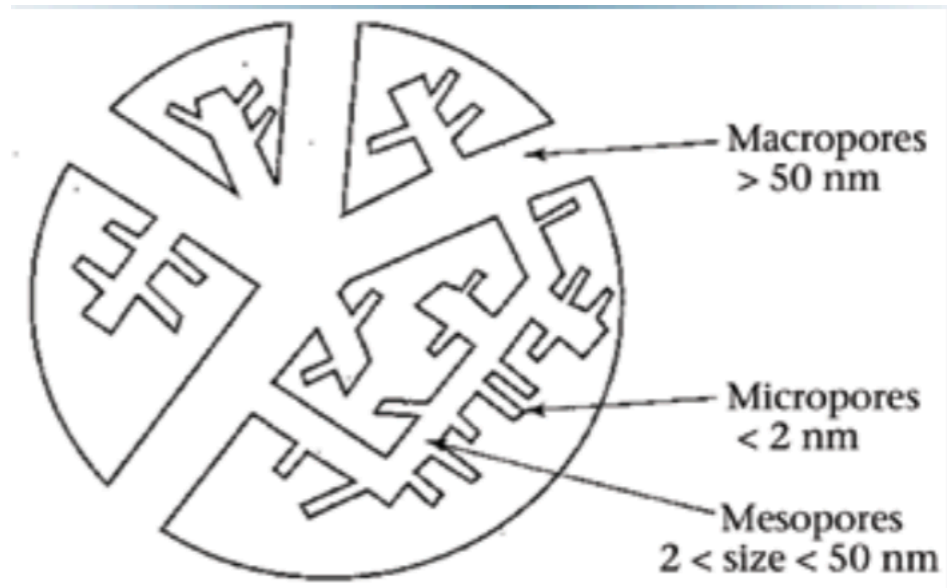


**Figure 2-7 Carbon properties and their role in supercapacitors[34]**

### **2.3.1.2 Carbon Aerogels**

Carbon aerogels (CA) are prepared by the pyrolysis of organic aerogels and usually synthesized by the poly-condensation of resorcinol and formaldehyde. CAs represent a promising material due to high surface area ( $500$  to  $1100 \text{ m}^2 \text{ g}^{-1}$ ), electrical conductivity ( $25$ - $100 \text{ S cm}^{-1}$ ), environmental compatibility, uniform pore size (between  $2$  to  $50 \text{ nm}$ ), high density and chemical stability, which make them very promising materials for future energy-related applications[34,38–40]. Due to pore structure, specific surface area of CA is lower than the activated carbon and carbon aerogel-based electrodes' power capabilities are generally high[36]. In the literature,  $Sc_m$  has been reported in the range of  $50$  and  $100 \text{ F g}^{-1}$  for the organic and aqueous electrolyte, respectfully [34].

### **2.3.1.3 Carbon nanotubes**

Carbon nanotubes (CNTs) have a particular interest as electrode materials for ESs and batteries due to their unique pore structure characteristics, such as good electrical conductivity, high strength, good electrolyte accessibility, good chemical and thermal stability which are important for ESs electrode applications[37][42][43][37,41].

CNTs are ideal hollow tubes rolled up from two-dimensional graphene sheet. CNTs were classified as Multi-Wall Carbon Nanotubes (MWCNTs) and Single-Wall Carbon Nanotubes (SWCNTs) combining both fully accessible external surface area and high electric conductivity (Figure 2-8)[41]. The presence of mesoporosity in CNT based electrodes is due to the central canal and entanglement enables easy access of ions from the electrolyte. SWCNTs are typically 1-2 nm in diameter and tens of microns in length. Surface functional groups and/or the impurities act as the redox centers, which cause broad Faradaic peaks of the MWCNT (multi-walled carbon nanotube) electrodes during CV scan in various aqueous electrolytes. The highest specific capacitance of pure CNT electrode is found to be  $\sim 100 \text{ F g}^{-1}$ [42].

Researchers are highly interested in focusing on the development of aligned, perpendicular to the collector, CNT forest, which shows promising results in the capacitance retention at high current for microelectronic applications[43,44].

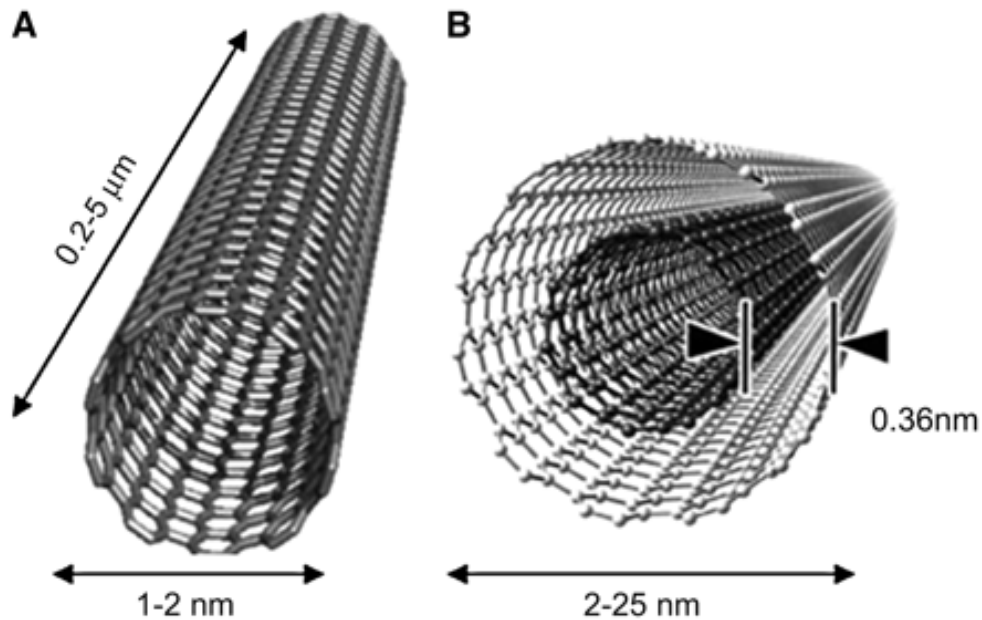


**Figure 2-8 Conceptual diagram of single-walled carbon nanotube (SWCNT) (A) and multiwalled carbon nanotube (MWCNT) (B) delivery systems showing typical dimensions of length, width, and the separation distance between graphene layers in MWCNTs[45].**

Comparing with other carbon based materials, CNTs have limited SSA, leading to moderate capacitance. Therefore, research was focused on creating composites combining both CNT and metal oxides/polymers[46].

#### **2.3.1.4 Graphene**

Graphene was discovered by Geim's group in 2004. Since then there is an increasing attention to graphene in composite electrodes because of its good conductivity, superior chemical stability, high elastic and mechanical strength, large surface area, suitable pore size distribution and rapid heterogeneous electron transfer[47]. The number of layers and the surface are directly related to the performance characteristics of graphene and

comparing with SWCNT and MWCNT, and graphene shows remarkable performance[48,49].

As mentioned before, hybrid material combinations have been getting more attractive nowadays. Recently researchers developed the chemically modified graphene sheets which also were combined with  $MnO_2$  to achieve not only very large surface area, fully accessible to electrolyte ions while maintaining the high electric conductivity and good mechanical properties, but also achieved good capacitive behavior and power density as well[50].

Researchers have similar perpendicular growth interest for graphene (Figure 2-9). The main goal of in-plane growth of graphene is to fully utilize the high surface area which gives electrolyte ions full access to the materials surface[51].

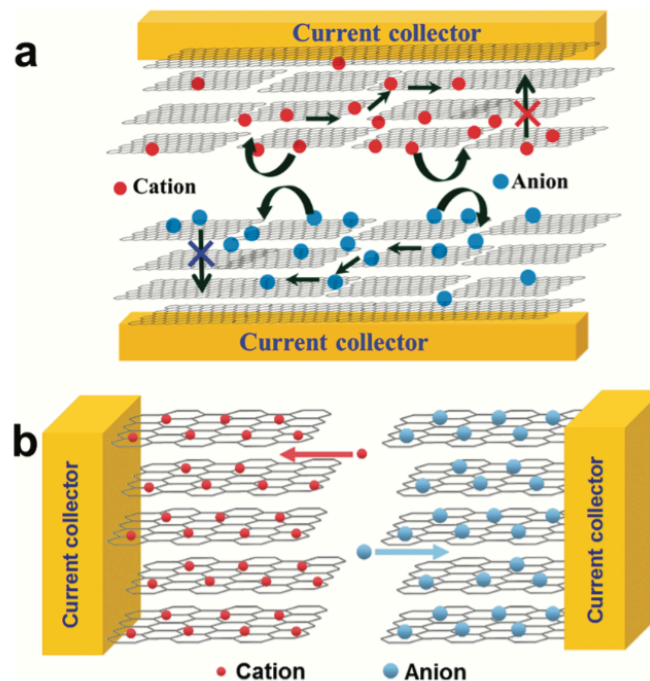


**Figure 2-9 Schematic depiction of (a) the stacked geometry (b) the operating principle in case of the in-plane supercapacitor device[51]**

Table 2-6[52] and Table 2-7[41] illustrate a comparison of different carbon materials' characteristic properties and SC based on the aqueous and organic electrolyte, respectively.

**Table 2-6 Comparison of different carbon materials and their properties in EDLC electrodes[52]**

| Material                                    | Activated carbon | Templated carbon | Carbide-derived carbon | Carbon aerogel | Carbon fiber | Graphene          | VA-CNT            | Graphene oxide |
|---|------------------|------------------|------------------------|----------------|--------------|-------------------|-------------------|----------------|
| Price                                       | Low              | High             | Medium                 | Medium         | Medium       | Medium            | High              | High           |
| Scalability                                 | High             | Low              | Medium                 | Medium         | High         | Medium            | Low               | Low            |
| Surface area [ $\text{m}^2 \text{g}^{-1}$ ] | ~2000            | <4500            | <3200                  | <700           | <200         | 2630 <sup>a</sup> | 1315 <sup>a</sup> | ~500           |
| Conductivity                                | Low              | Low              | Medium                 | Low            | Medium       | High              | High              | Variable       |
| Gravimetric capacitance                     | Medium           | High             | High                   | Medium         | Low          | Medium            | Low               | Low            |
| Volumetric capacitance                      | High             | Low              | High                   | Low            | Low          | Medium            | Low               | Low            |

<sup>a</sup> Theoretical values.

**Table 2-7 Properties and characteristics of various carbon and carbon-based materials as ESs electrode materials[41]**

| Materials                               | Specific surface area/ $\text{m}^2 \text{g}^{-1}$ | Density/ $\text{g cm}^{-3}$ | Aqueous electrolyte |                     | Organic electrolyte |                     |
|---|---|-----------------------------|---------------------|---------------------|---------------------|---------------------|
|   |   |                             | /F $\text{g}^{-1}$  | /F $\text{cm}^{-3}$ | /F $\text{g}^{-1}$  | /F $\text{cm}^{-3}$ |
| <b>Carbon materials</b>                 |   |                             |                     |                     |                     |                     |
| Commercial activated carbons (ACs)      | 1000–3500   | 0.4–0.7                     | < 200               | < 80                | < 100               | < 50                |
| Particulate carbon from SiC/TiC         | 1000–2000   | 0.5–0.7                     | 170–220             | < 120               | 100–120             | < 70                |
| Functionalized porous carbons           | 300–2200  | 0.5–0.9                     | 150–300             | < 180               | 100–150             | < 90                |
| Carbon nanotube (CNT)                   | 120–500   | 0.6                         | 50–100              | < 60                | < 60                | < 30                |
| Templated porous carbons (TC)           | 500–3000  | 0.5–1                       | 120–350             | < 200               | 60–140              | < 100               |
| Activated carbon fibers (ACF)           | 1000–3000   | 0.3–0.8                     | 120–370             | < 150               | 80–200              | < 120               |
| Carbon cloth                            | 2500  | 0.4                         | 100–200             | 40–80               | 60–100              | 24–40               |
| Carbon aerogels                         | 400–1000  | 0.5–0.7                     | 100–125             | < 80                | < 80                | < 40                |
| <b>Carbon-based composite materials</b> |   |                             |                     |                     |                     |                     |
| TC–RuO <sub>2</sub> composite           | 600   | 1                           | 630                 | 630                 | —                   | —                   |
| CNT–MnO <sub>2</sub> composite          | 234   | 1.5                         | 199                 | 300                 | —                   | —                   |
| AC–polyaniline composite                | 1000  | —                           | 300                 | —                   | —                   | —                   |

### 2.3.2 Metal oxides

Due to high theoretical specific capacitance, metal oxides have been highly attractive materials for ESs applications[53]. Many different metal oxides materials, RuO<sub>2</sub>[54,55], IrO<sub>2</sub>[56], MnO<sub>2</sub>[57], NiO[58], Co<sub>2</sub>O<sub>3</sub>[59], SnO<sub>2</sub>[60], V<sub>2</sub>O<sub>5</sub>[61], or MoO<sub>x</sub>[62], has been investigated so far. RuO<sub>2</sub> and MnO<sub>2</sub> are most studied materials[63]. Table 2-8 illustrates theoretical capacitance and conductivity of different metal oxides. As seen on the Table

2-8, metal oxides have high potentials for ESs application because of their theoretical capacitance. However, some of the drawbacks, listed below, they are not competitive with conventional or Li-ion batteries.

Unlike to RuO<sub>2</sub>, the conductivity of metal oxides is very low. Sheet resistance and transfer resistance of electrode are highly depended on metal oxides resistivity, which is so high. This issue causes to IR drops especially at high current density. Correspondingly, the power density and rate capability are lower. The surface area, the pore distribution as well as the porosity are difficult to tailor in metal oxides[25].

**Table 2-8 Pseudocapacitance and conductivity of selected metal oxides[25]**

| Oxide                                | Electrolyte  | Charge storage reaction   | Theoretical capacitance (F g <sup>-1</sup> ) | Conductivity (S cm <sup>-1</sup> )                                     |
|--------------------------------------|--|---|--|--|
| MnO <sub>2</sub>                     | Na <sub>2</sub> SO <sub>4</sub>                                  | MnO <sub>2</sub> + M <sup>+</sup> + e <sup>-</sup> = MMnO <sub>2</sub><br>(M could be H <sup>+</sup> , Li <sup>+</sup> , Na <sup>+</sup> , K <sup>+</sup> )   | 1380 (0.9 V) <sup>34</sup>                   | 10 <sup>-5</sup> to 10 <sup>-6</sup> (ref. 35)                         |
| NiO                                  | KOH, NaOH  | NiO + OH <sup>-</sup> = NiOOH + e <sup>-</sup>  | 2584 (0.5 V) <sup>36</sup>                   | 0.01–0.32 (ref. 37)  |
| Co <sub>3</sub> O <sub>4</sub>       | KOH, NaOH  | Co <sub>3</sub> O <sub>4</sub> + OH <sup>-</sup> + H <sub>2</sub> O =<br>3CoOOH + e <sup>-</sup> CoOOH +<br>OH <sup>-</sup> = CoO <sub>2</sub> + H <sub>2</sub> O + e <sup>-</sup>                    | 3560 (0.45 V) <sup>38,39</sup>               | 10 <sup>-4</sup> to 10 <sup>-2</sup> (ref. 40)                         |
| V <sub>2</sub> O <sub>5</sub>        | NaCl, Na <sub>2</sub> SO <sub>4</sub>                            | V <sub>2</sub> O <sub>5</sub> + 4M <sup>+</sup> + 4e <sup>-</sup> = M <sub>2</sub> V <sub>2</sub> O <sub>5</sub><br>(M could be H <sup>+</sup> , Li <sup>+</sup> , Na <sup>+</sup> , K <sup>+</sup> ) | 2120 (1 V)                                   | 10 <sup>-4</sup> to 10 <sup>-2</sup> (ref. 41)                         |
| RuO <sub>2</sub> , xH <sub>2</sub> O | H <sub>2</sub> SO <sub>4</sub> , Na <sub>2</sub> SO <sub>4</sub> | RuO <sub>2</sub> + xH <sup>+</sup> + xe <sup>-</sup> = RuO <sub>2-x</sub><br>(OH) <sub>x</sub> (0 < x < 2)  | 1200–2200 (1.23 V) <sup>42</sup>             | 10 <sup>3</sup> for polycrystalline,<br>~1 for amorphous <sup>43</sup> |

### 2.3.2.1 Ruthenium oxide

Ruthenium oxide (RuO<sub>2</sub>) theoretical capacitance has been calculated to be as high as 2200 F g<sup>-1</sup> from hydrogenation in acidic electrolytes and oxygenation in alkaline electrolytes[64,65]. RuO<sub>2</sub> is of particular interest due to a wide potential window, highly reversible redox reactions, high rate capability, long cycle life, high proton conductivity, metallic-type conductivity, and good thermal stability[66–69]. Additionally, low equivalent resistance (ESR), 10<sup>-5</sup> Ω , which is significantly lower than that of pseudocapacitive metal oxide materials, enables to achieve high energy and power

density[70]. Researchers suggested that although RuO<sub>2</sub> can exist in two different forms, such as a hydrous or an anhydrous state, the hydrous form of RuO<sub>2</sub> exhibited a higher specific capacitance. to the charge storage in the hydrous form involves a bulk redox reaction, and the structure keeps same pathways for proton and electron transfer; on the other hand, in anhydrous form crystalline morphology only involves surface reactions[67,69]. The amount of water content exhibit high roles for the specific capacitance of RuO<sub>2</sub>, for instance, SC of RuO<sub>2</sub>•0.5H<sub>2</sub>O reported ~900 F g<sup>-1</sup>; however, SC of RuO<sub>2</sub>•0.3H<sub>2</sub>O was only 29 F g<sup>-1</sup> [71]. The ability of the combination of the metallic type conductivity and excellent reversible faradaic (redox) reaction makes RuO<sub>2</sub> a perfect electrode material for ESs[72]. The redox reaction of RuO<sub>2</sub> can be expressed as:



where,  $0 \leq x \leq 2$ , Ru oxidation states can change from (II) to (IV)[12]. Annealing conditions directly affect the SC of the hydrous RuO<sub>2</sub> (600 to 1000 F g<sup>-1</sup>)[73]. Although SCs of RuO<sub>x</sub> can be achievable higher than 600 F g<sup>-1</sup>, voltage window limitation (1 V) and the cost of ruthenium are main drawbacks of aqueous RuO<sub>x</sub> electrodes for ESs applications[12,67].

High expenses of RuO<sub>2</sub> leads researchers to combine RuO<sub>x</sub> with CNT[64], NiO[74], TiO<sub>2</sub>[75,76]. Herewith, ESR of NiO decreased, voltage window increased, proton impregnation of TiO<sub>2</sub> improved, and SC of CNT with RuO<sub>2</sub> recorded 1340 F g<sup>-1</sup>.

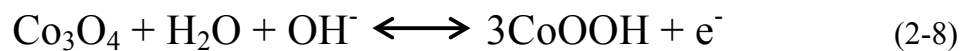
### 2.3.2.2 Nickel Oxide

Nickel oxide (NiO) is another promising transition metal oxide due to low cost, easy synthesis, low toxicity, and high theoretical capacitance (~2584 F g<sup>-1</sup>)[77,78]. The major

disadvantage of NiO is the small voltage window, 0.5 V and to surpass of this drawback, hybrid material combinations have been extensively studied. Some examples are; nickel oxide/CNT nanocomposite[79], activated carbon/nickel oxide[80], nickel oxide embedded titania nanotubes[81], cobalt-nickel oxides/CNT composites[82], Me/Al layered double hydroxides (Me = Ni, Co)[83], activated carbon/nickel hydroxide with polymer hydrogel electrolyte[84], porous nickel/activated carbon[85], multiwalled CNT/nickel oxide porous composite[86], mesoporous nickel oxide[87], and nickel oxide /CNT[88].

### 2.3.2.3 Cobalt oxide

Based on theoretical capacitance ( $\sim 3560 \text{ F g}^{-1}$ ), excellent reversible faradaic behavior, high conductivity, good corrosion rate and long-term performance, cobalt oxide ( $\text{Co}_3\text{O}_4$ ) has been reported to be a promising candidate for ESs applications [89,90]. The redox reaction of  $\text{Co}_3\text{O}_4$  originates from the following charge storage mechanism[89]:



The SCs had been reported for mesoporous  $\text{Co}_3\text{O}_4$  nanowire  $1160 \text{ F g}^{-1}$ [91], net-like  $\text{Co}_3\text{O}_4$  microstructures  $1090 \text{ F g}^{-1}$ [92], and  $\text{Co}_3\text{O}_4$  micro-flowers  $1936.7 \text{ F g}^{-1}$ [93]. The highest SC value of  $\text{Co}_{0.72}\text{Ni}_{0.28}$  LDHs (cobalt-nickel layered double hydroxides) has been reported  $2104 \text{ F g}^{-1}$ [94]. Therefore, Co/Ni composites are promising materials for ESs.

### 2.3.2.4 Iron oxide

Iron oxide ( $\text{Fe}_3\text{O}_4$ ) is being considered as another potential candidate material for ES electrode due to low cost and environmentally friendly properties[95]. However, low conductivity and specific capacitance, less than  $100 \text{ F g}^{-1}$ , are biggest drawbacks to

overcome[77]. According to Dr. Kim and Park[96], Fe<sub>3</sub>O<sub>4</sub>/MWCNT hybrid material coated Ni Foam electrode's SC reported as 165 F g<sup>-1</sup> at 0.2 A g<sup>-1</sup>. Composite of Fe<sub>3</sub>O<sub>4</sub>/MWCNT have a possible potential for ESs applications.

#### **2.3.2.5 Vanadium oxide**

Vanadium oxide can be found in various form such as H<sub>2</sub>V<sub>3</sub>O<sub>8</sub>, V<sub>2</sub>O<sub>5</sub>, which vanadium pentoxide (V<sub>2</sub>O<sub>5</sub>) has been more attractive material in ESs applications [97,98] and Li-ion batteries[99–101]. Since, low cost, high charge storage density, and different oxidation states ability are important factors for commercial applications[102–104]. The SC of amorphous V<sub>2</sub>O<sub>5</sub> has been reported 350 F g<sup>-1</sup> for the material prepared by hydro-thermal synthesis method by Dr. Lee and Goodenough[105].

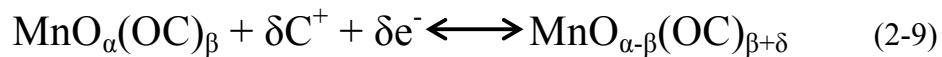
The low electronic conductivity is the biggest complication; however, metal fibers and carbonaceous materials composites have been prepared to improve the electronic conductivity of V<sub>2</sub>O<sub>5</sub>. Another drawback is the cyclic stability of V<sub>2</sub>O<sub>5</sub>. As mentioned earlier for other metal oxides, carbon or metal fibers additives will address these obstacles[106–108].

#### **2.3.2.6 Manganese oxide**

After RuO<sub>2</sub>, manganese oxides (MnO<sub>2</sub>) is extensively studied material due to its low cost and good capacitive properties. The high theoretical capacitance (~1300 F g<sup>-1</sup>)[109] makes it very attractive material for ESs applications. However, poor electronic and ionic conductivity and low surface area are main challenges to reach calculated theoretical capacitance at high active mass loadings[109–111]. Until Lee and Goodenough[112]

discovered  $\text{MnO}_x$  was a promising material for ES applications, it has also been used for lithium batteries[113], catalysts[114], alkaline  $\text{Zn/MnO}_2$  cells[115] and sensors[116] applications.

The main pseudocapacitive energy storage mechanism in this material is attributed to a reversible redox transition involving the exchange of protons and/or cations with the electrolyte and transitions between different oxidation states,  $\text{Mn(III)/Mn(II)}$ ,  $\text{Mn(IV)/Mn(III)}$ , and  $\text{Mn(VI)/Mn(IV)}$ [117,118]. The capacitive behavior is expressed below[63,118,119]:



where  $\text{C}^+$  represents the protons and alkali metal cations ( $\text{Li}^+$ ,  $\text{Na}^+$ ,  $\text{K}^+$ ) in the electrolyte, and  $\text{MnO}_\alpha(\text{OH})_\beta$  and  $\text{MnO}_{\alpha-\beta}(\text{OH})_{\beta+\delta}$  are  $\text{MnO}_2 \cdot n\text{H}_2\text{O}$  in high and low oxidation states, respectively.

There are many techniques that can be used to synthesize  $\text{MnO}_2$  nanostructures, such as sol-gel methods, electrodeposition methods, microwave-assisted methods, electrospinning methods and hydrothermal/solvothermal methods[120]. The studies mainly focused on the capacitive behavior of amorphous  $\text{MnO}_2$  and nanocrystalline compounds for ESs applications[118]. The crystallinity of  $\text{MnO}_2$  plays important roles, for instance, if it is too high, proton exchange will be limited and cause surface area loss; yet conductivity increase. Controversially, low crystallinity leads to conductivity decrease and surface area increase[46].

According to the literature, many conductive materials have been studied for composites with  $\text{MnO}_x$ . Especially, carbon based materials, CNT, graphene, porous carbon, carbon nanofiber, carbon sphere, carbon aerogel are so popular due to high conductivity and surface area, also polymer, poly(3,4-ethylenedioxythiophene) and metal oxides, noble metal (Au, Ag), porous Cu and Ni, binder free Ni-foam,  $\text{Co}_3\text{O}_4$ ,  $\text{NiO/Ni(OH)}_2$ ,  $\text{TiO}_2$ ,  $\text{ZnO}$  have been intensively studied[120].

Hung et al.[121] found that annealing of  $\text{MnO}_2$  in the nanocomposite to  $250^\circ\text{C}$  transformed it to another metal oxide,  $\text{Mn}_3\text{O}_4$ , which reduced the EIS resistance and the maximum capacitance of composite  $\text{Mn}_3\text{O}_4/\text{MWCNT}$  was reported to be  $469 \text{ F g}^{-1}$ . Additionally, even after 6000 cycles, 86% of capacitance remained. The charge storage reaction of  $\text{Mn}_3\text{O}_4$  is given below[121]:



### 2.3.2.7 Other metal oxides

Many other metal oxide materials, such as  $\text{SnO}_2$ ,  $\text{In}_2\text{O}_3$ ,  $\text{IrO}_2$ ,  $\text{Bi}_2\text{O}_3$ , et al. have also been studied as electrode materials for ES. Amongst the metal oxide materials,  $\text{RuO}_2$ ,  $\text{MnO}_2$ ,  $\text{Co}_3\text{O}_4$ , and  $\text{NiO}$  have been mostly studied because other metal oxides suffer from one problem or another, such as low capacity, poor cyclic capability, low electric conductivity, high cost and so on. Their applications as ES electrode materials seem unrealistic for today's technology. Figure 2-10 represents the comparison of different metal oxide thin film SC values as ES electrode materials.

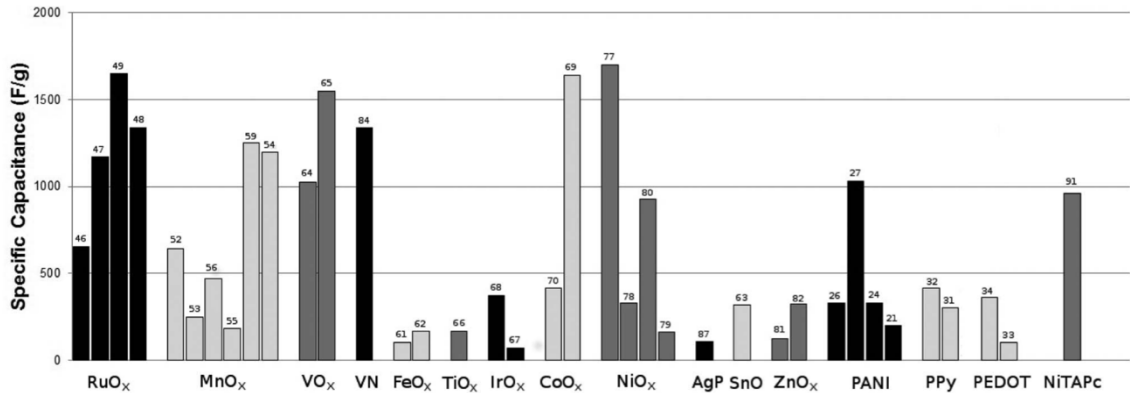


**Figure 2-10 The maximum specific capacitance values reported from the addition of different pseudocapacitive functionalizing materials[77].**

### 2.3.3 Conducting polymers

Conducting polymers (CPs) have been attractive materials for ESs applications due to low cost, high conductivity in doped state, high voltage window, low environmental impact, high porosity, high storage capacity, and high reversibility[122,123]. Poor mechanical stability during cycling is the main drawback of conducting polymers. Carbon based materials are the well-known additives with a great mechanical behavior. Three most popular CPs such as polyaniline (PANI), poly(3,4-ethylenedioxythiophene) (PEDOT) and polypyrrole were combined with CNT in composite electrodes[124]. The doping processes are based on two different types; positively charged polymers are termed as p-type ( $A^-$ ) (Eq. 2-11) also known as oxidative doping and negatively charged polymers as term n-type ( $C^+$ ) (Eq. 2-12), known as reduction doping[124,125]. The doping-undoping process was the charge-discharge process, which essentially was the insertion-deinsertion of counter ions in the polymer chains. The conductivities of conducting polymers were highly

depended on doped states. However, they were more conductive than most metal oxides in general, which resulted in better capacitance retention and power performance[124,125].

Their simplified equations for charging/discharge process are given below[125]:

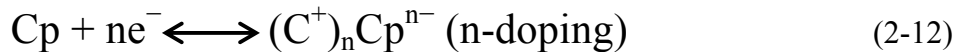
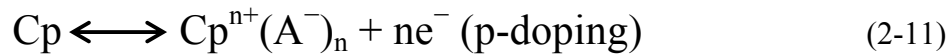
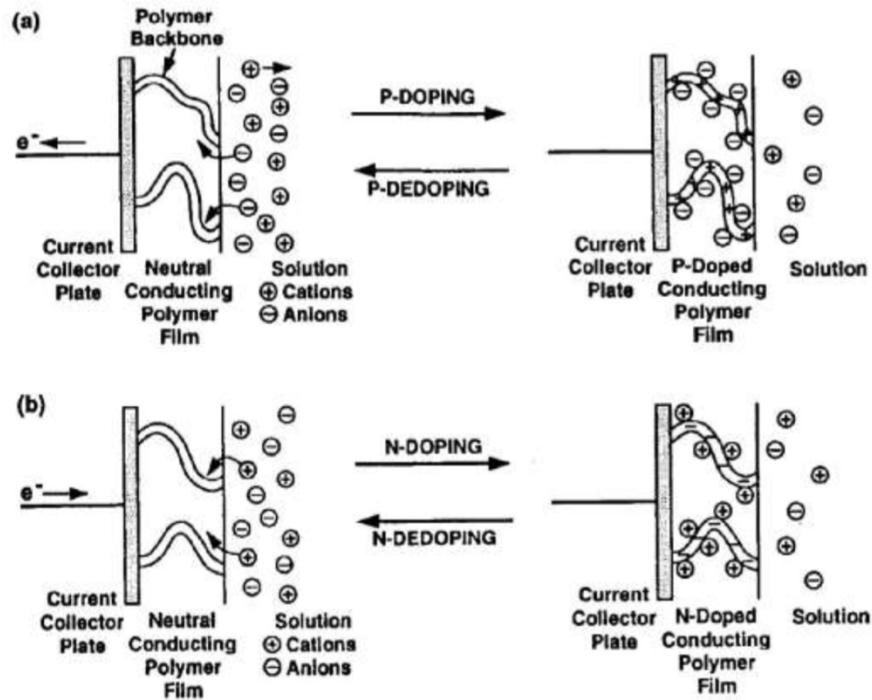


Table 2-9 illustrates the features of differences between CPs based on voltage window, theoretical capacitance and doping level[125].

**Table 2-9 Theoretical and experimental specific capacitances of conducting polymers[125].**

| <b>Conducting polymer</b> | <b>Mw (g mol<sup>-1</sup>)</b> | <b>Dopant level</b> | <b>Potential range (V)</b> | <b>Theoretical SC (F g<sup>-1</sup>)</b> | <b>Measured SC (F g<sup>-1</sup>)</b> |
|---------------------------|--------------------------------|---------------------|----------------------------|--|---------------------------------------|
| PAni                      | 93                             | 0.5                 | 0.7                        | 750                                      | 240                                   |
| PPy                       | 67                             | 0.33                | 0.8                        | 620                                      | 530                                   |
| PTh                       | 84                             | 0.33                | 0.8                        | 485                                      | -                                     |
| PEDOT                     | 142                            | 0.33                | 1.2                        | 210                                      | 92                                    |

The charge/discharge behavior of CPs electrode is related to Faradaic reaction process. As shown in Figure 2-11, when oxidation occurs, ions are transferred to the polymer backbone. During the discharge, both types of charged polymers, n-doped and p-doped, return to neutral states, and the ions are released from backbone into the electrolyte.



**Figure 2-11 Schematic diagram of charging-discharging state for (a) p-type and (b) n-type CP electrodes[8].**

Supercapacitor devices made solely from conducting polymers can have three configurations[126–128]:

Type I (symmetric) using the same p-dopable polymer for both electrodes.

Type II (asymmetric) using two different p-dopable polymers with a different range of electroactivity.

Type III (symmetric) using the same polymer for both electrodes with the p-doped form used as the positive electrode and the n-doped form used as the negative electrode.

### 2.3.4 Summary of Electrode Materials

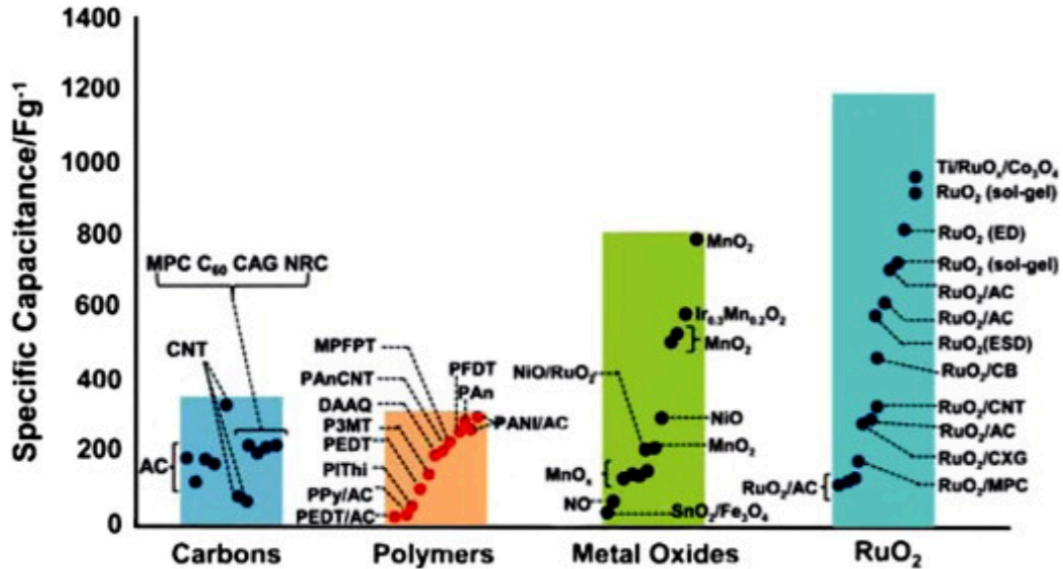


Figure 2-12 The reported specific capacitances for both EDLCs and pseudocapacitors including metal oxides and conducting polymers in single or composite electrode materials[129].

Figure 2-12 illustrates overall specific capacitance and popularity for both EDLCs and pseudocapacitor materials in single and composite electrode materials. As seen above, RuO<sub>2</sub> was reported more than any other materials, due to its best pseudocapacitive behavior. Yet, the high cost prompted to researchers to find new materials. MnO<sub>2</sub> and composites are the second materials extensively studied for ESs applications so far. Based on the analysis of literature, hybrid materials seem to be used in future of ESs applications due to the combination of two or more materials' best properties in a single electrode.

## 2.4 Electrolytes

The development of electrolytes is as crucial as the development of electrode materials. One of the component of energy density ( $1/2CV^2$ , Eq.2-2) is voltage and widening the potential window of electrolyte directly enhances the energy density. Due to energy density is proportional to square voltage, the development of electrolyte is more beneficial comparing with capacitance.

Besides the influence on energy density, electrolytes play an important role directly or indirectly (Figure 2-13) [130]. The fundamental aspects of electrolytes include; (1) a wide potential window range; (2) a high ionic conductivity and low resistance; (3) a high chemical and electrochemical stability; (4) high chemical and electrochemical inertness to ES components (e.g., electrodes, current collectors and packaging); (5) a wide operating temperature range; (6) well-matched with the electrode materials; (7) a low volatility and flammability; (8) environmentally friendly and (9) a low cost[130]. Realistically, it is very difficult to find an electrolyte containing all the best properties in one.

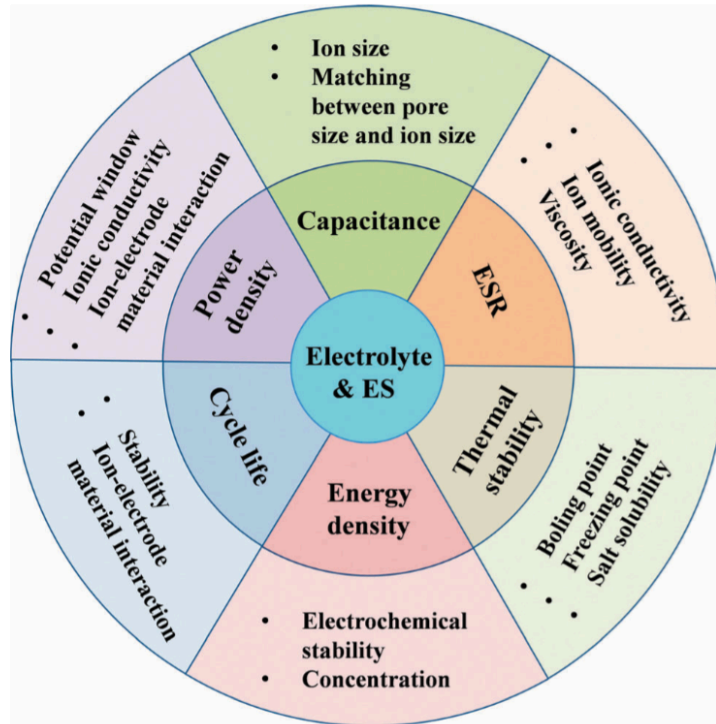


Figure 2-13 Effects of the electrolyte on the ES performance[130].

The electrolytes for ESs can be classified into three types: aqueous electrolyte, organic electrolyte, and ionic liquids.

#### 2.4.1 Aqueous electrolyte

According to the literature[130], the aqueous electrolytes become more popular since 1997. The main reason behind of this popularity is low cost and no need special equipment to handle it. Additionally, the aqueous electrolyte has higher conductivity, the high solubility of salt, ionic concentrations and lower resistance compared with organic and ionic liquid electrolytes[63,130,131]. The higher ionic conductivity ( $0.8 \text{ S cm}^{-2}$ [131]) and smaller ionic radius are beneficial for ESR which leads aqueous electrolytes to provide higher capacitance and higher power compared the organic electrolytes. Because of the

thermodynamic decomposition of water at 1.229 V and low over potential, hydrogen evolution at negative electrode 0 V vs SHE and oxygen evolution at positive electrode round 1.23 V vs SHE, voltage window of aqueous electrolytes is limited to 1.2 V. However, the voltage window is above 2 V in organic electrolytes[130,131]. According to Equation (2-2), the low operating voltage induces a low energy density. These disadvantages can be partially compensated by the low ESR of the aqueous electrolyte. Maximum voltage window successfully was extended to 1.6 - 2.2 V[132–134] in asymmetric devices. Figure 2-14 indicates that the asymmetric cell can be designed by choosing two different materials with different potential voltage windows.

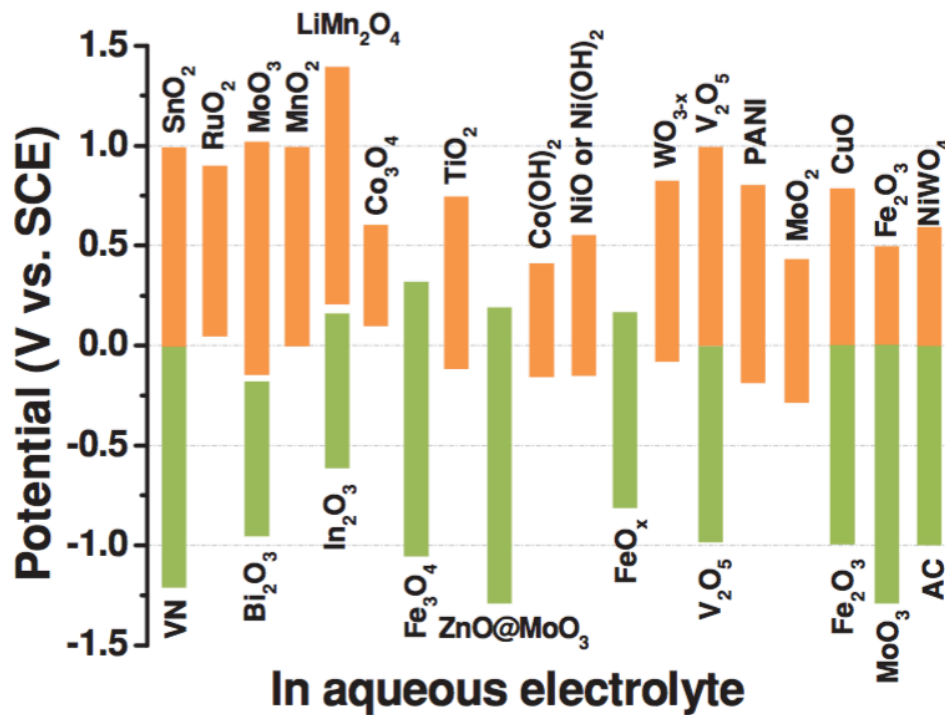


Figure 2-14 The working potential windows of various electrode materials in aqueous electrolyte[135].

Aqueous electrolytes can be grouped into neutral, acid and alkaline solutions and  $\text{H}_2\text{SO}_4$ ,  $\text{KOH}$ ,  $\text{Na}_2\text{SO}_4$ ,  $\text{NH}_4\text{Cl}$ ,  $\text{NaOH}$  have mostly used electrolytes in ESs applications due to high conductivity and ion transport mechanism[135].

### **2.4.2 Organic electrolytes**

Higher voltage window, as high as 2.5-3.0 V gives significant advantages to organic electrolytes. Compared with aqueous electrolytes, organic electrolytes have the capacity for 6-9 times larger energy density[130,131]. However, organic electrolytes inherited high resistivity (20-60  $\Omega$ ), higher cost, flammability and toxicity concern, low conductivity, large solvent ion sizes which causes low SC, high internal resistance, low power delivery, and fabrication sensitivity, which requires water and oxygen free assembly to achieve the high voltage and stability[130,131,136].

Acetonitrile, propylene carbonate (PC) and triethylmethylammonium tetrafluoroborate ( $\text{TEMABF}_4$ ) are most commonly used solvents. Although acetonitrile can dissolve large amounts of salt than other solvents, environmental and toxic effects pose problems. PC-based electrolytes are environmentally friendly and can contribute a wide electrochemical window as well as good conductivity[63].

### **2.4.3 Ionic liquids**

Low vapor pressure, high thermal and chemical stability, non-flammable and non-corrosive properties, wide voltage window ( $\sim 4-6$  V), adjustable viscosity, wide liquid phase range ( $-100 - 400^\circ\text{C}$ ), higher ionic conductivity than organic electrolyte, and non-toxicity have made ionic liquids (IL) as promising candidate for ESs applications[137]. Due to energy

density proportional to square voltage, ILs' energy density higher over sixteen times than aqueous electrolytes. Moreover, the high ionic concentration of ILs has possibly terminated the electrolyte depletion problem, which significantly improved capacitors performance. Despite all these advantages, ILs are too expensive for commercial applications for near future. ILs are also hygroscopic and must be handled in the inert atmosphere like organic electrolytes. Consequently, cost and fabrication sensitivity of ESs applications containing ILs are still challenging[135].

Based on their composition, ILs can be basically classified as aprotic, protic and zwitterionic types (Figure 2-15). The commonly used ILs for the applications in supercapacitor are imidazolium, pyrrolidinium as well as asymmetric, aliphatic quaternary ammonium salts with anions such as tetrafluoroborate, trifluoromethanesulfonate, bis(trifluoromethanesulfonyl)imide, bis(fluorosulfonyl)imide or hexafluorophosphate[63,129].

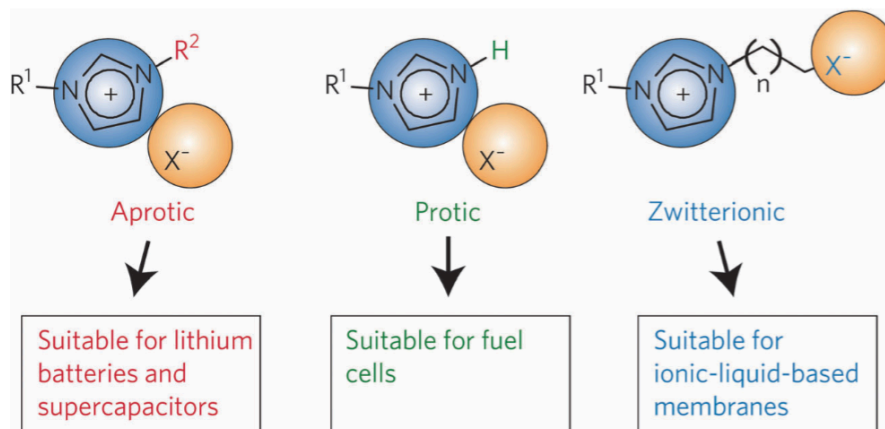


**Figure 2-15 Basic types of ionic liquids: aprotic, protic and zwitterionic types.**

## 2.5 Fundamentals of electrode fabrication

**Table 2-10 Different electrode synthesis methods in terms of materials, advantages, disadvantages[141]**

| Synthesis Methods                 | Materials  | Advantages   | Disadvantages                               |
|-----------------------------------|--|--|---|
| Electrochemical deposition method | <ul style="list-style-type: none"> <li>• Metal oxides</li> <li>• Conducting polymers</li> <li>• RuO<sub>2</sub>-carbon composites (electroless deposition)</li> </ul>                  | Mass production; low cost; precise control of film thickness and uniformity              | Process set up; current or voltage required |
| CBD                               | <ul style="list-style-type: none"> <li>• PANI</li> <li>• RuO<sub>2</sub></li> </ul>  | Simplicity; low temperature; inexpensive; large-area substrates                          | Limited flexibility; low material yield     |
| CVD                               | <ul style="list-style-type: none"> <li>• Carbon materials</li> </ul>   | High material yield than CBD; good film uniformity                                       | Expensive equipment and relative cost       |
| Sol-gel                           | <ul style="list-style-type: none"> <li>• Carbon aerogels</li> <li>• Carbon-Ru xerogels</li> <li>• SnO<sub>2</sub>, MnO<sub>2</sub></li> <li>• RuO<sub>2</sub>/active carbon</li> </ul> | Low cost; controllable film texture, composition, homogeneity, and structural properties | Complicated process                         |
| Chemical precipitation            | <ul style="list-style-type: none"> <li>• NiO/Carbon</li> <li>• MnO<sub>2</sub>/nanofibers</li> <li>• MnO<sub>2</sub>/CNTs</li> </ul>   | Allow synthesis of composite electrode materials; efficient; easy implemented            | May generate waste product                  |

Preparation of electrode plays crucial roles, because it directly affects resistance, SC, life expectancy, stability, charge/discharge behavior and as well as fabrication cost. Table 2-10 illustrates various types of methods with common materials used, advantages and disadvantages for coating ESs electrode, such as sol-gel method[138], chemical precipitation method[112], electrodeposition[57,139] and other methods[123,140]. MnO<sub>2</sub>

is one of the most attractive electrode materials for ESs application.  $\text{MnO}_2$  films generally are used for producing thin film electrodes and for modifying interface between the current collector and electrodes material, while composite materials are used to produce bulk electrodes. There are two kinds of electrodes, (i) thin film electrodes and (ii) composites electrodes.

### **2.5.1 Thin film electrodes**

Electrochemical deposition method is one of the most attractive methods due to high purity, high uniformity, low operating temperature, controlled deposition rate and controlled microstructure[142]. In this work, electrochemical deposition method was extensively used.

Electrodeposition is an attractive technique for surface engineering. Electrodeposition of ceramic and composite films is currently under investigation for various applications. Electrophoretic deposition (EPD) and electrolytic deposition (ELD) are the two most popular electrodeposition techniques due to low cost, rigid control of deposition rate, uniformity and rigid control of film thickness. Figure 2-16 illustrates schematic of electrolytic and electrophoretic deposition.

EPD is achieved via the electrophoretic motion of charged particles in a suspension and film formation at the electrode under an applied electric field. This method requires the fabrication of stable suspensions, containing well dispersed charged colloidal particles. In electrolytic deposition method, ceramic particles are produced in electrode reactions from solutions of metal salts and form a solid deposit at the electrode surface.

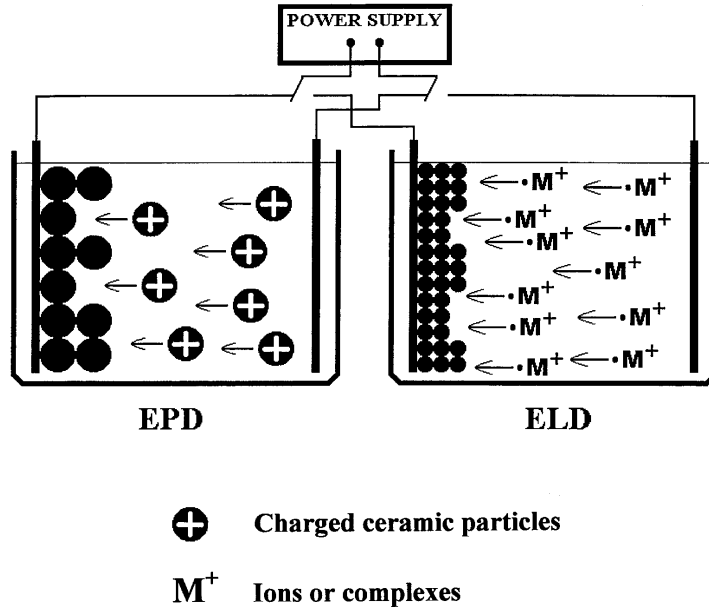


Figure 2-16 Schematic of cathodic EPD and ELD[143].

The DLVO, Derjaguin-Landau-Verwey-Overbeek, theory explains the fundamental aspects of EPD and ELD mechanisms. Double-layer repulsion ( $V_R$ ) and van der Waals' attractions ( $V_A$ ) are two forces between two particles are predicted by the DLVO theory.

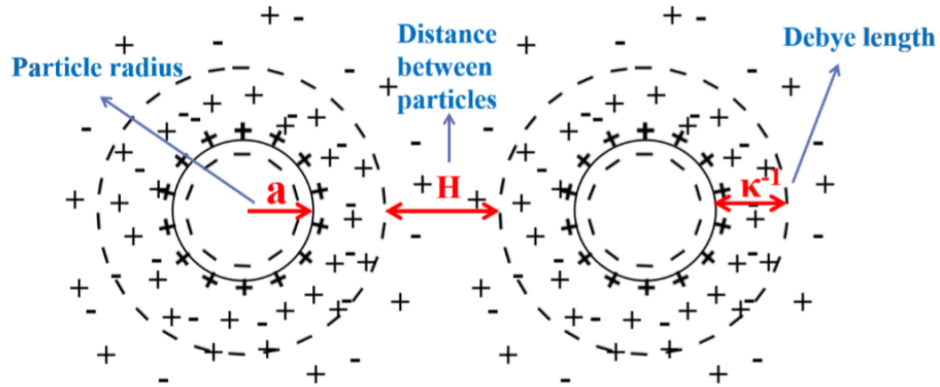


Figure 2-17 Schematic illustration of interaction between two particles in suspension

$$V_T = V_A + V_R \quad (2-13)$$

where  $V_T$  is the total internal energy between two particles in suspension. The  $V_A$  and  $V_R$  were expressed in detail in Eq.2.14 and Eq.2.15, respectively.

$$V_A = -A \frac{a}{12H^2} \quad (2-14)$$

and

$$V_R = 2\pi\epsilon\epsilon_0 a \xi^2 \ln[1 + e^{-\kappa H}] \quad (2-15)$$

where  $A$  is the Hamaker constant,  $H$  is the particle separation,  $a$  is the particle radius,  $\pi$  is the solvent permeability,  $\xi$  is the zeta potential, and  $\kappa$  is a function of the ionic composition. The Debye length is defined as  $\kappa^{-1}$ , which is expressed in Eq.2.16 and showed in Figure 2-17.

$$\kappa = \left( \frac{e_0^2 \sum n_i z_i^2}{\epsilon\epsilon_0 kT} \right)^{1/2} \quad (2-16)$$

where  $e_0$  is the electron charge,  $\epsilon_0$  is vacuum constant,  $k$  is the Boltzmann constant,  $T$  is the absolute temperature,  $n_i$  is the concentration of ions with valence  $z_i$ . The increase of free ion concentration and/or valence causes a reduction of Debye length and hence repulsive energy.

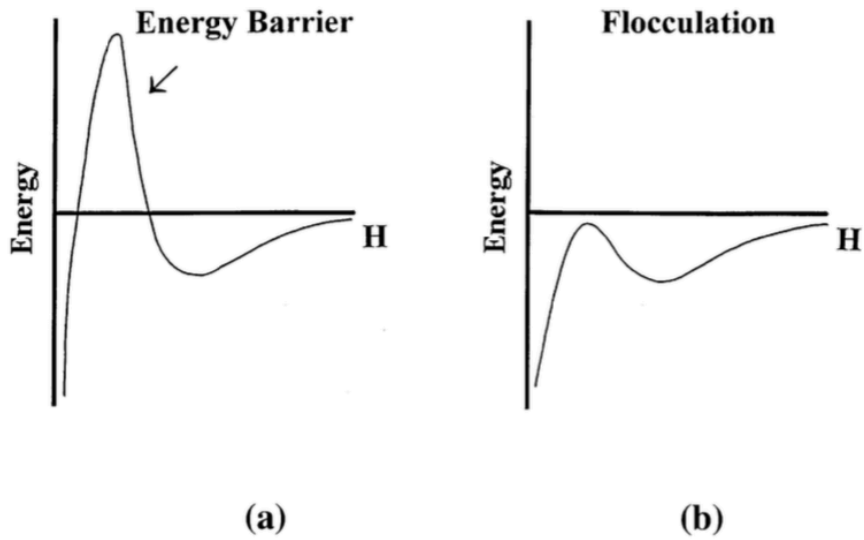
Figure 2-18 describes the relationship between double-layer repulsion and van der Waals' attraction. To achieve high energy barrier, the energy of double-layer repulsion has to be higher than the energy of van der Waals' attraction. As particles separation increases, the role of repulsive energy increases and becomes the domination of total internal energy. An

energy barrier (EB) exists, which prevents particle coagulation and agglomeration in suspension. Beyond the energy barrier, a secondary shallow minimum develops. Particles could form a reversible coagulation at the distance secondary minimum. However, once particles have enough energy to pass the energy barrier, irreversible coagulation occurs.

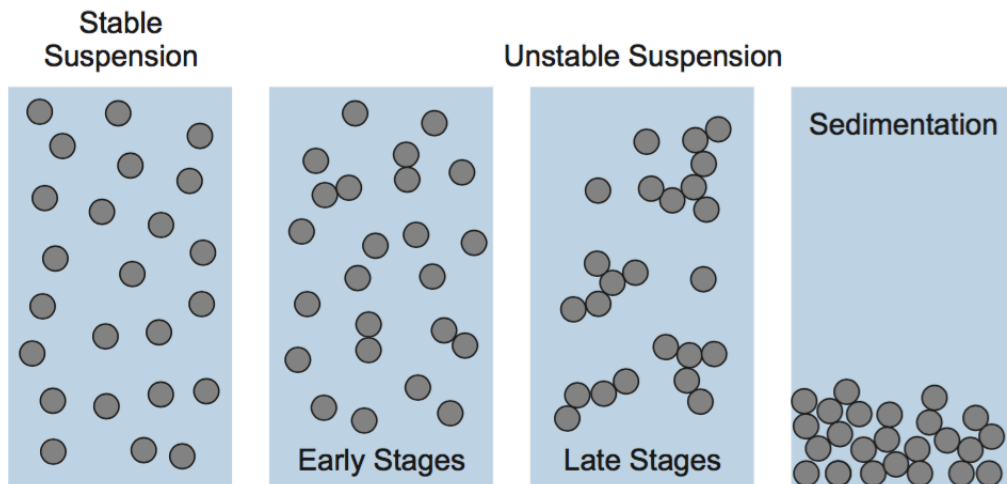
In the literature, electrolyte concentration plays a crucial role on the thickness of the double layer (characterized by the Debye length,  $1/\kappa$ ), explained by the DLVO theory[143]. It should also be noticed that Debye length will be decreased by increasing concentration of ions of the dispersion medium, resulting a thin electric double layer and shorter surface distance  $H$ . Total energy is inverse proportional to distance between two particles,  $H$  (Figure 2-17). Free ions act like electrolyte in suspension and with increasing electrolyte concentration in suspension, particles start to aggregate, and  $V_A$  becomes bigger than  $V_R$  so energy barrier peak decreases. As a result, sedimentation/flocculation occurs.

Figure 2-19 shows the effect of electrolyte increase on particle stability in suspension. To improve stability of colloidal suspension, steric, electrostatic and electrosteric stabilizations are common methods. The steric stability of a colloidal suspension can be achieved using polymers. The polymer molecules are attached to the particles and prevent them from contacting each other. Electrostatic stability is using the electrostatic force between particles to avoid contacting of particles. Colloidal particles adsorb ions and carry same charges in the suspension. The same charges create electrostatic repulsive force and hence improve colloidal stability. Polymer with appropriate functionalities can improve colloidal

stability with both steric stabilization and electrostatic stabilization, which is referred as electrosteric stabilization. Such polymers are named ionic polymeric dispersants[144].



**Figure 2-18 Schematic of the interaction energy as a function of separation between two particles in suspension[143].**



**Figure 2-19 Schematic aggregation process from stable suspension to sedimentation[146].**

EPD method has been widely used and continues to be used in many technologies such as fuel cells, ESs, protective coatings, solar cells and so on. Researchers mostly focused on the development of charging additives, dispersants, and binders for the EPD of ceramic particles and composites.

EPD is achieved via motion of charged particles dispersed in a liquid medium toward the electrode under an applied electric field. Deposit formation on the electrode is achieved via particle coagulation. ELD leads to thin ceramic films from solutions of metal salts by production of colloidal particles in electrode reactions. Thus, electrode reactions in ELD and electrophoretic motion of charged particles in EPD result in the accumulation of ceramic particles and formation of ceramic films at the relevant electrodes[147].

Table 2-11 explains the features of EPD and ELD methods. The solvents used in electrodeposition must dissolve inorganic salts and organic additives and should be inert with respect to the powder (EPD) and ions (ELD).

**Table 2-11 Electrophoretic and Electrolytic Deposition of Ceramic Materials[143].**

|                                 | <b>Electrophoretic Deposition</b> | <b>Electrolytic Deposition</b>  |
|---------------------------------|-----------------------------------|---|
| Medium                          | Suspension                        | Solution  |
| Moving Species                  | Particles                         | Ions or complexes   |
| Electrode Reactions             | None                              | Electrogeneration of OH <sup>-</sup> and neutralization of cationic species |
| Preferred Liquid                | Organic solvent                   | Mixed solvent (water-organic)   |
| Required Conductivity of Liquid | Low                               | High  |
| Deposition Rate                 | 1-10 <sup>3</sup> μm/min          | 10 <sup>-3</sup> -1 μm/min  |
| Deposit Thickness*              | 1-10 <sup>3</sup> μm              | 10 <sup>-3</sup> -10 μm   |
| Deposit Uniformity <sup>†</sup> | Limited by size of particles      | On nm scale   |

|   |  |  |
|---|--|--|
| Deposit Stoichiometry   | Controlled by stoichiometry of powders used for deposition | Can be controlled by use of precursors |
| *Controlled by variation of deposition time, voltage, or current density. |  |  |
| † Controlled by the electric field.                                       |  |  |

As described EPD process earlier, the particles in suspensions must be electrically charged and well dispersed to permit electrophoresis in an EPD process. In aqueous media, the charge at the particle-solvent interface could originate from adsorption or desorption of ions, or dissociation of surface groups. Surfaces of oxide particles dispersed in water tend to coordinate water molecules to form hydroxylated surfaces. The hydroxylated surfaces can be positively or negatively charged depending on pH[143]. A difference in pH near the electrodes compared with the rest of the suspension is believed to play a major role in this reduction of charge. The competing forces governing the formation of deposit in the vicinity of the electrode include: the Van der Waals' force between particles; the inter-particle repulsion of charged particles; the interaction of the deposit forming particles and ions or electrolytes in the suspension; and the pressure exerted by the motion of the charged particles under the influence of applied electric field. Several investigations were focused on the development of new mechanisms of particle charging and the study of the influence of charging additives on the deposition rate[145].

In a typical ELD process, the deposition is achieved by passing an electric current between two electrodes immersed in an electrolyte. The deposition current and the cell potential are the most important factors to determine the course of the reactions. ELD can be achieved by anodic deposition and cathodic deposition techniques and based on the place of electrode reaction, ELD can be categorized to cathodic ELD and anodic ELD. The mechanism of

ELD can be explained by DLVO theory. Applied voltage causes ions movement and creates regions with high ion concentration. According to the DLVO theory, flocculation is observed once electrolyte concentration exceeds its critical value. The deposition during ELD is caused by formation of a flocculate introduced by the electrolyte[147].

In cathodic ELD, cathodic reaction generates large amount of OH<sup>-</sup> groups. Therefore, the local pH increases near electrode. Metal ions adsorb OH<sup>-</sup> and hydrolyzed on electrode surface to form colloidal particles (Eq.2.17). The particles coagulated and deposited on the electrode gradually. In the bulk solution, metal ions are stable in the environment of low pH.



On the other hand, anodic ELD is an oxidation process, where metal ion in lower oxidation state is oxidized to higher oxidation state (Eq.2.18). Therefore, the criteria of electrolyte is that metal ion in lower oxidation state is stable. Metal ion in higher oxidation state is rapidly hydrolyzed to yield metal oxide or hydroxide (Eq.2.19).



### 2.5.2 Composite electrodes

The porosity of current collectors improves the performance of the electrochemically active materials. Therefore, porous nickel foams are used in industry as advanced current collectors for nickel-cadmium, nickel-metal hydride, nickel-zinc, and lithium ion

batteries[148]. For instance, in the batteries, nickel foams contain active material within their light weight web, which provides structural strength, improves electrolyte access to the active material, provides high electronic conductivity and reduces contact resistance.

The manufacturing of efficient ES requires higher materials loadings using light weight current collectors. Many successful efforts have been made in the area of the fabrication of composite materials, where higher electronic conductivity has been achieved by the use of conductive additives[132,149,150].

Composite electrodes are produced by pasting slurry of the active material into porous nickel foam, followed by impregnation, drying and calendaring. The high porosity and large pore size of nickel foams allow for easy impregnation of the active material slurry into the porous current collectors. However, the increase in foam porosity resulted in reduced electronic conductivity, but this problem has been addressed by the use of conductive additives[148].

Small particle size of active materials and high surface area are important for good electrolyte access to the active material. The important task is to develop advanced dispersing agents for the fabrication of small non-agglomerated particles. Fine particles of active materials must be well mixed with conductive additives in order to achieve good electrochemical performance and optimize the electrode composition. Therefore, new techniques are necessary for the dispersion of conductive additives and their mixing with active materials.

## References:

- [1] Becker, H. I., 1957, “Low Voltage Electrolytic Capacitor.”
- [2] Rightmire, R. A., 1966, “Electrical Energy Storage Apparatus.”
- [3] S. Iro, Z., Subramani, C., and Dass, S. S., 2016, “A Brief Review on Electrode Materials for Supercapacitor,” *Int. J. Electrochem. Sci.*, pp. 10628–10643.
- [4] Hadz, S., Angerstein-Kozłowska, H., Vuković, M., Conway, B. E., and others, 1978, “Reversibility and Growth Behavior of Surface Oxide Films at Ruthenium Electrodes,” *J. Electrochem. Soc.*, **125**(9), pp. 1471–1480.
- [5] Trasatti, S., and Buzzanca, G., 1971, “Ruthenium Dioxide: A New Interesting Electrode Material. Solid State Structure and Electrochemical Behaviour,” *J. Electroanal. Chem. Interfacial Electrochem.*, **29**(2), pp. A1–A5.
- [6] Miller, J. R., and Burke, A. F., 2008, “Electrochemical Capacitors: Challenges and Opportunities for Real-World Applications,” *Electrochem. Soc. Interface*, **17**(1), p. 53.
- [7] Brandt, A., Pohlmann, S., Varzi, A., Balducci, A., and Passerini, S., 2013, “Ionic Liquids in Supercapacitors,” *MRS Bull.*, **38**(7), pp. 554–559.
- [8] Conway, B. E., *Electrochemical Supercapacitors - Scientific Fundamentals and Technological Applications*, Springer.
- [9] Vangari, M., Pryor, T., and Li Jiang, 2013, “Supercapacitors: Review of Materials and Fabrication Methods,” *J. Energy Eng.*, **139**(2), pp. 72–9.
- [10] Jayalakshmi, M., and Balasubramanian, K., 2008, “Simple Capacitors to Supercapacitors-an Overview,” *Int J Electrochem Sci*, **3**(11), pp. 1196–1217.
- [11] Kötz, R., and Carlen, M., 2000, “Principles and Applications of Electrochemical Capacitors,” *Electrochimica Acta*, **45**(15–16), pp. 2483–2498.
- [12] Simon, P., and Gogotsi, Y., 2008, “Materials for Electrochemical Capacitors,” *Nat Mater*, **7**(11), pp. 845–854.
- [13] González, A., Goikolea, E., Barrena, J. A., and Mysyk, R., 2016, “Review on Supercapacitors: Technologies and Materials,” *Renew. Sustain. Energy Rev.*, **58**, pp. 1189–1206.

- [14] Chuang, C.-M., Huang, C.-W., Teng, H., and Ting, J.-M., 2010, “Effects of Carbon Nanotube Grafting on the Performance of Electric Double Layer Capacitors,” *Energy Fuels*, **24**(12), pp. 6476–6482.
- [15] Augustyn, V., Simon, P., and Dunn, B., 2014, “Pseudocapacitive Oxide Materials for High-Rate Electrochemical Energy Storage,” *Energy Environ. Sci.*, **7**(5), pp. 1597–1614.
- [16] Motoo, S., Shibata, M., and Watanabe, M., 1980, “Electrocatalysis by Ad-Atoms,” *J. Electroanal. Chem. Interfacial Electrochem.*, **110**(1), pp. 103–109.
- [17] Janssen, M. M. P., and Moolhuysen, J., 1976, “Platinum—tin Catalysts for Methanol Fuel Cells Prepared by a Novel Immersion Technique, by Electrocodeposition and by Alloying,” *Electrochimica Acta*, **21**(11), pp. 861–868.
- [18] Wu, N.-L., 2002, “Nanocrystalline Oxide Supercapacitors,” *ICMAT 2001 Symp. C Nov. Adv. Ceram.*, **75**(1–3), pp. 6–11.
- [19] Lang, J.-W., Kong, L.-B., Wu, W.-J., Luo, Y.-C., and Kang, L., 2008, “Facile Approach to Prepare Loose-Packed NiO Nano-Flakes Materials for Supercapacitors,” *Chem. Commun.*, **0**(35), pp. 4213–4215.
- [20] Brousse, T., Toupin, M., Dugas, R., Athouël, L., Crosnier, O., and Bélanger, D., 2006, “Crystalline MnO<sub>2</sub> as Possible Alternatives to Amorphous Compounds in Electrochemical Supercapacitors,” *J. Electrochem. Soc.*, **153**(12), pp. A2171–A2180.
- [21] Rudge, A., Davey, J., Raistrick, I., Gottesfeld, S., and Ferraris, J. P., 1994, “Conducting Polymers as Active Materials in Electrochemical Capacitors,” *J. Power Sources*, **47**(1), pp. 89–107.
- [22] Conway, B. E., and Pell, W. G., 2003, “Double-Layer and Pseudocapacitance Types of Electrochemical Capacitors and Their Applications to the Development of Hybrid Devices,” *J. Solid State Electrochem.*, **7**(9), pp. 637–644.
- [23] Faraji, S., and Ani, F. N., 2015, “The Development Supercapacitor from Activated Carbon by Electroless plating—A Review,” *Renew. Sustain. Energy Rev.*, **42**, pp. 823–834.
- [24] Halper, M. S., and Ellenbogen, J. C., 2006, “Supercapacitors: A Brief Overview.”
- [25] Zhi, M., Xiang, C., Li, J., Li, M., and Wu, N., 2013, “Nanostructured Carbon-Metal Oxide Composite Electrodes for Supercapacitors: A Review,” *Nanoscale*, **5**(1), pp. 72–88.

- [26] Pandolfo, A. G., and Hollenkamp, A. F., 2006, “Carbon Properties and Their Role in Supercapacitors,” *J. Power Sources*, **157**(1), pp. 11–27.
- [27] Miller, J. R., and Simon, P., 2008, “Electrochemical Capacitors for Energy Management,” *Science*, **321**(5889), pp. 651–652.
- [28] Lam, L. T., and Louey, R., 2006, “Development of Ultra-Battery for Hybrid-Electric Vehicle Applications,” *Spec. Issue Sel. Pap. 6th Int. Conf. Lead-Acid Batter. LABAT 2005 Varna Bulg. 11th Asian Battery Conf. 11 ABC Ho Chi Minh City Vietnam Together Regul. Pap.*, **158**(2), pp. 1140–1148.
- [29] Zhang, Y., Feng, H., Wu, X., Wang, L., Zhang, A., Xia, T., Dong, H., Li, X., and Zhang, L., 2009, “Progress of Electrochemical Capacitor Electrode Materials: A Review,” *2nd Int. Workshop Hydrog. Int. Workshop Hydrog.*, **34**(11), pp. 4889–4899.
- [30] Gamby, J., Taberna, P. L., Simon, P., Fauvarque, J. F., and Chesneau, M., 2001, “Studies and Characterisations of Various Activated Carbons Used for Carbon/Carbon Supercapacitors,” *J. Power Sources*, **101**(1), pp. 109–116.
- [31] Shi, H., 1996, “Activated Carbons and Double Layer Capacitance,” *Electrochimica Acta*, **41**(10), pp. 1633–1639.
- [32] Qu, D., and Shi, H., 1998, “Studies of Activated Carbons Used in Double-Layer Capacitors,” *J. Power Sources*, **74**(1), pp. 99–107.
- [33] Cooney, D. O., 1980, “Activated Charcoal: Antidotal and Other Medical Uses,” *J. Pharm. Sci.*, **69**(11), p. 1361.
- [34] Simon, P., and Burke, A. F., 2008, “Nanostructured Carbons: Double-Layer Capacitance and More,” *Electrochem. Soc. Interface*, **17**(1), p. 38.
- [35] Wei, L., and Yushin, G., 2012, “Nanostructured Activated Carbons from Natural Precursors for Electrical Double Layer Capacitors,” *Nano Energy*, **1**(4), pp. 552–565.
- [36] Pandolfo, A. G., and Hollenkamp, A. F., 2006, “Carbon Properties and Their Role in Supercapacitors,” *J. Power Sources*, **157**(1), pp. 11–27.
- [37] Frackowiak, E., and Beguin, F., 2001, “Carbon Materials for the Electrochemical Storage of Energy in Capacitors,” *Carbon*, **39**(6), pp. 937–950.
- [38] Mayer, S. T., Pekala, R. W., and Kaschmitter, J. L., 1993, “The Aerocapacitor: An Electrochemical Double-Layer Energy-Storage Device,” *J. Electrochem. Soc.*, **140**(2), pp. 446–451.

- [39] Saliger, R., Fischer, U., Herta, C., and Fricke, J., 1998, "High Surface Area Carbon Aerogels for Supercapacitors," *J. Non-Cryst. Solids*, **225**, pp. 81–85.
- [40] Wei, Y.-Z., Fang, B., Iwasa, S., and Kumagai, M., 2005, "A Novel Electrode Material for Electric Double-Layer Capacitors," *J. Power Sources*, **141**(2), pp. 386–391.
- [41] Li Zhang, L., and S. Zhao, X., 2009, "Carbon-Based Materials as Supercapacitor Electrodes," *Chem. Soc. Rev.*, **38**(9), pp. 2520–2531.
- [42] Pan, H., Li, J., and Feng, Y., 2010, "Carbon Nanotubes for Supercapacitor," *Nanoscale Res. Lett.*, **5**(3), p. 654.
- [43] Talapatra S., Kar S., Pal S. K., Vajtai R., Ci L., Victor P., Shaijumon M. M., Kaur S., Nalamasu O., and Ajayan P. M., 2006, "Direct Growth of Aligned Carbon Nanotubes on Bulk Metals:," *Nat Nano*, **1**(2), pp. 112–116.
- [44] Pushparaj, V. L., Shaijumon, M. M., Kumar, A., Murugesan, S., Ci, L., Vajtai, R., Linhardt, R. J., Nalamasu, O., and Ajayan, P. M., 2007, "Flexible Energy Storage Devices Based on Nanocomposite Paper," *Proc. Natl. Acad. Sci.*, **104**(34), pp. 13574–13577.
- [45] Reilly, R. M., 2007, "Carbon Nanotubes: Potential Benefits and Risks of Nanotechnology in Nuclear Medicine," *J. Nucl. Med.*, **48**(7), pp. 1039–1042.
- [46] González, A., Goikolea, E., Barrena, J. A., and Mysyk, R., 2016, "Review on Supercapacitors: Technologies and Materials," *Renew. Sustain. Energy Rev.*, **58**, pp. 1189–1206.
- [47] Lu, T., Zhang, Y., Li, H., Pan, L., Li, Y., and Sun, Z., 2010, "Electrochemical Behaviors of graphene–ZnO and graphene–SnO<sub>2</sub> Composite Films for Supercapacitors," *Electrochimica Acta*, **55**(13), pp. 4170–4173.
- [48] Vivekchand, S. R. C., Rout, C. S., Subrahmanyam, K. S., Govindaraj, A., and Rao, C. N. R., 2008, "Graphene-Based Electrochemical Supercapacitors," *J. Chem. Sci.*, **120**(1), pp. 9–13.
- [49] Stoller, M. D., Park, S., Zhu, Y., An, J., and Ruoff, R. S., 2008, "Graphene-Based Ultracapacitors," *Nano Lett.*, **8**(10), pp. 3498–3502.
- [50] Cheng, Q., Tang, J., Ma, J., Zhang, H., Shinya, N., and Qin, L.-C., 2011, "Graphene and Nanostructured MnO<sub>2</sub> Composite Electrodes for Supercapacitors," *Carbon*, **49**(9), pp. 2917–2925.

- [51] Yoo, J. J., Balakrishnan, K., Huang, J., Meunier, V., Sumpter, B. G., Srivastava, A., Conway, M., Mohana Reddy, A. L., Yu, J., Vajtai, R., and others, 2011, "Ultrathin Planar Graphene Supercapacitors," *Nano Lett.*, **11**(4), pp. 1423–1427.
- [52] Borchardt, L., Oschatz, M., and Kaskel, S., 2014, "Tailoring Porosity in Carbon Materials for Supercapacitor Applications," *Mater. Horiz.*, **1**(2), pp. 157–168.
- [53] Sharma, P., and Bhatti, T. S., 2010, "A Review on Electrochemical Double-Layer Capacitors," *Energy Convers. Manag.*, **51**(12), pp. 2901–2912.
- [54] Ahn, Y. R., Song, M. Y., Jo, S. M., Park, C. R., and Kim, D. Y., 2006, "Electrochemical Capacitors Based on Electrodeposited Ruthenium Oxide on Nanofibre Substrates," *Nanotechnology*, **17**(12), p. 2865.
- [55] Patake, V. D., Lokhande, C. D., and Joo, O. S., 2009, "Electrodeposited Ruthenium Oxide Thin Films for Supercapacitor: Effect of Surface Treatments," *Appl. Surf. Sci.*, **255**(7), pp. 4192–4196.
- [56] Hu, C.-C., Huang, Y.-H., and Chang, K.-H., 2002, "Annealing Effects on the Physicochemical Characteristics of Hydrous Ruthenium and Ruthenium–iridium Oxides for Electrochemical Supercapacitors," *J. Power Sources*, **108**(1–2), pp. 117–127.
- [57] Ata, M. S., and Zhitomirsky, I., 2013, "Preparation of MnO<sub>2</sub> and Composites for Ultracapacitors," *Mater. Manuf. Process.*, **28**(9), pp. 1014–1018.
- [58] Patil, U. M., Salunkhe, R. R., Gurav, K. V., and Lokhande, C. D., 2008, "Chemically Deposited Nanocrystalline NiO Thin Films for Supercapacitor Application," *Appl. Surf. Sci.*, **255**(5, Part 2), pp. 2603–2607.
- [59] Kandalkar, S. G., Gunjekar, J. L., and Lokhande, C. D., 2008, "Preparation of Cobalt Oxide Thin Films and Its Use in Supercapacitor Application," *Appl. Surf. Sci.*, **254**(17), pp. 5540–5544.
- [60] Miura, N., Oonishi, S., and Prasad, K. R., 2004, "Indium Tin Oxide/Carbon Composite Electrode Material for Electrochemical Supercapacitors," *Electrochem. Solid-State Lett.*, **7**(8), pp. A247–A249.
- [61] Hu, C.-C., Huang, C.-M., and Chang, K.-H., 2008, "Anodic Deposition of Porous Vanadium Oxide Network with High Power Characteristics for Pseudocapacitors," *J. Power Sources*, **185**(2), pp. 1594–1597.

- [62] Nakayama, M., Tanaka, A., Sato, Y., Tonosaki, T., and Ogura, K., 2005, "Electrodeposition of Manganese and Molybdenum Mixed Oxide Thin Films and Their Charge Storage Properties," *Langmuir*, **21**(13), pp. 5907–5913.
- [63] Wang, G., Zhang, L., and Zhang, J., 2012, "A Review of Electrode Materials for Electrochemical Supercapacitors," *Chem. Soc. Rev.*, **41**(2), pp. 797–828.
- [64] Hu, C.-C., Chen, W.-C., and Chang, K.-H., 2004, "How to Achieve Maximum Utilization of Hydrous Ruthenium Oxide for Supercapacitors," *J. Electrochem. Soc.*, **151**(2), pp. A281–A290.
- [65] Wu, N.-L., Kuo, S.-L., and Lee, M.-H., 2002, "Preparation and Optimization of RuO<sub>2</sub>-Impregnated SnO<sub>2</sub> Xerogel Supercapacitor," *J. Power Sources*, **104**(1), pp. 62–65.
- [66] Sakiyama, K., Onishi, S., Ishihara, K., Orita, K., Kajiyama, T., Hosoda, N., and Hara, T., 1993, "Deposition and Properties of Reactively Sputtered Ruthenium Dioxide Films," *J. Electrochem. Soc.*, **140**(3), pp. 834–839.
- [67] Kim, I.-H., and Kim, K.-B., 2006, "Electrochemical Characterization of Hydrous Ruthenium Oxide Thin-Film Electrodes for Electrochemical Capacitor Applications," *J. Electrochem. Soc.*, **153**(2), pp. A383–A389.
- [68] Jia, Q. X., Song, S. G., Wu, X. D., Cho, J. H., Foltyn, S. R., Findikoglu, A. T., and Smith, J. L., 1996, "Epitaxial Growth of Highly Conductive RuO<sub>2</sub> Thin Films on (100) Si," *Appl. Phys. Lett.*, **68**(8), pp. 1069–1071.
- [69] Lee, H., Cho, M. S., Kim, I. H., Nam, J. D., and Lee, Y., 2010, "RuO<sub>x</sub>/Polypyrrole Nanocomposite Electrode for Electrochemical Capacitors," *Synth. Met.*, **160**(9–10), pp. 1055–1059.
- [70] Zheng, J. P., Cygan, P. J., and Jow, T. R., 1995, "Hydrous Ruthenium Oxide as an Electrode Material for Electrochemical Capacitors," *J. Electrochem. Soc.*, **142**(8), pp. 2699–2703.
- [71] Long, J. W., Swider, K. E., Merzbacher, C. I., and Rolison, D. R., 1999, "Voltammetric Characterization of Ruthenium Oxide-Based Aerogels and Other RuO<sub>2</sub> Solids: The Nature of Capacitance in Nanostructured Materials," *Langmuir*, **15**(3), pp. 780–785.
- [72] Zheng, J. P., and Jow, T. R., 1995, "A New Charge Storage Mechanism for Electrochemical Capacitors," *J. Electrochem. Soc.*, **142**(1), pp. L6–L8.

- [73] Sugimoto, W., Yokoshima, K., Murakami, Y., and Takasu, Y., 2006, "Charge Storage Mechanism of Nanostructured Anhydrous and Hydrated Ruthenium-Based Oxides," *Electrochimica Acta*, **52**(4), pp. 1742–1748.
- [74] Liu, X. M., and Zhang, X. G., 2004, "NiO-Based Composite Electrode with RuO<sub>2</sub> for Electrochemical Capacitors," *Electrochimica Acta*, **49**(2), pp. 229–232.
- [75] Ahn, Y. R., Park, C. R., Jo, S. M., and Kim, D. Y., 2007, "Enhanced Charge-Discharge Characteristics of RuO<sub>2</sub> Supercapacitors on Heat-Treated TiO<sub>2</sub> Nanorods," *Appl. Phys. Lett.*, **90**(12), p. 122106.
- [76] Xie, Y., and Fu, D., 2010, "Supercapacitance of Ruthenium Oxide Deposited on Titania and Titanium Substrates," *Mater. Chem. Phys.*, **122**(1), pp. 23–29.
- [77] Fisher, R. A., Watt, M. R., and Ready, W. J., 2013, "Functionalized Carbon Nanotube Supercapacitor Electrodes: A Review on Pseudocapacitive Materials," *ECS J. Solid State Sci. Technol.*, **2**(10), pp. M3170–M3177.
- [78] Nam, K.-W., Kim, K.-H., Lee, E.-S., Yoon, W.-S., Yang, X.-Q., and Kim, K.-B., 2008, "Pseudocapacitive Properties of Electrochemically Prepared Nickel Oxides on 3-Dimensional Carbon Nanotube Film Substrates," *J. Power Sources*, **182**(2), pp. 642–652.
- [79] Lee, J. Y., Liang, K., An, K. H., and Lee, Y. H., 2005, "Nickel Oxide/Carbon Nanotubes Nanocomposite for Electrochemical Capacitance," *Synth. Met.*, **150**(2), pp. 153–157.
- [80] Yuan, G., Jiang, Z., Aramata, A., and Gao, Y., 2005, "Electrochemical Behavior of Activated-Carbon Capacitor Material Loaded with Nickel Oxide," *Carbon*, **43**(14), pp. 2913–2917.
- [81] Xie, Y., Zhou, L., Huang, C., Huang, H., and Lu, J., 2008, "Fabrication of Nickel Oxide-Embedded Titania Nanotube Array for Redox Capacitance Application," *Electrochimica Acta*, **53**(10), pp. 3643–3649.
- [82] Fan, Z., Chen, J., Cui, K., Sun, F., Xu, Y., and Kuang, Y., 2007, "Preparation and Capacitive Properties of Cobalt–nickel Oxides/Carbon Nanotube Composites," *Electrochimica Acta*, **52**(9), pp. 2959–2965.
- [83] Liu, X.-M., Zhang, Y.-H., Zhang, X.-G., and Fu, S.-Y., 2004, "Studies on Me/Al-Layered Double Hydroxides (Me= Ni and Co) as Electrode Materials for Electrochemical Capacitors," *Electrochimica Acta*, **49**(19), pp. 3137–3141.

- [84] Nohara, S., Asahina, T., Wada, H., Furukawa, N., Inoue, H., Sugoh, N., Iwasaki, H., and Iwakura, C., 2006, "Hybrid Capacitor with Activated Carbon Electrode, Ni(OH)<sub>2</sub> Electrode and Polymer Hydrogel Electrolyte," *J. Power Sources*, **157**(1), pp. 605–609.
- [85] Ganesh, V., Pitchumani, S., and Lakshminarayanan, V., 2006, "New Symmetric and Asymmetric Supercapacitors Based on High Surface Area Porous Nickel and Activated Carbon," *J. Power Sources*, **158**(2), pp. 1523–1532.
- [86] Zheng, Y., Zhang, M., and Gao, P., 2007, "Preparation and Electrochemical Properties of Multiwalled Carbon Nanotubes–nickel Oxide Porous Composite for Supercapacitors," *Mater. Res. Bull.*, **42**(9), pp. 1740–1747.
- [87] Xing, W., Li, F., Yan, Z., and Lu, G. Q., 2004, "Synthesis and Electrochemical Properties of Mesoporous Nickel Oxide," *J. Power Sources*, **134**(2), pp. 324–330.
- [88] Wang, X.-F., Wang, D.-Z., and Liang, J., 2003, "Electrochemical Capacitor Using Nickel Oxide/Carbon Nanotube Composites Electrode," *J. Inorg. Mater.*, **2**, p. 12.
- [89] Hamdani, M., Singh, R. N., and Chartier, P., 2010, "Co<sub>3</sub>O<sub>4</sub> and Co-Based Spinel Oxides Bifunctional Oxygen Electrodes," *Int J Electrochem Sci*, **5**(4), p. 556.
- [90] Yuan, C., Yang, L., Hou, L., Shen, L., Zhang, X., and Lou, X. W. D., 2012, "Growth of Ultrathin Mesoporous Co<sub>3</sub>O<sub>4</sub> Nanosheet Arrays on Ni Foam for High-Performance Electrochemical Capacitors," *Energy Environ. Sci.*, **5**(7), pp. 7883–7887.
- [91] Zhang, F., Yuan, C., Lu, X., Zhang, L., Che, Q., and Zhang, X., 2012, "Facile Growth of Mesoporous Co<sub>3</sub>O<sub>4</sub> Nanowire Arrays on Ni Foam for High Performance Electrochemical Capacitors," *J. Power Sources*, **203**, pp. 250–256.
- [92] Wang, H., Zhang, L., Tan, X., Holt, C. M., Zahiri, B., Olsen, B. C., and Mitlin, D., 2011, "Supercapacitive Properties of Hydrothermally Synthesized Co<sub>3</sub>O<sub>4</sub> Nanostructures," *J. Phys. Chem. C*, **115**(35), pp. 17599–17605.
- [93] Qing, X., Liu, S., Huang, K., Lv, K., Yang, Y., Lu, Z., Fang, D., and Liang, X., 2011, "Facile Synthesis of Co<sub>3</sub>O<sub>4</sub> Nanoflowers Grown on Ni Foam with Superior Electrochemical Performance," *Electrochimica Acta*, **56**(14), pp. 4985–4991.
- [94] Lokhande, C. D., Dubal, D. P., and Joo, O.-S., 2011, "Metal Oxide Thin Film Based Supercapacitors," *Curr. Appl. Phys.*, **11**(3), pp. 255–270.

- [95] Reddy, M. V., Yu, T., Sow, C.-H., Shen, Z. X., Lim, C. T., Subba Rao, G. V., and Chowdari, B. V. R., 2007, “ $\alpha$ - $\text{Fe}_2\text{O}_3$  Nanoflakes as an Anode Material for Li-Ion Batteries,” *Adv. Funct. Mater.*, **17**(15), pp. 2792–2799.
- [96] Kim, Y.-H., and Park, S.-J., 2011, “Roles of Nanosized  $\text{Fe}_3\text{O}_4$  on Supercapacitive Properties of Carbon Nanotubes,” *Curr. Appl. Phys.*, **11**(3), pp. 462–466.
- [97] Dong, W., Rolison, D. R., and Dunna, B., 2000, “Electrochemical Properties of High Surface Area Vanadium Oxide Aerogels,” *Electrochem. Solid-State Lett.*, **3**(10), pp. 457–459.
- [98] Kudo, T., Ikeda, Y., Watanabe, T., Hibino, M., Miyayama, M., Abe, H., and Kajita, K., 2002, “Amorphous  $\text{V}_2\text{O}_5$ /Carbon Composites as Electrochemical Supercapacitor Electrodes,” *Solid State Ion.*, **152–153**, pp. 833–841.
- [99] Chaloner-Gill, B., Shackle, D. R., and Andersen, T. N., 2000, “A Vanadium-Based Cathode for Lithium-Ion Batteries,” *J. Electrochem. Soc.*, **147**(10), pp. 3575–3578.
- [100] Shembel, E., Apostolova, R., Nagirny, V., Aurbach, D., and Markovsky, B., 1999, “Interrelation between Structural and Electrochemical Properties of the Cathode Based on Vanadium Oxide for Rechargeable Batteries,” *J. Power Sources*, **81**, pp. 480–486.
- [101] Trikalitis, P. N., Petkov, V., and Kanatzidis, M. G., 2003, “Structure of Redox Intercalated  $(\text{NH}_4)_{0.5}\text{V}_2\text{O}_5 \cdot m\text{H}_2\text{O}$  Xerogel Using the Pair Distribution Function Technique,” *Chem. Mater.*, **15**(17), pp. 3337–3342.
- [102] Ponzio, E. A., Benedetti, T. M., and Torresi, R. M., 2007, “Electrochemical and Morphological Stabilization of  $\text{V}_2\text{O}_5$  Nanofibers by the Addition of Polyaniline,” *Electrochimica Acta*, **52**(13), pp. 4419–4427.
- [103] Vernardou, D., Sapountzis, A., Spanakis, E., Kenanakis, G., Koudoumas, E., and Katsarakis, N., 2013, “Electrochemical Activity of Electrodeposited  $\text{V}_2\text{O}_5$  Coatings,” *J. Electrochem. Soc.*, **160**(1), pp. D6–D9.
- [104] Zhou, X., Chen, H., Shu, D., He, C., and Nan, J., 2009, “Study on the Electrochemical Behavior of Vanadium Nitride as a Promising Supercapacitor Material,” *J. Phys. Chem. Solids*, **70**(2), pp. 495–500.
- [105] Lee, H. Y., and Goodenough, J. B., 1999, “Ideal Supercapacitor Behavior of Amorphous  $\text{V}_2\text{O}_5 \cdot n\text{H}_2\text{O}$  in Potassium Chloride (KCl) Aqueous Solution,” *J. Solid State Chem.*, **148**(1), pp. 81–84.

- [106] Jayalakshmi, M., Rao, M. M., Venugopal, N., and Kim, K.-B., 2007, "Hydrothermal Synthesis of  $\text{SnO}_2\text{-V}_2\text{O}_5$  Mixed Oxide and Electrochemical Screening of Carbon Nano-Tubes (CNT),  $\text{V}_2\text{O}_5$ ,  $\text{V}_2\text{O}_5\text{-CNT}$ , and  $\text{SnO}_2\text{-V}_2\text{O}_5\text{-CNT}$  Electrodes for Supercapacitor Applications," *J. Power Sources*, **166**(2), pp. 578–583.
- [107] Cottineau, T., Toupin, M., Delahaye, T., Brousse, T., and Bélanger, D., 2006, "Nanostructured Transition Metal Oxides for Aqueous Hybrid Electrochemical Supercapacitors," *Appl. Phys. A*, **82**(4), pp. 599–606.
- [108] Kim, I.-H., Kim, J.-H., Cho, B.-W., and Kim, K.-B., 2006, "Pseudocapacitive Properties of Electrochemically Prepared Vanadium Oxide on Carbon Nanotube Film Substrate," *J. Electrochem. Soc.*, **153**(8), pp. A1451–A1458.
- [109] Toupin, M., Brousse, T., and Bélanger, D., 2004, "Charge Storage Mechanism of  $\text{MnO}_2$  Electrode Used in Aqueous Electrochemical Capacitor," *Chem. Mater.*, **16**(16), pp. 3184–3190.
- [110] Devaraj, S., and Munichandraiah, N., 2005, "High Capacitance of Electrodeposited  $\text{MnO}_2$  by the Effect of a Surface-Active Agent," *Electrochem. Solid-State Lett.*, **8**(7), pp. A373–A377.
- [111] Toupin, M., Brousse, T., and Bélanger, D., 2002, "Influence of Microstructure on the Charge Storage Properties of Chemically Synthesized Manganese Dioxide," *Chem. Mater.*, **14**(9), pp. 3946–3952.
- [112] Lee, H. Y., and Goodenough, J. B., 1999, "Supercapacitor Behavior with KCl Electrolyte," *J. Solid State Chem.*, **144**(1), pp. 220–223.
- [113] Hill, L. I., Portal, R., Verbaere, A., and Guyomard, D., 2001, "One-Step Electrochemical Synthesis of  $\alpha$   $\text{MnO}_2$  and  $\alpha\cdot\gamma$   $\text{MnO}_2$  Compounds for Lithium Batteries," *Electrochem. Solid-State Lett.*, **4**(11), pp. A180–A183.
- [114] Volotovskiy, V., and Kim, N., 1998, "Ascorbic Acid Determination with an Ion-Sensitive Field Effect Transistor-Based Peroxidase Biosensor," *Anal. Chim. Acta*, **359**(1), pp. 143–148.
- [115] Bai, L., Qu, D. Y., Conway, B. E., Zhou, Y. H., Chowdhury, G., and Adams, W. A., 1993, "Rechargeability of a Chemically Modified  $\text{MnO}_2/\text{Zn}$  Battery System at Practically Favorable Power Levels," *J. Electrochem. Soc.*, **140**(4), pp. 884–889.
- [116] Luo, X.-L., Xu, J.-J., Zhao, W., and Chen, H.-Y., 2004, "Ascorbic Acid Sensor Based on Ion-Sensitive Field-Effect Transistor Modified with  $\text{MnO}_2$  Nanoparticles," *Anal. Chim. Acta*, **512**(1), pp. 57–61.

- [117] Messaoudi, B., Joiret, S., Keddami, M., and Takenouti, H., 2001, "Anodic Behaviour of Manganese in Alkaline Medium," *Electrochimica Acta*, **46**(16), pp. 2487–2498.
- [118] Hu, C.-C., and Tsou, T.-W., 2002, "Ideal Capacitive Behavior of Hydrous Manganese Oxide Prepared by Anodic Deposition," *Electrochem. Commun.*, **4**(2), pp. 105–109.
- [119] Pang, S.-C., Anderson, M. A., and Chapman, T. W., 2000, "Novel Electrode Materials for Thin-Film Ultracapacitors: Comparison of Electrochemical Properties of Sol-Gel-Derived and Electrodeposited Manganese Dioxide," *J. Electrochem. Soc.*, **147**(2), pp. 444–450.
- [120] Huang, M., Li, F., Dong, F., Zhang, Y. X., and Zhang, L. L., 2015, "MnO<sub>2</sub>-Based Nanostructures for High-Performance Supercapacitors," *J. Mater. Chem. A*, **3**(43), pp. 21380–21423.
- [121] Hung, C. J., Hung, J. H., Lin, P., and Tseng, T. Y., 2011, "Electrophoretic Fabrication and Characterizations of Manganese Oxide/Carbon Nanotube Nanocomposite Pseudocapacitors," *J. Electrochem. Soc.*, **158**(8), pp. A942–A947.
- [122] Rudge, A., Raistrick, I., Gottesfeld, S., and Ferraris, J. P., 1994, "A Study of the Electrochemical Properties of Conducting Polymers for Application in Electrochemical Capacitors," *Electrochimica Acta*, **39**(2), pp. 273–287.
- [123] Ryu, K. S., Kim, K. M., Park, N.-G., Park, Y. J., and Chang, S. H., 2002, "Symmetric Redox Supercapacitor with Conducting Polyaniline Electrodes," *J. Power Sources*, **103**(2), pp. 305–309.
- [124] Ramya, R., Sivasubramanian, R., and Sangaranarayanan, M. V., 2013, "Conducting Polymers-Based Electrochemical supercapacitors—Progress and Prospects," *Electrochimica Acta*, **101**, pp. 109–129.
- [125] Snook, G. A., Kao, P., and Best, A. S., 2011, "Conducting-Polymer-Based Supercapacitor Devices and Electrodes," *J. Power Sources*, **196**(1), pp. 1–12.
- [126] Villers, D., Jobin, D., Soucy, C., Cossement, D., Chahine, R., Breau, L., and Bélanger, D., 2003, "The Influence of the Range of Electroactivity and Capacitance of Conducting Polymers on the Performance of Carbon Conducting Polymer Hybrid Supercapacitor," *J. Electrochem. Soc.*, **150**(6), pp. A747–A752.
- [127] Hashmi, S. A., and Upadhyaya, H. M., 2002, "Polypyrrole and Poly (3-Methyl Thiophene)-Based Solid State Redox Supercapacitors Using Ion Conducting Polymer Electrolyte," *Solid State Ion.*, **152**, pp. 883–889.

- [128] Ryu, K. S., Kim, K. M., Park, Y. J., Park, N.-G., Kang, M. G., and Chang, S. H., 2002, "Redox Supercapacitor Using Polyaniline Doped with Li Salt as Electrode," Proc. Int. Conf. SOLID STATE Ion. Mater. Process. ENERGY Environ. CAIRNS Aust. 8-13 JULY 2001, **152–153**, pp. 861–866.
- [129] Ho, M. Y., Khiew, P. S., Isa, D., Tan, T. K., Chiu, W. S., and Chia, C. H., 2014, "A Review of Metal Oxide Composite Electrode Materials for Electrochemical Capacitors," *Nano*, **9**(6), p. 1430002.
- [130] Zhong, C., Deng, Y., Hu, W., Qiao, J., Zhang, L., and Zhang, J., 2015, "A Review of Electrolyte Materials and Compositions for Electrochemical Supercapacitors," *Chem. Soc. Rev.*, **44**(21), pp. 7484–7539.
- [131] Galiński, M., Lewandowski, A., and Stępnia, I., 2006, "Ionic Liquids as Electrolytes," *Electrochimica Acta*, **51**(26), pp. 5567–5580.
- [132] Ata, M. S., Ghosh, S., and Zhitomirsky, I., 2016, "Electrostatic Assembly of Composite Supercapacitor Electrodes, Triggered by Charged Dispersants," *J. Mater. Chem. A*, **4**(45), pp. 17857–17865.
- [133] Gao, Q., Demarconnay, L., Raymundo-Piñero, E., and Béguin, F., 2012, "Exploring the Large Voltage Range of Carbon/Carbon Supercapacitors in Aqueous Lithium Sulfate Electrolyte," *Energy Environ. Sci.*, **5**(11), pp. 9611–9617.
- [134] Wang, Q., Yan, J., Wang, Y., Ning, G., Fan, Z., Wei, T., Cheng, J., Zhang, M., and Jing, X., 2013, "Template Synthesis of Hollow Carbon Spheres Anchored on Carbon Nanotubes for High Rate Performance Supercapacitors," *Carbon*, **52**, pp. 209–218.
- [135] Yan, J., Wang, Q., Wei, T., and Fan, Z., 2014, "Recent Advances in Design and Fabrication of Electrochemical Supercapacitors with High Energy Densities," *Adv. Energy Mater.*, **4**(4).
- [136] Burke, A., 2000, "Ultracapacitors: Why, How, and Where Is the Technology," *J. Power Sources*, **91**(1), pp. 37–50.
- [137] Pandey, G. P., Kumar, Y., and Hashmi, S. A., 2010, "Ionic Liquid Incorporated Polymer Electrolytes for Supercapacitor Application."
- [138] Reddy, R. N., and Reddy, R. G., 2003, "Sol-gel MnO<sub>2</sub> as an Electrode Material for Electrochemical Capacitors," *J. Power Sources*, **124**(1), pp. 330–337.
- [139] Broughton, J. N., and Brett, M. J., 2005, "Variations in MnO<sub>2</sub> Electrodeposition for Electrochemical Capacitors," *Electrochimica Acta*, **50**(24), pp. 4814–4819.

- [140] Nam, K.-W., and Kim, K.-B., 2006, "Manganese Oxide Film Electrodes Prepared by Electrostatic Spray Deposition for Electrochemical Capacitors," *J. Electrochem. Soc.*, **153**(1), pp. A81–A88.
- [141] Vangari, M., Pryor, T., and Jiang, L., 2013, "Supercapacitors: Review of Materials and Fabrication Methods," *J. Energy Eng.*, **139**(2), pp. 72–79.
- [142] Switzer, J. A., 1987, "Electrochemical Synthesis of Ceramic Films and Powders," *Am. Ceram. Soc. Bull.*, **66**(10), pp. 1521–1524.
- [143] Zhitomirsky, I., 2002, "Cathodic Electrodeposition of Ceramic and Organoceramic Materials. Fundamental Aspects," *Adv. Colloid Interface Sci.*, **97**(1–3), pp. 279–317.
- [144] Farrokhpay, S., 2009, "A Review of Polymeric Dispersant Stabilisation of Titania Pigment," *Adv. Colloid Interface Sci.*, **151**(1), pp. 24–32.
- [145] Sarkar, P., and Nicholson, P. S., 1996, "Electrophoretic Deposition (EPD): Mechanisms, Kinetics, and Application to Ceramics," *J. Am. Ceram. Soc.*, **79**(8), pp. 1987–2002.
- [146] Trefalt, G., and Borkovec, M., 2014, Overview of DLVO Theory, Creative Commons Attribution 4.0 International.
- [147] Boccaccini, A. R., and Zhitomirsky, I., 2002, "Application of Electrophoretic and Electrolytic Deposition Techniques in Ceramics Processing," *Curr. Opin. Solid State Mater. Sci.*, **6**(3), pp. 251–260.
- [148] Yang, Q. M., Ettel, V. A., Babjak, J., Charles, D. K., and Mosoiu, M. A., 2003, "Pasted Ni(OH)<sub>2</sub> Electrodes Using Ni Powders for High-Drain-Rate, Ni-Based Batteries," *J. Electrochem. Soc.*, **150**(4), pp. A543–A550.
- [149] Ata, M. S., and Zhitomirsky, I., 2015, "Colloidal Methods for the Fabrication of Carbon Nanotube–manganese Dioxide and Carbon Nanotube–polypyrrole Composites Using Bile Acids," *J. Colloid Interface Sci.*, **454**, pp. 27–34.
- [150] Ata, M. S., Zhu, G.-Z., Botton, G. A., and Zhitomirsky, I., 2014, "Electrophoretic Deposition of Manganese Dioxide Films Using New Dispersing Agents," *Adv. Appl. Ceram.*, **113**(1), pp. 22–27.

## Chapter 3 Objectives

The objective of this investigation was the development of advanced thin film and bulk supercapacitor electrodes and devices with enhanced electrochemical performance.

This was achieved by:

- Development of advanced materials and techniques for dispersion of oxide particles and CNT.
- Development of advanced techniques for fabrication of composites by electrochemical and chemical methods.
- Development of advanced slurry formulation for EPD and deposition mechanism.
- Discovery of new dopants for PPy and synthesis of PPy coated MWCNT for ES application.
- Development of negative electrodes for ES devices
- Development, fabrication and testing of asymmetric bulk supercapacitor electrodes and devices with high active mass loading and enhanced performance.

In order to address objectives of this work, we investigated advanced dispersing agents and dispersion mechanisms, new techniques for design of electrodes and devices and applied obtained results for the fabrication of advanced supercapacitors, which showed enhanced capacitive behavior.

## Chapter 4 Experimental procedures

### 4.1 Starting materials

The following materials were purchased from Sigma-Aldrich Co., USA

- (i) Potassium permanganate ( $\text{KMnO}_4$ )
- (ii) Manganese(II) nitrate tetrahydrate ( $\text{Mn}(\text{NO}_3)_2 \cdot 4\text{H}_2\text{O}$ )
- (iii) Pyrrole (Py)
- (iv) Ammonium peroxydisulfate ( $(\text{NH}_4)_2\text{S}_2\text{O}_8$ ) (APS)
- (v) Tiron
- (vi) Sodium cholate (ChNa)
- (vii) Taurocholic acid sodium salt (TChNa)
- (viii) Deoxycholic acid sodium salt (DChNa)
- (ix) Pamoic acid (PA)
- (x) Folic acid (FA)
- (xi) Humic acid (HA)
- (xii) 3-Phosphonopropionic acid (3PHA)
- (xiii) 16-Phosphonohexadecanoic acid (16PHA)
- (xiv) Octadecylphosphonic acid (octaPHA)
- (xv) 6-Phosphonohexanoic acid (PHA)
- (xvi) 2,6-Pyridinedicarboxylic acid (PCA)
- (xvii) Azure A chloride (AZA)
- (xviii) Nile Blue chloride (NB)

- (xix) Celestine blue (CLB)
- (xx) Caffeic acid (CA)
- (xxi) Ethyl violet (EV)
- (xxii) Pyronin Y (PY)
- (xxiii) Poly(4-styrenesulfonic acid-*co*-maleic acid) sodium salt (P(SSA-MA))
- (xxiv) Poly(vinyl butyral-*co*-vinyl alcohol-*co*-vinyl acetate), ( $M_w=50000-80000$ ) (PVB)
- (xxv) Sodium hydroxide (NaOH)
- (xxvi) Sodium sulfate ( $Na_2SO_4$ )
- (xxvii) Polyvinylidene Fluoride (PVDF)
- (xxviii) N-methylpyrrolidone (MP)

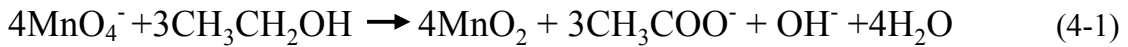
Other materials

- (i) Multiwalled carbon nanotubes (MWCNTs), Bayer Inc., Germany
- (ii) Activated carbon (AC), PICA, USA
- (iii) Carbon black (CB), Cabot, USA
- (iv) Polyethylenimine (PEI), Polyscience Inc., USA
- (v) Pyrogallol red (PGR), Alfa Aesar, USA
- (vi) 316L stainless steel foils, Alfa Aesar, USA
- (vii) Nickel foam (porosity ~95%), Vale Canada

## 4.2 Materials synthesis

### (i) MnO<sub>2</sub> particles

MnO<sub>2</sub> nanoparticles were prepared by reduction of KMnO<sub>4</sub> using ethanol (Eq.4-1).



50 mL of ethanol was added to 100 mL of 0.21 M KMnO<sub>4</sub> solution, vigorous stirring was performed for 20 hours. The dark brown precipitate was collected using filtration and washed using 2 L water and 0.5 L ethanol. The final powder was further dried in air for 48 hours and stored in a desiccator. The full process is schematically shown in Figure 4-1. The MnO<sub>2</sub> nanoparticles obtained using this method had an diameters varying from 30 to 60 nm[1].

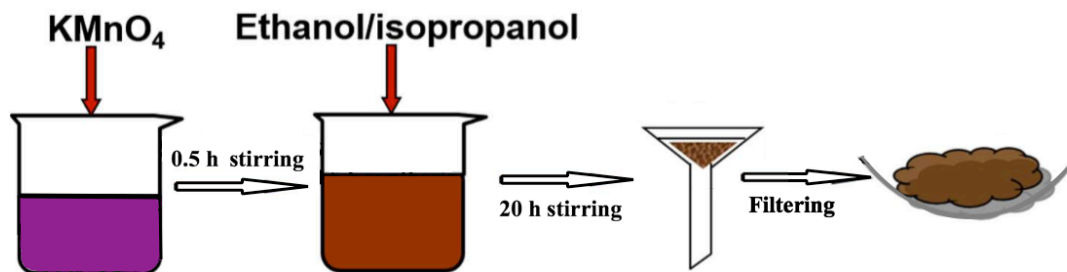


**Figure 4-1 Schematic illustration of MnO<sub>2</sub> synthesizing process**

### (ii) Mn<sub>3</sub>O<sub>4</sub> particles synthesis at room temperature

The synthesis of Mn<sub>3</sub>O<sub>4</sub> particles[2] was performed using Mn(NO<sub>3</sub>)<sub>2</sub>•4H<sub>2</sub>O solutions. In a

typical procedure 0.5 mol L<sup>-1</sup> of Mn(NO<sub>3</sub>)<sub>2</sub>•4H<sub>2</sub>O was dissolved in 60 mL of water. Certain amount of NaOH was added dropwise to achieve pH=10. The obtained suspension was ultrasonicated for 15min and stirred during 4 hours. The precipitate was washed with water and dried in air. The typical particle size was about ~30 nm.

(iii) Mn<sub>3</sub>O<sub>4</sub> particles synthesis at 60°C

The procedure for the fabrication of Mn<sub>3</sub>O<sub>4</sub> nanoparticles involved slow addition of ~15 ml of NH<sub>4</sub>OH solution to 100 ml of aqueous 0.1 M Mn(NO<sub>3</sub>)<sub>2</sub> solution at a temperature of 60°C in order to achieve pH = 11. Then 1 ml of H<sub>2</sub>O<sub>2</sub> was added to the mixture and stirring was continued during 1 h at 60 °C. The precipitate was washed and dried at in air. The typical particle size was about 20–50 nm.

(iv) PPy coated MWCNT

PPy coated MWCNT were prepared by a chemical polymerization method. In this procedure, MWCNT were dispersed in water using TChNa. Then PPy monomer solution, containing Tiron as a dopant, was added to the suspension. The polymerization of Py was performed by addition of APS. The concentrations of Py, Tiron and APS were 10, 1 and 30 mM, respectively. The Py:MWCNT mass ratio was 4:1. The temperature of the suspension was kept at 2 °C and the reaction was carried out for 4 h.

### **4.3 Electrophoretic deposition procedure**

EPD was performed using a constant voltage power supply (EPS 2A200, Amersham Biosciences). The whole procedure was schematically illustrated in Figure 4-2, where

suspension was used for EPD. Stainless steel (SS) 304 foils ( $25 \times 50 \times 0.1$  mm) and Ni plaques ( $10 \times 30 \times 0.3$  mm) were used as substrates with two platinum counter electrodes. The distance between substrate and platinum counter electrode ( $50 \times 50 \times 0.1$  mm) was 15 mm. Depending on whether it was cathodic reaction or anodic reaction, proper potential difference was applied to two electrodes. Before the deposition, the suspensions were ultrasonicated for 30 min to achieve a homogenous dispersion. The deposition yield was measured using balance with 0.01 mg accuracy. After deposition, the deposits were dried in air for 48 h. The deposition yield-concentration, deposition yield-deposition time, and deposition yield-deposition voltage dependences were analyzed.

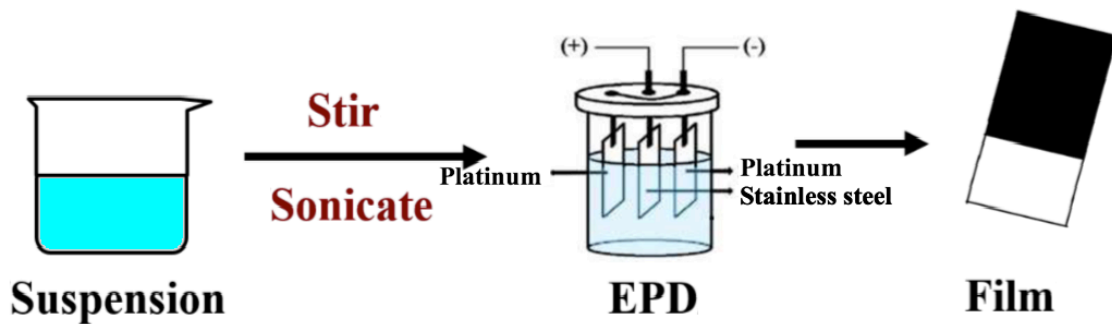


**Figure 4-2 Schematic procedure of EPD**

(i) Electrode fabrication by EPD using ChNa film forming dispersant

The concentration of ChNa was varied in the range of  $0-10 \text{ g L}^{-1}$ . EPD was obtained on SS substrates and performed at a deposition voltage of 10 V, the deposition time was varied in the range of 0-5 min.

EPD of composites, containing MWCNT was obtained on stainless SS using suspensions, containing  $1 \text{ g L}^{-1}$  MWCNT in water. The concentration of ChNa in the suspensions was varied in the range of  $0\text{-}1 \text{ g L}^{-1}$ . The deposition was performed at constant voltages of  $10\text{V}$ . EPD of  $\text{MnO}_2$  was performed on SS substrates using suspensions, containing  $4 \text{ g L}^{-1}$   $\text{MnO}_2$  in water. The concentration of ChNa in the suspensions was  $0.5 \text{ g L}^{-1}$ . The deposition was performed at constant voltages of  $10 \text{ V}$ . The deposition time was varied in the range of  $0\text{-}5 \text{ min}$ .

The EPD from suspensions containing  $\text{MnO}_2$  and MWCNT, dispersed using ChNa, allowed the formation of composite films.  $\text{MnO}_2\text{-MWCNT}$  electrodes were obtained by EPD from suspensions, containing  $4 \text{ g L}^{-1}$   $\text{MnO}_2$ ,  $1 \text{ g L}^{-1}$  MWCNT and  $1 \text{ g L}^{-1}$  ChNa. Ni plaques were used as substrates for deposition. After deposition with variation of time and voltages, different  $\text{MnO}_2\text{-MWCNTs}$  composite electrodes were obtained.

(ii) EPD of MWCNT using TChNa as dispersant

The obtained suspensions were used for anodic EPD of MWCNT. Anodic deposits were obtained on SS substrates from  $1 \text{ g L}^{-1}$  MWCNT suspensions, the concentration of TChNa in the suspensions was varied in the range of  $0\text{-}1 \text{ g L}^{-1}$ . The deposition was performed at constant voltages of  $10 \text{ V}$ . The deposition time was varied in the range of  $0\text{-}5 \text{ min}$ .

(iii) EPD of DChNa

The concentration of DChNa was varied in the range of  $0\text{-}8 \text{ g L}^{-1}$ . EPD was obtained on SS substrates and performed at a deposition voltage of  $10 \text{ V}$ , the deposition time was varied in the range of  $0\text{-}5 \text{ min}$ .

Anodic MWCNT deposits were obtained on SS substrate from  $1 \text{ g L}^{-1}$  MWCNT suspensions, the concentration of DChNa in the suspensions was varied in the range of 0- $1 \text{ g L}^{-1}$ . The deposition was performed at constant voltages of 10 V. The deposition time was varied in the range of 0-5 min.

The EPD from suspensions containing  $\text{MnO}_2$  and MWCNT, dispersed using DChNa, allowed the formation of composite films.  $\text{MnO}_2$ -MWCNT electrodes were obtained by EPD from suspensions, containing  $4 \text{ g L}^{-1}$   $\text{MnO}_2$ ,  $1 \text{ g L}^{-1}$  MWCNT and  $1 \text{ g L}^{-1}$  DChNa. Ni plaques were used as substrates for deposition. After deposition with variation of time and voltages, different  $\text{MnO}_2$ -MWCNTs composite electrodes were obtained.

(iv) EPD of  $\text{MnO}_2$  using FA and HA dispersants

Anodic EPD was successfully achieved on SS substrates from the  $4 \text{ g L}^{-1}$   $\text{MnO}_2$  suspensions containing FA. The concentration of FA in the suspensions was varied in the range of 0- $0.5 \text{ g L}^{-1}$ . The deposition was performed at a constant voltage of 20 V.

EPD was obtained on SS substrates containing HA, as a film forming dispersant. The concentration of HA was varied in range of 0- $0.7 \text{ g L}^{-1}$ . EPD was performed at a constant voltage of 100 V and deposition time of 5 min.

(v) EPD of  $\text{MnO}_2$  using 3PHA and 16PHA dispersants

Anodic EPD was obtained on SS substrates from  $4 \text{ g L}^{-1}$   $\text{MnO}_2$  suspension containing 0.3 and  $0.5 \text{ g L}^{-1}$  3PHA or 16PHA. The deposition time was varied in range of 0-8 min.

(vi) EPD of  $\text{MnO}_2$  containing PHA and PCA

Anodic EPD was successfully achieved on SS substrates from the  $4 \text{ g L}^{-1}$   $\text{MnO}_2$  suspension containing PHA or PCA. The concentrations of PHA or PCA were varied in the range of  $0\text{-}0.3 \text{ g L}^{-1}$ . The depositions were performed at constant voltages of 20 V and a deposition time of 5 min.

(vii) EPD of  $\text{Mn}_3\text{O}_4$  using CA and CIB

Anodic EPD was performed on SS substrates from  $10 \text{ g L}^{-1}$   $\text{Mn}_3\text{O}_4$  water suspension. CA concentration was varied in range of  $0\text{-}0.5 \text{ g L}^{-1}$ . EPD was performed at a deposition voltage 20 V and a deposition time of 5 min.

Cathodic EPD was achieved on SS substrates from the  $4 \text{ g L}^{-1}$   $\text{Mn}_3\text{O}_4$  in ethanol suspensions. The concentration of CIB was varied in the range of  $0\text{-}0.5 \text{ g L}^{-1}$ . EPD was performed at a deposition voltage of 20 V and a deposition time of 5 min.

#### **4.4 Electrode and ES device fabrication using slurry impregnation**

The slurry was prepared by mixing  $\text{MnO}_x$  or PPy with MWCNT, different dispersants and 2% of polyvinyl butyral (PVB) binder. The slurry was then impregnated into the porous INCOFOAM® current collectors. Once dried, the electrode was pressed into 30% of its original thickness using roller to improve contact between the electrode material and current collector. INCOFOAM® current collectors with a volumetric porosity of 95% were made by Vale Inco using carbonyl technology. The total mass loading of composite electrodes was  $20\text{-}55 \text{ mg cm}^{-2}$ . A schematic representation of the electrode fabrication process by impregnation of nickel foam current collector is shown in Figure 4-3.

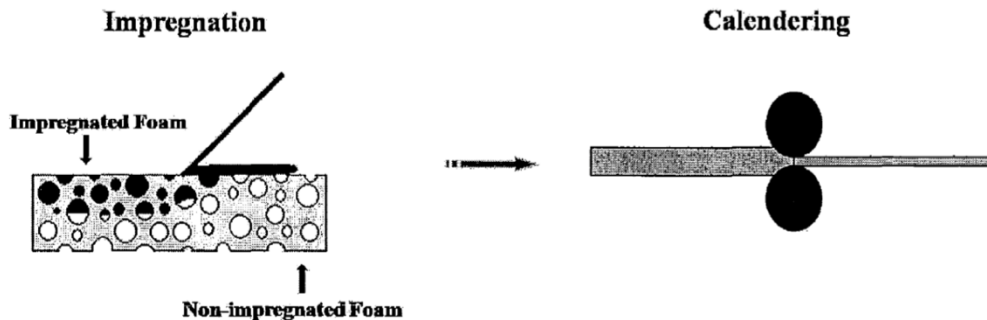


**Figure 4-3 Schematic representation of material impregnation into Ni foam collector**

Different types of ES devices were prepared. The separator of all ES device was a porous polyethylene membrane (mean pore size 0.4  $\mu\text{m}$ , Vale, Canada). The coin cell devices (CR2032 type, MTI Corporation, USA) were sealed using a hydraulic crimping machine (MSK-110, MTI Corporation, USA). Other cell devices contained two electrodes with area of 1.5 - 3  $\text{cm}^2$ . The asymmetric devices included  $\text{MnO}_2$ -MWCNT and AC-CB electrodes.

#### **4.5 Fabrication of negative electrodes for ES devices**

AC with specific area of 2300  $\text{m}^2 \text{g}^{-1}$  and CB were used for the fabrication of electrodes. Poly(vinylidene flouride) (PVDF) binder and 1-Methyl-2-pyrrolidinone (MP) solvent were used. The Ni foams were impregnated using slurries, containing AC, CB and PVDF in MP, and then dried at 70°C in air for 4 h.

#### **4.6 Materials characterization**

(i) X-ray diffraction studies

X-ray diffraction (XRD) investigations were carried out using Bruker D8 diffractometer and  $\text{Co K}\alpha$  radiation.

(ii) Morphology study

Electron microscopy studies were performed using JEOL JSM-7000F scanning electron microscope (SEM) and FEI Tecnai Osiris transmission electron microscope (TEM) equipped with super X field emission gun (X-FEG).

ChemiSTEM™ X-ray detection system was used for energy-dispersive X-ray (EDX) spectroscopy. High angle annular dark field (HAADF) method in the STEM mode was used to form images and perform EDX analysis. The Esprit software was used for elemental mapping.

(iii) FTIR, UV-Vis, thermogravimetric and differential thermal analysis studies

- Fourier transform infrared spectroscopy (FTIR) studies were performed on Bio-Rad FTS- 40 instrument.
- The Ultraviolet-Visible (UV-vis) spectra were obtained using a Cary-50 UV-Vis spectrophotometer.
- The thermogravimetric analysis (TGA) and differential thermal analysis (DTA) investigations were carried out in air at a heating rate of 5 °C min<sup>-1</sup> using a Netzsch STA-409 thermoanalyzer.

(iv) *In-situ* deposit yield study

The deposition kinetics has been investigated in-situ using a quartz crystal microbalance (QCM 922, Princeton Applied Research) controlled by a computer. The deposit mass  $\Delta m$  was calculated using Sauerbrey's equation (Eq.4-2)[3].

$$\Delta F = \frac{2F_0^2}{A\sqrt{\rho_q\mu_q}} x \Delta m \quad (4-2)$$

where  $\Delta F$  is the frequency decrease of the QCM,  $F_0$  is the parent frequency of QCM (9 MHz),  $A$  is the area of the gold electrode ( $0.2 \text{ cm}^2$ ),  $\rho_q$  is the density of quartz ( $2.65 \text{ g cm}^{-3}$ ) and  $\mu_q$  is the shear modulus of quartz ( $2.95 \times 10^{11} \text{ dyne cm}^{-2}$ ).

## 4.7 Electrochemical characterization

### 4.7.1 Cyclic voltammetry

Cyclic voltammetry (CV) of single electrodes, coin cell devices, and modules of several devices was tested using a potentiostat (PARSTAT 2273, Princeton Applied Research). Single electrodes were tested using three electrodes setup (Figure 4-4), where the reference electrode and counter electrode were the standard calomel electrode (SCE) and platinum gauze, respectively.

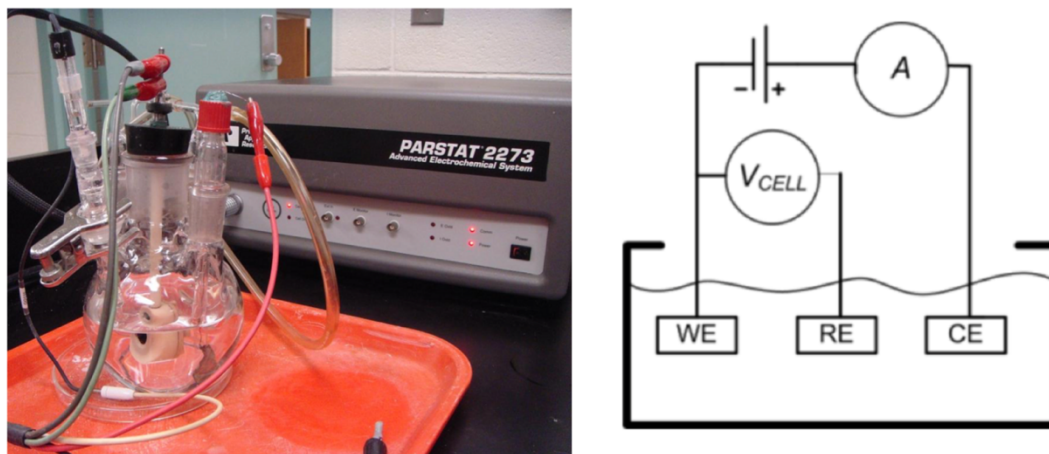


**Figure 4-4 Princeton PARSTAT 2273 potentiostat and scheme of three-electrode setup.**

CV was performed in  $0.5 \text{ M Na}_2\text{SO}_4$  aqueous electrolyte. The scan rates for CVs were varied from  $2 \text{ mV s}^{-1}$  to  $100 \text{ mV s}^{-1}$ . The SC was calculated using half the integrated area of the CV curve to obtain the charge ( $Q$ ), and subsequently dividing the charge by the width

of the potential window ( $\Delta U$ ) and film mass ( $m$ ) for gravimetric SC ( $C_m$ , Eq.4-3) or electrode area ( $S$ ) for areal SC ( $C_s$ , Eq.4-4).

$$C_m = Q/\Delta U \cdot m \quad (\text{Eq.4-3})$$

$$C_s = Q/\Delta U \cdot S \quad (\text{Eq.4-4})$$

#### 4.7.2 Electrochemical impedance spectroscopy

The electrochemical impedance spectroscopy (EIS) was also tested using a potentiostat (PARSTAT 2273, Princeton Applied Research). Complex impedance data,  $Z^*$  (Eq.4-5) was analyzed in a frequency range of 10 mHz-100 kHz under sinusoidal signal with amplitude of 5 mV.

$$Z^* = Z' - iZ'' \quad (\text{Eq.4-5})$$

The complex capacitance ( $C^*$ , Eq.4-6) was calculated from corresponding impedance data. The real part ( $C'$ , Eq.4-7) reflected the capacitance performance and the imaginary part ( $C''$ , Eq.4-8) reflected the energy dispersion of ES electrode or device[4].

$$C^* = C' - iC'' \quad (\text{Eq.4-6})$$

$$C' = Z''/w * |Z|^2 \quad (\text{Eq.4-7})$$

$$C'' = Z'/w * |Z|^2 \quad (\text{Eq.4-8})$$

where  $w=2\pi f$ ,  $f$  - frequency. The relaxation times  $\tau=1/f_m$  were obtained from the relaxation frequencies  $f_m$ , corresponding to the  $C''_s$  maxima.

### 4.7.3 Cyclic charge-discharge

Cyclic charge-discharge is a technique to characterize capacitive performance and cyclic stability of ES devices. A complete charge and discharge loop is called one charge-discharge cycle.

The charge-discharge loops were conducted at constant current (I) varying from 0.1 mA to 50 mA with voltage limits ( $\Delta U$ ) of 1.8 V for MnO<sub>2</sub>/MWCNT-AC/CB devices, using charge-discharge analyzer (BST8-3 and BST8-MA, MTI Corporation). The total charge (Q) was calculated ( $Q=I \cdot t$ , t-discharging time) from each cycle and the capacitance (C) is calculated from Eq.4-3 and Eq.4-4.

### References:

- [1] M. Cheong and I. Zhitomirsky, "Electrophoretic deposition of manganese oxide films," *Surf. Eng.*, vol. 25, no. 5, pp. 346–352, 2009.
- [2] F. Giovannelli, C. Autret-Lambert, C. Mathieu, T. Chartier, F. Delorme, and A. Seron, "Synthesis of manganese spinel nanoparticles at room temperature by coprecipitation," *J. Solid State Chem.*, vol. 192, pp. 109–112, Aug. 2012.
- [3] M. R. Deakin and D. A. Buttry, "Electrochemical applications of the quartz crystal microbalance," *Anal. Chem.*, vol. 61, no. 20, 1989.
- [4] P. L. Taberna, P. Simon, and J.-F. Fauvarque, "Electrochemical characteristics and impedance spectroscopy studies of carbon-carbon supercapacitors," *J. Electrochem. Soc.*, vol. 150, no. 3, pp. A292–A300, 2003.

## **Chapter 5 Colloidal methods for the fabrication of MnO<sub>2</sub>-MWCNT and PPy-MWCNT composites using bile acids**

### **5.1 Fundamental aspects of bile acids**

The methods of nanoparticles synthesis, surface modification, and dispersion play important roles in the development of colloidal nanotechnologies. The fundamental investigation of natural materials is an important source for new ideas in this area. Among the important examples are investigations, focused on applications of bile acids and their derivatives for the synthesis and dispersion of nanomaterials, which attracted the significant interest of different scientific communities.

Bile acids, such as cholic acid and deoxycholic acid, were found to be efficient reducing[1] and chelating[2] agents for the synthesis of nanoparticles. Of special interest are gel-forming properties of bile acids, which were utilized[3] for the fabrication of hybrid Ag-Au nanoparticles with the particle size of 1-2 nm and nanoparticles of ZnS and CdS with the typical size of 3-10 nm. Deoxycholic acid has been utilized for the synthesis of CdSe nanocrystals with controlled nanodot or nanorod morphologies, which exhibited enhanced photoluminescence[3]. Several investigations were focused on the application of bile acids and their derivatives for the development of photovoltaic devices[4–6]. Deoxycholamide crystalline network[7] was used as a platform for the assembly of dye molecules, which showed high fluorescence quantum yields. Deoxycholate was found to be an efficient stabilizer of luminescent silicon nanocrystals[8].

Bile acids are powerful natural surfactants, which solubilize proteins, fatty acids, lipids, vitamins, monoglycerides and cholesterol[9]. Bile acids' steroid molecular structure plays an important role in the dissolving power[10]. This structure is fundamentally different from the structure of conventional head-and-tail surfactants, which are composed of a hydrophobic tail and a polar head group. In contrast, bile acids have concave hydrophilic and convex hydrophobic surfaces[11]. Such surfaces play an important role in the interactions of bile acids with other molecules. Bile acids readily form mixed micelles with surfactants[12] and intermolecular compounds with various organic molecules[10]. It was found that cholic and deoxycholic acids crystallized to form channels in which the second component of the intermolecular compound can be closely confined[10,13].

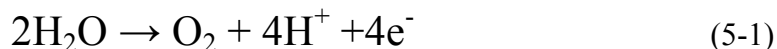
The goal of this investigation was the application of bile acid salts for the fabrication of composites, containing multiwalled carbon nanotubes (MWCNT) for application in electrodes of electrochemical supercapacitors. We demonstrate that pure cholic acid films can be obtained from the solutions of sodium cholate by anodic electrophoretic deposition (EPD). The deposition process was monitored by quartz crystal microbalance (QCM). The data analysis provides an insight into the influence of anionic groups on the deposition mechanism. The results presented below indicate that cholate can be used as dispersing, charging, film forming and binding agents for the deposition of MWCNT. As an extension of these investigations, we demonstrate the EPD of composite  $\text{MnO}_2$ -MWCNT films. In another strategy, taurocholic acid was used as a dispersing agent for colloidal fabrication of polypyrrole (PPy) coated MWCNT. Due to good dispersion of MWCNT, the

composites, prepared by colloidal methods showed promising performance for application in electrodes of electrochemical supercapacitors.

## 5.2 Dispersion and deposition mechanism of ChNa and TChNa

Chemical structures of ChNa and TChNa are given in Figure 5-1. Both structures include a rigid steroid backbone[14], which possesses a hydrophobic convex side and hydrophilic concave side. The hydroxyl groups are located on the concave side of the steroid backbone[14]. The anionic properties of ChNa and TChNa are attributed to  $\text{COO}^-$  and  $\text{SO}_3^-$  groups, respectively.

Thin films were obtained from ChNa solutions by anodic EPD. However, no EPD was achieved from TChNa solutions. The EPD mechanism involved the pH decrease at the anode surface due to the following electrode reaction



The electrophoresis of anionic  $\text{Ch}^-$  species resulted in their accumulation at the anode surface, protonation and charge neutralization:



As a result, ChH films were deposited on the anodic substrates. It is known that pH decrease leads to protonation of  $\text{COO}^-$  groups of  $\text{Ch}^-$  and formation of ChH, which has low solubility[15]. The charge neutralization and low solubility of ChH were beneficial for the deposit formation. Moreover, it is known that bile acids show a tendency to self-assembly[16,17], which involves aligning their hydrophobic or hydrophilic surfaces toward one another. In contrast, TCh $^-$  species are highly soluble at low and high pH. It is suggested

that mutual electrostatic repulsion of the TCh<sup>-</sup> species, containing anionic SO<sub>3</sub><sup>-</sup> groups, prevented deposit formation at the electrode surface.

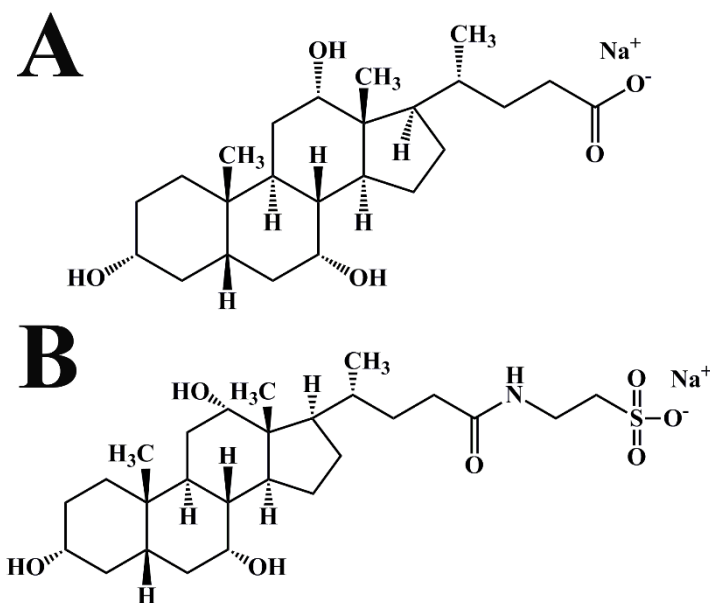
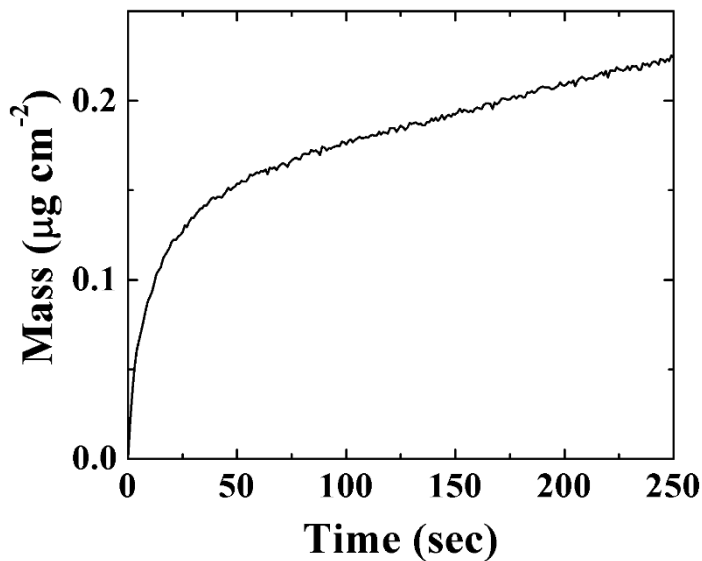


Figure 5-1 Chemical structures of (A) ChNa and (B) TChNa

### 5.3 Mechanism of ChNa film formation by using QCM and EPD methods

The deposition process was investigated in-situ using ChNa solutions of low concentrations by QCM method. Figure 5-2 shows deposit mass versus deposition time dependence for the ChH films. The deposited mass increased with increasing time, indicating continuous film growth. The decrease in the deposition rate with time was attributed to the increase in voltage drop in growing insulating film and a corresponding decrease in electric field in the solution[18]. The deposition yield increased with increasing ChNa concentration in solutions at a constant voltage and constant deposition time (Figure 5-3). The deposited

mass versus concentration dependence was non-linear. Significant increase in the deposition yield was observed at ChNa concentrations above  $1 \text{ g L}^{-1}$ . It is important to note that Hamaker equation predicts a linear increase in the electrophoretic deposition yield with increasing concentration[19]. The non-linear behavior can be attributed to different factors, such as the continuous motion of deposit-solution boundary during deposition[19] or influence of the concentration of particles, accumulated at the electrode surface, on their coagulation and film formation rate[20].



**Figure 5-2 Deposit mass versus time measured by QCM for  $0.1 \text{ g L}^{-1}$  ChNa solution at a deposition voltage 3 V.**

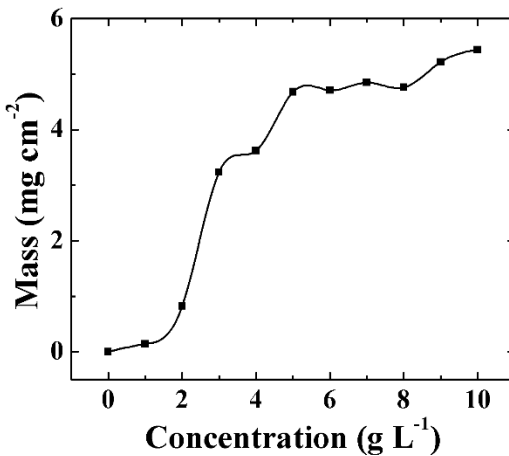


**Figure 5-3 Deposit mass versus ChNa concentration in solutions at deposit voltage of 10 V and deposition time of 5 min.**

The deposition process has been investigated potentiodynamically. Figure 5-4 shows cyclic voltammetry data for a stainless-steel electrode in the 1 g L<sup>-1</sup> ChNa solution. The anodic current increased significantly at electrode potential of about 1.2 V due to reaction (2). The current decreased with increasing cycle number due to the formation of insulating film in reaction (3). Therefore, cycling voltammetry data, presented in Figure 5-4, is in agreement with proposed deposition mechanism.

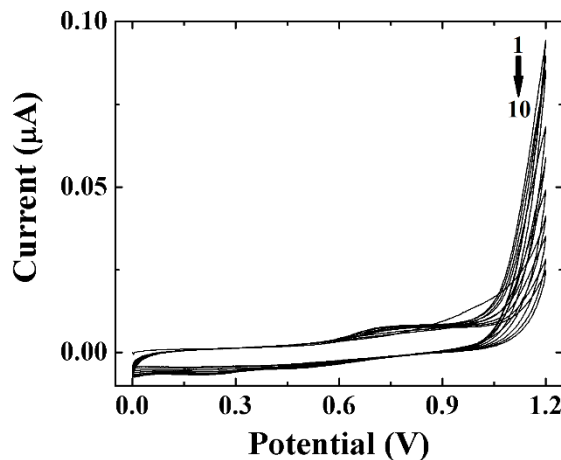


**Figure 5-4 CVs for stainless steel electrode in  $2\text{ g L}^{-1}$  ChNa solution at a scan rate of  $20\text{ mV s}^{-1}$ , arrow shows increasing cycle number.**

#### **5.4 Adsorption and methodology study of ChNa**

The deposition mechanism was also confirmed by FTIR investigations. Figure 5-5 compares the FTIR spectra of as-received ChNa and deposited ChH. The absorptions at  $1564$  and  $1406\text{ cm}^{-1}$  in the spectrum of ChNa can be attributed[2] to asymmetric and symmetric stretching vibrations of  $\text{COO}^-$  groups, respectively. The peaks at  $1078$  and  $1076\text{ cm}^{-1}$  in the spectra of ChNa and ChH, respectively, are related to stretching vibrations of C-O bonds[21]. The absorption at  $1710\text{ cm}^{-1}$  in the spectrum of ChH is attributed to stretching vibrations of protonated  $\text{COOH}$  groups[22,23]. Such absorption has not been observed in the spectrum of ChNa.

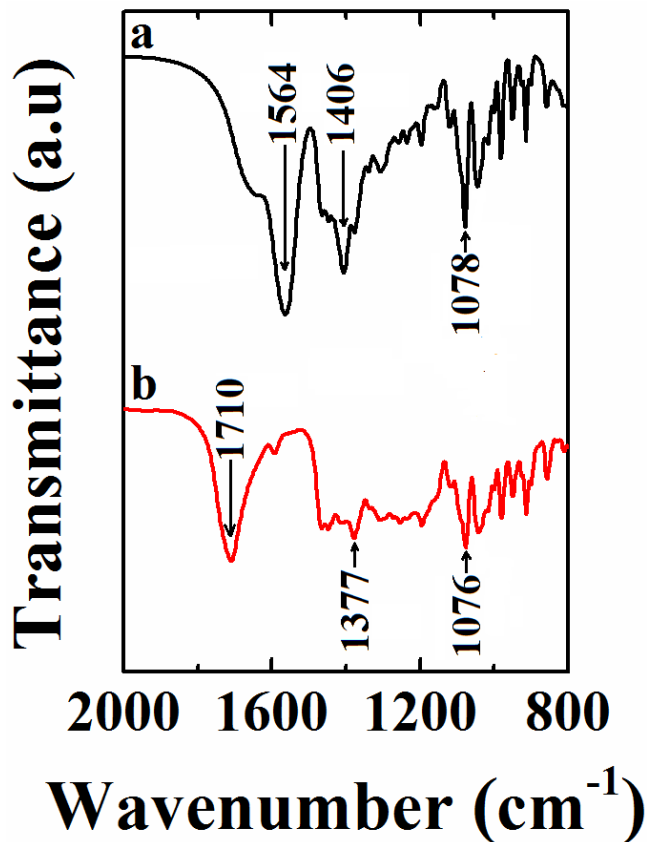


**Figure 5-5** FTIR spectra for (a) as received ChNa and (b) deposit, prepared from 1 g L<sup>-1</sup> ChNa solution at a deposition voltage of 10 V.

Figure 5-6 illustrates SEM images of a ChH film at different magnifications. The film contained a continuous thin layer (Figure 5-6A) and many particles of nearly spherical shape. The size of the spherical particles was in the range of 0.1-2 microns (Figure 5-6B). It is suggested that the increase in ChH concentration at the electrode surface during EPD resulted in enhanced self-assembly, driven by hydrophobic effect and hydrogen binding[24]. The ChH self-assembly can result in spherical particles at the electrode surface.

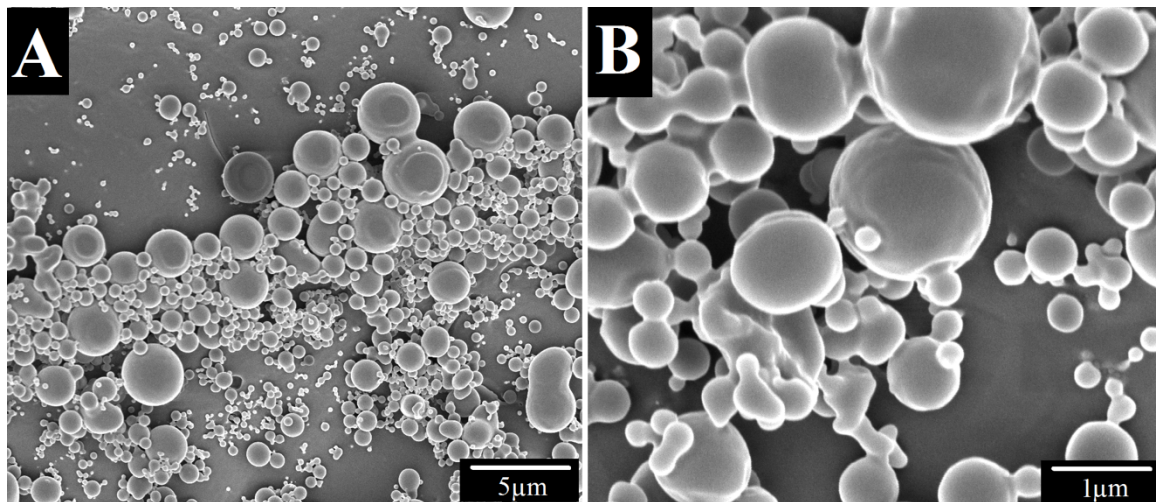


**Figure 5-6 (A and B) SEM images at different magnifications for deposit, prepared from  $2 \text{ g L}^{-1}$  ChNa solution at a deposition voltage of 10 V.**

### **5.5 EPD and characterization of MWCNT dispersed by ChNa and TChNa dispersants**

It is known that cholesterol groups of bile acids form very stable and homogeneous micelle structures around carbon nanotubes[25] and allow efficient dispersion of individual nanotubes. Bile acids wrap around the carbon nanotubes like a ring[14] and allow good dispersion stability. MWCNT were dispersed in water using ChNa and TChNa as dispersants. The suspensions were stable and did not show precipitation for more than one month. The obtained suspensions were used for anodic EPD of MWCNT. Anodic deposits were obtained from  $1 \text{ g L}^{-1}$  MWCNT suspensions, containing  $0.25\text{-}1.0 \text{ g L}^{-1}$  ChNa. The deposition yield increased with increasing ChNa concentration in the suspensions and with increasing deposition time at a constant ChNa concentration (Figure 5-7A,B). The increase in the concentration of  $\text{Ch}^-$  species in the suspension resulted in increasing  $\text{Ch}^-$  adsorption

on MWCNT and increasing charge, which, in turn, resulted in the increasing deposition yield. The addition of TChNa to the MWCNT suspension allowed the formation of anodic deposits. However, the deposits showed poor adhesion. The deposition yield increased with increasing TChNa concentration in the range of 0-0.3 g L<sup>-1</sup> and then decreased (Figure 5-7C). At concentrations above 0.5 g L<sup>-1</sup> significant deposit spalling was observed, which resulted in the reduced deposition yield. The deposition yield increased with increasing deposition time (Figure 5-7D). The deposition yield, obtained from MWCNT suspensions, containing TChNa was significantly lower, compared to that obtained from MWCNT suspensions, containing ChNa. It is important to note that the charge of the Ch<sup>-</sup> species, adsorbed on the MWCNT, was neutralized in the low pH region at the electrode surface (Eq.3). The charge neutralization promoted deposit formation. Moreover, the binding properties of ChH formed at the electrode surface promoted MWCNT adhesion to the electrode. The accumulation theory[20] of electrophoretic deposit formation can explain the deposition of MWCNT from suspensions, containing TChNa. The electrophoretic motion of MWCNT, containing adsorbed TCh<sup>-</sup> species resulted in the accumulation of MWCNT at the electrode surface. The coagulation of MWCNT can result from depletion forces, electrohydrodynamic flows, arising from electrode reactions, geometric confinement effect, long-range attraction forces and other factors[20].

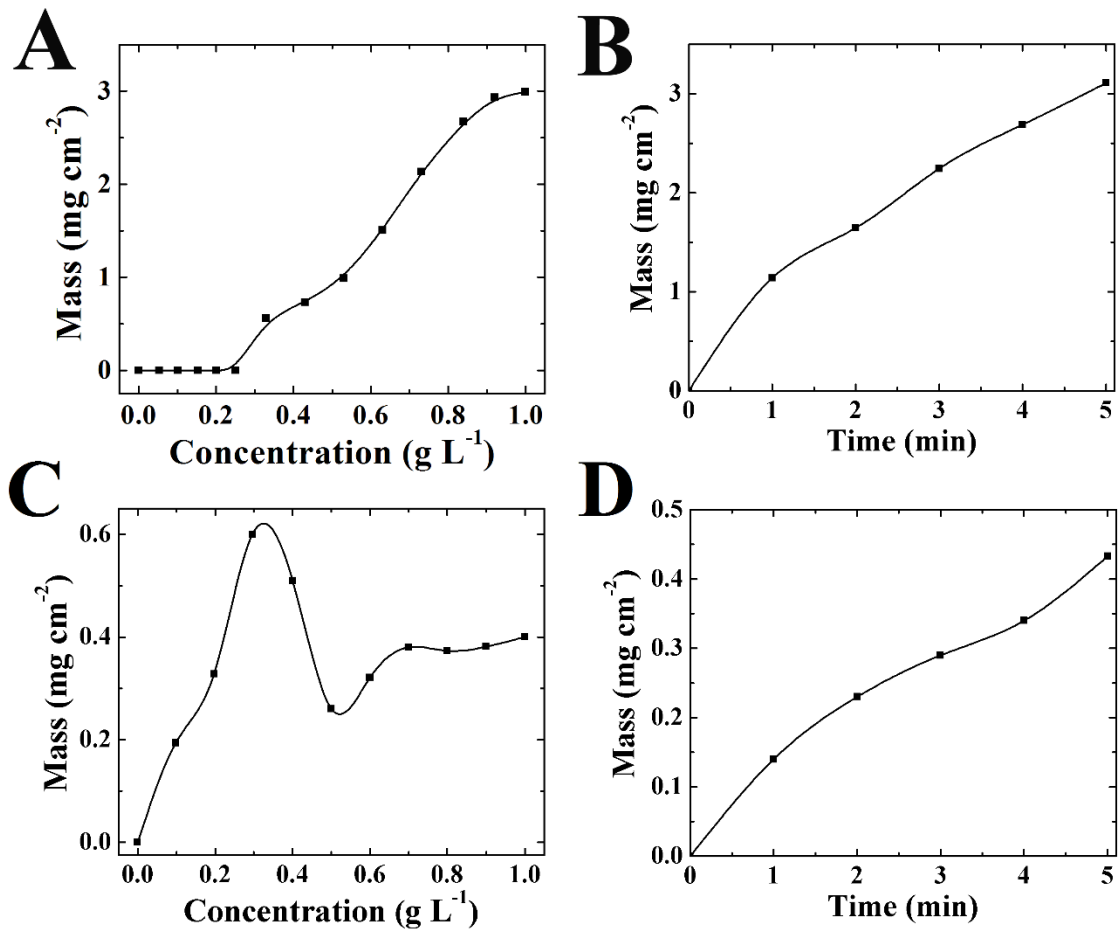
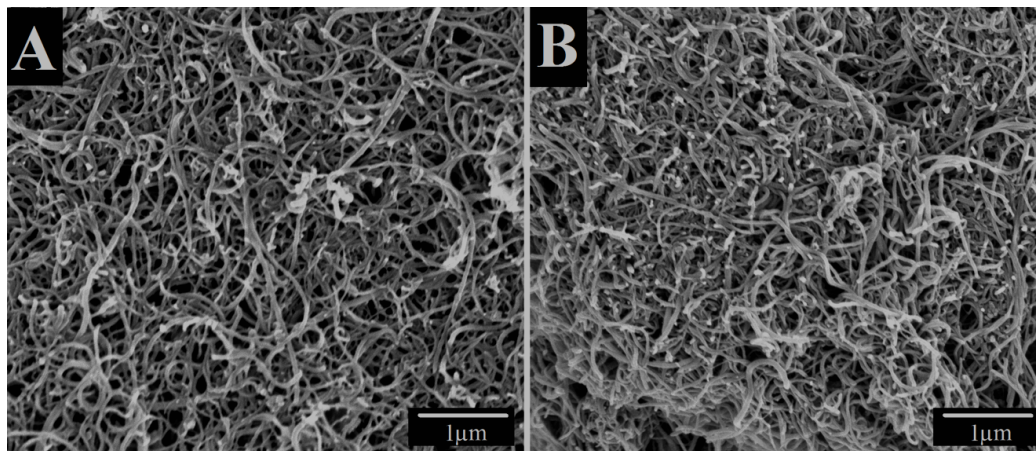


Figure 5-7 Deposit mass for deposits prepared from 1 g L<sup>-1</sup> MWCNT suspensions at a deposition voltage of 10 V versus (A) ChNa concentration at a deposition time of 5 min, (B) time at ChNa concentration of 1 g L<sup>-1</sup>, (C) TChNa concentration at a deposition time of 5 min, and (D) time at TChNa concentration of 1 g L<sup>-1</sup>.



**Figure 5-8 SEM images of deposits prepared at a deposition voltage of 10 V for 1 g L<sup>-1</sup> MWCNT suspension containing (A) 1 g L<sup>-1</sup> ChNa and (B) 1 g L<sup>-1</sup> TChNa.**

However, the electrostatic repulsion of MWCNT, attributed to adsorbed TCh<sup>-</sup> species, resulted in poor adhesion and low deposition yield. Figure 5-8 represents typical SEM images of the MWCNT, deposited on stainless steel substrates. MWCNT deposits formed a continuous fibrous network at the substrate surface.

### **5.6 EPD of MnO<sub>2</sub> in the presence of ChNa**

The use of ChNa and TChNa as dispersants for MWCNT paved the way for the fabrication of composites, containing MWCNT. As a step in this direction we fabricated and tested electrodes for electrochemical supercapacitors. Two different colloidal methods were explored. One strategy was based on the use of EPD for the fabrication of composite MnO<sub>2</sub>-MWCNT films using commercial Ni plaque current collectors. Another strategy involved the use of PPy coated MWCNT, prepared using TChNa as a dispersant and impregnation of commercial Ni foam current collectors. In the first strategy, we utilized ChNa as a dispersing, charging and film forming agent for EPD of MWCNT. Due to their low

isoelectric point[26], the  $\text{MnO}_2$  particles were negatively charged in pure water and in aqueous ChNa solutions and allowed the formation of anodic deposits. Figure 5-9 shows deposit mass versus deposition time dependence obtained from  $4 \text{ g L}^{-1}$   $\text{MnO}_2$  suspensions, containing  $0.5 \text{ g L}^{-1}$  ChNa. The deposit mass increased with increasing deposition time, indicating continuous  $\text{MnO}_2$  film growth.

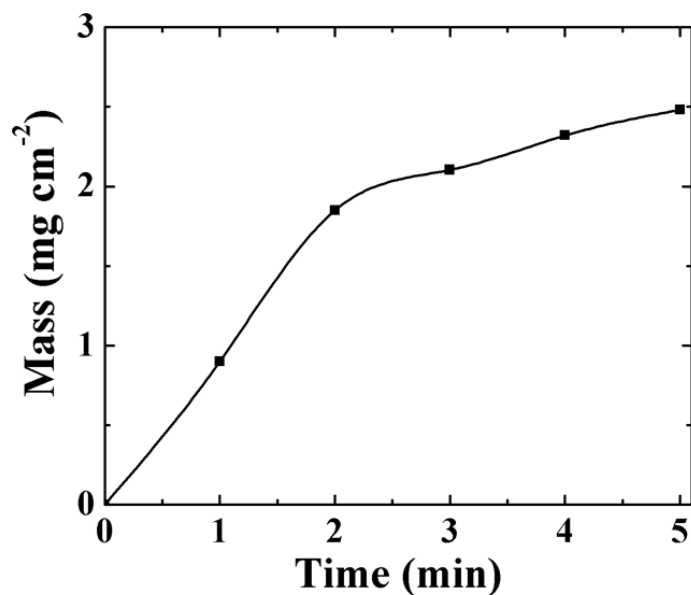


**Figure 5-9 Deposit mass versus time for  $4 \text{ g L}^{-1}$   $\text{MnO}_2$  suspensions, containing  $0.5 \text{ g L}^{-1}$  ChNa at a deposition voltage of 10 V.**

### **5.7 Morphology and electrochemical characterization of $\text{MnO}_2$ -MWCNT composite electrodes prepared using ChNa**

The EPD from suspensions containing  $\text{MnO}_2$  and MWCNT, dispersed using ChNa, allowed the formation of composite films. The SEM image of the composite film, presented in Figure 5-10 shows particles of  $\text{MnO}_2$  and MWCNT.

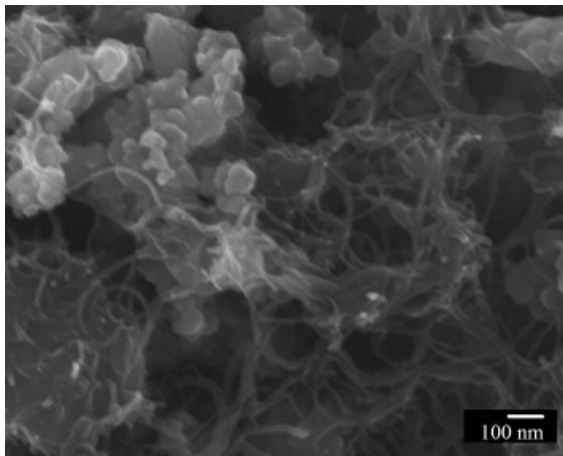


**Figure 5-10 SEM images of deposit obtained from a suspension, containing  $4 \text{ g L}^{-1} \text{ MnO}_2$ ,  $1 \text{ g L}^{-1} \text{ MWCNT}$  and  $1 \text{ g L}^{-1} \text{ ChNa}$ .**

The composite films showed a capacitive behavior in  $0.5 \text{ M Na}_2\text{SO}_4$  solutions. Cyclic voltammetry data showed nearly box shape CV (Figure 5-11A). The capacitance, calculated from CV data decreased from  $248 \text{ mF cm}^{-2}$ , with increasing scan rate from  $2$  to  $100 \text{ mV s}^{-1}$ , showing a capacitance retention of  $61 \%$  at  $100 \text{ mV s}^{-1}$ . The capacitance retention was significantly higher compared to that for  $\text{MnO}_2$ -MWCNT electrodes prepared by EPD using other dispersants[27,28]. It is important to note that capacitance, calculated from CV data is integral capacitance in a voltage window of  $0.9 \text{ V}$ , whereas impedance data allowed calculating a differential capacitance at AC voltage with amplitude of  $5 \text{ mV}$ . The frequency dependence of real and imaginary components of complex capacitance showed typical relaxation type dispersion, as indicated by decrease in capacitance  $C'$  with increasing frequency above  $0.1 \text{ Hz}$  and relaxation maximum in the frequency dependence of  $C''$  at  $0.2 \text{ Hz}$ . The differential capacitance at a frequency of  $10 \text{ mHz}$  was comparable with integral capacitance at a scan rate of  $2 \text{ mV s}^{-1}$ .

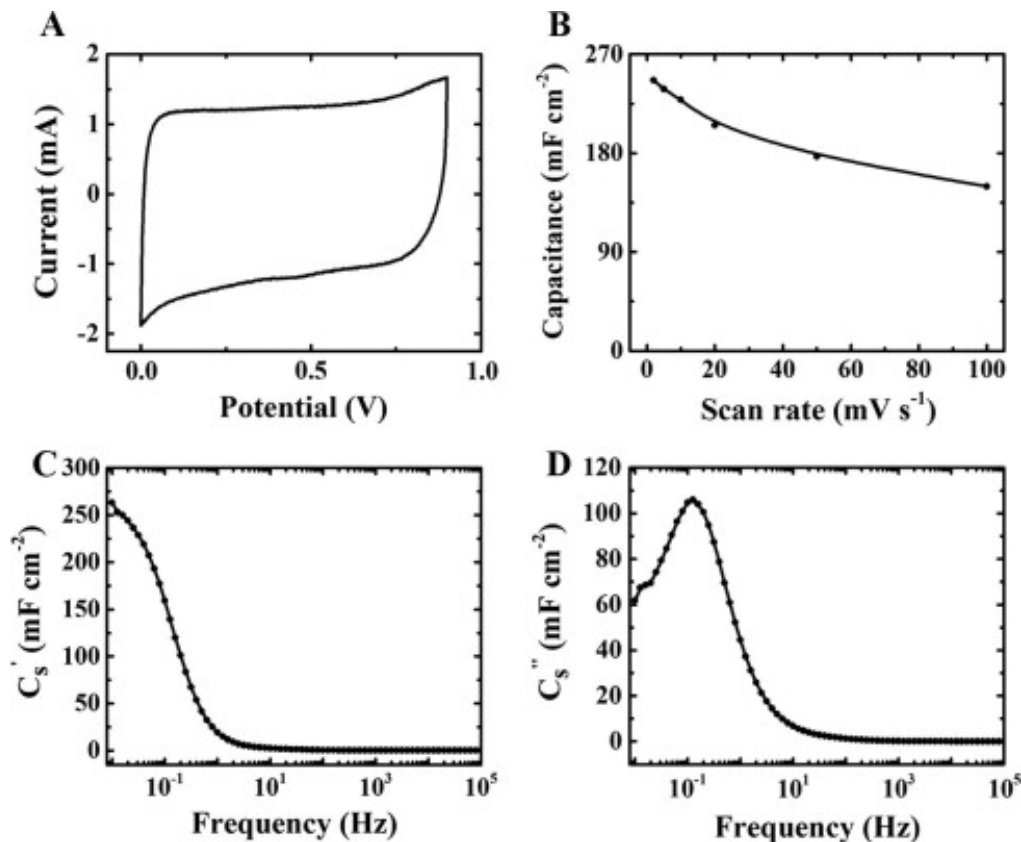


Figure 5-11 (A) CV at a scan rate at 5 mV s<sup>-1</sup>, (B) specific capacitance versus scan rate, (C) real part C' and (D) imaginary part C'' of capacitance, calculated from the impedance data for MnO<sub>2</sub>-MWCNT composite, prepared by EPD using ChNa as a dispersant.

## 5.8 Morphology and electrochemical characterization of PPy-MWCNT composite electrodes with TChNa

Figure 5-12 shows SEM image of PPy coated MWCNT, prepared using TChNa as a dispersant. The SEM observations clearly indicate the formation of PPy coated MWCNT. The SEM image shows fibers with typical diameter of 70-100 nm, which is significantly larger, compared to typical diameter of 10-15 nm of uncoated MWCNT. Good dispersion of MWCNT, achieved using TChNa dispersant during polymerization allowed the

formation of PPy coated MWCNT. The  $\pi$ - $\pi$  and hydrophobic interactions of PPy and MWCNT promoted PPy coating formation on the MWCNT surface. The PPy coating formation improved charge transfer between MWCNT and PPy. As a result, the electrodes showed excellent capacitive performance at mass loading as high as  $34 \text{ mg cm}^{-2}$ . The cyclic voltammetry data showed nearly ideal box shape CV (Figure 5-13A). The capacitance, calculated from the CV data decreased from  $2.95 \text{ F cm}^{-2}$  at a scan rate of  $2 \text{ mV s}^{-1}$  to  $1.65 \text{ F cm}^{-2}$  at  $100 \text{ mV s}^{-1}$ , showing a capacitance retention of 56%. The decrease in capacitance with increasing scan rate is usually attributed to diffusion limitations of electrolyte in pores and low electronic conductivity. The specific capacitance and capacitance retention usually decrease with increasing mass loading. Previous investigations[29] showed poor capacitance retention at high scan rates for PPy electrodes with high mass loadings in the range of  $20\text{-}40 \text{ mg cm}^{-2}$ . The use of PPy-MWCNT prepared by a simple method, utilizing TChNa dispersant is promising for the fabrication of advanced supercapacitor electrodes. Further improvement can be achieved by the use of advanced dopants and optimization of processing conditions.

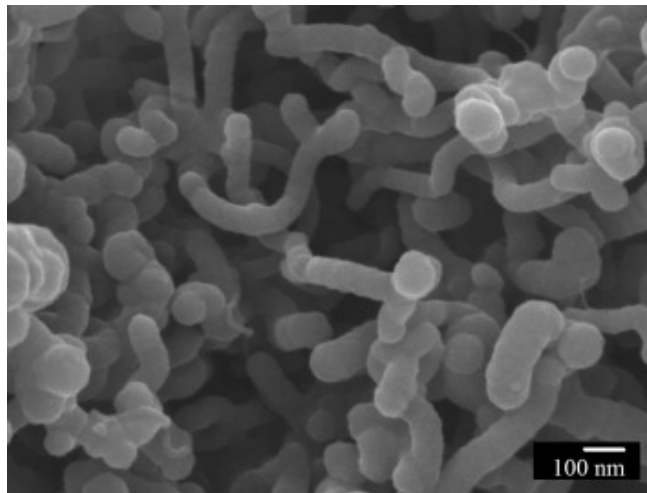


Figure 5-12 SEM image of PPy coated MWCNT prepared using TChNa as a dispersant

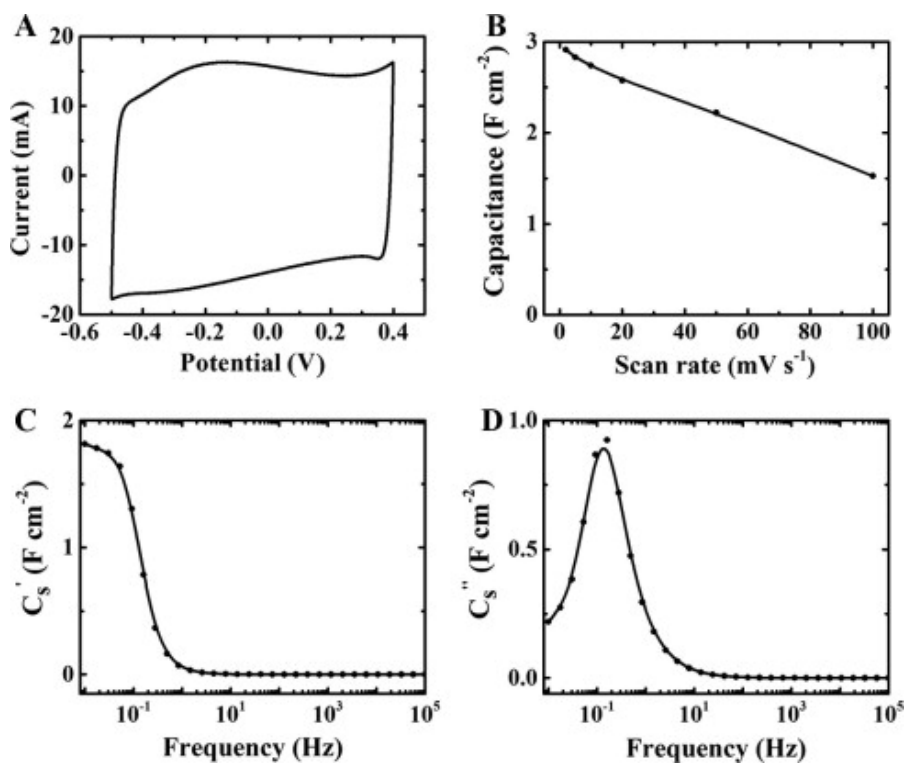


Figure 5-13 (A) CV at a scan rate at  $5 \text{ mV s}^{-1}$ , (B) specific capacitance versus scan rate, (C) real part  $C'$  and (D) imaginary part  $C''$  of capacitance, calculated from the impedance data for PPy coated MWCNT, prepared using TChNa as a dispersant.

## 5.9 Conclusions

Nature-inspired strategies have been developed for the fabrication of MWCNT films and composites. It was found that ChH films can be prepared by anodic EPD from ChNa solutions. The deposition mechanism involved electrophoresis of  $\text{Ch}^-$  species, surface pH decrease at the anode, protonation and charge neutralization of the  $\text{COO}^-$  groups and precipitation of ChH at the electrode surface. The outstanding colloidal stability of MWCNT, dispersed using anionic bile acids, allowed the EPD of MWCNT. The use of ChNa allowed higher deposition yield due to pH dependent charge, binding and film forming properties of this material. Two different colloidal strategies have been utilized for the fabrication of electrodes for electrochemical supercapacitors. Composite  $\text{MnO}_2$ -MWCNT films were obtained by anodic EPD using ChNa as a dispersant. In another strategy, good dispersion of MWCNT during Py polymerization was achieved using TChNa. The method allowed the formation of PPy coated MWCNT, which were utilized for the fabrication of electrodes with high active mass loading by a colloidal slurry impregnation method. The film and bulk electrodes, prepared by EPD and slurry impregnation methods, respectively, showed high capacitance and good capacitance retention at high charge-discharge rates.

## References;

- [1] Qiao, Y., Chen, H., Lin, Y., and Huang, J., 2011, "Controllable Synthesis of Water-Soluble Gold Nanoparticles and Their Applications in Electrocatalysis and Surface-Enhanced Raman Scattering," *Langmuir*, **27**(17), pp. 11090–11097.
- [2] Culita, D. C., Patron, L., Teodorescu, V. S., and Balint, I., 2007, "Synthesis and Characterization of Spinelic Ferrites Obtained from Coordination Compounds as Precursors," *J. Alloys Compd.*, **432**(1–2), pp. 211–216.
- [3] Chakrabarty, A., Maitra, U., and Das, A. D., 2012, "Metal Cholate Hydrogels: Versatile Supramolecular Systems for Nanoparticle Embedded Soft Hybrid Materials," *J Mater Chem*, **22**(35), pp. 18268–18274.
- [4] Kay, A., and Graetzel, M., 1993, "Artificial Photosynthesis. 1. Photosensitization of Titania Solar Cells with Chlorophyll Derivatives and Related Natural Porphyrins," *J. Phys. Chem.*, **97**(23), pp. 6272–6277.
- [5] Wang, Z.-S., Hara, K., Dan-oh, Y., Kasada, C., Shinpo, A., Suga, S., Arakawa, H., and Sugihara, H., 2005, "Photophysical and (Photo)electrochemical Properties of a Coumarin Dye," *J. Phys. Chem. B*, **109**(9), pp. 3907–3914.
- [6] Wang, Z.-S., Cui, Y., Dan-oh, Y., Kasada, C., Shinpo, A., and Hara, K., 2007, "Thiophene-Functionalized Coumarin Dye for Efficient Dye-Sensitized Solar Cells: Electron Lifetime Improved by Coadsorption of Deoxycholic Acid," *J. Phys. Chem. C*, **111**(19), pp. 7224–7230.
- [7] Hisaki, I., Murai, T., Yabuguchi, H., Shigemitsu, H., Tohnai, N., and Miyata, M., 2011, "Deoxycholamide Crystalline Frameworks as a Platform of Highly-Efficient Fluorescence Materials," *Cryst. Growth Des.*, **11**(10), pp. 4652–4659.
- [8] Froner, E., D'Amato, E., Adamo, R., Prtljaga, N., Larcheri, S., Pavesi, L., Rigo, A., Potrich, C., and Scarpa, M., 2011, "Deoxycholate as an Efficient Coating Agent for Hydrophilic Silicon Nanocrystals," *J. Colloid Interface Sci.*, **358**(1), pp. 86–92.
- [9] Wang, Z., Wu, T., Zhou, W., Wei, X., and Zhao, J., 2011, "Surface Properties and Micellar Molecular Interaction in Binary Systems of a Biosurfactant Sodium Deoxycholate (NaDC) with Conventional Surfactants," *J. Surfactants Deterg.*, **14**(3), pp. 391–400.
- [10] Herndon, W. C., 1967, "The Structure of Choleic Acids," *J. Chem. Educ.*, **44**(12), p. 724.

- [11] Bogdanova, L. R., Gnezdilov, O. I., Idiyatullin, B. Z., Kurbanov, R. K., Zuev, Y. F., and Us'yarov, O. G., 2012, "Micellization in Sodium Deoxycholate Solutions," *Colloid J.*, **74**(1), pp. 1–6.
- [12] Fernández-Leyes, M. D., Messina, P. V., and Schulz, P. C., 2007, "Aqueous Sodium Dehydrocholate–sodium Deoxycholate Mixtures at Low Concentration," *J. Colloid Interface Sci.*, **314**(2), pp. 659–664.
- [13] Nakano, K., Sada, K., Nakagawa, K., Aburaya, K., Yoswathananont, N., Tohnai, N., and Miyata, M., 2005, "Organic Intercalation Material: Reversible Change in Interlayer Distances by Guest Release and Insertion in Sandwich-Type Inclusion Crystals of Cholic Acid," *Chem. – Eur. J.*, **11**(6), pp. 1725–1733.
- [14] Lin, S., and Blankshtein, D., 2010, "Role of the Bile Salt Surfactant Sodium Cholate in Enhancing the Aqueous Dispersion Stability of Single-Walled Carbon Nanotubes: A Molecular Dynamics Simulation Study," *J. Phys. Chem. B*, **114**(47), pp. 15616–15625.
- [15] Tomašić, V., Tušek-Božić, L., Preočanin, T., and Kallay, N., 2009, "Influence of the pH on the Formation of the Catanionic N-Tetradecylammonium Cholate Surfactant Salt," *J. Dispers. Sci. Technol.*, **30**(1), pp. 38–47.
- [16] Jover, A., Meijide, F., Rodríguez Núñez, E., and Vázquez Tato, J., 1998, "Aggregation Kinetics of Sodium Deoxycholate in Aqueous Solution," *Langmuir*, **14**(16), pp. 4359–4363.
- [17] Das, S., Dey, J., Mukhim, T., and Ismail, K., 2011, "Effect of Sodium Salicylate, Sodium Oxalate, and Sodium Chloride on the Micellization and Adsorption of Sodium Deoxycholate in Aqueous Solutions," *J. Colloid Interface Sci.*, **357**(2), pp. 434–439.
- [18] Zhitomirsky, I., 2000, "Electrophoretic Hydroxyapatite Coatings and Fibers," *Mater. Lett.*, **42**(4), pp. 262–271.
- [19] Pang, X., Casagrande, T., and Zhitomirsky, I., 2009, "Electrophoretic Deposition of hydroxyapatite–CaSiO<sub>3</sub>–chitosan Composite Coatings," *J. Colloid Interface Sci.*, **330**(2), pp. 323–329.
- [20] Zhitomirsky, I., 2002, "Cathodic Electrodeposition of Ceramic and Organoceramic Materials. Fundamental Aspects," *Adv. Colloid Interface Sci.*, **97**(1–3), pp. 279–317.

- [21] Sun, X., Xin, X., Tang, N., Guo, L., Wang, L., and Xu, G., 2014, “Manipulation of the Gel Behavior of Biological Surfactant Sodium Deoxycholate by Amino Acids,” *J. Phys. Chem. B*, **118**(3), pp. 824–832.
- [22] Yang, L., Xu, Y., Su, Y., Wu, J., Zhao, K., Wang, M., and others, 2005, “FT-IR Spectroscopic Study on the Variations of Molecular Structures of Some Carboxyl Acids Induced by Free Electron Laser,” *Spectrochim. Acta. A. Mol. Biomol. Spectrosc.*, **62**(4), pp. 1209–1215.
- [23] Cheong, M., and Zhitomirsky, I., 2008, “Electrodeposition of Alginate Acid and Composite Films,” *Colloids Surf. Physicochem. Eng. Asp.*, **328**(1), pp. 73–78.
- [24] Madenci, D., and Egelhaaf, S. U., 2010, “Self-Assembly in Aqueous Bile Salt Solutions,” *Curr. Opin. Colloid Interface Sci.*, **15**(1), pp. 109–115.
- [25] Wenseleers, W., Vlasov, I. I., Goovaerts, E., Obraztsova, E. D., Lobach, A. S., and Bouwen, A., 2004, “Efficient Isolation and Solubilization of Pristine Single-Walled Nanotubes in Bile Salt Micelles,” *Adv. Funct. Mater.*, **14**(11), pp. 1105–1112.
- [26] Kosmulski, M., 2002, “The pH-Dependent Surface Charging and the Points of Zero Charge,” *J. Colloid Interface Sci.*, **253**(1), pp. 77–87.
- [27] Li, J., and Zhitomirsky, I., 2009, “Electrophoretic Deposition of Manganese Dioxide–carbon Nanotube Composites,” *J. Mater. Process. Technol.*, **209**(7), pp. 3452–3459.
- [28] Wang, Y., and Zhitomirsky, I., 2009, “Electrophoretic Deposition of Manganese Dioxide- Multiwalled Carbon Nanotube Composites for Electrochemical Supercapacitors,” *Langmuir*, **25**(17), pp. 9684–9689.
- [29] Zhu, Y., and Zhitomirsky, I., 2013, “Influence of Dopant Structure and Charge on Supercapacitive Behavior of Polypyrrole Electrodes with High Mass Loading,” *Synth. Met.*, **185**, pp. 126–132.

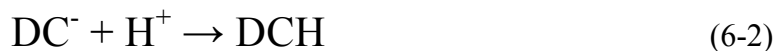
## Chapter 6 EPD of Composites Using Deoxycholic Acid Dispersant

### 6.1 Mechanism of DCH electrodeposition

This work showed that DCNa can be used as a dispersant for MWCNT and film forming agent for deposition of MWCNT films. The molecular structure of DCNa is shown in Figure 6-1. It includes a steroid backbone, containing a hydrophobic convex side and hydrophilic concave side. The hydroxyl groups are located on the concave side of the steroid backbone. The anionic properties of DCNa are attributed to the  $\text{COO}^-$  group. We found that anodic films can be obtained by potentiodynamic or constant cell voltage deposition from DCNa solutions of various concentrations in the range of  $0.1\text{-}8.0\text{ g L}^{-1}$ . The suggested deposition mechanism involved electromigration of anionic  $\text{DC}^-$  species and their accumulation at the anode surface in an electric field. The surface pH of the anode decreased due to the reaction:



The protonation of the  $\text{DC}^-$  species resulted in the formation of DCH:



It is known that DCH has a low solubility and forms a gel in acidic solutions[1–3]. The gel formation involves a self-assembly[4,3], which is attributed to aligning DCH hydrophobic or hydrophilic surfaces toward one another.

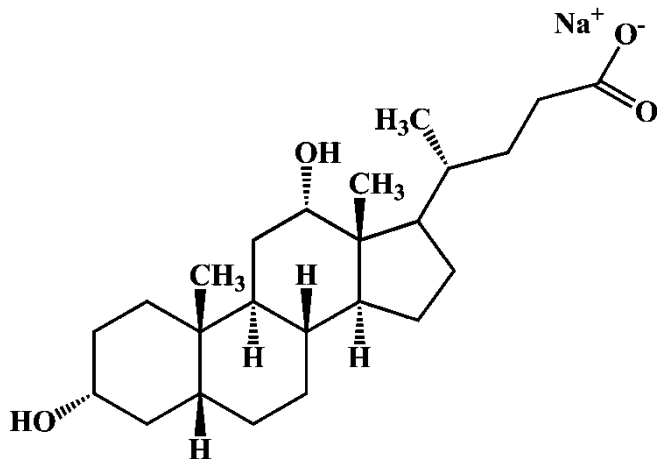


**Figure 6-1 Structure of DCNa**

The deposition process has been investigated potentiodynamically. Figure 6-2 shows cyclic voltammetry data for a stainless-steel (SS) electrode in the 1 g L<sup>-1</sup> DCNa solution. The anodic current increased significantly at electrode potential of about 1.2 V due to reaction (Eq.6-1). The current decreased with increasing cycle number due to the formation of insulating film in reaction (Eq.6-2). Therefore, cycling voltammetry data, presented in Figure 6-2, is in agreement with proposed deposition mechanism.

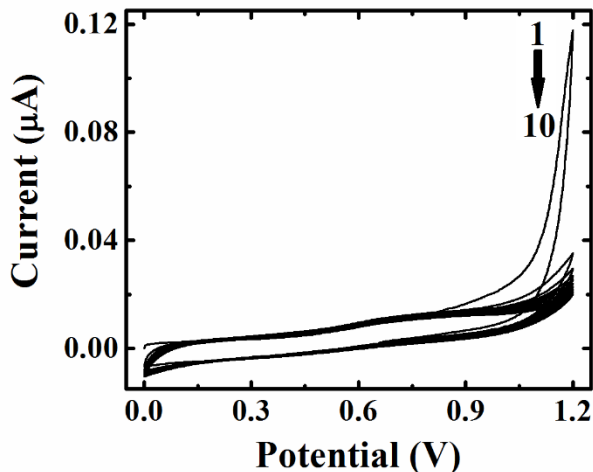


**Figure 6-2 CVs for a SS electrode in 1 g L<sup>-1</sup> DCNa solution at 0.02 V s<sup>-1</sup> for different cycle numbers from 1 to 10, obtained using a standard SCE reference electrode.**

Anodic films were also electrodeposited from DCNa solutions of various concentrations in the range of 0.1-8.0 g L<sup>-1</sup> at constant cell deposition voltages of 3-10 V. The electrodeposition was investigated *in-situ* by the QCM method using 0.1 g L<sup>-1</sup> DCNa solution. The deposit mass increased with increasing time, indicating a continuous film growth (Figure 6-3). Figure 6-4 shows the deposition yield versus DCNa concentration in solutions at a constant voltage and constant deposition duration. The deposition yield increased with increasing DCNa concentration.

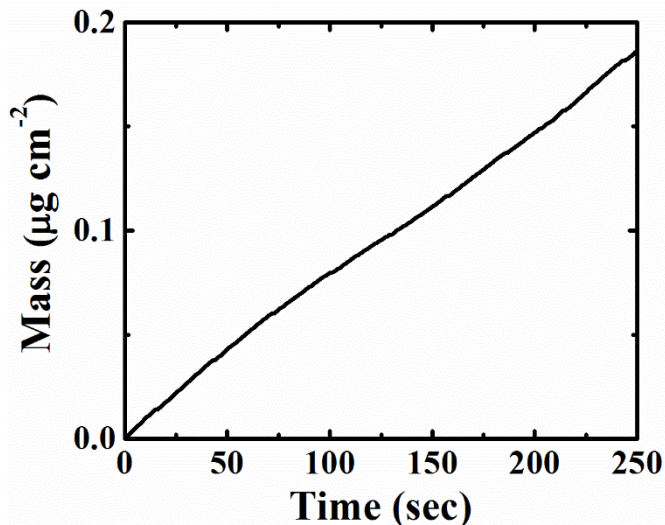


Figure 6-3 QCM in-situ measurements data for deposition yield in  $0.1 \text{ g L}^{-1}$  DCNa solution at a voltage of 3V.

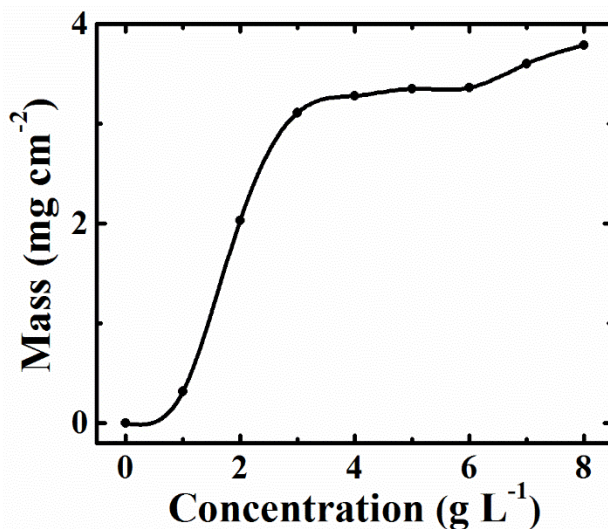


Figure 6-4 Film mass as a function of DCNa concentration in solutions at a constant cell voltage of 10 V and deposition duration of 5 min.

## 6.2 Morphology and adsorption study of DCNa

The SEM images of DCH films were presented in Figure 6-5 at different magnifications.

The low magnification image (Figure 6-5A) shows a continuous porous film. The size of

the pores is in the range of 0.1-0.5  $\mu\text{m}$  (Figure 6-5B). The deposited DCH material formed a fibrous network (Figure 6-5B).

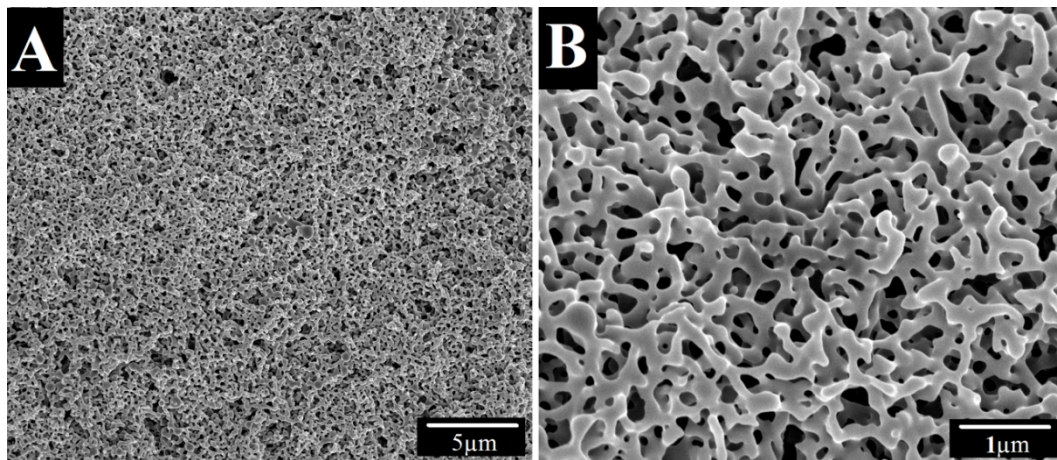


**Figure 6-5 (A, B) SEM images at different magnifications of a DCH film, deposited using 2 g L<sup>-1</sup> DCNa solution at a constant cell voltage of 10 V.**

The analysis of FTIR data (Figure 6-6) for as-received DCNa and deposited material showed absorptions at 1044 and 1041  $\text{cm}^{-1}$ , respectively, attributed to C—O stretching[2]. The absorptions at 1564 and 1408  $\text{cm}^{-1}$  in the spectrum of DCNa can be attributed[5] to asymmetric and symmetric stretching vibrations of  $\text{COO}^-$  groups, respectively. The peaks at 1377 and 1448  $\text{cm}^{-1}$  in the spectrum of the deposited material are related to C—C and C—H vibrations[6]. The absorption at 1709  $\text{cm}^{-1}$  in the spectrum of the deposited material is attributed to stretching vibrations of protonated COOH groups[6]. Such absorption has not been observed in the spectrum of DCNa. Therefore, the FTIR data confirmed the formation of DCH deposit in agreement with proposed deposition mechanism.

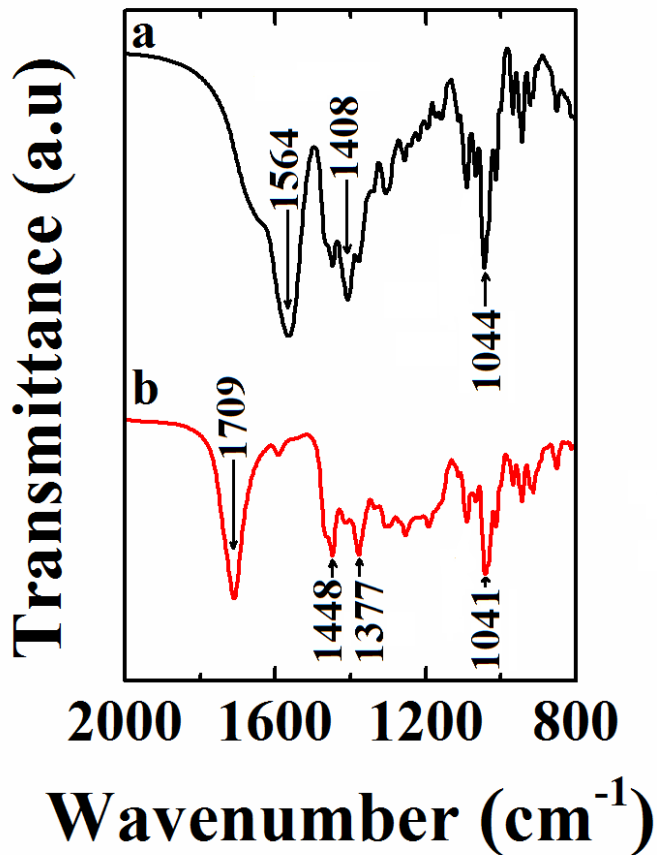


Figure 6-6 FTIR for (a) DCNa and (b) DCH film material, obtained from 1 g L<sup>-1</sup> DCNa solution at a constant cell voltage of 10 V.

### 6.3 The advantages of using DCNa as a dispersant for MWCNT

MWCNT exhibit a set of properties[7–11], which make them desirable functional components of advanced composites. The manufacturing of composites by electrodeposition requires good dispersion of MWCNT in solutions[12] and MWCNT charging[13]. In this investigation, we utilized a new bio-inspired approach for electrodeposition of MWCNT and composites, using a commercial synthetic bile acid (BA), such as DCNa as advanced dispersing agent.

Recently, commercial BAs generated interest for the dispersion of MWCNT. It was shown[14] that BAs allowed efficient dispersion of individual MWCNT, therefore the formation of MWCNT bundles can be avoided. The possibility to disperse individual MWCNT is important for the utilization of unique properties of MWCNT in composites. These studies[14] highlighted the kinetic aspects of the MWCNT dispersion in BAs solutions. The dispersion efficiency of BAs is related to the steroid structure of their molecules. Due to their unique structure, BAs are powerful natural dispersants, which allow efficient dispersion of fatty acids, proteins, vitamins, lipids, cholesterol and monoglycerides[15].

The BAs structure is different from that of conventional surfactants, which are composed of a hydrophilic head group and a long chain hydrophobic hydrocarbon group[16]. Due to the hydrophobic interactions with MWCNT, the adsorbed surfactants are oriented perpendicular to the MWCNT surface. In contrast, BAs have hydrophilic concave and hydrophobic convex surfaces[4,16]. Adsorbed BAs form a ring around MWCNT[17]. Due to the unique structure and orientation of BAs at the MWCNT surface, they allowed superior MWCNT dispersion, compared to other commercial surfactants[14,17].

The analysis of literature indicates the DCH [1,2,4,18–20] belongs to the family of BAs and exhibits interesting properties, such as strong adsorption on different surfaces and gel-forming properties. Therefore, DCH is a promising functional additive for electrodeposition of MWCNT and composites. Further investigations showed that DCNa can be used as a charging and film forming agent for electrodeposition of MWCNT and composites.

#### **6.4 EPD of MWCNT using DCNa as a dispersant**

DCNa is a promising additive for the electrodeposition of MWCNT due to the pH dependent charge, binding and film-forming properties of this material. MWCNT must be well dispersed and charged in the electrodeposition bath. Sedimentation tests showed that the addition of DCNa to MWCNT resulted in good suspension stability. The  $1 \text{ g L}^{-1}$  MWCNT suspensions, containing  $1 \text{ g L}^{-1}$  DCNa, were stable for 1 month. The sedimentation tests indicated that  $\text{DC}^-$  species were adsorbed on MWCNT and imparted a negative charge to the MWCNT. The mechanism of MWCNT deposition involved the electromigration of MWCNT, containing adsorbed  $\text{DC}^-$  to the anode surface. It should be noted that electrostatic repulsion of MWCNT must be eliminated at the electrode surface for the deposit formation. The protonation of  $\text{DC}^-$  at the anode resulted in charge neutralization and promoted deposition. Moreover, the binding properties of DCH were beneficial for the deposition of MWCNT.

The MWCNT deposition yield increased with increasing DCNa concentration in the suspensions (Figure 6-7) in the range of  $0.1\text{-}0.8 \text{ g L}^{-1}$  DCNa. The deposit yield from DCNa solutions, containing MWCNT, was by order of magnitude higher than the deposition yield, obtained from pure DCNa solutions without MWCNT at similar DCNa concentrations. At DCNa concentrations above  $0.8 \text{ g L}^{-1}$ , the deposit mass decreased (Figure 6-7). Such decrease can result from competitive deposition of DCH and MWCNT, containing adsorbed DCH. The increase in DCNa concentration resulted in enhanced deposition of non-conductive DCH, which prevented charge transfer, reduced the rate of reaction (1) and

blocked the deposition of MWCNT. This suggestion is in agreement with the results of SEM analysis of deposits prepared from  $1 \text{ g L}^{-1}$  DCNa solution, containing  $1 \text{ g L}^{-1}$  MWCNT. The SEM image at low magnification showed that the morphology of the film is characterized by the fibrous MWCNT network (Figure 6-8A). DCH was co-deposited with MWCNT and formed coatings on the individual MWCNT or filled the voids between the nanotubes (Figure 6-8B). The analysis of SEM images at different magnifications (Figure 6-8A, B) indicated that DCH binding properties were beneficial for the formation of MWCNT deposit, however the amount of DCH in the deposit must be reduced due to the insulating properties of DCH. In order to reduce the DCH deposition rate and achieve high deposition rate of MWCNT (Figure 6-7), the amount of DCNa in the  $1 \text{ g L}^{-1}$  MWCNT suspension was optimized at the level of  $0.5 \text{ g L}^{-1}$ .

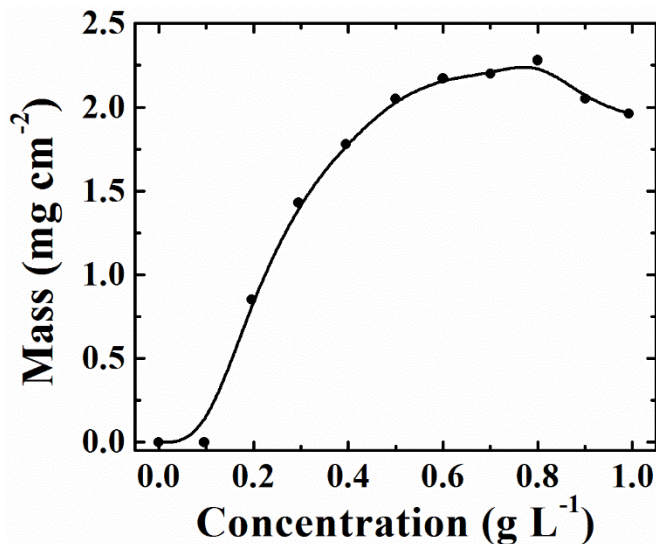


**Figure 6-7 Deposit mass as a function of DCNa concentrations in  $1 \text{ g L}^{-1}$  MWCNT suspension at a deposition voltage of 10 V and deposition duration of 5 min.**

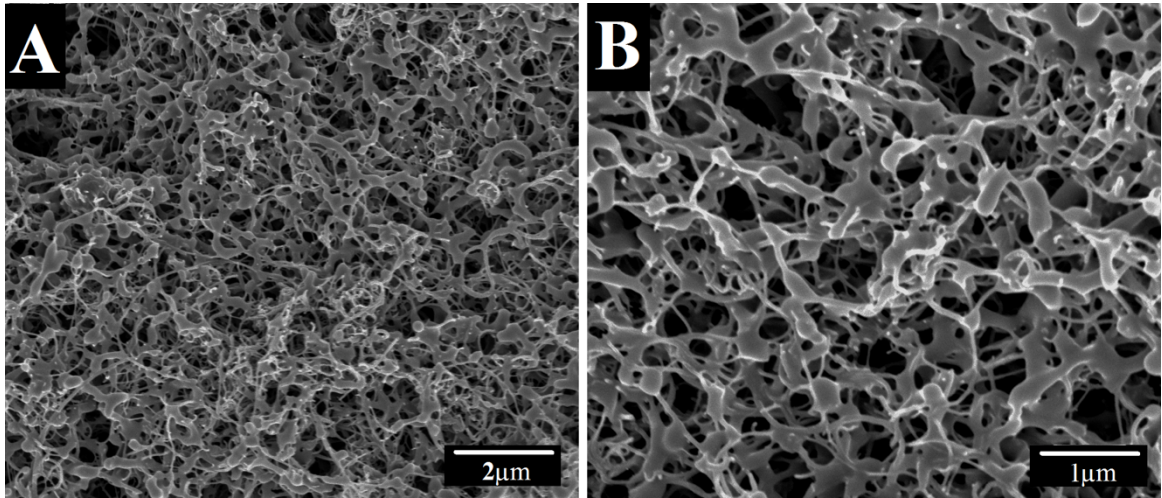


**Figure 6-8 SEM images of a MWCNT film at different magnifications**

The co-deposition of MWCNT and DCH was also confirmed by the analysis of FTIR data. The FTIR (Figure 6-9a) of carbon nanotubes show peaks at  $1579$  and  $1335\text{ cm}^{-1}$ , related to aromatic C—C vibrations and surface C-OH vibrations, respectively[21]. The comparison of FTIR for as-received (Figure 6-9a) and deposited (Figure 6-9b) MWCNT revealed additional absorptions in the spectrum of deposited MWCNT, compared to as-received MWCNT. The absorption at  $1705\text{ cm}^{-1}$  is attributed to stretching vibrations of protonated COOH groups[6] of DCH.

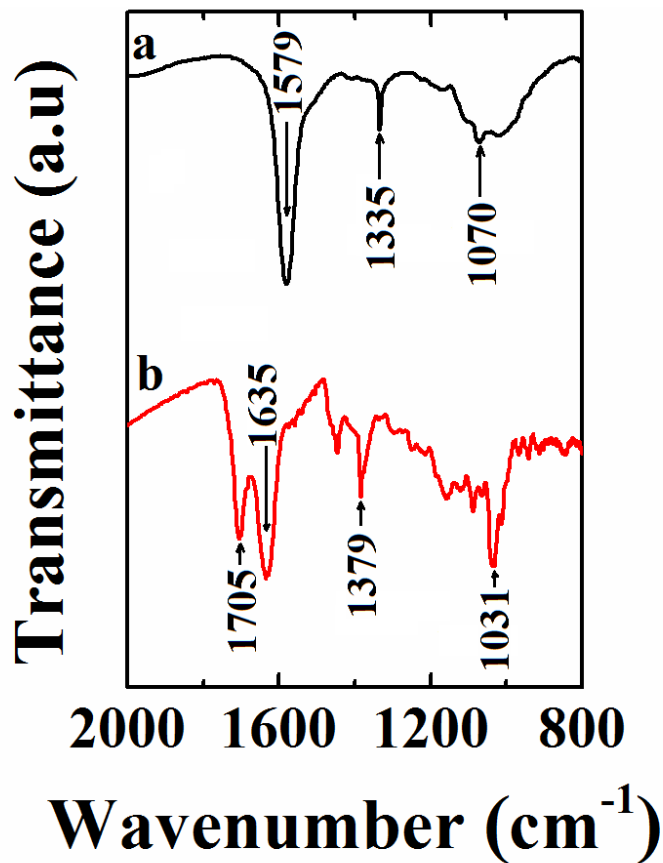
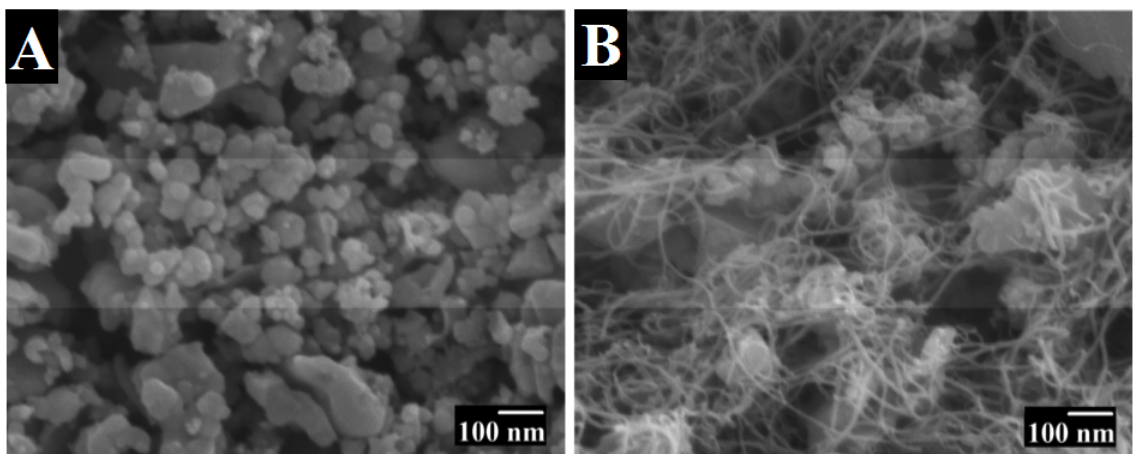


Figure 6-9 FTIR for (a) as-received MWCNT and (b) deposited MWCNT

### 6.5 Morphology study of MnO<sub>2</sub> and MnO<sub>2</sub>-MWCNT composites

The possibility of MWCNT dispersion and deposition using DCNa as a dispersant paved the way for the fabrication of composites, containing MWCNT. MnO<sub>2</sub>-MWCNT composites are of significant interest for application in electrodes of supercapacitors. Therefore, electrodeposition method has been developed for the manufacturing of such composites. Due to their low isoelectric point[22], the MnO<sub>2</sub> particles were negatively charged in water and allowed the formation of anodic deposits. Figure 6-10A shows typical SEM image of MnO<sub>2</sub> film prepared from MnO<sub>2</sub> suspension in water by electrodeposition.

The film was porous and contained MnO<sub>2</sub> nanoparticles. The film porosity was attributed to packing of the MnO<sub>2</sub> particles. The addition of MnO<sub>2</sub> particles to the MWCNT suspension, prepared using DCNa as a dispersant allowed the formation of composite films. Figure 6-10B shows SEM image of a composite film, which contained MnO<sub>2</sub> particles and MWCNT. The SEM image (Figure 6-10B) proved that suspension containing MnO<sub>2</sub> and MWCNT was successfully homogenously dispersed and the composite material was deposited by EPD using DCNa dispersant.



**Figure 6-10 SEM images of (A) MnO<sub>2</sub> and (B) MnO<sub>2</sub>-MWCNT composite film.**

## **6.6 Capacitive performance of MnO<sub>2</sub>-MWCNT composite film**

The MnO<sub>2</sub>-MWCNT composites, prepared by electrodeposition, were investigated for application in supercapacitors. The CV analysis (Figure 6-11) showed good capacitive behavior as indicated by nearly box shape CV curve. The capacitance (Figure 6-11B) of the electrode with active mass loading of 1.17 mg cm<sup>-2</sup>, obtained from the CVs, decreased from 138 to 52 mF cm<sup>-2</sup> with increasing scan rate from 2 to 100 mV s<sup>-1</sup>. The components of differential complex capacitance, calculated from the impedance data showed a

dispersion of the relaxation type with decrease in the real part of capacitance with increase in AC frequency and corresponding maximum in the frequency dependence of the imaginary part (Figure 6-11 C and D).

The capacitance calculated from the CVs at low scan rates was comparable with real part of capacitance, calculated from the impedance at low frequency. The decrease in capacitance with increasing scan rate or frequency is related to diffusion limitations of electrolyte in pores of active material.

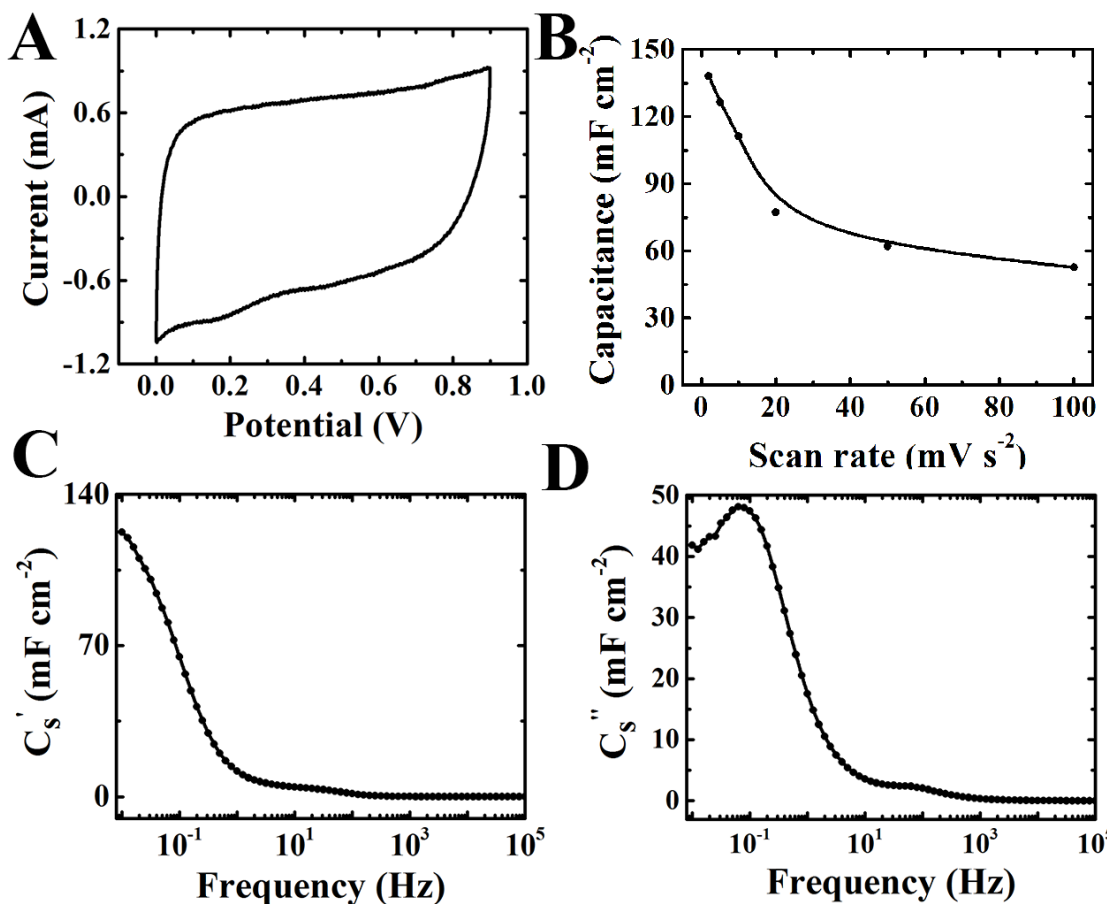


**Figure 6-11 (A) CV at 5 mV s<sup>-1</sup> obtained using a standard SCE reference electrode (B) capacitance as a function of scan rate, (C, D) frequency dependencies of C<sub>s</sub><sup>\*</sup> components for MnO<sub>2</sub>-MWCNT composite electrode in 0.5 M Na<sub>2</sub>SO<sub>4</sub> solutions.**

## 6.7 Conclusions

This investigation revealed that DCH films can be electrodeposited from DCNa solutions potentiodynamically or galvanostatically. The mechanism of DCH deposition involved the electromigration of anionic  $DC^-$ , pH decrease at the anode surface, protonation and charge neutralization of  $DC^-$  species. MWCNT can be electrodeposited from aqueous suspensions using DCNa as a dispersant, charging and film forming agent. The use of DCNa as a dispersant for MWCNT allowed the fabrication of composite  $MnO_2$ -MWCNT electrodes for electrochemical supercapacitors on Ni plaque substrate. The normalized areal capacitance  $138 \text{ mF g}^{-1}$  was achieved at  $2 \text{ mV s}^{-1}$  scan rate. DCNa is a promising MWCNT dispersant for the manufacturing of other composites by electrochemical methods.

## Reference

- [1] Jover, A., Mejjide, F., Nunez, E. R., and Tato, J. V., 2002, "Dynamic Rheology of Sodium Deoxycholate Gels," *Langmuir*, **18**(4), pp. 987–991.
- [2] Sun, X., Xin, X., Tang, N., Guo, L., Wang, L., and Xu, G., 2014, "Manipulation of the Gel Behavior of Biological Surfactant Sodium Deoxycholate by Amino Acids," *J. Phys. Chem. B*, **118**(3), pp. 824–832.
- [3] Jover, A., Mejjide, F., Nunez, E. R., and Tato, J. V., 1998, "Aggregation Kinetics of Sodium Deoxycholate in Aqueous Solution," *Langmuir*, **14**(16), pp. 4359–4363.
- [4] Das, S., Dey, J., Mukhim, T., and Ismail, K., 2011, "Effect of Sodium Salicylate, Sodium Oxalate, and Sodium Chloride on the Micellization and Adsorption of Sodium Deoxycholate in Aqueous Solutions," *J. Colloid Interface Sci.*, **357**(2), pp. 434–439.
- [5] Culita, D. C., Patron, L., Teodorescu, V. S., and Balint, L., 2007, "Synthesis and Characterization of Spinelic Ferrites Obtained from Coordination Compounds as Precursors," *J. Alloys Compd.*, **432**(1–2), pp. 211–216.

- [6] Yang, L. M., Xu, Y. Z., Su, Y. L., Wu, J. G., Zhao, K., Chen, J. E., and Wang, M. K., 2005, "FT-IR Spectroscopic Study on the Variations of Molecular Structures of Some Carboxyl Acids Induced by Free Electron Laser," *Spectrochim. Acta Part -Mol. Biomol. Spectrosc.*, **62**(4–5), pp. 1209–1215.
- [7] Termehyousefi, A., Bagheri, S., Kadri, N. A., Elfghi, F. M., Rusop, M., and Ikeda, S., 2015, "Synthesis of Well-Crystalline Lattice Carbon Nanotubes via Neutralized Cooling Method," *Mater. Manuf. Process.*, **30**(1), pp. 59–62.
- [8] Saghafi, M., Mahboubi, F., Mohajerzadeh, S., and Holze, R., 2015, "Preparation of Co-Ni Oxide/Vertically Aligned Carbon Nanotube and Their Electrochemical Performance in Supercapacitors," *Mater. Manuf. Process.*, **30**(1), pp. 70–78.
- [9] Fu, L., Yong, J., Lai, G., Tamanna, T., Notley, S., and Yu, A., 2014, "Nanocomposite Coating of Multilayered Carbon Nanotube-Titania," *Mater. Manuf. Process.*, **29**(9), pp. 1030–1036.
- [10] Schneider, M., Weiser, M., Schroetke, C., Meissner, F., Endler, I., and Michaelis, A., 2015, "Pulse Plating of Manganese Oxide Nanoparticles on Aligned MWCNT," *Surf. Eng.*, **31**(3), pp. 214–220.
- [11] Anand, E. E., and Natarajan, S., 2014, "Preparation and Characterisation of Nanocrystalline Cobalt-Phosphorus Coatings Reinforced with Carbon Nanotubes," *Surf. Eng.*, **30**(10), pp. 716–721.
- [12] Maharaja, J., Raja, M., and Mohan, S., 2014, "Pulse Electrodeposition of Cr-SWCNT Composite from Choline Chloride Based Electrolyte," *Surf. Eng.*, **30**(10), pp. 722–727.
- [13] Ata, M. S., and Zhitomirsky, I., 2013, "Preparation of MnO<sub>2</sub> and Composites for Ultracapacitors," *Mater. Manuf. Process.*, **28**(9), pp. 1014–1018.
- [14] Wenseleers, W., Vlasov, I. I., Goovaerts, E., Obratsova, E. D., Lobach, A. S., and Bouwen, A., 2004, "Efficient Isolation and Solubilization of Pristine Single-Walled Nanotubes in Bile Salt Micelles," *Adv. Funct. Mater.*, **14**(11), pp. 1105–1112.
- [15] Wang, Z., Wu, T., Zhou, W., Wei, X., and Zhao, J., 2011, "Surface Properties and Micellar Molecular Interaction in Binary Systems of a Biosurfactant Sodium Deoxycholate (NaDC) with Conventional Surfactants," *J. Surfactants Deterg.*, **14**(3), pp. 391–400.

- [16] Bogdanova, L. R., Gnezdilov, O. I., Idiyatullin, B. Z., Kurbanov, R. K., Zuev, Y. F., and Us'yarov, O. G., 2012, "Micellization in Sodium Deoxycholate Solutions," *Colloid J.*, **74**(1), pp. 1–6.
- [17] Lin, S., and Blankschtein, D., 2010, "Role of the Bile Salt Surfactant Sodium Cholate in Enhancing the Aqueous Dispersion Stability of Single-Walled Carbon Nanotubes: A Molecular Dynamics Simulation Study," *J. Phys. Chem. B*, **114**(47), pp. 15616–15625.
- [18] Si, R., Wang, H., Wei, L., Chen, Y., Wang, Z., and Wei, J., 2013, "Length-Dependent Performances of Sodium Deoxycholate-Dispersed Single-Walled Carbon Nanotube Thin-Film Transistors," *J. Mater. Res.*, **28**(7), pp. 1004–1011.
- [19] Hobbie, E. K., Fagan, J. A., Becker, M. L., Hudson, S. D., Fakhri, N., and Pasquali, M., 2009, "Self-Assembly of Ordered Nanowires in Biological Suspensions of Single-Wall Carbon Nanotubes," *Acs Nano*, **3**(1), pp. 189–196.
- [20] Froner, E., D'Amato, E., Adamo, R., Prtljaga, N., Larcheri, S., Pavesi, L., Rigo, A., Potrich, C., and Scarpa, M., 2011, "Deoxycholate as an Efficient Coating Agent for Hydrophilic Silicon Nanocrystals," *J. Colloid Interface Sci.*, **358**(1), pp. 86–92.
- [21] Shi, K., and Zhitomirsky, I., 2013, "Electrophoretic Nanotechnology of Graphene-Carbon Nanotube and Graphene-Polypyrrole Nanofiber Composites for Electrochemical Supercapacitors," *J. Colloid Interface Sci.*, **407**, pp. 474–481.
- [22] Kosmulski, M., 2002, "The pH-Dependent Surface Charging and the Points of Zero Charge," *J. Colloid Interface Sci.*, **253**(1), pp. 77–87.

## **Chapter 7     EPD of MnO<sub>2</sub>-CNT composites using new dispersants**

### **7.1 Introduction**

EPD is a promising method for the deposition of MnO<sub>2</sub> and composite films due to high deposition rate and possibility of deposition of thick films of controlled thickness. Uniform films can be obtained on large substrates of complex shape. Successful applications of EPD require the development of efficient dispersing and charging agents for MnO<sub>2</sub> particles and understanding of dispersion mechanisms and kinetics of deposition. Of particular importance are film-forming properties of dispersing agents, which facilitate the formation of adherent films. In this investigation several promising additives were selected and tested for EPD of MnO<sub>2</sub> and composite MnO<sub>2</sub>-MWCNT films. Based on the cationic, adsorption and film forming properties of polyethylenimine (PEI), this polyelectrolyte was tested for cathodic deposition. Folic acid (FA), pantoic acid sodium salt (PANa) and humic acid (HA) are anionic molecules, which were selected as promising dispersing agents for anodic EPD. It was expected that the aromatic structure of such molecules can be beneficial for their adsorption on MWCNT due to  $\pi$ - $\pi$  interactions. Therefore, such molecules can potentially be used as co-dispersants for MnO<sub>2</sub> and CNT. This chapter presents analysis of electrophoretic behavior of MnO<sub>2</sub> and MWCNT in the presence of PEI, FA, PAH and HA. The experimental results presented in this chapter showed superior performance of HA as a dispersing and film forming agent for co-deposition of MnO<sub>2</sub>-MWCNT and deposition of composites, which were tested for the application in the supercapacitor electrodes.

## 7.2 Structures of PEI, FA, PAH and HA

Figure 7-1 shows chemical structures of PEI, FA, PAH and HA. Figure 7-1A illustrates a chemical structure of PEI. The protonation of NH groups allowed the formation of cationic LPEI-H<sup>+</sup>, which electro-migrated toward the cathode under the influence of an electric field[1], [2]. The structure of FA (Figure 7-1B) includes aromatic rings and a catechol group, which can facilitate FA adsorption on inorganic nanoparticles. PAH (Figure 7-1C) belongs to salicylate family and exhibits strong chelating properties[3], [4]. The chelating properties of salicylates promote their adsorption on various metal oxides and allow good dispersion of oxide particles in water[5]. Figure 7-1D shows a schematic of the chemical structure of HA, which includes aromatic rings, hydrocarbon chains and anionic functional groups, such as carboxyl and phenol groups. The structural properties of HA facilitate chemical interactions with a variety of organic and inorganic materials via multiple reaction pathways. According to Sasaki *et al.* [6], a discrete fragment model has been developed for the analysis of contributions of different ligands to the chelating properties of HA. Of particular interest are catechol and salicylate ligands (Figure 7-1D), which showed strong complexation with metal atoms[7].

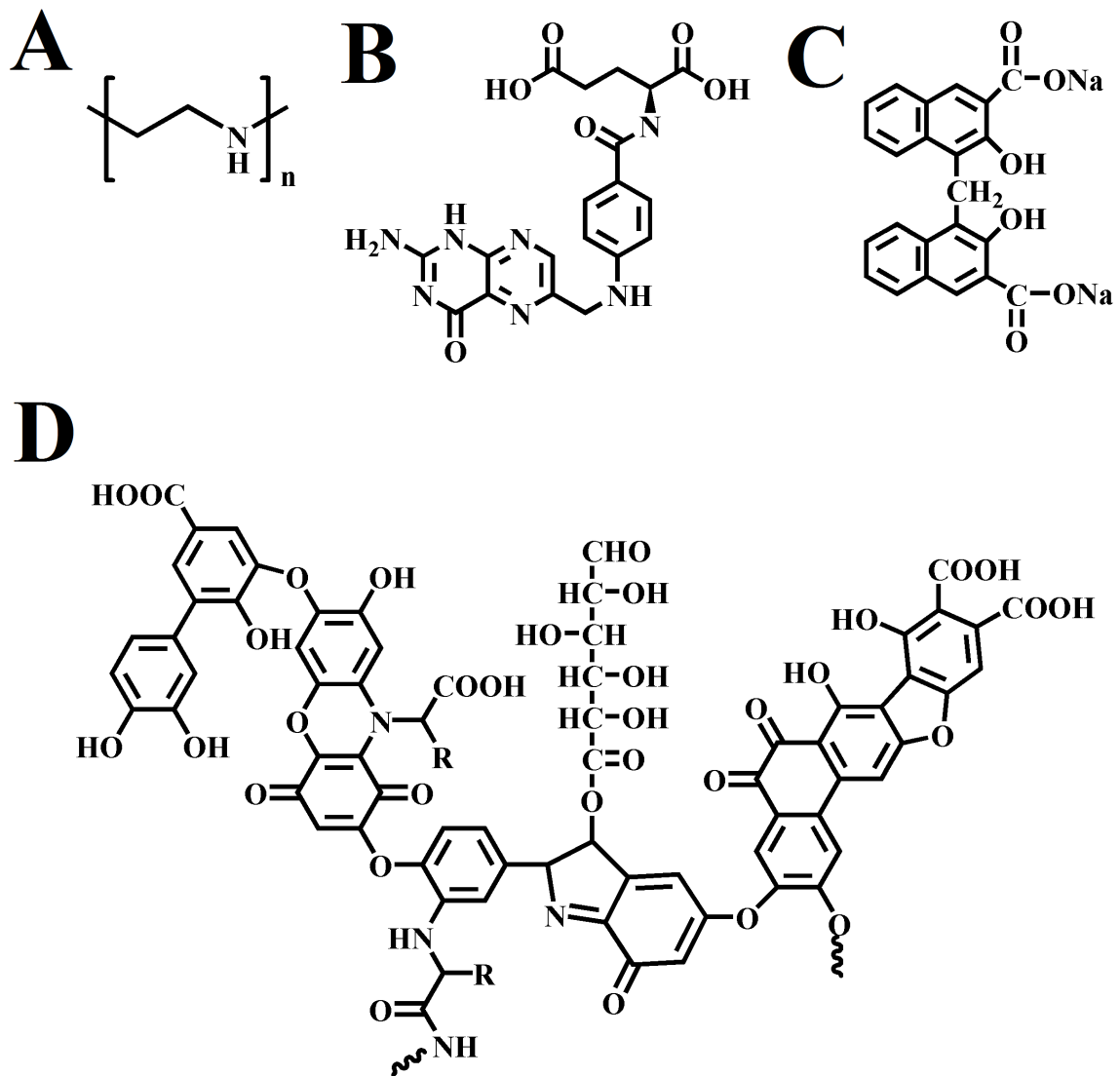


Figure 7-1 Chemical structures of (A) PEI, (B) FA, (C) PAH and (D) HA

### 7.3 EPD of PEI and composite film

#### 7.3.1 Advantages of using polyethylenimine

Polymers are of special interest for the surface modification of materials[8]–[10]. PEI has been widely used as a coating material for particles of various materials, such as hydroxyapatite for chromatography of biomolecules[11], magnetic particles for biomedical

and other applications[12], [13], platinum nanoparticles for catalysis[14] and carbon nanotubes for application in sensors[15]. Several investigations were focused on the fabrication of composite films by combined electrochemical methods, based on electrophoresis of PEI and electrosynthesis or EPD of metal oxides and hydroxides[16]–[18]. The film forming and binding properties of PEI allowed crack prevention in metal hydroxide films prepared by cathodic electrosynthesis[18]. The binding properties of PEI allowed the formation of oxide films by EPD[18]. Moreover, PEI was adsorbed on ceramic particles and provided a positive charge for cathodic EPD. Another strategy was based on polymer mediated electrosynthesis[19], which involved the use of PEI–metal ion complexes. The previous investigation on electrodeposition of PEI and composites was focused on the use of branched PEIs, which contained primary, secondary and tertiary amino groups. The use of branched PEIs for film applications is limited due to their solubility in water. Moreover, branched PEIs are liquids at all molecular weights. In contrast, the chemical structure of linear PEI (LPEI) contains only secondary amines and LPEIs are water insoluble solids. Therefore, the use of LPEI offers advantages for practical applications of thin films and composites.

This part of the chapter explains the development of EPD method for the deposition of LPEI films. The results presented below indicated the feasibility of controlled deposition of LPEI films. The deposition mechanism and kinetics of deposition were investigated. The use of LPEI as a charging and film forming agent allowed the fabrication of composite films, containing MnO<sub>2</sub> particles in the LPEI matrix.

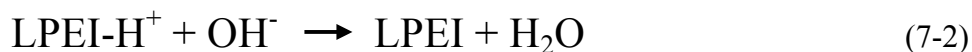
### 7.3.2 Preparation, kinetics and morphology of LPEI

The electrically neutral LPEI is insoluble in water and ethanol. 5 vol % of acetic acid protonated LPEI and allowed for complete and rapid dissolution of the polymer in water or mixed water-ethanol solvent. Cathodic deposits were obtained from LPEI solutions in a mixed ethanol–water solvent (80 mass-% ethanol). It is suggested that the deposition mechanism is based on the electrophoretic motion of protonated LPEI–H<sup>+</sup> towards the cathode, where the pH is high due to the decomposition of water.

The protonation of NH (Figure 7-1A) groups allowed the formation of cationic LPEI-H<sup>+</sup>, which electro-migrated toward the cathode under the influence of electric field. The following reaction resulted in the pH increase at the cathode surface:



The charge neutralization of LPEI-H<sup>+</sup> at the cathode surface allowed the formation of water insoluble LPEI films:



The deposition process required a certain amount of water for OH<sup>-</sup> generation in the cathodic reaction (Eq.7-1). However, the use of mixed ethanol–water solvent allowed lower electric current during constant voltage EPD and reduced gas evolution at the cathode surface. The film mass increased with increasing deposition time, indicating continuous film growth (Figure 7-2). The increase in the deposition voltage resulted in the increased deposition rate. The QCM data indicated that the deposition yield can be varied and controlled.

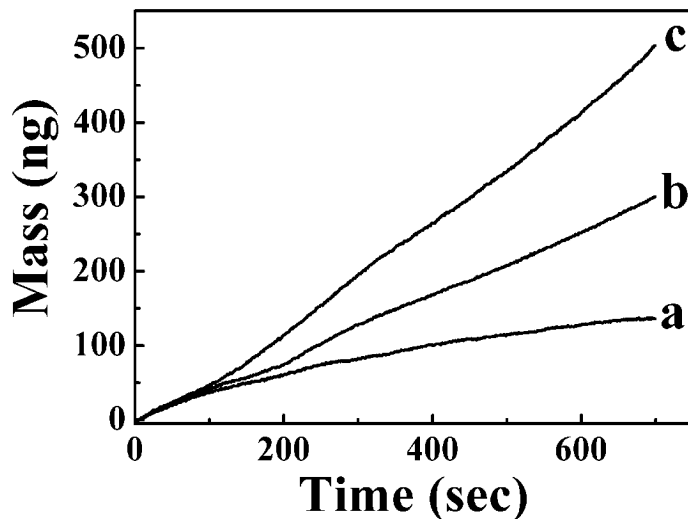


Figure 7-2 Film mass versus deposition time, measured using QCM for  $0.1\text{ g L}^{-1}$  LPEI- $\text{H}^+$  solutions at deposition voltages of (a) 4 V, (b) 7 V and (c) 10 V.

Figure 7-3 shows typical SEM images of film cross-sections. Scanning electron microscopy studies revealed the formation of relatively uniform and dense films. The analysis of film cross sections at different deposition times showed that film thickness increased with increasing deposition time in agreement with the QCM data.

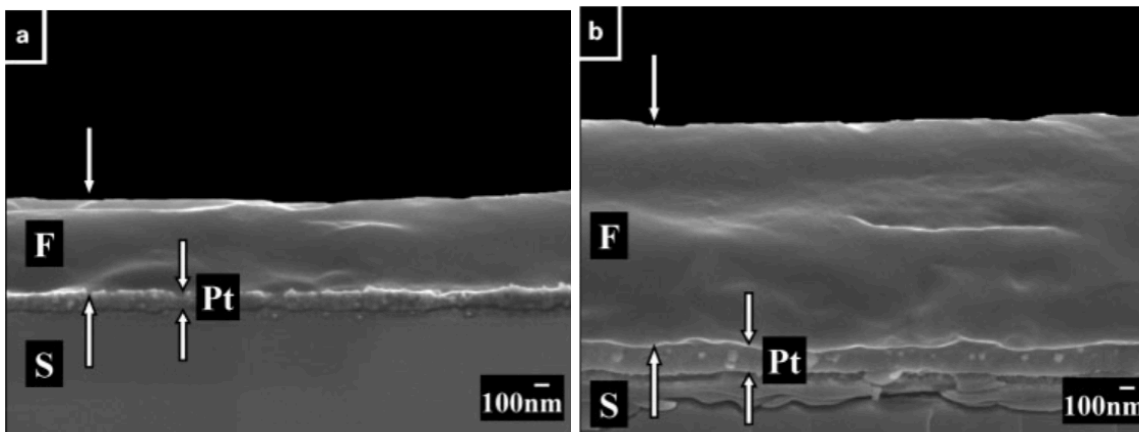


Figure 7-3 SEM images of cross-sections of LPEI films obtained from  $1\text{ g L}^{-1}$  LPEI- $\text{H}^+$  solutions at deposition voltage of 10 V and deposition times of (a) 3 min and (b) 10 min [arrows show film (F) and conductive Pt layer deposited on silicon substrate (S)]

### 7.3.3 Morphology study of MnO<sub>2</sub>, deposited using PEI

The film forming properties of LPEI can be used for the deposition of new composites, containing inorganic particles of various functional materials, such as MnO<sub>2</sub>. The suspensions of MnO<sub>2</sub> without LPEI were unstable and showed rapid sedimentation immediately after the ultrasonic agitation. In contrast, the addition of LPEI-H<sup>+</sup> allowed improved suspension stability. The 10 g L<sup>-1</sup> suspension of MnO<sub>2</sub> particles, containing 1 g L<sup>-1</sup> LPEI-H<sup>+</sup>, was stable for 2 months. The results indicated that LPEI-H<sup>+</sup> adsorbed on the ceramic particles and provided their electrosteric stabilization. The adsorbed LPEI-H<sup>+</sup> imparted an electric charge for cathodic EPD of MnO<sub>2</sub>. The analysis of film cross-sections (Figures 7-4) showed increased surface roughness compared to pure LPEI films. It is known[20] that uniformity of EPD is controlled by electric field. However, film uniformity is limited by the size of particles used for deposition.

The thickness of the composite films was varied in the range of 0.1–4 mm by variation of the deposition time in the range of 0.5–10 min at a deposition voltage of 20 V. The formation of composite films was confirmed by TGA. Figure 7-5 compared the TGA data for starting materials and MnO<sub>2</sub> composite film. The TGA data for LPEI (Figure 5A) showed several steps in mass loss below 650°C, which can mainly be attributed to thermal degradation and burning out of LPEI. However, part of the mass loss in the range of 90–150°C can be related to water desorption. Thermal dehydration of MnO<sub>2</sub> resulted in the mass loss of 18.6 mass % (Figure 7-5B, a). The composite material showed (Figure 7-5B, b) a mass loss of 66.7 mass %. Therefore, the mass content of MnO<sub>2</sub>, calculated for

anhydrous material, was 33.3 mass %. The result of this investigation indicated that LPEI can be used for the fabrication of composite films, containing  $\text{MnO}_2$ .

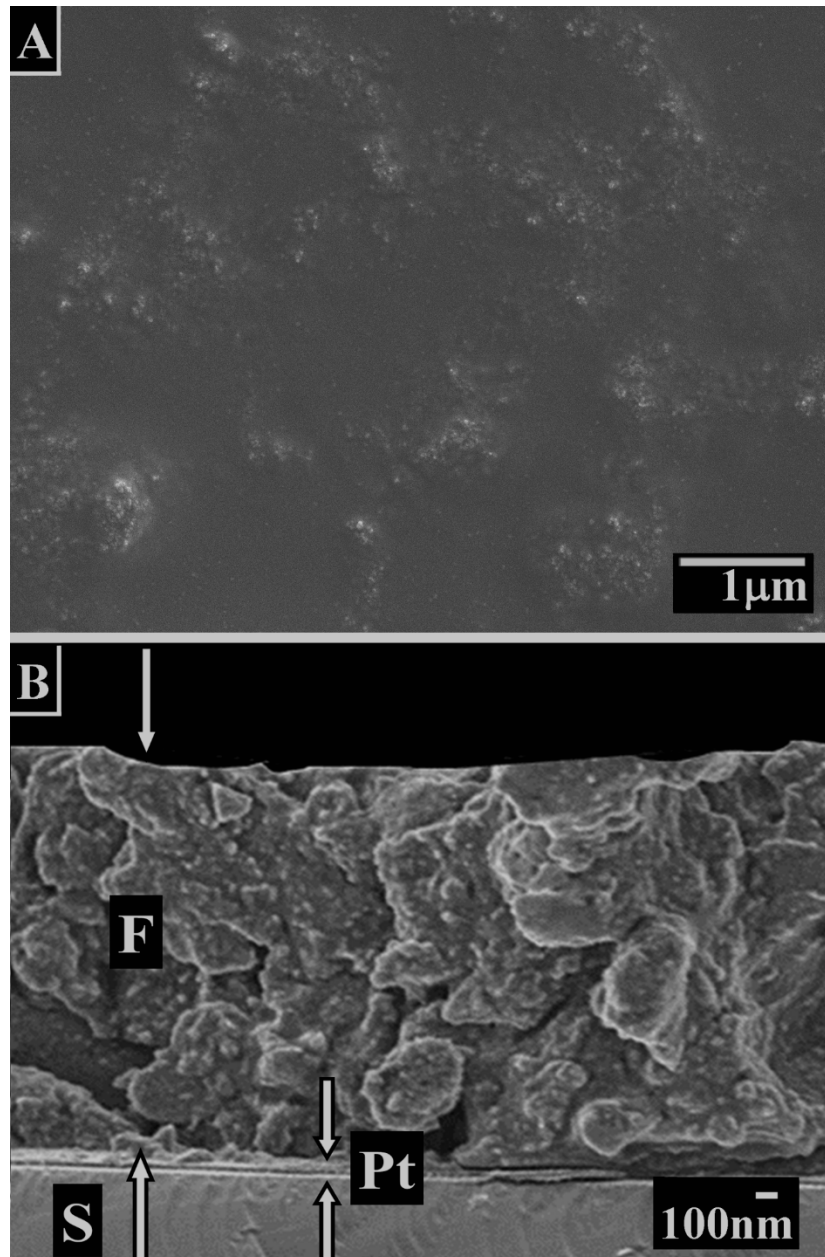


**Figure 7-4 SEM images of (A) surface and (B) cross-section of film deposited from  $1 \text{ g L}^{-1}$  LPEI- $\text{H}^+$  solution, containing  $10 \text{ g L}^{-1}$   $\text{MnO}_2$  at a deposition voltage of 20 V during 5 min.**

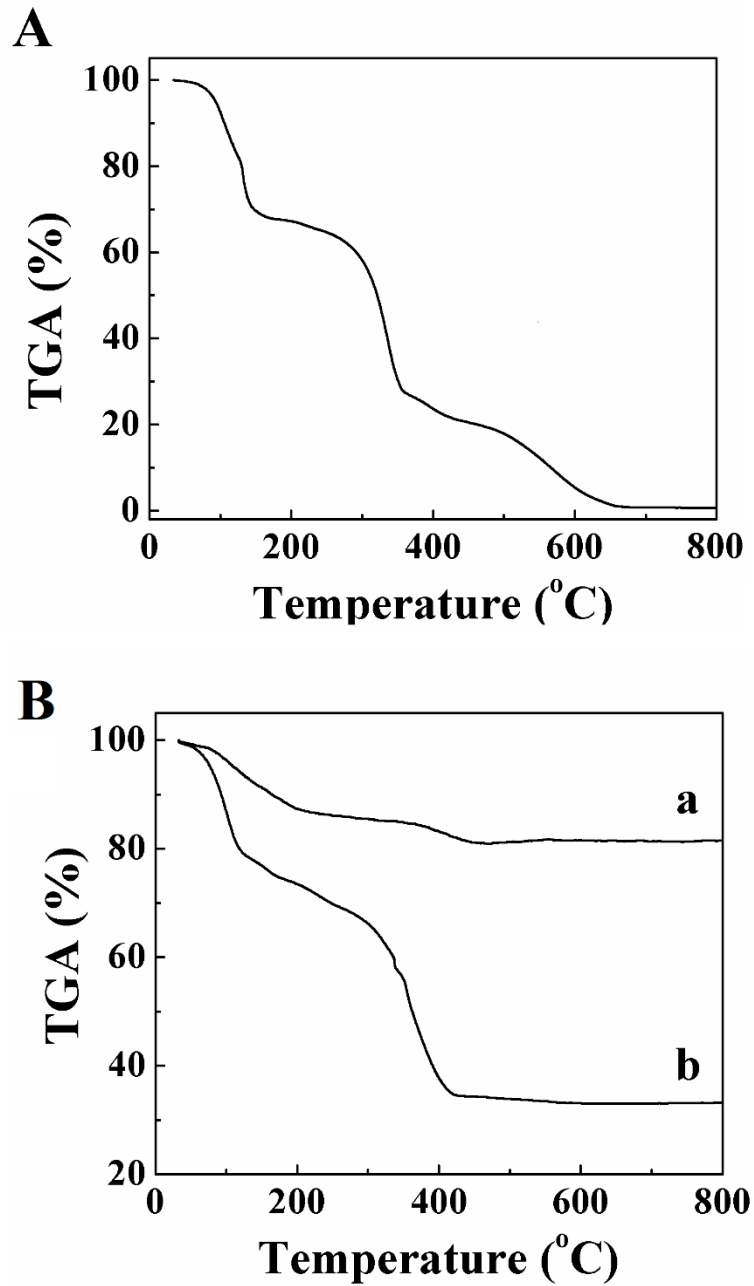


Figure 7-5 TGA data for (A) pure-LPEI and (B) a-pure-MnO<sub>2</sub> and b-composite deposits prepared from 1 g L<sup>-1</sup> LPEI-H<sup>+</sup> solution, containing 10 g L<sup>-1</sup> MnO<sub>2</sub>

## **7.4 Properties and applications of FA**

Folic acid is an ethanol soluble fortification vitamin. FA is a natural biocompatible material. The lack of FA increases the chance of the gigantocytic anemia, leucopenia, mentality devolution, psychosis, heart attack, and stroke etc., FA is an important component for human body immunity system[21]. Determination of FA is often required in pharmaceutical, clinical and food samples. Since 1992, US Public Health Service encourages women to consume FA especially during the pregnancy period[22]. Recently, FA/MWCNT composites become attractive due to the advantages of carbon nanotubes, high conductivity, high surface area, good chemical stability[23], which also have been successfully used in the electrochemical study of dopamine[24], proteins and other materials.[25], [26]. FA has been widely investigated by researchers for its impacts on tumor/cancer cells targeting[27]–[31], biochemical reactions[32]–[34], biosensing[35]–[37] and pregnancy[38]–[41].

### **7.4.1 EPD of MnO<sub>2</sub> using FA**

The mechanism of FA adsorption on MWCNT was related to  $\pi$ - $\pi$  interactions. Although FA gives high stability with MWCNT, however, EPD wasn't observed from MWCNT suspension. The FA adsorption mechanism on MnO<sub>2</sub> was attributed to carboxylic group[5], [42], the FA adsorption on particles allows electrosteric stabilization.

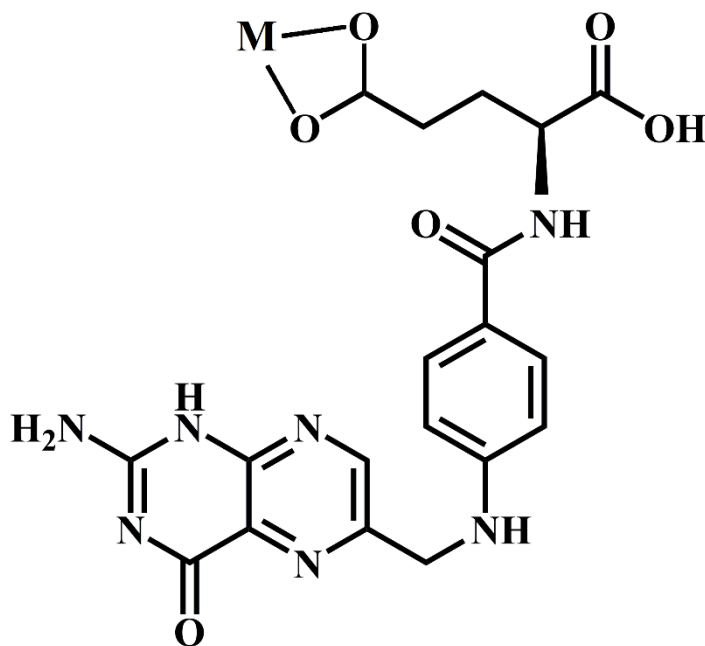


**Figure 7-6 Adsorption mechanism of FA**

The adsorption mechanism involving a carboxylic group[43], [42] is shown in Figure 7-6. Anodic EPD was successfully achieved from the MnO<sub>2</sub> suspension containing FA (Figure 7-7). Anodic deposits were obtained at FA concentrations above 0.03 g L<sup>-1</sup> FA. The deposition yield increased significantly with increasing the FA concentration in the range from 0.025 to 0.2 g L<sup>-1</sup> and slightly decreased after 0.4 g L<sup>-1</sup>. The deposit mass increased with increasing deposition time (Figure 7-8). Therefore, the amount of the material deposited anodically can be varied.

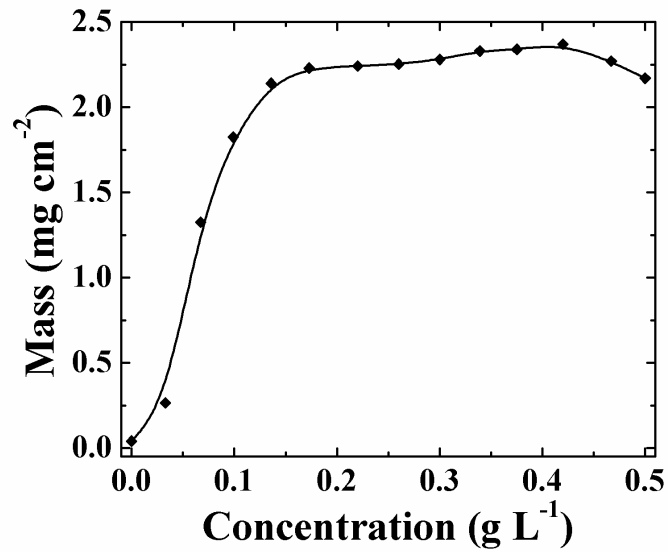


Figure 7-7 Deposit mass versus FA concentration in 4 g L<sup>-1</sup> MnO<sub>2</sub> suspension at a deposition voltage 20 V and a deposition time 5min.

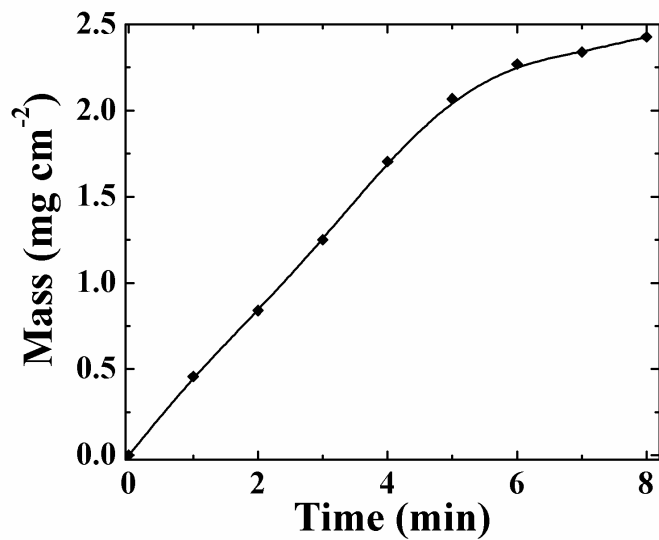


Figure 7-8 Deposit mass versus deposition time for 4 g L<sup>-1</sup> MnO<sub>2</sub> suspension, containing 0.5 g L<sup>-1</sup> FA at a deposition voltage 20V.

#### 7.4.2 FTIR characterization of FA adsorption

The results presented above indicated that FA is an efficient dispersing and charging agent for EPD of MnO<sub>2</sub>. The adsorption of FA on MnO<sub>2</sub> was confirmed by the FTIR method. Figure 7-9 shows FTIR spectra for the deposits obtained from pure FA powder and MnO<sub>2</sub> suspensions, containing FA. The peak assignments are presented in Table 7.1. The FTIR spectrum of MnO<sub>2</sub> deposit showed absorptions attributed to stretching vibrations of the aromatic ring, COO<sup>-</sup> group and other vibrations of adsorbed FA. The FTIR results confirmed that FA was adsorbed on MnO<sub>2</sub>. The FA adsorption on MnO<sub>2</sub> was attributed to carboxylic type of bonding.

**Table 7-1 Band assignments for pure FA and MnO<sub>2</sub> deposits obtained using FA dispersant.**

| FA               | MnO <sub>2</sub> | Band Assignment                           |
|------------------|------------------|---|
| 3542, 3415, 3325 | 3421             | $\nu(\text{O-H})$ [43]–[45]               |
| 3105, 2927       | ----             | $\nu(\text{C-H})$ [43], [45]              |
| 1695             | 1606             | $\nu_{\text{as}}(\text{COO}^-)$ [43]      |
| 1606             | ----             | $\delta(\text{N-H})$ [44]                 |
| 1484             | ----             | $\nu_{\text{s}}(\text{COO}^-)$ [43], [46] |
| 1336,1192        | 1192             | $\nu(\text{C-N})$ [43]                    |

The wavenumbers were given in cm<sup>-1</sup>.  $\nu$ -stretching mode,  $\delta$ -bending mode

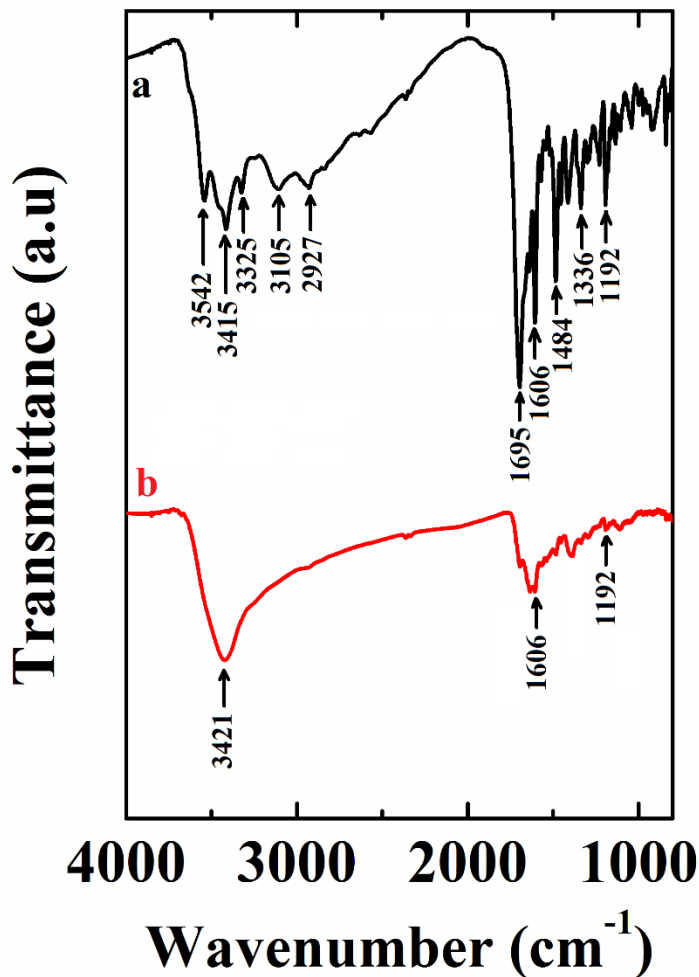
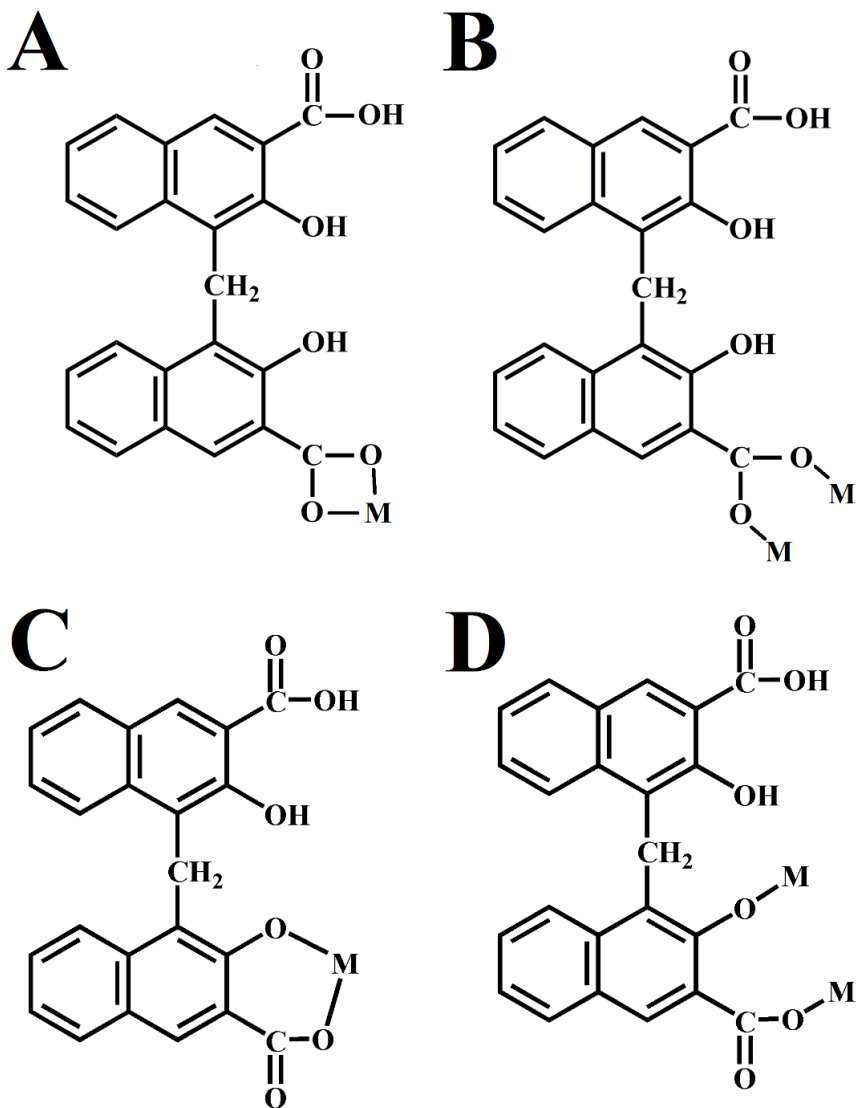


Figure 7-9 FTIR spectra of (a) pure FA powder and (b) 4 g L<sup>-1</sup> MnO<sub>2</sub> suspensions containing 0.5 g L<sup>-1</sup> FA.

### 7.5 Pamoic acid as a film forming dispersant

PAH is a multifunctional molecule, containing both carboxylic and phenolic groups, which has one half-molecule in the asymmetric unit and the two naphthyl rings are linked with a methylene bridge. According to Shi *et al.*[47], relationship between flexibility and rigidity depends on PAH as a bridging ligand possesses, due to flexible skeleton can easily rotate. In the literature, PAH complexes have been attracted to synthesize and structurally

characterize[47]–[49]. Chelating bis-bidentate and bis-monodentate adsorption mechanisms of PAH[47] (Figure 7-10) has been investigated in pharmaceutical applications[50], [51], also, self-penetrating properties makes PAH highly attractive material for metal-organic frameworks application[52]–[55]. Further investigation shows salicylic bonding mechanism (Figure 7-10C,D) stronger than Figure 7-10A,B.



**Figure 7-10 Adsorption mechanisms of PAH (A) bis-bidentate and (B) bis-monodentate (C) bidendate chelatin and (D) bidendate bridging bonding.**

### 7.5.1 Deposition kinetics and morphology study of PAH

PANa exhibit film forming properties, which are of special interest for EPD. It is important to note that in contrast to PANa, pamoic acid (PAH) is insoluble in water. The deposition mechanism involved the surface pH decrease at the anode due to the reaction:



Electric field provided electrophoretic motion of anionic  $\text{PA}^-$  toward the anode, where the charge neutralization of  $\text{COO}^-$  groups of  $\text{PA}^-$  resulted in the formation of water insoluble PAH.



Figure 7-11 shows film mass versus deposition time for PAH deposition from aqueous PANa solution. The increase in film mass indicates continuous film growth. The decrease in deposition rate with time can be attributed to voltage drop in the growing film. The PAH films showed a porous fibrous morphology (Figure 7-12A). The SEM image at high magnification (Figure 7-12B) indicated that the nanofiber diameter was in the range of 20–50 nm. The fibrous microstructure of such films can result from  $\pi$ – $\pi$  interactions of the dyes[56].

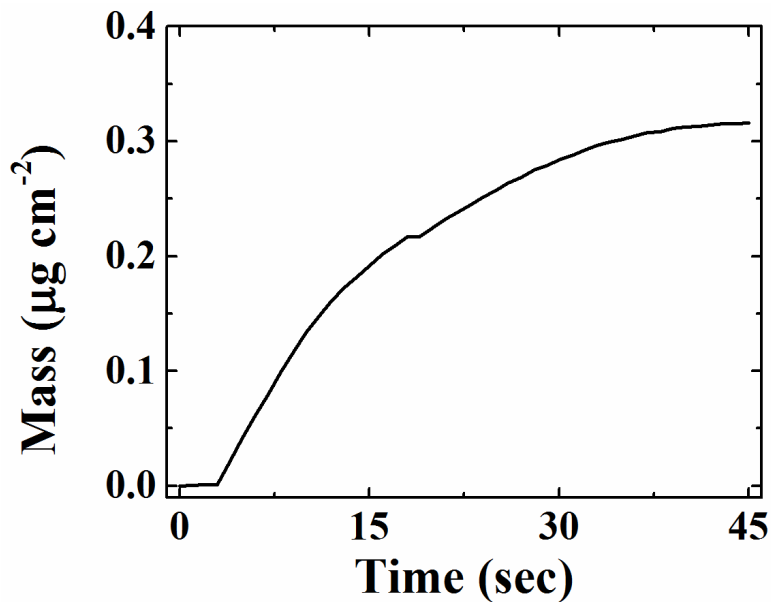


Figure 7-11 Film mass measured using QCM for PAH film on a gold coated quartz electrode with area of  $0.2 \text{ cm}^2$  at a deposition voltage of 3 V (distance between electrodes 10 mm), deposited from  $0.1 \text{ g L}^{-1}$  PANa solution in water.

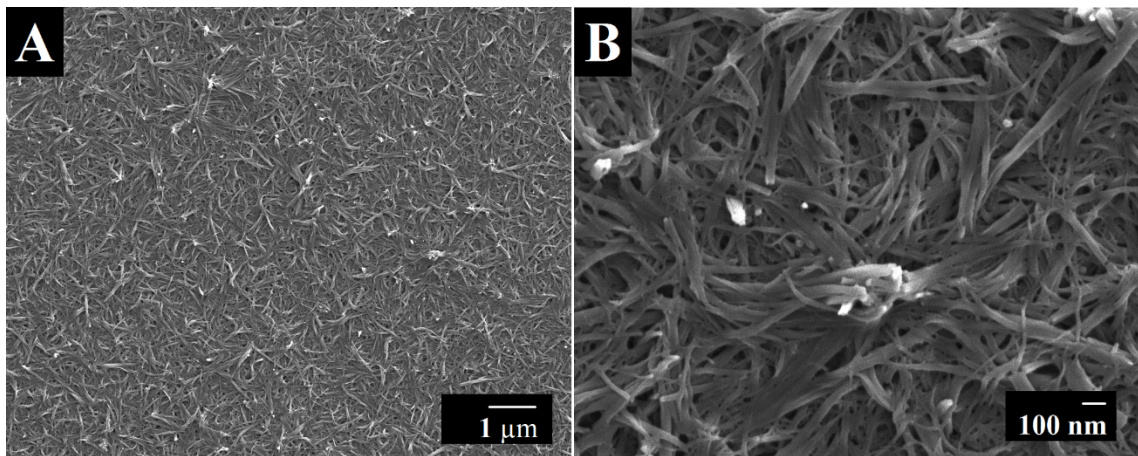


Figure 7-12 (A and B) SEM images of PAH film at different magnifications.

## 7.6 Humic acid as a dispersant and film forming agent

Humic acid is one of the abundant organic macromolecules, which offers many advantages for colloidal processing of materials, such as strong adsorption on organic and inorganic

materials and ability to bind all transition metals and high binding capacity [57]. Metal chelation is a salient feature of HA, which allows for HA adsorption on surfaces of various inorganic materials. HA showed strong adsorption on different oxides such as  $\text{Al}_2\text{O}_3$ [58],  $\text{SiO}_2$ [59], magnetite[60] and  $\text{ZnO}$ [61] and different minerals, such as palygorskite[62], kaolinite and hematite[63], [64], smectite[65]. HA, adsorbed on mineral particles, promoted the sorption of organic molecules as well as cations of metals[66], [67]. Hybrid double hydroxides-HA materials have been developed, which allowed good adsorption of heavy metals[68]. The adsorption of metal ions on alumina nanoparticles was enhanced in the presence of HA due to the formation of ternary complexes[69]. Moreover, HA efficiently adsorbed on hydroxides[70], polymers[71], [72], MWCNT[73] and other carbon materials[74], [75]. HA showed strong interactions with various polyaromatic molecules. The interactions involved different chemical mechanisms, such as ion exchange reactions, ion bridging, hydrogen bonds, charge transfer, covalent bond formation and hydrophobic interactions[76]. Of particular importance are investigations[57] of HA interactions with herbicides and pesticides used in agriculture.

This part of the chapter is the investigation for the application of HA as a charging and dispersing agent for EPD. An important finding was the possibility of the deposition of HA films by anodic EPD. The film forming properties of HA offered additional benefits for the EPD of various materials. HA was used as an anionic dispersant and film forming agent for the EPD of materials of different types, such as  $\text{MnO}_2$ , MWCNT, Ni and Pd. The films, prepared by EPD are promising for supercapacitor and other applications. HA was used as

a co-dispersant for the fabrication of MnO<sub>2</sub>-MWCNT composites, which showed promising performance for applications in electrodes of electrochemical supercapacitors.

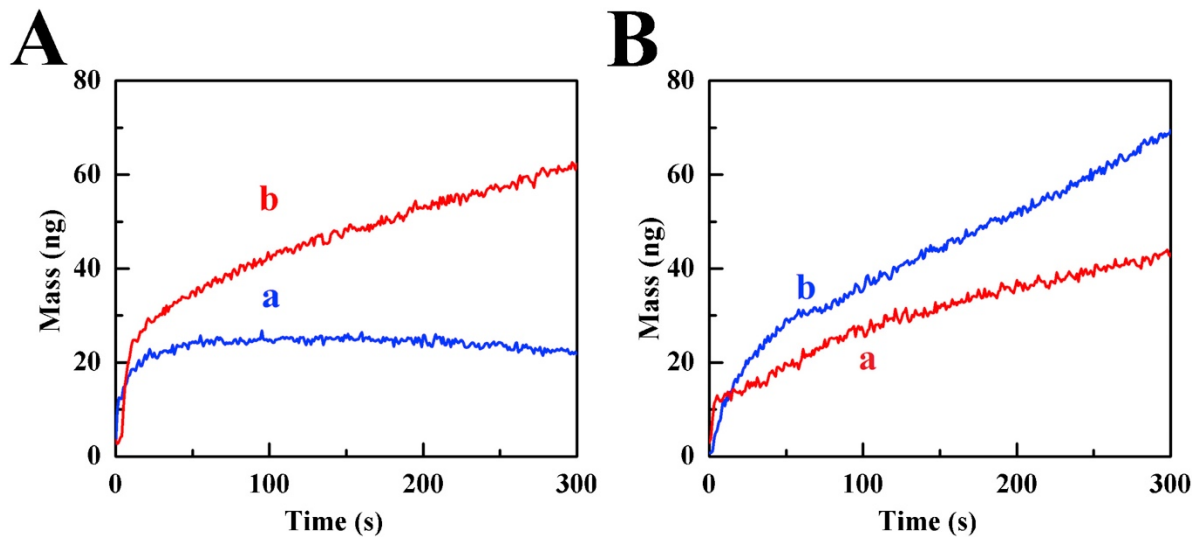
### 7.6.1 Mechanism of electrodeposition of HA

Figure 7-1D shows a schematic of the chemical structure of HA, which includes aromatic rings, hydrocarbon chains and anionic functional groups, such as carboxyl and phenol groups. The structural properties of HA facilitate chemical interactions with a variety of organic and inorganic materials via multiple reaction pathways. According to Sasaki *et al.* [6], a discrete fragment model has been developed for the analysis of contributions of different ligands to the chelating properties of HA. Of particular interest are catechol and salicylate ligands (Figure 7-13a,b), which showed strong complexation with metal atoms[7]. Many investigations were focused on the analysis of adsorption mechanisms[70], [77] and kinetics[78]. It was found[77] that HA adsorption on oxides exhibited a complex behavior. The adsorption was governed by different factors[58], [73], including solution pH and ionic strength. According to the literature, adsorption mechanism of HA was based on the complexation of metal atoms on the material surface with chelating ligands[60] and electrostatic attraction[69]. Based on Yang *et al.* research, the adsorption of HA on reduced graphene oxide involved  $\pi$ - $\pi$  interactions [79].



improved colloidal stability of montmorillonite[82], nano zero-valent iron[83], hematite[84], and magnetite[60]. The literature data on the adsorption of HA on inorganic and organic materials and dispersion of different materials indicate that HA is a promising dispersant for application in EPD technology.

EPD from HA solutions allowed the fabrication of anodic films. Figure 7-14 shows deposition yield data, obtained by the QCM method, at different conditions. EPD was performed from HA solutions in water or mixed water–ethanol solvent. The deposit mass increased with increasing deposition time, indicating continuous film growth. The deposition rate decreased with increasing deposition time due to the increase in the voltage drop in the growing insulating film and the corresponding decrease in the voltage drop in the solution[85]. The deposition yield in the aqueous solutions slightly decreased at deposition times above 200 s at a deposition voltage of 3 V. Such reduction can result from enhanced gas evolution in aqueous solutions and low adhesion of the deposits at low deposition voltages. It is known that a certain value of electric field is necessary in order to allow the deposited material to bond to the substrate[86]. The deposition yield increased with increasing voltage (Figure7-14).



**Figure 7-14 Deposit mass versus time obtained using QCM from  $0.1 \text{ g L}^{-1}$  HA solutions in (A) water and (B) mixed ethanol–water (50% water) solvent at deposition voltages of (a) 3 V and (b) 5 V.**

Figure 7-15 shows deposit mass versus HA concentration in the suspension at a constant deposition time. The slope of the curve increased with increasing HA concentration in the range of  $0\text{--}0.4 \text{ g L}^{-1}$ . The deviation from the linear Hamaker equation[87], describing the deposition yield in the EPD process, was also observed in other investigations[88], [89]. The non-linear increase in the deposition yield was attributed to the shifting of the deposit-suspension interface during the film growth[89]. At HA concentrations above  $0.5 \text{ g L}^{-1}$  the slope of the dependence decreased due to the increase in deposit thickness and voltage drop in the deposited material and corresponding decrease in voltage drop in the HA solution. The mechanism of HA deposition was suggested using literature data on the pH dependence of HA solubility. It was found[90] that HA solubility decreases with decreasing pH and HA precipitation was observed at  $\text{pH} < 3$ . The electric charge of HA in the neutral solutions is

related to the deprotonated carboxylic groups. The protonation of the carboxylic groups at low pH resulted in the HA precipitation.

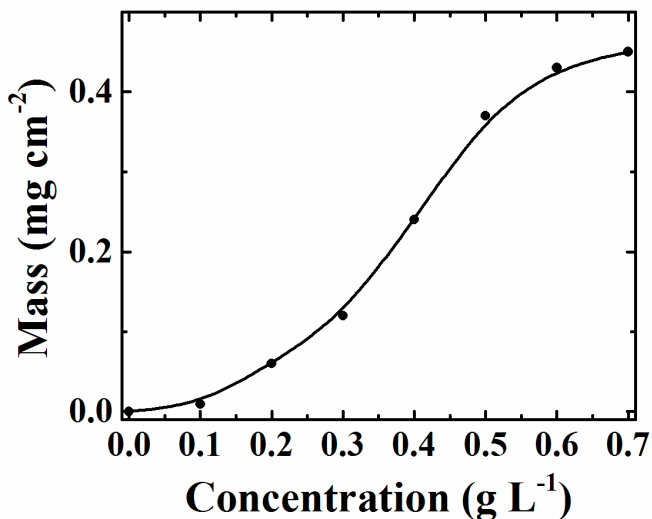


**Figure 7-15 Deposit mass versus HA concentration in a mixed water-ethanol solvent (50%water) at a deposition voltage of 100 V and deposition time of 5 min.**

It is suggested that electrophoresis of the anionic HA molecules resulted in their accumulation at the anode surface. The electrochemical decomposition of the water molecules at the anode resulted in a local pH decrease:



The protonation of the carboxylic groups at the anode surface and charge neutralization promoted precipitation of insoluble HA:



It is suggested that  $\pi$ - $\pi$  interactions of the HA molecules, depletion forces and other interactions at the electrode surface[91] promoted deposit formation. The deposition yield

data, presented in Figure 7-14 and 7-15, confirmed that the deposition mechanism and kinetics are based on the electrophoretic transport, as indicated by the increase in the deposition yield with time and concentration of the anionic HA species in the solutions.

Figure 7-16 shows a typical SEM image of a HA film prepared by EPD. The EPD method allowed for the formation of continuous, crack free and adherent films with the thickness of 1–2  $\mu\text{m}$ . The films adhered well to the substrates and showed low porosity. The film forming properties of HA, coupled with strong adsorption on different materials and electric charge make HA a very promising additive for the EPD of different materials.

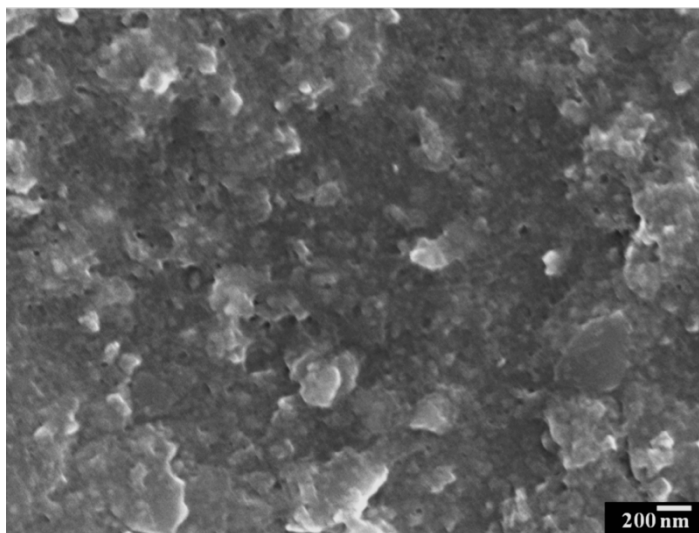


**Figure 7-16 SEM image of HA film prepared from 1 g L<sup>-1</sup> HA solution in a mixed water–ethanol solvent (50% water).**

### **7.6.2 EPD of different materials using HA as a dispersant**

It was found that HA adsorption on different materials such as MnO<sub>2</sub> oxide, Ni and Pd metals, MWCNT allowed for the fabrication of stable suspensions. The adsorption of HA on the oxides and metals was attributed to chelation of metal atoms of the particle surface

with catecholate, salicylate or other ligands of HA. The adsorption of HA on MWCNT involved  $\pi$ - $\pi$  interactions. The relatively large size and anionic properties of HA allowed for electrosteric stabilization. The adsorbed HA imparted a negative charge to the particles and allowed for their electrophoretic motion toward the electrode surface and deposition. The charged particles were dispersed and deposited on the anode surface by EPD. The formation of anodic deposits provided additional evidence of HA adsorption on particles. It is important to note that EPD requires the use of a binder, which allows for the fabrication of adherent and crack-free films. The bath formulations for EPD usually include dispersants and binders[92], [93]. The charged particles, containing an adsorbed charged dispersant and a binder provide electrophoretic transport of the binder macromolecules to the electrode surface. Difficulties are related to the competitive adsorption of the binder and dispersant on the particle surface[92], [93]. Such difficulties can be avoided using HA as a binder and charged dispersant for EPD. Figure 7-17 shows SEM images of MnO<sub>2</sub> films, prepared using HA. The EPD method allowed for the formation of continuous and crack-free films. The MnO<sub>2</sub> films showed larger porosity, which can be attributed to gas evolution at the electrode surface during EPD.

HA can be used for EPD of other materials of different types, such as MWCNT (Figure 7-18). The SEM images showed the formation of continuous and crack-free films. HA was distributed between MWCNT and acted as a binder. However, some HA particles were also observed in the SEM images.

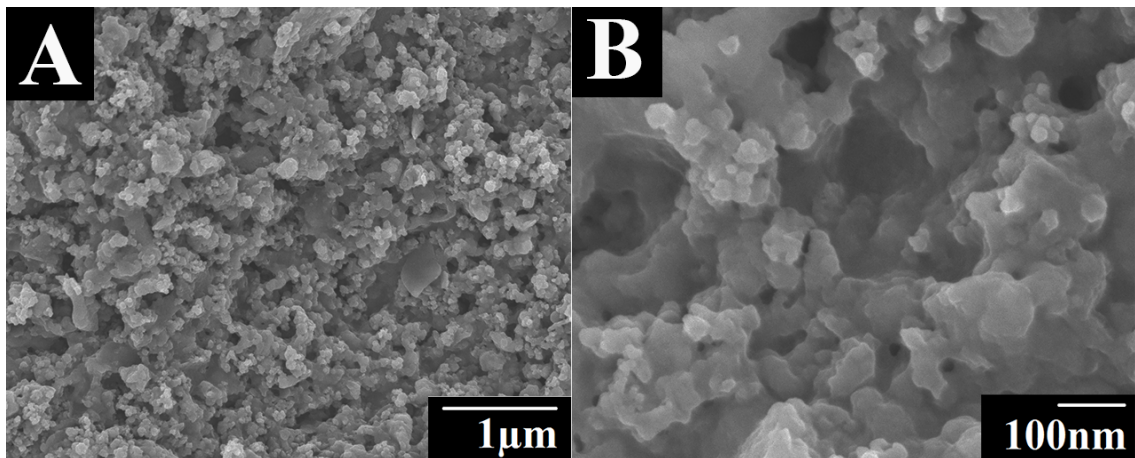


**Figure 7-17 (A and B) SEM images at different magnifications of a deposit obtained from  $0.5 \text{ g L}^{-1}$  HA solutions in a mixed water-ethanol solvent (50% water), containing  $4 \text{ g L}^{-1} \text{ MnO}_2$ .**

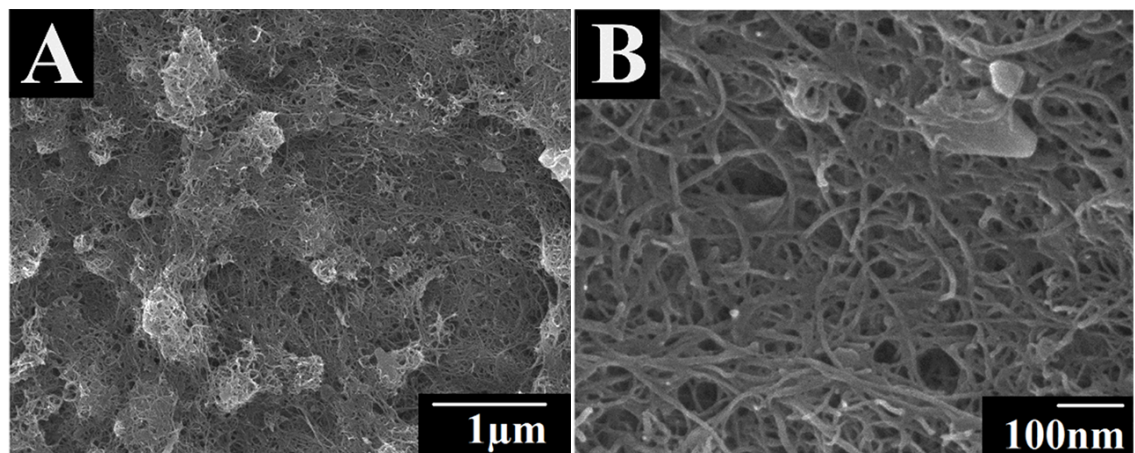


**Figure 7-18 (A and B) SEM images at different magnifications of a deposit, prepared from  $0.5 \text{ g L}^{-1}$  HA solutions in a mixed water-ethanol solvent (50% water), containing  $4 \text{ g L}^{-1}$  MWCNT.**

Of particular interest is the possibility of EPD of metallic particles. The analysis of the literature indicated that relatively limited success was achieved in the EPD of metals[87], [94], [95]. Some problems are attributed to poor dispersion of metals in the suspensions and high electrical conductivity of the suspensions. Additional difficulties result from

magnetic interactions of Ni particles, which promote agglomeration and sedimentation. It was found that Ni and Pd particles can be deposited from the suspensions, containing HA. Figure 7-19 shows SEM images of the Pd and Ni deposits. The low magnification images show the formation of continuous porous films, containing nanoparticles of Pd and Ni. Particles of HA were also observed in the images. The analysis of the SEM images at higher magnification showed relatively low agglomeration of the metal particles. Particles of metals can be used as conductive additives for the fabrication of composite electrodes. However, MWCNT offer advantages of low density and low percolation limit.

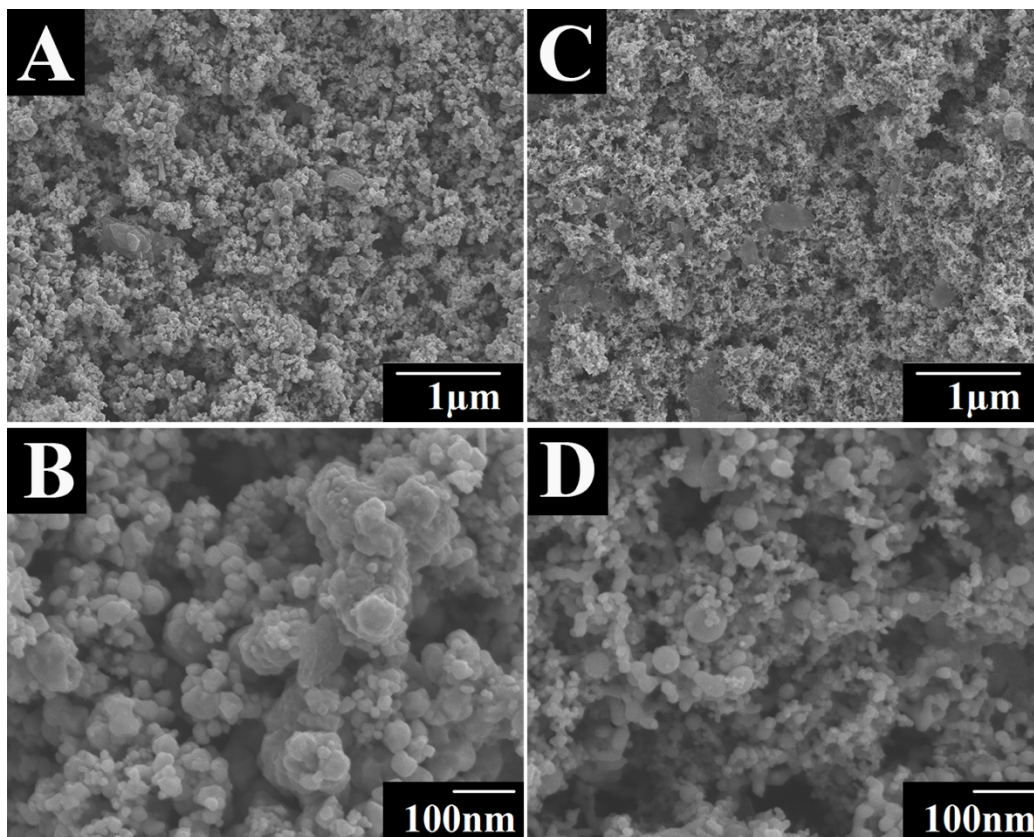


**Figure 7-19 SEM images at different magnifications of deposits, prepared from  $0.5 \text{ g L}^{-1}$  HA solutions in a mixed water–ethanol solvent (50% water), containing  $4 \text{ g L}^{-1}$  (A, B) Pd and (C, D) Ni nanoparticles.**

### 7.6.3 Co-deposition of MnO<sub>2</sub> and MWCNT nanoparticles

The possibility of the co-deposition of different materials using HA paved the way for the fabrication of composites. Figure 7-20 compares the SEM images of the composites, prepared from the 4 g L<sup>-1</sup> MnO<sub>2</sub> suspensions, containing different amounts of MWCNT. Both images show particles of MnO<sub>2</sub> and MWCNT. The increase in the MWCNT concentration in the suspension resulted in the increasing MWCNT content in the deposit. The EPD method for the deposition of HA and composites represents an alternative to the layer-by-layer self-assembly method (LbL)[96], which involves multiple steps and has disadvantages of low deposition rate and limited film thickness. Other difficulties of the LbL method are related to the controlled incorporation of various functional materials into the films. In contrast, EPD is a versatile technique for the deposition of various functional materials. The composite films prepared in this investigation can be used for various applications, based on the functional properties of the deposited materials. Pd and Ni particles are important materials for catalysis[97], [98]. Many applications of MWCNT are based on excellent mechanical properties and high conductivity[99]. However, difficulties are related to the MWCNT dispersion. Many dispersion techniques are based on the functionalization methods, which damage the MWCNT structure and result in the degradation of mechanical and electrical properties. In contrast, HA adsorbed on MWCNT and allowed for good dispersion. Moreover, due to its unique adsorption properties, HA was used as a co-dispersant for MWCNT and MnO<sub>2</sub>. Therefore, we utilized the EPD method for the fabrication of MnO<sub>2</sub>-MWCNT electrodes for electrochemical

supercapacitors, where MWCNT provided improved electronic conductivity of the composites.

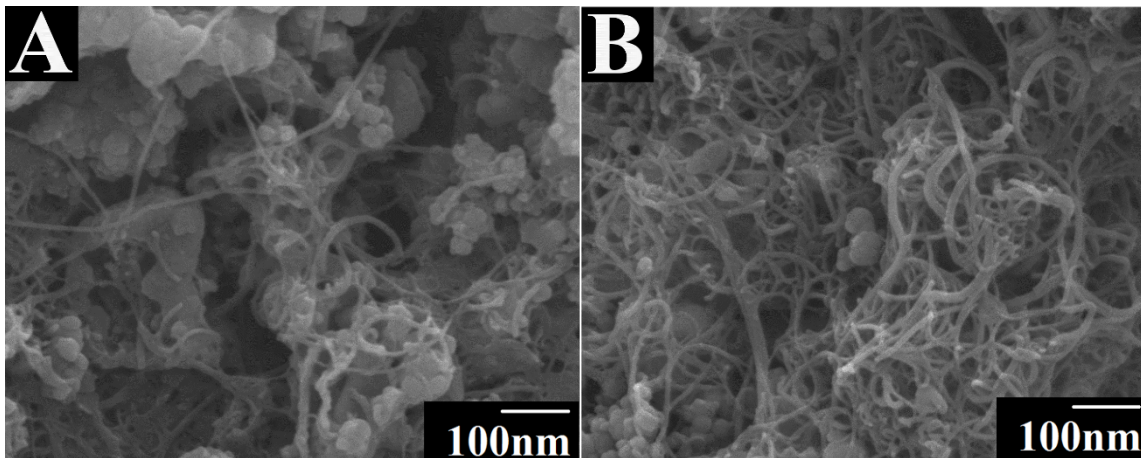


**Figure 7-20 SEM images of composites, deposited from  $0.5 \text{ g L}^{-1}$  HA solutions in a mixed water–ethanol solvent (50% water), containing  $4 \text{ g L}^{-1} \text{ MnO}_2$  and (A)  $0.25$ , (B)  $0.5 \text{ g L}^{-1}$  MWCNT.**

#### **7.6.4 Capacitive performance of $\text{MnO}_2$ -MWCNT composite film**

One of the difficulties related to the  $\text{MnO}_2$  applications as a charge storage material in supercapacitors is related to low conductivity of  $\text{MnO}_2$ , which results in significant reduction in specific capacitance with increasing film mass. The composite  $\text{MnO}_2$ -MWCNT electrodes, prepared using HA as a co-dispersant for EPD showed good electrochemical performance, as indicated by nearly ideal box shape CV, presented in Figure 7-21A. The integral capacitances in the voltage window of  $0.9 \text{ V}$  were calculated from the CV data (Figure 7-21B). Relatively high specific capacitance of  $202 \text{ F g}^{-1}$  ( $0.84 \text{ F cm}^{-2}$ ) was obtained at a film mass of  $4.18 \text{ mg cm}^{-2}$  and a scan rate of  $2 \text{ mV s}^{-1}$ . The mass normalized specific capacitance was comparable with the data[100] for the  $\text{MnO}_2$ -MWCNT films, prepared by EPD, with mass loading of  $0.24 \text{ mg cm}^{-2}$ . The

capacitance of  $185 \text{ F g}^{-1}$  was obtained for  $\text{MnO}_2$ -MWCNT film composites[101] at active mass loading of  $2.2 \text{ mg cm}^{-2}$ . However, significantly higher area normalized capacitance was achieved (Figure 7-21B) due to significantly higher active mass loading of  $4.18 \text{ mg cm}^{-2}$ . The capacitance decreased with increasing scan rate due to the diffusion limitation in pores of the  $\text{MnO}_2$ -MWCNT composite. The capacitance retention at  $100 \text{ mV s}^{-1}$  was found to be 41% of the capacitance value at  $2 \text{ mV s}^{-1}$ . Figure 7-21(C, D) shows frequency dependences of components of differential capacitance, derived from the impedance data. The dependencies showed typical relaxation type dispersion[102], as indicated by the reduction in real component of the capacitance and relaxation maximum of the imaginary component. It is important to note that integral capacitance depends on the scan rate, whereas the differential capacitance depends on the frequency. The capacitance, measured by both methods showed comparable values for similar charge-discharge periods. Figure 7-22 shows capacitance retention versus cycle number for the composite electrodes. Small increase in capacitance during cycling can be attributed to the changes in the electrode microstructure[102] during cycling. However, no reduction in capacitance was observed after 1000 cycles. Therefore, the composite  $\text{MnO}_2$ -MWCNT films, prepared by EPD using HA are promising for the fabrication of supercapacitor electrodes. The results, presented above indicate that HA is a versatile dispersing and film forming agent for the deposition of various materials. Therefore, the films, prepared by EPD using HA can be used for other applications, based on the functional properties of the deposited materials.

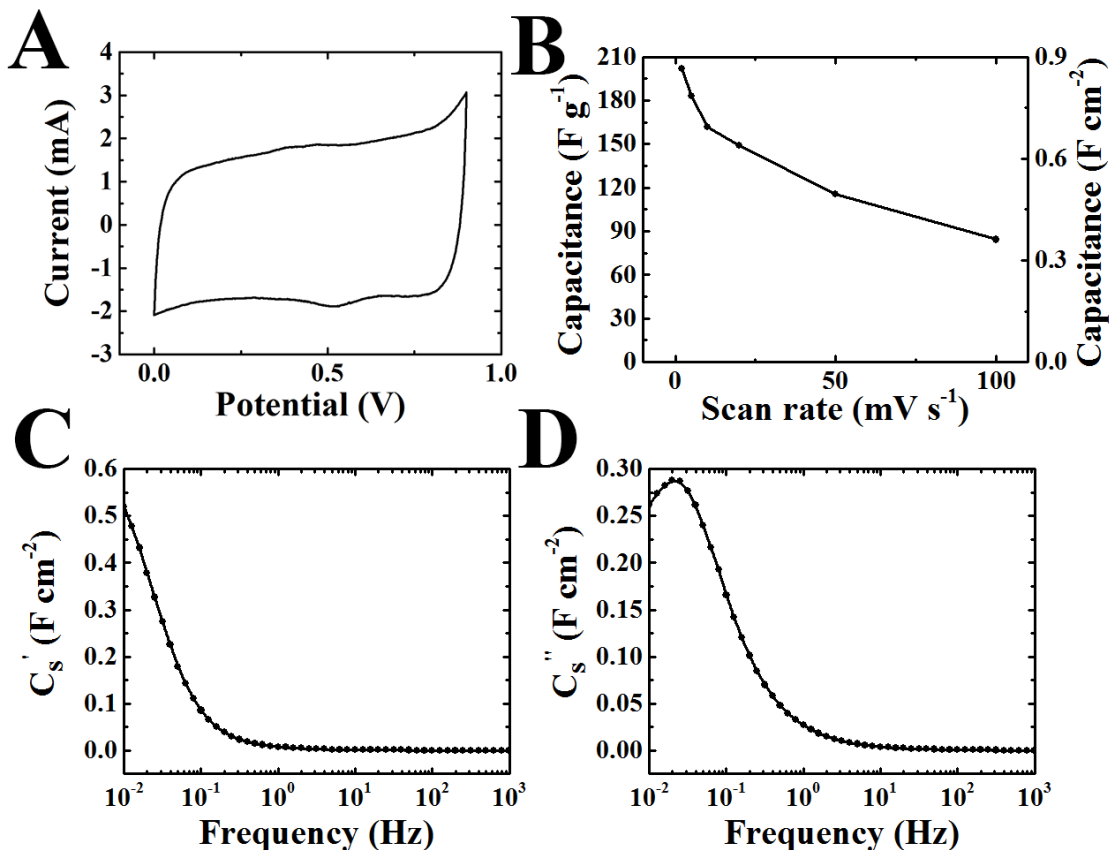
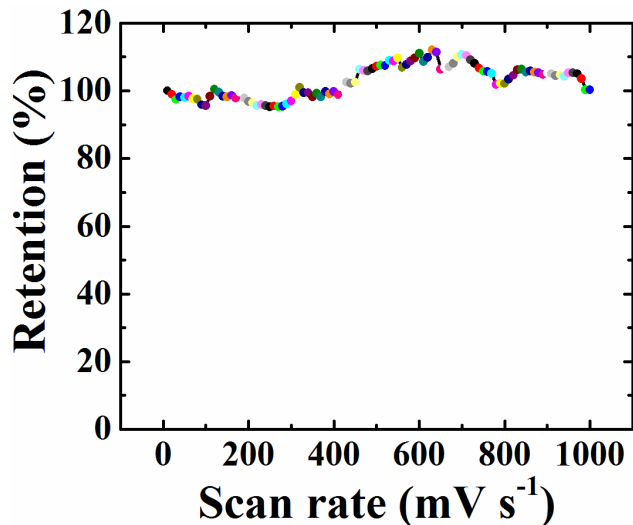


Figure 7-21 (A) CV at a scan rate of 2 mV s<sup>-1</sup>, (B) specific capacitance versus scan rate, (C) real  $C'$  and (D) imaginary  $C''$  parts of capacitance, derived from the impedance data, versus frequency for MnO<sub>2</sub>-MWCNT electrodes, prepared from 0.5 g L<sup>-1</sup> HA solutions in a mixed water-ethanol solvent (50% water), containing 4 g L<sup>-1</sup> MnO<sub>2</sub> and 0.5 g L<sup>-1</sup> MWCNT.



**Figure 7-22** Capacitance retention versus cycle number for the composite MnO<sub>2</sub>-MWCNT electrodes, prepared from 0.5 g L<sup>-1</sup> HA solutions in a mixed water-ethanol solvent (50% water), containing 4 g L<sup>-1</sup> MnO<sub>2</sub> and 0.5 g L<sup>-1</sup> MWCNT.

## 7.7 Conclusions

Various organic additives, such as LPEI, PAH, FA and HA, were used for the EPD of MnO<sub>2</sub> and MWCNT. The feasibility of cathodic EPD of LPEI has been demonstrated. The EPD mechanism is based on the electrophoresis of protonated LPEI-H<sup>+</sup> and deprotonation at the electrode surface. QCM data showed that the deposition yield can be varied and controlled by variation of the deposition time and voltage. A composite film, containing MnO<sub>2</sub> particles in the LPEI matrix, was obtained using LPEI as a charging, dispersing and film forming agent. The composite film is a promising material for various applications, utilizing functional properties of the inorganic particles and LPEI.

The anodic EPD method has been developed for the fabrication of MnO<sub>2</sub> films using FA. FTIR spectrum results proved that the adsorption mechanism of the organic molecule on the oxide

particles involved complexation of COOH and OH groups with Mn atoms on the particle surface.

PAH showed good film forming properties. The discovery of dispersing agents with film forming properties opens the door to making advanced films and composites. The  $\pi$ - $\pi$  stacking of PAH molecules (Figure 7-12) resulted in anisotropic particle growth during EPD and formation of fibrous microstructure. However, PAH showed poor efficiency as a charging agent for EPD of MnO<sub>2</sub>.

HA also showed good film forming properties, which allowed for anodic EPD of HA films from aqueous or water-ethanol solutions at various deposition voltages and concentrations of HA in the solutions. The deposition mechanism is based on the electrophoresis of anionic HA species, local pH decrease at the anode surface and charge neutralization, followed by the precipitation of insoluble HA molecules and film formation. HA showed strong adsorption on inorganic particles due to the chelating properties of this molecule, which facilitated the formation of chemical bonds with metal atoms on the particle surface. The adsorbed HA provided electrosteric dispersion of the particles and allowed their EPD. HA was used as a charging, dispersing and film forming agent for the EPD of materials of different types, such as oxide nanoparticles of MnO<sub>2</sub>, metal nanoparticles of Ni and Pd, MWCNT. The use of HA as a co-dispersant allowed for the fabrication of MnO<sub>2</sub>-MWCNT composites with various MWCNT content. Testing results showed promising performance of MnO<sub>2</sub>-MWCNT composites for applications in electrodes of electrochemical supercapacitors.

## 7.8 Acknowledgement

Yanchou Sun has contribution on providing QCM test data to this work.

## References:

- [1] B. L. Rivas and K. E. Geckeler, "Synthesis and metal complexation of poly(ethyleneimine) and derivatives," in *Polymer Synthesis Oxidation Processes*, Springer Berlin Heidelberg, 1992, pp. 171–188.
- [2] P. C. Griffiths, A. Paul, P. Stilbs, and E. Petterson, "Charge on Poly(ethylene imine): Comparing Electrophoretic NMR Measurements and pH Titrations," *Macromolecules*, vol. 38, no. 8, pp. 3539–3542, Apr. 2005.
- [3] Y. Su and I. Zhitomirsky, "Electrophoretic Nanotechnology of Composite Electrodes for Electrochemical Supercapacitors," *J. Phys. Chem. B*, vol. 117, no. 6, pp. 1563–1570, Feb. 2013.
- [4] H. Atabey and H. Sari, "Potentiometric, Theoretical, and Thermodynamic Studies on Equilibrium Constants of Aurintricarboxylic Acid and Determination of Stability Constants of Its Complexes with  $\text{Cu}^{2+}$ ,  $\text{Ni}^{2+}$ ,  $\text{Zn}^{2+}$ ,  $\text{Co}^{2+}$ ,  $\text{Hg}^{2+}$ , and  $\text{Pb}^{2+}$  Metal Ions in Aqueous Solution," *J. Chem. Eng. Data*, vol. 56, no. 10, pp. 3866–3872, Oct. 2011.
- [5] M. S. Ata, Y. Liu, and I. Zhitomirsky, "A review of new methods of surface chemical modification, dispersion and electrophoretic deposition of metal oxide particles," *RSC Adv.*, vol. 4, no. 43, pp. 22716–22732, 2014.
- [6] T. Sasaki, T. Kobayashi, I. Takagi, and H. Moriyama, "Discrete fragment model for complex formation of europium (III) with humic acid," *J. Nucl. Sci. Technol.*, vol. 45, no. 8, pp. 718–724, 2008.
- [7] M. S. Ata, Y. Liu, and I. Zhitomirsky, "A review of new methods of surface chemical modification, dispersion and electrophoretic deposition of metal oxide particles," *Rsc Adv.*, vol. 4, no. 43, pp. 22716–22732, 2014.

- [8] M. Bellmann, C. Gerhard, C. Haese, S. Wieneke, and W. Vioel, "DBD plasma improved spot repair of automotive polymer surfaces," *Surf. Eng.*, vol. 28, no. 10, pp. 754–758, Nov. 2012.
- [9] P. B. Srinivasan, N. Scharnagl, C. Blawert, and W. Dietzel, "Enhanced corrosion protection of AZ31 magnesium alloy by duplex plasma electrolytic oxidation and polymer coatings," *Surf. Eng.*, vol. 26, no. 5, pp. 354–360, Jul. 2010.
- [10] E. Zumelzu, C. Ortega, F. Rull, and C. Cabezas, "Degradation mechanism of metal-polymer composites undergoing electrolyte induced delamination," *Surf. Eng.*, vol. 27, no. 7, pp. 485–490, Aug. 2011.
- [11] Y. Murakami, K. Sugo, M. Hirano, and T. Okuyama, "Surface chemical analysis and chromatographic characterization of polyethylenimine-coated hydroxyapatite with various amount of polyethylenimine," *Talanta*, vol. 85, no. 3, pp. 1298–1303, Sep. 2011.
- [12] H. H. P. Yiu, S. C. McBain, Z. A. D. Lethbridge, M. R. Lees, and J. Dobson, "Preparation and characterization of polyethylenimine-coated Fe<sub>3</sub>O<sub>4</sub>-MCM-48 nanocomposite particles as a novel agent for magnet-assisted transfection," *J. Biomed. Mater. Res. A*, vol. 92A, no. 1, pp. 386–392, Jan. 2010.
- [13] A. Tomitaka, K. Ueda, T. Yamada, and Y. Takemura, "Heat dissipation and magnetic properties of surface-coated Fe<sub>3</sub>O<sub>4</sub> nanoparticles for biomedical applications," *J. Magn. Magn. Mater.*, vol. 324, no. 21, pp. 3437–3442, Oct. 2012.
- [14] K. R. Knowles, C. C. Hanson, A. L. Fogel, B. Warhol, and D. A. Rider, "Layer-by-Layer Assembled Multilayers of Polyethylenimine-Stabilized Platinum Nanoparticles and PEDOT:PSS as Anodes for the Methanol Oxidation Reaction," *Acs Appl. Mater. Interfaces*, vol. 4, no. 7, pp. 3575–3583, Jul. 2012.
- [15] V. L. C. Fai, Y. D. Lee, K. Lee, K.-S. Lee, D.-J. Ham, and B.-K. Ju, "Sensing properties of polyethylenimine coated carbon nanotubes in oxidized oil," *Talanta*, vol. 85, no. 1, pp. 463–468, Jul. 2011.
- [16] I. Zhitomirsky, "Electrodeposition of composite ceria-polyethylenimine films," *Surf. Eng.*, vol. 20, no. 1, pp. 43–47, Feb. 2004.
- [17] A. F. Carley, P. R. Davies, J. Hurcom, and J. MacSorley, "An investigation into the chemistry of electrodeposited lanthanum hydroxide-polyethylenimine films," *Thin Solid Films*, vol. 520, no. 7, pp. 2735–2738, Jan. 2012.

- [18] I. Zhitomirsky, "Cathodic electrodeposition of ceramic and organoceramic materials. Fundamental aspects," *Adv. Colloid Interface Sci.*, vol. 97, no. 1–3, pp. 279–317, Mar. 2002.
- [19] N. Nagarajan, H. Humadi, and I. Zhitomirsky, "Cathodic electrodeposition of MnOx films for electrochemical supercapacitors," *Electrochimica Acta*, vol. 51, no. 15, pp. 3039–3045, Apr. 2006.
- [20] I. Zhitomirsky, "Electrophoretic and electrolytic deposition of ceramic coatings on carbon fibers," *J. Eur. Ceram. Soc.*, vol. 18, no. 7, pp. 849–856, 1998.
- [21] B. B. Prasad, R. Madhuri, M. P. Tiwari, and P. S. Sharma, "Electrochemical sensor for folic acid based on a hyperbranched molecularly imprinted polymer-immobilized sol–gel-modified pencil graphite electrode," *Sens. Actuators B Chem.*, vol. 146, no. 1, pp. 321–330, Apr. 2010.
- [22] M. A. Honein, L. J. Paulozzi, T. J. Mathews, J. D. Erickson, and L.-Y. C. Wong, "Impact of Folic Acid Fortification of the US Food Supply on the Occurrence of Neural Tube Defects," *JAMA*, vol. 285, no. 23, pp. 2981–2986, Jun. 2001.
- [23] Y. Zhang *et al.*, "Progress of electrochemical capacitor electrode materials: A review," *2nd Int. Workshop Hydrog. Int. Workshop Hydrog.*, vol. 34, no. 11, pp. 4889–4899, Jun. 2009.
- [24] P. J. Britto, K. S. V. Santhanam, and P. M. Ajayan, "Carbon nanotube electrode for oxidation of dopamine," *Bioelectrochem. Bioenerg.*, vol. 41, no. 1, pp. 121–125, 1996.
- [25] P. J. Britto, K. S. Santhanam, A. Rubio, J. A. Alonso, P. M. Ajayan, and others, "Improved charge transfer at carbon nanotube electrodes," *Adv. Mater.*, vol. 11, no. 2, pp. 154–157, 1999.
- [26] J. J. Davis, R. J. Coles, H. Allen, and O. Hill, "Protein electrochemistry at carbon nanotube electrodes," *J. Electroanal. Chem.*, vol. 440, no. 1–2, pp. 279–282, 1997.
- [27] J. Sudimack and R. J. Lee, "Targeted drug delivery via the folate receptor," *Adv. Drug Deliv. Rev.*, vol. 41, no. 2, pp. 147–162, 2000.
- [28] A. Gabizon, H. Shmeeda, A. T. Horowitz, and S. Zalipsky, "Tumor cell targeting of liposome-entrapped drugs with phospholipid-anchored folic acid–PEG conjugates," *Adv. Drug Deliv. Rev.*, vol. 56, no. 8, pp. 1177–1192, 2004.
- [29] K. Cho, X. U. Wang, S. Nie, D. M. Shin, and others, "Therapeutic nanoparticles for drug delivery in cancer," *Clin. Cancer Res.*, vol. 14, no. 5, pp. 1310–1316, 2008.

- [30] Y. Bae, W.-D. Jang, N. Nishiyama, S. Fukushima, and K. Kataoka, "Multifunctional polymeric micelles with folate-mediated cancer cell targeting and pH-triggered drug releasing properties for active intracellular drug delivery," *Mol. Biosyst.*, vol. 1, no. 3, pp. 242–250, 2005.
- [31] C. Fabbro, H. Ali-Boucetta, T. Da Ros, K. Kostarelos, A. Bianco, and M. Prato, "Targeting carbon nanotubes against cancer," *Chem. Commun.*, vol. 48, no. 33, pp. 3911–3926, 2012.
- [32] R. L. Blakley and others, "Biochemistry of folic acid and related pteridines," 1969.
- [33] S. Farber, L. K. Diamond, R. D. Mercer, R. F. Sylvester Jr, and J. A. Wolff, "Temporary remissions in acute leukemia in children produced by folic acid antagonist, 4-aminopteroyl-glutamic acid (aminopterin)," *N. Engl. J. Med.*, vol. 238, no. 23, pp. 787–793, 1948.
- [34] C. J. Boushey, S. A. Beresford, G. S. Omenn, and A. G. Motulsky, "A quantitative assessment of plasma homocysteine as a risk factor for vascular disease: probable benefits of increasing folic acid intakes," *Jama*, vol. 274, no. 13, pp. 1049–1057, 1995.
- [35] M. B. Caselunghe and J. Lindeberg, "Biosensor-based determination of folic acid in fortified food," *Food Chem.*, vol. 70, no. 4, pp. 523–532, 2000.
- [36] L. Mirmoghtadaie, A. A. Ensafi, M. Kadivar, and P. Norouzi, "Highly selective electrochemical biosensor for the determination of folic acid based on DNA modified-pencil graphite electrode using response surface methodology," *Mater. Sci. Eng. C*, vol. 33, no. 3, pp. 1753–1758, 2013.
- [37] J. J. Castillo, W. E. Svendsen, N. Rozlosnik, P. Escobar, F. Martínez, and J. Castillo-León, "Detection of cancer cells using a peptide nanotube–folic acid modified graphene electrode," *Analyst*, vol. 138, no. 4, pp. 1026–1031, 2013.
- [38] B. M. Hibbard, "The role of folic acid in pregnancy," *BJOG Int. J. Obstet. Gynaecol.*, vol. 71, no. 4, pp. 529–542, 1964.
- [39] T. O. Scholl and W. G. Johnson, "Folic acid: influence on the outcome of pregnancy," *Am. J. Clin. Nutr.*, vol. 71, no. 5, p. 1295s–1303s, 2000.
- [40] A. Milunsky *et al.*, "Multivitamin/folic acid supplementation in early pregnancy reduces the prevalence of neural tube defects," *Jama*, vol. 262, no. 20, pp. 2847–2852, 1989.

- [41] K. A. Lillycrop, E. S. Phillips, A. A. Jackson, M. A. Hanson, and G. C. Burdge, "Dietary protein restriction of pregnant rats induces and folic acid supplementation prevents epigenetic modification of hepatic gene expression in the offspring," *J. Nutr.*, vol. 135, no. 6, pp. 1382–1386, 2005.
- [42] S. Mohapatra, S. K. Mallick, T. K. Maiti, S. K. Ghosh, and P. Pramanik, "Synthesis of highly stable folic acid conjugated magnetite nanoparticles for targeting cancer cells," *Nanotechnology*, vol. 18, no. 38, p. 385102, 2007.
- [43] E. Hamed, M. S. Attia, and K. Bassiouny, "Synthesis, Spectroscopic and Thermal Characterization of Copper(II) and Iron(III) Complexes of Folic Acid and Their Absorption Efficiency in the Blood," *Bioinorg. Chem. Appl.*, vol. 2009, p. e979680, Sep. 2009.
- [44] Y. Y. He, X. C. Wang, P. K. Jin, B. Zhao, and X. Fan, "Complexation of anthracene with folic acid studied by FTIR and UV spectroscopies," *Spectrochim. Acta. A. Mol. Biomol. Spectrosc.*, vol. 72, no. 4, pp. 876–879, May 2009.
- [45] T. Rajh, L. X. Chen, K. Lukas, T. Liu, M. C. Thurnauer, and D. M. Tiede, "Surface restructuring of nanoparticles: an efficient route for ligand- metal oxide crosstalk," *J. Phys. Chem. B*, vol. 106, no. 41, pp. 10543–10552, 2002.
- [46] K. Wu and I. Zhitomirsky, "Electrophoretic Deposition of Ceramic Nanoparticles," *Int. J. Appl. Ceram. Technol.*, vol. 8, no. 4, pp. 920–927, Jul. 2011.
- [47] X.-M. Shi, M.-X. Li, X. He, H.-J. Liu, and M. Shao, "Crystal structures and properties of four coordination polymers constructed from flexible pamoic acid," *Polyhedron*, vol. 29, no. 9, pp. 2075–2080, Jun. 2010.
- [48] Q. Shi *et al.*, "Anion-Dependent Crystallization of Four Supramolecular Cadmium Complexes: Structures and Property Studies," *Cryst. Growth Des.*, vol. 8, no. 9, pp. 3401–3407, Sep. 2008.
- [49] M. Du, C.-P. Li, X.-J. Zhao, and Q. Yu, "Interplay of coordinative and supramolecular interactions in engineering unusual crystalline architectures of low-dimensional metal–pamoate complexes under co-ligand intervention," *CrystEngComm*, vol. 9, no. 11, pp. 1011–1028, Oct. 2007.
- [50] M. Du, Z.-H. Zhang, W. Guo, and X.-J. Fu, "Multi-component hydrogen-bonding assembly of a pharmaceutical agent pamoic acid with piperazine or 4, 4'-bipyridyl: A channel hydrated salt with multiple-helical motifs vs a bimolecular cocrystal," *Cryst. Growth Des.*, vol. 9, no. 4, pp. 1655–1657, 2009.

- [51] P. Zhao *et al.*, “Targeting of the orphan receptor GPR35 by pamoic acid: a potent activator of extracellular signal-regulated kinase and  $\beta$ -arrestin2 with antinociceptive activity,” *Mol. Pharmacol.*, vol. 78, no. 4, pp. 560–568, 2010.
- [52] J. Yang, J.-F. Ma, and S. R. Batten, “Polyrotaxane metal–organic frameworks (PMOFs),” *Chem. Commun.*, vol. 48, no. 64, pp. 7899–7912, 2012.
- [53] S. Wang *et al.*, “A series of four-connected entangled metal–organic frameworks assembled from pamoic acid and pyridine-containing ligands: interpenetrating, self-penetrating, and supramolecular isomerism,” *Cryst. Growth Des.*, vol. 12, no. 1, pp. 79–92, 2011.
- [54] S. Wang *et al.*, “Temperature-dependent supramolecular isomerism in three zinc coordination polymers with pamoic acid and 1, 4-bis (imidazol-1-ylmethyl)-benzene,” *CrystEngComm*, vol. 13, no. 17, pp. 5313–5316, 2011.
- [55] F. Luo, Y.-T. Yang, Y.-X. Che, and J.-M. Zheng, “An unusual metal–organic framework showing both rotaxane-and catenane-like motifs,” *CrystEngComm*, vol. 10, no. 8, pp. 981–982, 2008.
- [56] Y. Su and I. Zhitomirsky, “Electrophoretic assembly of organic molecules and composites for electrochemical supercapacitors,” *J. Colloid Interface Sci.*, vol. 392, pp. 247–255, Feb. 2013.
- [57] M. N. Jones and N. D. Bryan, “Colloidal properties of humic substances,” *Adv. Colloid Interface Sci.*, vol. 78, no. 1, pp. 1–48, Aug. 1998.
- [58] N. Janot, P. E. Reiller, X. Zheng, J.-P. Croué, and M. F. Benedetti, “Characterization of humic acid reactivity modifications due to adsorption onto  $\alpha$ -Al<sub>2</sub>O<sub>3</sub>,” *Water Res.*, vol. 46, no. 3, pp. 731–740, 2012.
- [59] A. Pitois, L. G. Abrahamsen, P. I. Ivanov, and N. D. Bryan, “Humic acid sorption onto a quartz sand surface: A kinetic study and insight into fractionation,” *J. Colloid Interface Sci.*, vol. 325, no. 1, pp. 93–100, 2008.
- [60] E. Tombácz *et al.*, “Adsorption of organic acids on magnetite nanoparticles, pH-dependent colloidal stability and salt tolerance,” *Colloids Surf. Physicochem. Eng. Asp.*, vol. 435, pp. 91–96, 2013.
- [61] K. Yang, D. Lin, and B. Xing, “Interactions of Humic Acid with Nanosized Inorganic Oxides,” *Langmuir*, vol. 25, no. 6, pp. 3571–3576, Mar. 2009.
- [62] M. Wang, L. Liao, X. Zhang, and Z. Li, “Adsorption of low concentration humic acid from water by palygorskite,” *Clay Water Treat.*, vol. 67–68, pp. 164–168, Oct. 2012.

- [63] A. M. Shaker, Z. R. Komy, S. E. M. Heggy, and M. E. A. El-Sayed, "Kinetic Study for Adsorption Humic Acid on Soil Minerals," *J. Phys. Chem. A*, vol. 116, no. 45, pp. 10889–10896, Nov. 2012.
- [64] A. W. P. Vermeer, W. H. van Riemsdijk, and L. K. Koopal, "Adsorption of Humic Acid to Mineral Particles. 1. Specific and Electrostatic Interactions," *Langmuir*, vol. 14, no. 10, pp. 2810–2819, May 1998.
- [65] L. ZHANG *et al.*, "Studies on the adsorption mechanisms of fulvic acid and humic acid on smectite," *Res. Environ. Sci.*, vol. 12, p. 12, 2013.
- [66] M. Arias, M. T. Barral, and J. C. Mejuto, "Enhancement of copper and cadmium adsorption on kaolin by the presence of humic acids," *Chemosphere*, vol. 48, no. 10, pp. 1081–1088, 2002.
- [67] E. M. Murphy, J. M. Zachara, and S. C. Smith, "Influence of mineral-bound humic substances on the sorption of hydrophobic organic compounds," *Environ. Sci. Technol.*, vol. 24, no. 10, pp. 1507–1516, 1990.
- [68] M. A. González, I. Pavlovic, R. Rojas-Delgado, and C. Barriga, "Removal of Cu<sup>2+</sup>, Pb<sup>2+</sup> and Cd<sup>2+</sup> by layered double hydroxide–humate hybrid. Sorbate and sorbent comparative studies," *Chem. Eng. J.*, vol. 254, pp. 605–611, 2014.
- [69] M. H. Stietiya and J. J. Wang, "Zinc and cadmium adsorption to aluminum oxide nanoparticles affected by naturally occurring ligands," *J. Environ. Qual.*, vol. 43, no. 2, pp. 498–506, 2014.
- [70] M. S. Gasser, H. T. Mohsen, and H. F. Aly, "Humic acid adsorption onto Mg/Fe layered double hydroxide," *Colloids Surf. Physicochem. Eng. Asp.*, vol. 331, no. 3, pp. 195–201, 2008.
- [71] W. S. Ngah and A. Musa, "Adsorption of humic acid onto chitin and chitosan," *J. Appl. Polym. Sci.*, vol. 69, no. 12, pp. 2305–2310, 1998.
- [72] X. Zhang and R. Bai, "Deposition/adsorption of colloids to surface-modified granules: effect of surface interactions," *Langmuir*, vol. 18, no. 9, pp. 3459–3465, 2002.
- [73] D. Lin, T. Li, K. Yang, and F. Wu, "The relationship between humic acid (HA) adsorption on and stabilizing multiwalled carbon nanotubes (MWNTs) in water: effects of HA, MWNT and solution properties," *J. Hazard. Mater.*, vol. 241, pp. 404–410, 2012.

- [74] G. N. Kasozi, A. R. Zimmerman, P. Nkedi-Kizza, and B. Gao, "Catechol and humic acid sorption onto a range of laboratory-produced black carbons (biochars)," *Environ. Sci. Technol.*, vol. 44, no. 16, pp. 6189–6195, 2010.
- [75] J. Duan, F. Wilson, N. Graham, and J. H. Tay, "Adsorption of humic acid by powdered activated carbon in saline water conditions," *Desalination*, vol. 151, no. 1, pp. 53–66, 2003.
- [76] K. G. Karthikeyan and J. Chorover, "Humic acid complexation of basic and neutral polycyclic aromatic compounds," *Chemosphere*, vol. 48, no. 9, pp. 955–964, 2002.
- [77] D. D. Sun and P. F. Lee, "TiO<sub>2</sub> microsphere for the removal of humic acid from water: complex surface adsorption mechanisms," *Sep. Purif. Technol.*, vol. 91, pp. 30–37, 2012.
- [78] M. Eita, "In situ study of the adsorption of humic acid on the surface of aluminium oxide by QCM-D reveals novel features," *Soft Matter*, vol. 7, no. 2, pp. 709–715, 2011.
- [79] S. Yang *et al.*, "Effects of humic acid on copper adsorption onto few-layer reduced graphene oxide and few-layer graphene oxide," *Carbon*, vol. 75, pp. 227–235, 2014.
- [80] A. Schierz and H. Zänker, "Aqueous suspensions of carbon nanotubes: surface oxidation, colloidal stability and uranium sorption," *Environ. Pollut.*, vol. 157, no. 4, pp. 1088–1094, 2009.
- [81] N. Akaike *et al.*, "Humic acid-induced silver nanoparticle formation under environmentally relevant conditions," *Environ. Sci. Technol.*, vol. 45, no. 9, pp. 3895–3901, 2011.
- [82] M. M. Ramos-Tejada, J. De Vicente, A. Ontiveros, and J. D. G. Durán, "Effect of humic acid adsorption on the rheological properties of sodium montmorillonite suspensions," *J. Rheol.*, vol. 45, no. 5, pp. 1159–1172, 2001.
- [83] H. Dong and I. M. Lo, "Influence of humic acid on the colloidal stability of surface-modified nano zero-valent iron," *Water Res.*, vol. 47, no. 1, pp. 419–427, 2013.
- [84] D. Dickson, G. Liu, C. Li, G. Tachiev, and Y. Cai, "Dispersion and stability of bare hematite nanoparticles: effect of dispersion tools, nanoparticle concentration, humic acid and ionic strength," *Sci. Total Environ.*, vol. 419, pp. 170–177, 2012.
- [85] I. Zhitomirsky, "Electrophoretic hydroxyapatite coatings and fibers," *Mater. Lett.*, vol. 42, no. 4, pp. 262–271, 2000.

- [86] I. Zhitomirsky and L. Gal-Or, "Electrophoretic deposition of hydroxyapatite," *J. Mater. Sci. Mater. Med.*, vol. 8, no. 4, pp. 213–219, 1997.
- [87] O. O. Van der Biest and L. J. Vandeperre, "Electrophoretic deposition of materials," *Annu. Rev. Mater. Sci.*, vol. 29, no. 1, pp. 327–352, 1999.
- [88] P. M. Biesheuvel and H. Verweij, "Theory of cast formation in electrophoretic deposition," *J. Am. Ceram. Soc.*, vol. 82, no. 6, pp. 1451–1455, 1999.
- [89] X. Pang, T. Casagrande, and I. Zhitomirsky, "Electrophoretic deposition of hydroxyapatite–CaSiO<sub>3</sub>–chitosan composite coatings," *J. Colloid Interface Sci.*, vol. 330, no. 2, pp. 323–329, 2009.
- [90] H. Kipton, J. Powell, and R. M. Town, "Solubility and fractionation of humic acid; effect of pH and ionic medium," *Anal. Chim. Acta*, vol. 267, no. 1, pp. 47–54, 1992.
- [91] I. Zhitomirsky, "Cathodic electrodeposition of ceramic and organoceramic materials. Fundamental aspects," *Adv. Colloid Interface Sci.*, vol. 97, no. 1–3, pp. 279–317, Mar. 2002.
- [92] I. Zhitomirsky and A. Petric, "Electrophoretic deposition of ceramic materials for fuel cell applications," *J. Eur. Ceram. Soc.*, vol. 20, no. 12, pp. 2055–2061, 2000.
- [93] I. Zhitomirsky and A. Petric, "Electrophoretic deposition of electrolyte materials for solid oxide fuel cells," *J. Mater. Sci.*, vol. 39, no. 3, pp. 825–831, 2004.
- [94] L. Besra and M. Liu, "A review on fundamentals and applications of electrophoretic deposition (EPD)," *Prog. Mater. Sci.*, vol. 52, no. 1, pp. 1–61, 2007.
- [95] B. Ferrari and R. Moreno, "Electrophoretic deposition of aqueous alumina slips," *J. Eur. Ceram. Soc.*, vol. 17, no. 4, pp. 549–556, 1997.
- [96] Z. Xu, C. Hu, and H. Guoxin, "Layer-by-layer self-assembly of multilayer films based on humic acid," *Thin Solid Films*, vol. 519, no. 13, pp. 4324–4328, 2011.
- [97] J. Zhong *et al.*, "Graphene nanosheet-supported Pd nano-leaves with highly efficient electrocatalytic performance for formic acid oxidation," *Colloids Surf. Physicochem. Eng. Asp.*, vol. 488, pp. 1–6, 2016.
- [98] Y. Tian, Y. Liu, F. Pang, F. Wang, and X. Zhang, "Green synthesis of nanostructured Ni-reduced graphene oxide hybrids and their application for catalytic reduction of 4-nitrophenol," *Colloids Surf. Physicochem. Eng. Asp.*, vol. 464, pp. 96–103, 2015.

- [99] S. Hanumansetty, E. O’Rear, and D. E. Resasco, “Hydrophilic encapsulation of multi-walled carbon nanotubes using admicellar polymerization,” *Colloids Surf. Physicochem. Eng. Asp.*, vol. 474, pp. 1–8, 2015.
- [100] J. Li and I. Zhitomirsky, “Electrophoretic deposition of manganese dioxide–carbon nanotube composites,” *J. Mater. Process. Technol.*, vol. 209, no. 7, pp. 3452–3459, 2009.
- [101] M. S. Ata and I. Zhitomirsky, “Preparation of MnO<sub>2</sub> and Composites for Ultracapacitors,” *Mater. Manuf. Process.*, vol. 28, no. 9, pp. 1014–1018, Sep. 2013.
- [102] K. Shi and I. Zhitomirsky, “Influence of current collector on capacitive behavior and cycling stability of Tiron doped polypyrrole electrodes,” *J. Power Sources*, vol. 240, pp. 42–49, 2013.

## **Chapter 8     Surface modification and EPD of materials using carboxyalkylphosphonic acids**

### **8.1 Fundamental aspects and adsorption mechanisms of phosphonic acids**

Recent studies[1] analyzed molecules, containing catecholate, salicylate and gallate ligands, which provided strong bonding to the particle surface and allowed efficient particle dispersion and EPD. These studies highlighted the importance of further development of dispersants with special ligands for efficient adsorption and analysis of their interactions with metal atoms on a particle surface.

It is known that monodentate ligands allow relatively weak bonding[2]. More stable bonding can be achieved using polydentate ligands[2]. Therefore, organic molecules from the phosphonate family have a potential for surface functionalization and dispersion of inorganic particles. The three oxygen atoms of the phosphonate ligands allow for bi- or tri-dentate (Figure 8-1A(a)–(d)) bonding[2]. Three oxygen atoms can bind to the same metal site by chelation mechanism (Figure 8-1A(a) and (d)) or bind to different metal atoms on the particle surface (Figure 8-1A(b) and (c)). The adsorption of phosphonates from aqueous solutions was studied on different materials, such as  $\text{Al}_2\text{O}_3$ ,  $\text{TiO}_2$ ,  $\text{SiO}_2$ ,  $\text{ZnO}$ , indium tin oxide, ilmenite,  $\text{Fe}_3\text{O}_4$ , hydroxyapatite, clay, and calcium carbonate[2–5].

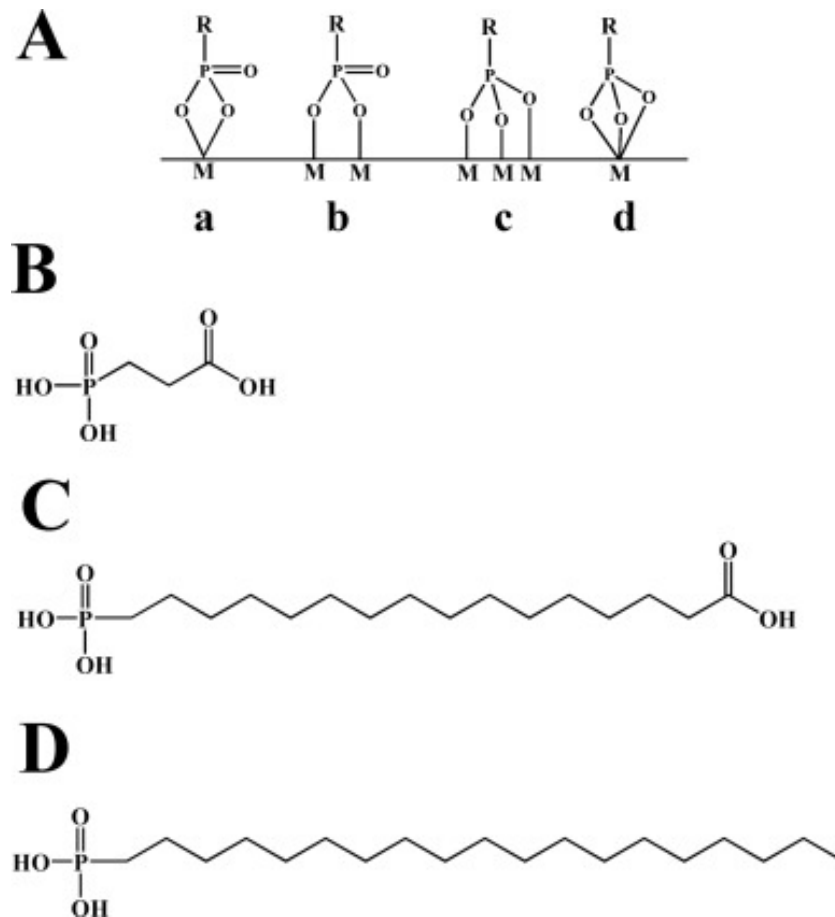


**Figure 8-1 Bonding modes (A) of phosphonic acids to metal atoms (M) on inorganic surfaces: (a) chelating bidentate, (b) bridging bidentate, (c) bridging tridentate and (d) chelating tridentate; chemical structures of (B) 3PHA, (C) 16PHA and (D) octaPHA.**

The goal of this investigation was the application of bipolar carboxyalkylphosphonic acids for dispersion, charging and EPD of  $\text{MnO}_2$ . We analyzed the adsorption of the molecules on inorganic particles, particle charging mechanisms and kinetics of EPD.

Bipolar carboxyalkylphosphonic acids, such as 3PHA and 16PHA molecules (Figure 8-1(B) and (C)), containing  $\text{COOH}$  and  $\text{PO}_3\text{H}_2$  polar groups were used as dispersants for EPD. For comparison, octaPHA molecules without  $\text{COOH}$  groups (Figure 8-1D) were

used. Both COOH and PO<sub>3</sub>H<sub>2</sub> polar groups can provide adsorption of the molecules on the particle surface. However, numerous investigations showed that alkyl phosphonates and phosphonic acid bond much more strongly than carboxylic acids to a wide range of inorganic materials[2,3,6,7]. Therefore, it was hypothesized that bonding of PO<sub>3</sub>H<sub>2</sub> polar groups to metal atoms on the particle surface can provide adsorption of the bipolar molecules on the particles, whereas the dissociated of COOH groups can impart a negative charge.

## **8.2 EPD of MnO<sub>2</sub> in presence of 3PHA and 16PHA**

The analysis of pure MnO<sub>2</sub> suspension in ethanol showed poor suspension stability and EPD has not been achieved from such suspensions. The addition of 0.1–0.5 g L<sup>-1</sup> 3PHA or 16PHA to the MnO<sub>2</sub> suspensions resulted in improved suspension stability and anodic deposits were obtained from the suspensions. However, EPD of MnO<sub>2</sub> has not been achieved by the addition of 0–0.5 g L<sup>-1</sup> octaPHA. Figure 8-2 shows typical deposit mass versus time dependencies for 4 g L<sup>-1</sup> MnO<sub>2</sub> suspensions, containing 0.3 g L<sup>-1</sup> of 3PHA and 16PHA. The deposit mass increased with time, indicating film growth. The deposition rate decreased with time due to the formation of insulating deposit layer and increasing voltage drop in the deposit. As a result, no mass gain was achieved at deposition durations above 4 min for suspensions, containing 3PHA. The higher deposition yield from suspensions containing 16PHA can be attributed to improved suspension stability due to the larger size of the dispersant. It is suggested that PO<sub>3</sub>H<sub>2</sub> groups of 3PHA or 16PHA provided adsorption of the molecules on MnO<sub>2</sub> particles. The adsorption mechanism involved bi- or tri-dentate

bonding to the surface  $\text{MnO}_2$  atoms (Figure 8-1A). The dissociated  $\text{COOH}$  groups of the adsorbed molecules imparted a negative charge. Therefore, it is not surprising that EPD has not been achieved using octaPHA molecules without  $\text{COOH}$  groups. The cathodic deposition yield increased with increasing deposition time, indicating continuous film growth.

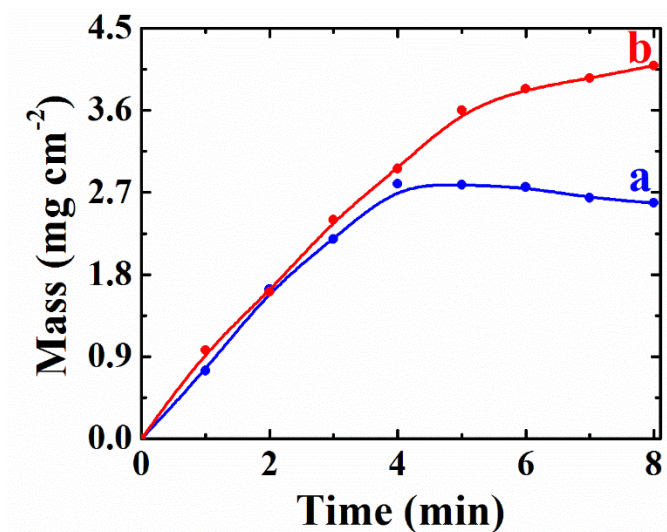


**Figure 8-2** Deposit mass versus deposition time at a deposition voltage of 20 V for (A)  $4 \text{ g L}^{-1} \text{ MnO}_2$  suspensions, containing  $0.3 \text{ g L}^{-1}$  of (a) 3PHA and (b) 16PHA.

### 8.3 Adsorption and morphology study of 3PHA and 16PHA

The adsorption of 3PHA and 16PHA on  $\text{MnO}_2$  was confirmed by FTIR analysis of the deposited material (Figure 8-3). The FTIR spectrum of 3PHA (Figure 8-3a) was in agreement with literature data[6]. The adsorptions at  $964 \text{ cm}^{-1}$  in the spectrum can be attributed to P-OH stretching vibration. The peaks at  $1108 \text{ cm}^{-1}$  indicated P=O vibration. The absorption at  $1305 \text{ cm}^{-1}$  is related to stretching vibration of C-O bond. The absorption at  $1535 \text{ cm}^{-1}$  can be attributed to asymmetric and symmetric stretching vibration of  $\text{COO}^-$

group. Figure 8-3b shows FTIR spectrum of MnO<sub>2</sub> deposited using 16PHA. The absorptions at 1041, 1135, 1308 and 1527 cm<sup>-1</sup> are attributed to P-OH, P=O, C-O, COO<sup>-</sup> vibrations[6], respectively., The peaks at 2850 and 2918 cm<sup>-1</sup> are related to  $\nu_s$ (C-H) and  $\nu_{as}$ (C-H) vibrations of long hydrocarbon chain of 16PHA , respectively.

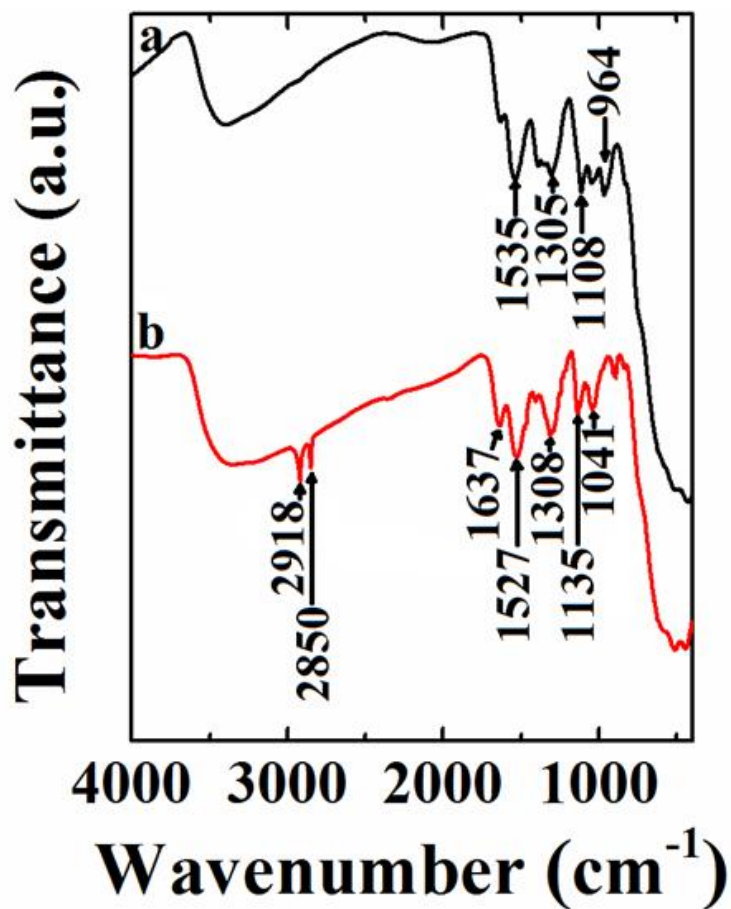


**Figure 8-3** FTIR spectra of MnO<sub>2</sub> deposits prepared using (a) 3PHA and (b) 16PHA.

The SEM images of 3PHA and 16PHA are shown in Figure 8-4(A and B). The EPD method allowed for the fabrication of porous deposits.

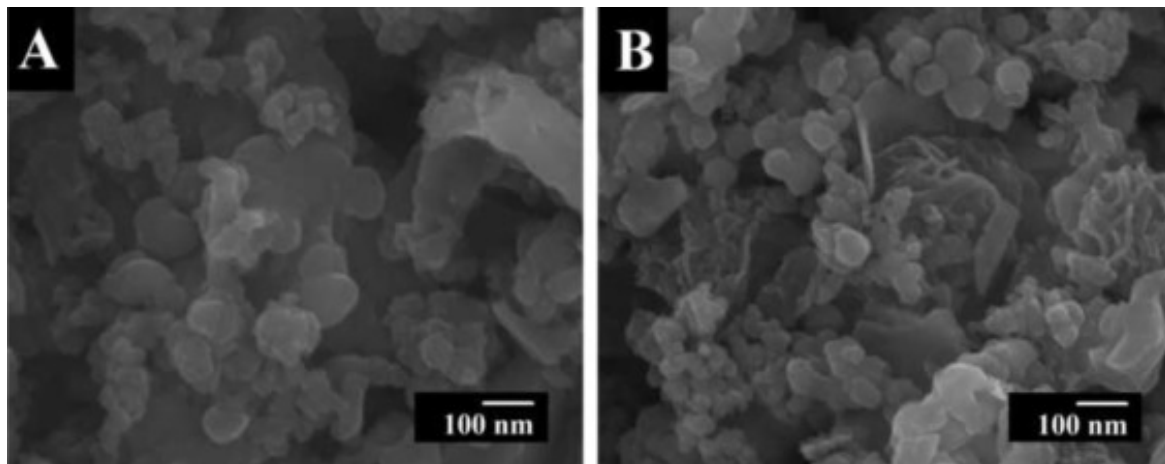


**Figure 8-4 SEM images of MnO<sub>2</sub> films, deposited from 4 g L<sup>-1</sup> MnO<sub>2</sub> suspensions, containing 0.3 g L<sup>-1</sup> of (A) 3PHA and (B) 16PHA at a deposition voltage of 20 V.**

#### **8.4 Electrochemical characterization of MnO<sub>2</sub>–MWCNT composite electrodes in presence of 3PHA and 16PHA**

The interest in MnO<sub>2</sub> is related to the high electrochemical capacitance of this material, which is currently under investigation for application in electrochemical supercapacitors[8]. EPD resulted in the formation of porous films. For the supercapacitor applications, the film porosity is beneficial for electrolyte access to electrochemically active MnO<sub>2</sub> nanoparticles. The use of 3PHA and 16PHA as dispersants allowed for the fabrication of MnO<sub>2</sub> based composites for energy storage in electrochemical supercapacitors (Figures 8-5 and 8-6).

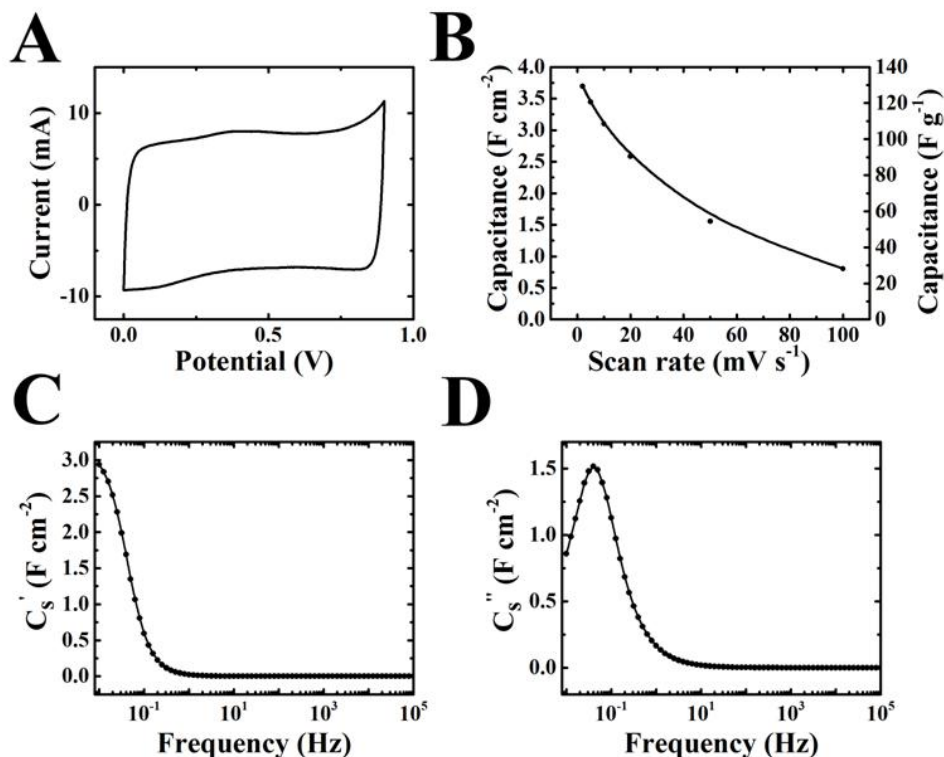


**Figure 8-5 (A) Cyclic voltammetry (CV) data at a scan rate of 2 mV s<sup>-1</sup> (B) capacitance, calculated from the CV data versus scan rate, (C) real part C'<sub>s</sub> and (D) imaginary part C''<sub>s</sub> of complex areal capacitance C<sup>\*</sup><sub>s</sub> = C'<sub>s</sub> - iC''<sub>s</sub> versus frequency, calculated from the impedance data for the MnO<sub>2</sub> electrodes, prepared using 3PHA as a dispersant and multiwalled carbon nanotubes (20 mass %) as a conductive additive, using 0.5 M Na<sub>2</sub>SO<sub>4</sub> electrolyte.**

Cyclic voltammetry data showed nearly box shape CV (Figure 8-5A,8-6A). The capacitances of electrodes, prepared using 3PHA and 16PHA, calculated from CV data decreased from 3.75 and 2.95 F cm<sup>-2</sup> to 0.98 and 0.30 F cm<sup>-2</sup>, respectively, with increasing scan rate (Figure 8-5B, 8-6B) from 2 to 100 mV s<sup>-1</sup>. It is important to note that capacitance, calculated from CV data is integral capacitance in a voltage window of 0.9 V, whereas impedance data allowed calculating a differential capacitance at AC voltage with amplitude

of 5 mV. The frequency dependence (Figure 8-5C,D, 8-6C,D) of real and imaginary components of complex capacitance showed typical relaxation type dispersion, as indicated by decrease in capacitance  $C'$  with increasing frequency and relaxation maximum in the frequency dependence of  $C''$  at 0.1 and 0.08 Hz, for electrodes, prepared using 3PHA and 16PHA, respectively. The differential capacitance at a frequency of 10 mHz was comparable with integral capacitance at a scan rate of  $2 \text{ mV s}^{-1}$ .

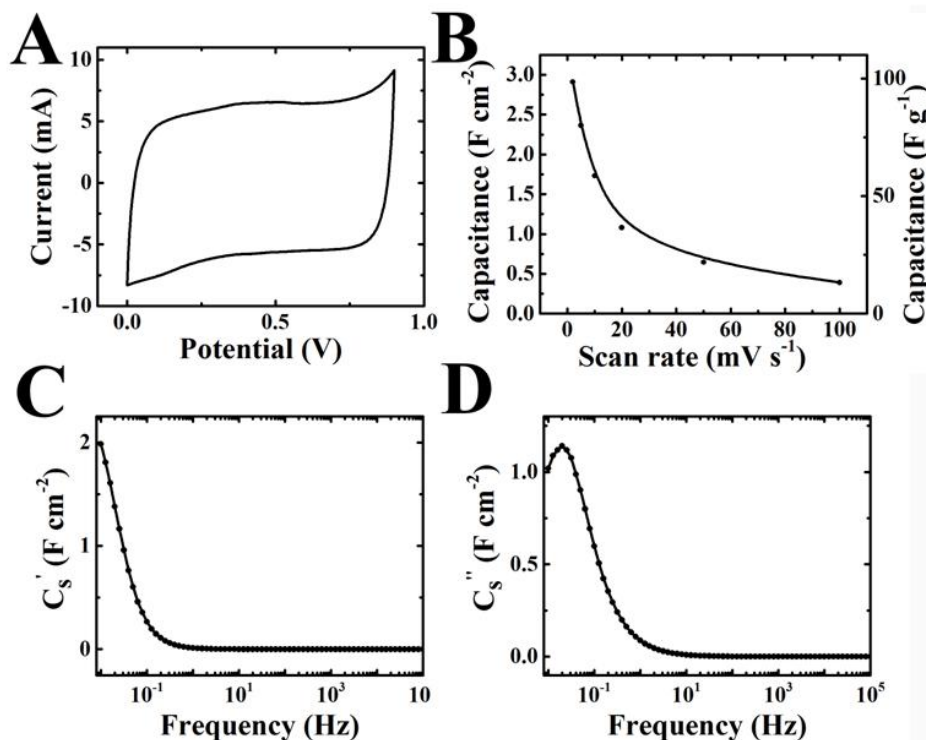


**Figure 8-6 (A) Cyclic voltammetry (CV) data at a scan rate of  $2 \text{ mV s}^{-1}$  (B) capacitance, calculated from the CV data versus scan rate, (C) real part  $C'_s$  and (D) imaginary part  $C''_s$ , of complex areal capacitance  $C_s^* = C'_s - iC''_s$  versus frequency, calculated from the impedance data for the  $\text{MnO}_2$  electrodes, prepared using 16PHA as a dispersant and multiwalled carbon nanotubes (20 mass %) as a conductive additive, using  $0.5 \text{ M Na}_2\text{SO}_4$  electrolyte.**

## 8.5 Conclusions

From the present study, it is evident that charge of inorganic particles in solutions of carboxyalkylphosphonic acids in ethanol is influenced by interactions of the acids with metal atoms on the particle surface. The strong interaction of phosphonate ligands of 3PHA and 16PHA with Mn atoms resulted in the formation of negatively charged  $\text{MnO}_2$  particles, which were dispersed in ethanol solutions and allowed for film formation by anodic EPD. The stronger steric repulsion effect of longer chained 16PHA allowed for improved dispersion and higher deposition yield. The composite electrode, prepared in presence of 3PHA showed better performance than 16PHA. The areal SCs of electrodes were achieved 3.75 and 2.95  $\text{F cm}^{-2}$  at scan rate of 2  $\text{mV s}^{-1}$  for 3PHA and 16PHA, respectively.

## References;

- [1] Ata, M. S., Liu, Y., and Zhitomirsky, I., 2014, "A Review of New Methods of Surface Chemical Modification, Dispersion and Electrophoretic Deposition of Metal Oxide Particles," *Rsc Adv.*, **4**(43), pp. 22716–22732.
- [2] Pujari, S. P., Scheres, L., Marcelis, A., and Zuilhof, H., 2014, "Covalent Surface Modification of Oxide Surfaces," *Angew. Chem. Int. Ed.*, **53**(25), pp. 6322–6356.
- [3] Boissezon, R., Muller, J., Beaugeard, V., Monge, S., and Robin, J.-J., 2014, "Organophosphonates as Anchoring Agents onto Metal Oxide-Based Materials: Synthesis and Applications," *RSC Adv.*, **4**(67), pp. 35690–35707.
- [4] Kalska-Szostko, B., Rogowska, M., and Satuła, D., 2013, "Organophosphorous Functionalization of Magnetite Nanoparticles," *Colloids Surf. B Biointerfaces*, **111**, pp. 656–662.
- [5] Li, F., Zhong, H., Zhao, G., Wang, S., and Liu, G., 2016, "Adsorption of  $\alpha$ -Hydroxyoctyl Phosphonic Acid to Ilmenite/Water Interface and Its Application in Flotation," *Colloids Surf. Physicochem. Eng. Asp.*, **490**, pp. 67–73.
- [6] Zhang, B., Kong, T., Xu, W., Su, R., Gao, Y., and Cheng, G., 2010, "Surface Functionalization of Zinc Oxide by Carboxyalkylphosphonic Acid Self-Assembled Monolayers," *Langmuir*, **26**(6), pp. 4514–4522.
- [7] Pawsey, S., Yach, K., and Reven, L., 2002, "Self-Assembly of Carboxyalkylphosphonic Acids on Metal Oxide Powders," *Langmuir*, **18**(13), pp. 5205–5212.
- [8] Cheong, M., and Zhitomirsky, I., 2009, "Electrophoretic Deposition of Manganese Oxide Films," *Surf. Eng.*, **25**(5), pp. 346–352.

## **Chapter 9 Electrostatic assembly of composite supercapacitor electrodes, triggered by charged dispersants**

### **9.1 Electrostatic heterocoagulation in non-aqueous solvent**

The development of composites, containing conductive additives, increased the efficiency of MnO<sub>2</sub> electrodes[1,2]. Carbon nanotubes (CNT) are popular for application as conductive additives[1,3] due to their high conductivity and low percolation limit. The important task is the design of MnO<sub>2</sub>-CNT composites with good dispersion and mixing of individual components. Many strategies in the dispersion of CNT are based on the chemical functionalization methods[4,5], which result in degradation of CNT microstructure and properties.

The goal of this investigation is the development of advanced methods for the fabrication of MnO<sub>2</sub>-MWCNT electrodes. Good mixing of the individual components was achieved by the use of negatively charged MnO<sub>2</sub> nanoparticles and positively charged MWCNT and their electrostatic heterocoagulation. Our studies have been motivated by the need to enhance the performance of electrodes at high charge-discharge rates and high active mass loadings. The electrostatic heterocoagulation technique was based on the use of advanced dispersants. The dispersant molecules used for MnO<sub>2</sub> have chelating functional groups, which allow their strong adsorption on the particle surface. We demonstrate efficient dispersion of pristine MWCNT using small aromatic dispersant molecules. The dispersion

is achieved in ethanol solvent, allowing the dissolution of water insoluble binder, which is critical for the fabrication of aqueous devices. We used negatively charged dispersants, 6-Phosphonohexanoic acid (PHA), Pyrogallol red (PGR), and 2,6-Pyridinedicarboxylic acid (PCA) for MnO<sub>2</sub> with selective adsorption (Figure 9-1A-C) and positively charged dispersants, Azure A chloride (AZA) and Nile Blue chloride (NB), for MWCNT. The chemical structures of the dispersants are shown in Figure9-1(D, E).

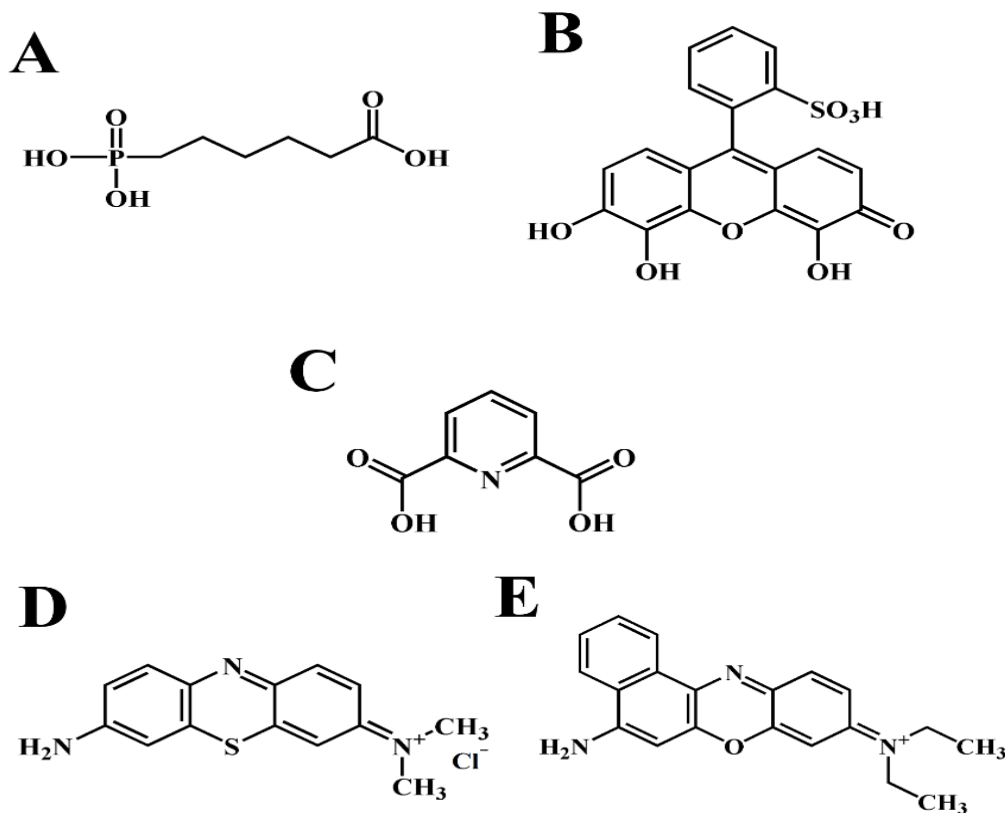


**Figure 9-1 Chemical structures of (A) PHA, (B) PGR, (C) PCA, (D) AZA and (E) NB**

Due to chelating properties and negative electric charge, PGR, PCA, and PHA were used as dispersants for MnO<sub>2</sub>. The molecules contain different functional groups, which can

provide their adsorption on the  $\text{MnO}_2$  particles. The structure of the functional groups is important for the adsorption of the molecules on the particle surface. As described in the literature[6], monodentate ligands have relatively weak bonding properties; however, polydentate ligands have significantly stronger bonding properties. Therefore, we selected PGR, PCA and PHA molecules which offer the advantage of polydentate bonding.

PGR belongs to the catechol family of organic molecules, which are among the most intriguing building blocks[6] in colloidal technology. The adsorption of PHA on particles can involve phosphonate or carboxylate groups. However, the analysis of literature[7–11] indicates that bonding of phosphonates to a wide range of inorganic materials is much stronger than bonding of carboxylates. The phosphonates show strong adsorption in water on various inorganic materials[7,9,11–15], such as in hydroxyapatite,  $\text{Fe}_3\text{O}_4$ , clay, calcium carbonate, indium tin oxide,  $\text{SiO}_2$ ,  $\text{ZnO}$ ,  $\text{Al}_2\text{O}_3$  and  $\text{TiO}_2$ . However, the adsorption of organic molecules on inorganic surfaces is influenced by the nature of a solvent. The oxygen atoms of the phosphonate ligand allow for bi- or tri-dentate bonding (Figure 9-2A-D). The chelation bonding (Figure 9-2A,C) involves the formation of the coordination bonds between two or three oxygen atoms of PHA and a metal atom on the particle surface. The oxygen atoms of the phosphonate ligand can also be bonded to different metal atoms on the particle surface (Figure 9-2B,D).

Pyrogallol red belongs to the catechol family of materials, containing two OH groups bonded to adjacent carbon atoms of the aromatic rings. It is known that catechol is a powerful complexing agent, which allows high bonding strength[16]. Similar to other molecules of the catechol family, PGR[6,17] can be adsorbed on inorganic surfaces by

bidentate chelating bonding (Figure 9-2E) or bidentate bridging bonding (Figure 9-2F) mechanisms.

PCA is another promising molecule for application as a dispersant in the colloidal nanotechnology. It is known that PCA strongly chelates heavy metals to form anionic complexes[18–22]. Therefore, PCA adsorption on inorganic particles can be expected. Taking into account the literature data[18–22] on the structure of PCA-metal ion complexes, the adsorption mechanism shown in the Figure 9-2G can be suggested for the PCA adsorption on inorganic particles.

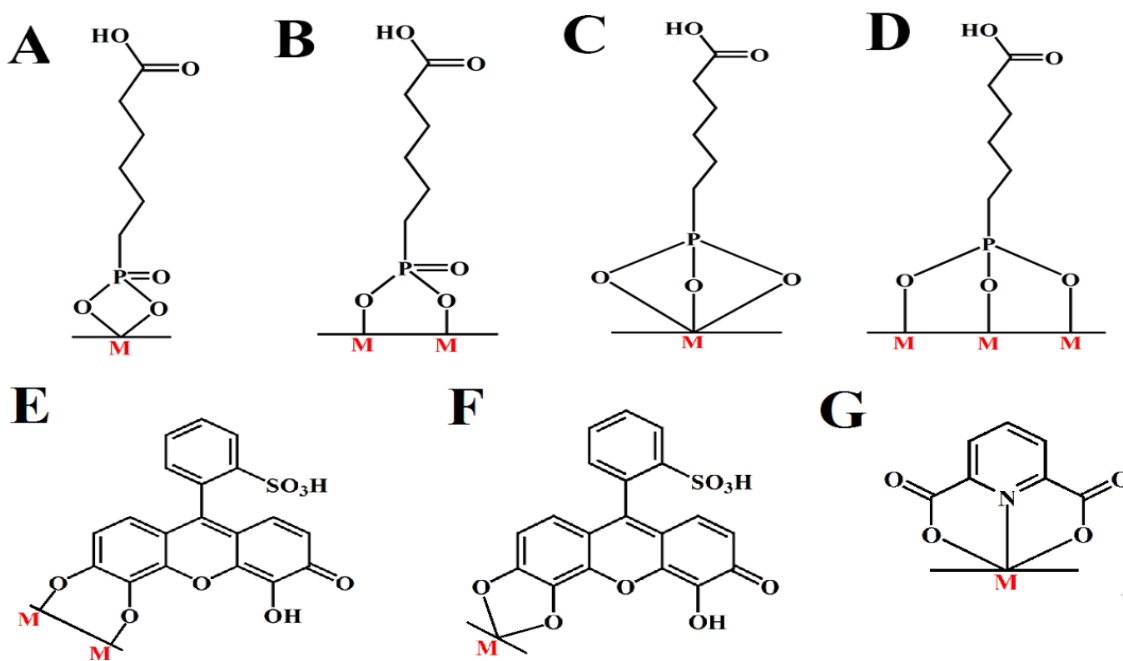


**Figure 9-2 Bonding mechanisms of (A-D) PHA, (E, D) PGR, and (G) PCA, involving Mn atoms (M) on the particle surface.**

## 9.2 EPD of $\text{MnO}_2$ using PHA, PGR and PCA as dispersants

The suspensions of MD particles in ethanol were unstable, and no EPD was achieved from such suspensions. The PHA, PGR and PCA adsorption allowed improved dispersion.

The analysis of  $\text{MnO}_2$  suspensions in ethanol revealed strong PHA, PGR, and PCA adsorption on  $\text{MnO}_2$  particles. The suspensions of  $\text{MnO}_2$ , prepared without dispersants showed poor colloidal stability. In contrast, the addition of dispersant agents allowed the formation of stable suspensions (Figure 9-3). The sedimentation tests indicated that PHA, PGR and PCA adsorbed on  $\text{MnO}_2$  particles and allowed for electrostatic dispersion. The suggested bonding mechanisms are presented in Figure 2. The PCA and PHA adsorption was also confirmed in EPD experiments.

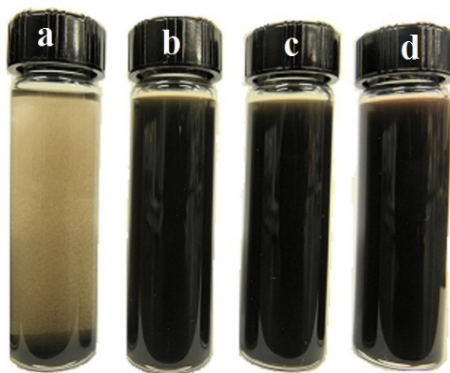


**Figure 9-3 Comparison of suspension stability of (a) without dispersant, (b) PHA, (c) PGR, and (d) PCA in  $4 \text{ g L}^{-1} \text{ MnO}_2$  suspension with  $0.2 \text{ g L}^{-1}$  additive concentration after 3 days.**

The increase in PCA and PHA concentration in the suspension in the range of  $0\text{-}0.2 \text{ g L}^{-1}$  resulted in increasing anodic deposition yield (Figure 9-4 A, C). The formation of anodic deposits indicated that PCA and PHA adsorbed on the  $\text{MnO}_2$  particles and imparted a

negative charge to the particles, thus allowing for their EPD. The increase in the PCA and PHA concentration in the suspension resulted in increasing adsorption of the charged dispersants on particles and allowed the corresponding raise of the deposition yield. It is important to note that relatively high deposition yield (Figure 9-4) was achieved at low dispersant concentrations, indicating efficient adsorption of the dispersant molecules on the MnO<sub>2</sub> particles. The reduction in the deposition yield at PCA and PHA concentrations above ~0.2 g L<sup>-1</sup> resulted from increasing the ionic strength of the suspensions, which according to the Derjaguin - Landau - Verwey - Overbeek (DLVO) theory results in reduced colloidal stability and lower deposition yield[23]. The anodic deposition was performed at a deposition voltage of 20 V and deposition time of 5 min. Similar results were achieved by using PGR as a dispersing agent. The addition of PGR to the suspensions resulted in improved suspension stability and allowed film formation by EPD. The previous investigations[17] showed that PGR adsorbed on MnO<sub>2</sub> and allowed for good dispersion of MnO<sub>2</sub> in ethanol. Anodic films were obtained at a deposition voltage of 50 V and PGR concentrations above 0.2 g L<sup>-1</sup>. The deposition yield measurements showed a rapid increase in the film mass with increasing PGR concentration in the range of 0.3–0.5 g L<sup>-1</sup> (Figure 9-4 B).

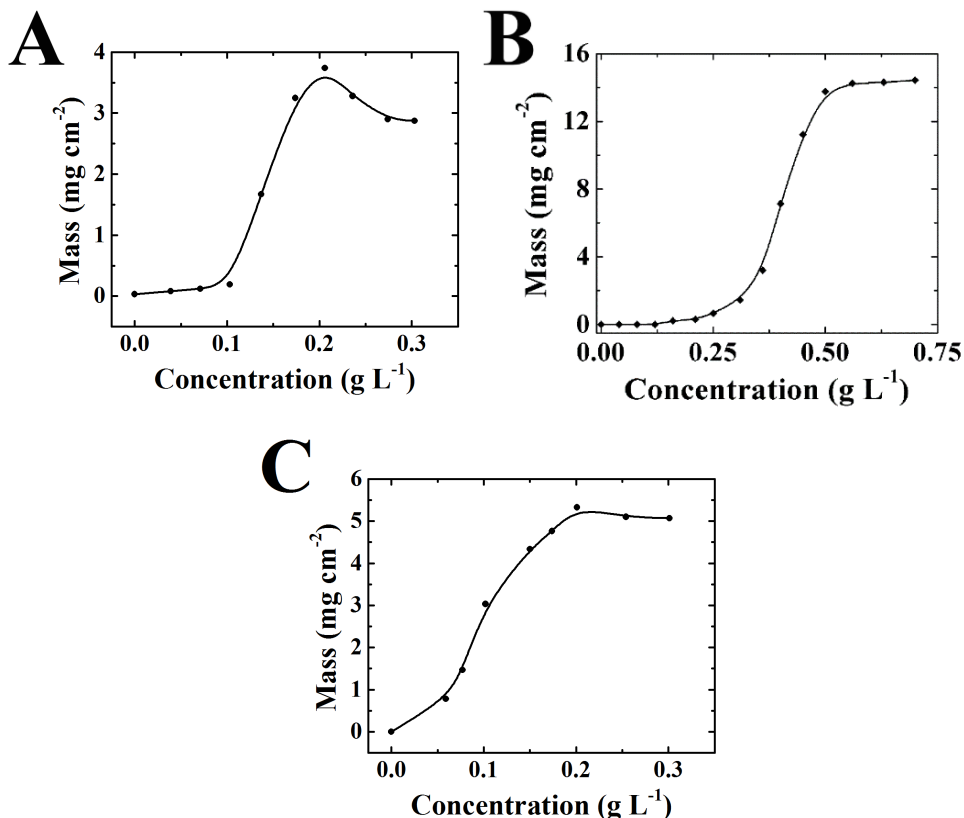


**Figure 9-4 Deposit mass as a function of the concentration of (A) PHA and (C) PCA in 4 g L<sup>-1</sup> MnO<sub>2</sub> at a deposition voltage of 20 V and (B) PGR 10 g L<sup>-1</sup> MnO<sub>2</sub> suspension at a deposition voltage of 50 V and deposition time of 5 min.**

The adsorption of PGR on MnO<sub>2</sub> was confirmed by FTIR analysis of the deposited material[17].

The FTIR studies of the deposits revealed the adsorption of PHA, PGR and PCA on the particle surface. The FTIR spectrum (Figure 9-5a) of the MD deposit prepared from the suspension containing PHA showed peaks attributed[12,15] to CO<sub>2</sub><sup>-</sup> stretching at 1630, 1539, and 1402 cm<sup>-1</sup> and P=O stretching at 1076 cm<sup>-1</sup>.

The main bands and their assignments for different vibrations of adsorbed PGR were as follows[24–28]: C–C ring vibrations at 1629, 1550 and 1412  $\text{cm}^{-1}$ ; C–O stretching at 1344 and 1227  $\text{cm}^{-1}$ ; bending vibrations of C–OH groups at 1189  $\text{cm}^{-1}$ ; C–H in-plane bending at 1142  $\text{cm}^{-1}$ ; and asymmetric and symmetric vibrations of  $\text{SO}_3^-$  at 1090 and 1021  $\text{cm}^{-1}$ . The adsorbed PCA showed (Figure 9-5c) peaks attributed[28–30] to (C–C)/ (C=C) and (C–N)/ (N=C) stretching at 1589, 1570, 1441, 1396  $\text{cm}^{-1}$ , C=O stretching at 1375  $\text{cm}^{-1}$ , C–O stretching at 1279  $\text{cm}^{-1}$ , C–OH deformation vibration at 1192  $\text{cm}^{-1}$ , C-H bending at 1084 and 1017  $\text{cm}^{-1}$ . The absorption assignments summarized in Table 9-1.

**Table 9-1 Band Assignments for  $\text{MnO}_2$  deposits obtained using PHA, PGR and PCA**

| PHA ( $\text{cm}^{-1}$ ) | PGR ( $\text{cm}^{-1}$ ) | PCA ( $\text{cm}^{-1}$ ) | Band Assignment                      |
|--------------------------|--------------------------|--------------------------|--------------------------------------|
| 1630, 1539, 1402         | –                        | –                        | $\text{CO}_2^-$ stretching           |
| 1076                     | –                        | –                        | P=O stretching                       |
| –                        | 1629, 1550, 1412         | 1589                     | C-C stretching                       |
| –                        | –                        | 1570, 1441 and 1396      | C=C, C-N and N=C stretching          |
| –                        | –                        | 1375                     | C=O stretching                       |
| –                        | 1344, 1227               | 1279                     | C-O stretching                       |
| –                        | 1189                     | 1192                     | C-OH bending vibration               |
| –                        | 1142                     | 1084, 1017               | C-H bending                          |
| –                        | 1090                     | –                        | $\text{SO}_3^-$ asymmetric vibration |
| –                        | 1021                     | –                        | $\text{SO}_3^-$ symmetric vibration  |

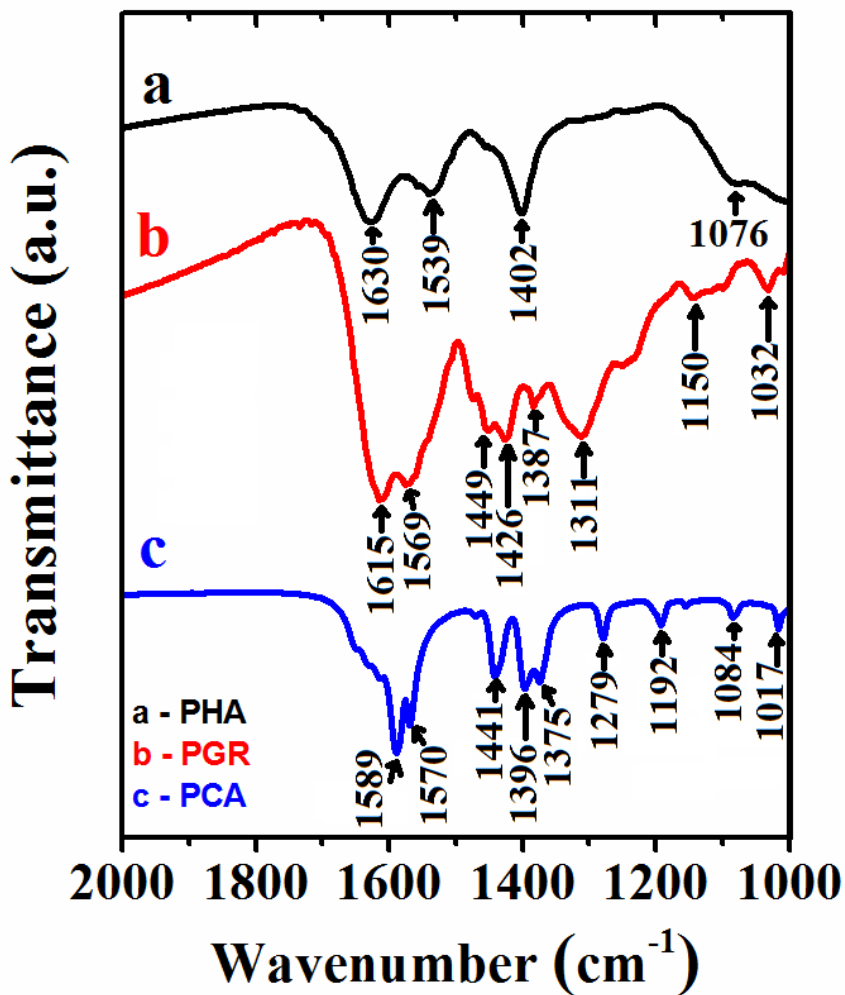


Figure 9-5 FTIR spectra for MnO<sub>2</sub> particles, deposited by EPD using (a) PHA, (b) PGR and (c) PCA.

### 9.3 Electrochemical characterization of deposited films

The MWCNT suspensions, containing PGR, PCA and PHA were unstable due to poor adsorption of the molecules on the MWCNT. On the other hand, AZA and NB (Figure 9-1 D, E) allowed for the formation of stable MWCNT suspension in ethanol. It must be noted

that various dispersants for MWCNT, such as polyelectrolytes, surfactants and commercial bile acids provide MWCNT dispersion in water[4,31,32]. However, limited progress has been achieved in MWCNT dispersion in simple alcohols, such as ethanol. The ability to disperse MWCNT in ethanol is important for the fabrication of electrodes, containing water insoluble binders for application in aqueous supercapacitors. The use of ethanol slurries, containing dissolved PVB binder and well dispersed MWCNT was of critical importance for electrode fabrication. It is suggested that the adsorption of aromatic AZA and NB molecules on MWCNT involved  $\pi$ - $\pi$  interactions. Previous investigations showed AZA and NB adsorption on CNT in water[33,34]. The adsorbed AZA and NB were used as redox charge transfer mediators for application in sensors[33,34]. The small size of the adsorbed dispersants is important for MWCNT applications, based on the conductive properties of MWCNT. EPD experiments confirmed that MWCNT were positively charged in ethanol and accumulated at the cathode surface during deposition. However, detailed analysis of deposition yield at different conditions presented difficulties due to poor adhesion of MWCNT to the metallic substrates.

The use of dispersions of positively charged  $\text{MnO}_2$  particles and dispersions of negatively charged MWCNT allowed for their improved mixing and formation of composites by an electrostatic assembly. As a result, significant improvement in electrochemical performance of the  $\text{MnO}_2$ -MWCNT electrodes was observed. Fig. 5-6A-C compares CVs at different scan rates for  $\text{MnO}_2$ -MWCNT electrodes prepared without dispersants and prepared using PGR as a dispersant for  $\text{MnO}_2$  and AZA or NB as dispersants for MWCNT. The comparison of the CV data at different scan rates indicated a significant increase in the

CV areas and higher capacitance of the composites, prepared by the electrostatic assembly methods. Nearly box shape CVs (Figure 9-6B, C) indicated good capacitive behavior in a voltage window of 0.9 V. The capacitance of the electrodes, prepared without dispersant was  $1.01 \text{ F cm}^{-2}$  at a scan rate of  $2 \text{ mV s}^{-1}$ . The capacitance reduced to the value of  $0.43 \text{ F cm}^{-2}$  at a scan rate of  $100 \text{ mV s}^{-1}$ . The electrodes, prepared using PGR and AZA or NB showed significantly higher capacitances (Table 5-2), especially at a scan rate of  $100 \text{ mV s}^{-1}$ . Moreover, the electrodes, prepared using dispersants showed significant improvement in capacitance retention in the scan rate range of 2-100  $\text{mV s}^{-1}$ . The enhanced capacitive performance indicates better utilization of the active material, which is especially evident at high scan rates.

**Table 9-2 Capacitances, calculated from CV data at scan rates of 2 and 100  $\text{mV s}^{-1}$  and capacitance retention in the scan rate range of 2-100  $\text{mV s}^{-1}$  for  $\text{MnO}_2$  –MWCNT electrodes, prepared without and with different dispersants.**

| Dispersants    |       | $C_S$ at $2 \text{ mV s}^{-1}$<br>$\text{F cm}^{-2}$ | $C_S$ at $100 \text{ mV s}^{-1}$<br>$\text{F cm}^{-2}$ | Capacitance<br>retention, % |
|----------------|-------|--|--|-----------------------------|
| $\text{MnO}_2$ | MWCNT |  |  |                             |
| -              | -     | 1.01   | 0.43   | 42.6                        |
| PGR            | AZA   | 3.18   | 2.38   | 74.8                        |
| PGR            | NB    | 3.12   | 2.02   | 64.7                        |
| PCA            | AZA   | 2.95   | 1.68   | 56.9                        |
| PCA            | NB    | 2.99   | 2.02   | 67.6                        |
| PHA            | AZA   | 3.04   | 1.82   | 59.9                        |
| PHA            | NB    | 3.23   | 2.39   | 74.0                        |

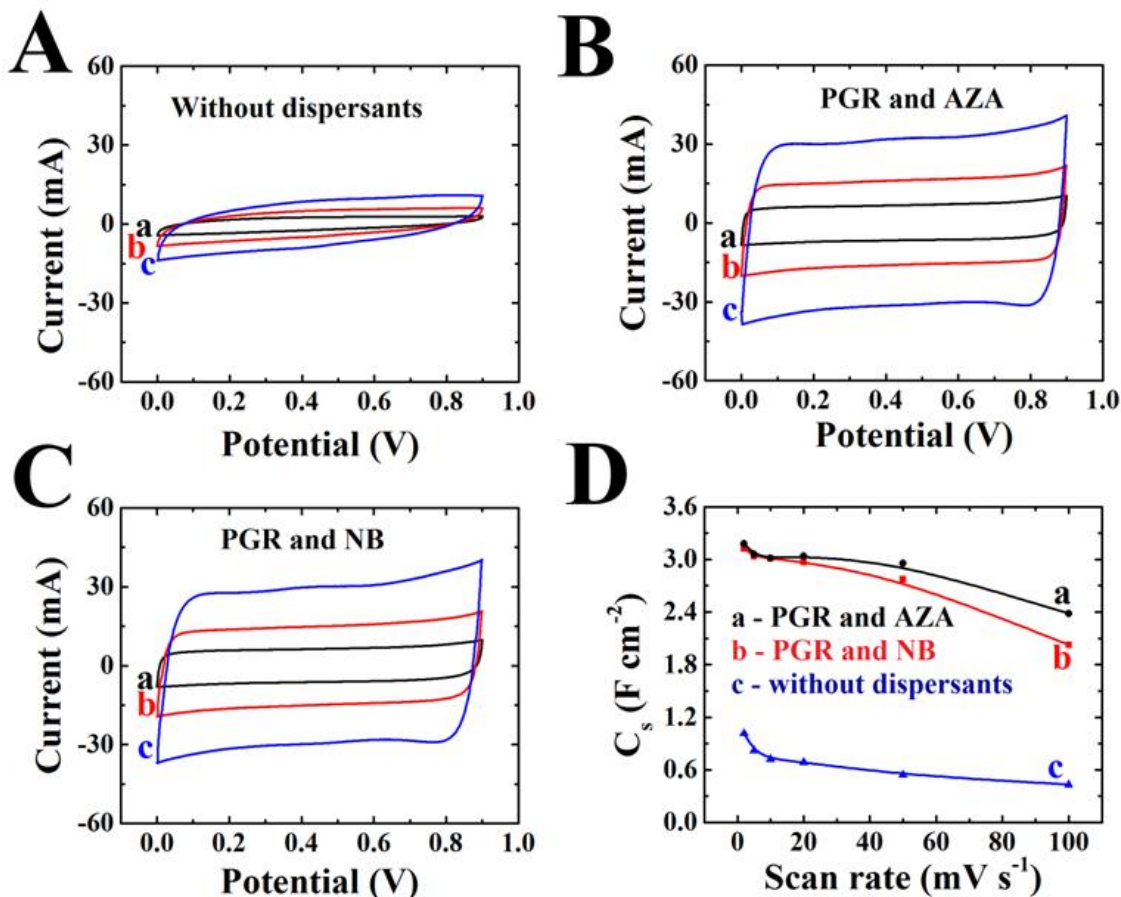


**Figure 9-6 (A,B,C) CVs for  $MnO_2$ -MWCNT electrodes prepared (A) without dispersant, (B) using PGR and AZA, (C) using PGR and NB at scan rates of (a) 2, (b) 5 and (c)  $10\ mV\ s^{-1}$  and (D) SC versus scan rate for electrodes prepared using (a) PGR and AZA, (b) PGR and NB**

The analysis of complex impedance data, presented in the Nyquist plot (Figure 9-7A) showed significantly lower resistance  $R=Z'$  of the electrodes, prepared using dispersants, compared to the electrodes, prepared without dispersants. The lower imaginary part of impedance  $Z''$  of the electrodes, prepared in the presence of dispersants, indicated higher capacitance. The slopes of the Nyquist plots for the electrodes, prepared using dispersants were close to  $90^\circ$ , indicating good capacitive behavior. The components of complex

capacitance, calculated from the impedance data, were presented as the function of frequency in the Figure 9-7B,C.

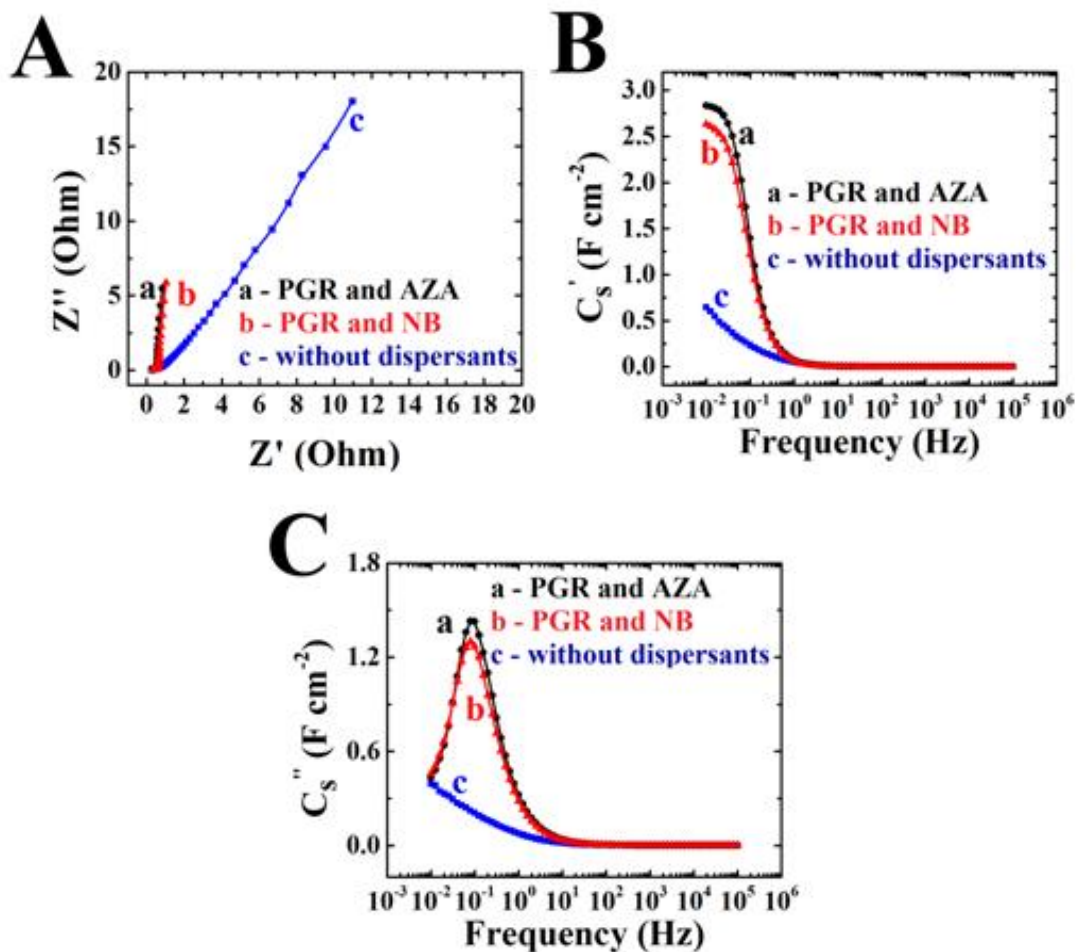


**Figure 9-7 (A) Nyquist plot for complex impedance and frequency dependences of (B)  $C_s'$  and (C)  $C_s''$  for  $MnO_2$ -MWCNT electrodes prepared using (a) PGR and AZA, (b) PGR and NB and (c) without dispersants.**

The electrodes prepared using dispersants showed relaxation type dispersions[35], as indicated by the reduction in real part of capacitance  $C_s'$  with frequency and corresponding relaxation maxima in the frequency dependences of the imaginary parts  $C_s''$ . The relatively

high relaxation frequencies, corresponding to  $C_s''$  maxima indicated good performance at relatively high charge-discharge rates. The electrodes, prepared without dispersants showed significantly lower  $C_s'$ , the relaxation maximum has not been observed at frequencies above 10 mHz.

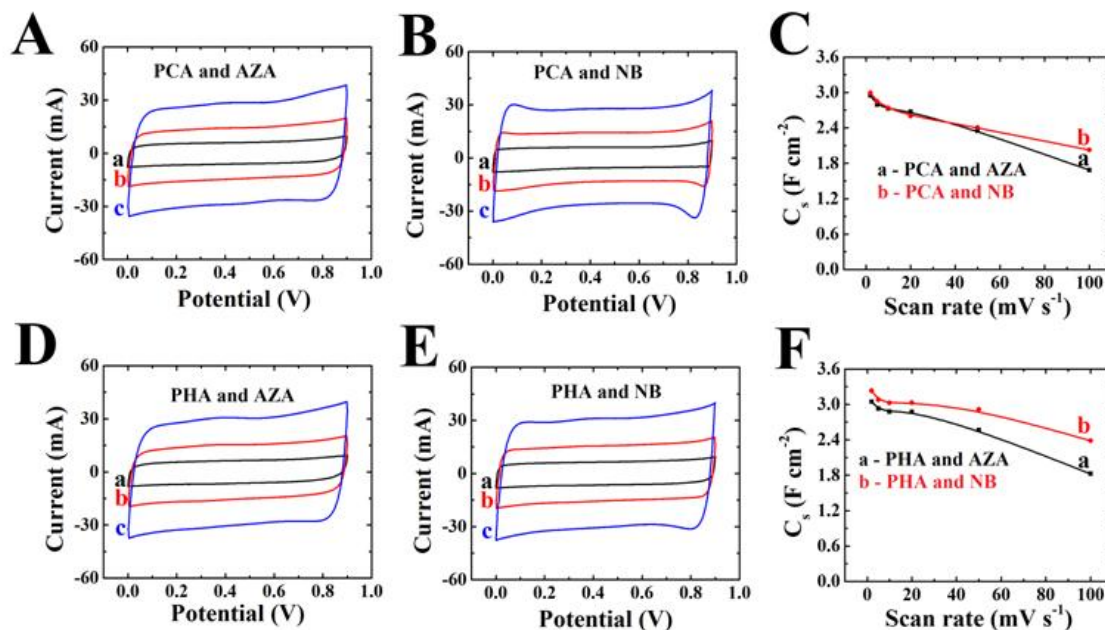


**Figure 9-8 (A,B,D,E) CVs at scan rates of (a) 2, (b) 5 and (c) 10 mV s<sup>-1</sup> and (C,F)  $C_s$  versus scan rate dependences for MnO<sub>2</sub>-MWCNT electrodes prepared using (A), (C(a)) PCA and AZA, (B), (C(b)) PCA and NB; (D), (F(a)) PHA and AZA and (E), (F(b)) PHA and NB.**

The electrodes, prepared using PCA or PHA dispersants for MnO<sub>2</sub> and AZA or NB for MWCNT showed larger CV areas (Figure 9-8) and higher capacitances (Figure 9-8, Table 1), compared to the electrodes prepared without dispersants (Figure 9-6). Moreover, the electrodes, prepared using PCA and PHA showed good capacitance retention. The highest capacitance was achieved using PHA and NB dispersants.

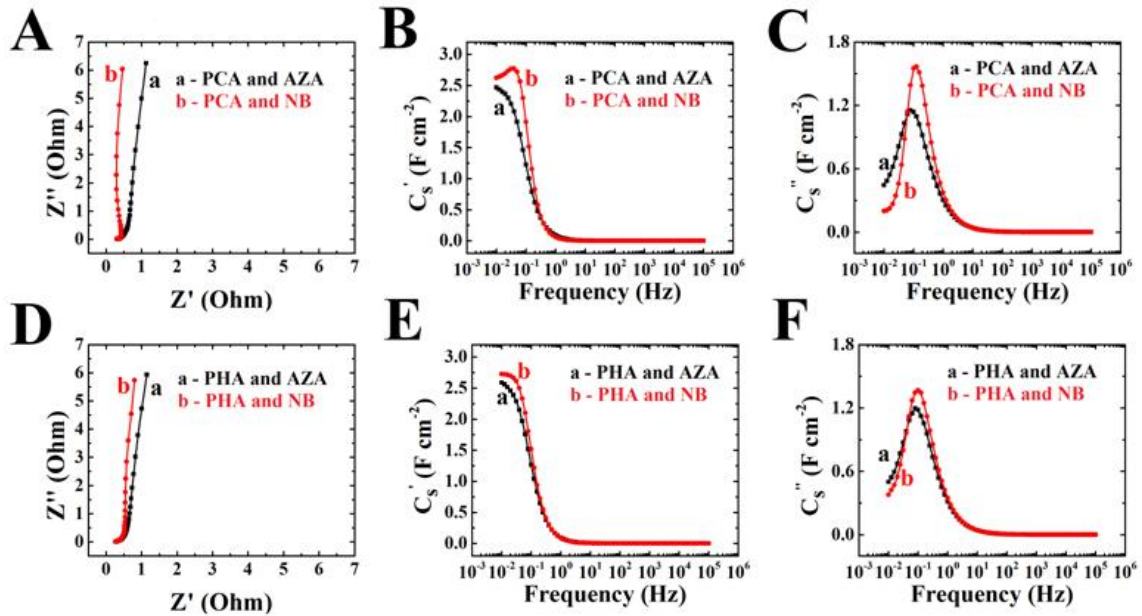


**Figure 9-9 (A,D) Nyquist plots of complex impedance; frequency dependences of (B,E)  $C_s'$  and (C,F)  $C_s''$  for  $MnO_2$ -MWCNT electrodes, prepared using (A(a)), (B(a)) and (C(a)) PCA and AZA, (A(b)), (B(b)) and (C(b)) PCA and NB, (D(a)), (E(a)) and (F(a)) PHA and AZA, (D(b)), (E(b)) and (F(b)) PHA and NB.**

The Nyquist plots of electrochemical impedance showed significantly lower resistance (Figure 9-9), compared to the resistance of electrodes, prepared without dispersants (Figure 9-7). The slopes of the  $Z''$  versus  $Z'$  curves were close to  $90^\circ$ , indicating good capacitive behavior. The frequency dependences of the components of complex capacitance showed relaxation type dispersions, with well-defined relaxation maxima in the frequency dependence of  $C_s''$ . The low frequency values of  $C_s'$  were significantly higher, compared to the corresponding data for electrodes, prepared without dispersants. At low frequencies, the differential capacitances  $C_s''$ , calculated from the impedance data at low voltages, were

comparable with the corresponding integral capacitances  $C_s$ , obtained from the CV data at low scan rates in the voltage window of 0.9 V.

Several additional observations are noteworthy from Figures 5-6 and 5-8. The presented results indicate that relatively high areal capacitance can be achieved at a scan rate of  $100 \text{ mV s}^{-1}$  and active mass loading of  $23.8 \text{ mg cm}^{-2}$ . The high areal capacitance at high charge-discharge rates is of critical importance for practical applications of supercapacitor devices. The previous investigations[36] showed that improved areal capacitance at low scan rates can be achieved using co-dispersants for  $\text{MnO}_2$  and MWCNT. However, the method resulted in poor capacitance retention at high scan rates. The areal capacitance[36] at  $100 \text{ mV s}^{-1}$  for active mass loading of  $40 \text{ mg cm}^{-2}$  was  $\sim 1 \text{ F cm}^{-2}$ . In contrast, the electrodes prepared using electrostatic assembly method, using PHA and NB showed a capacitance of  $2.39 \text{ F cm}^{-2}$  at significantly lower active mass loading.

#### **9.4 Morphology of composite electrodes before and after cycling tests**

The comparison of the SEM images of the electrodes, prepared with and without dispersants (Figure 9-10B,C) showed that the use of dispersants resulted in improved dispersion of MWCNT in the  $\text{MnO}_2$  matrix and reduced agglomeration of  $\text{MnO}_2$  and MWCNT, which allowed for higher capacitance and lower resistance.

Figure 9-11 shows that the electrodes exhibited a capacitance retention of 92% after 1000 charge-discharge cycles, the material microstructure and crystallinity were practically unaffected by cycling (Figures 5-10C,D and 5-12a,b). The electrodes, prepared using PHA

and NB, were used for the fabrication of asymmetric devices, containing  $\text{MnO}_2$ -MWCNT positive electrodes and AC-CB negative electrodes.

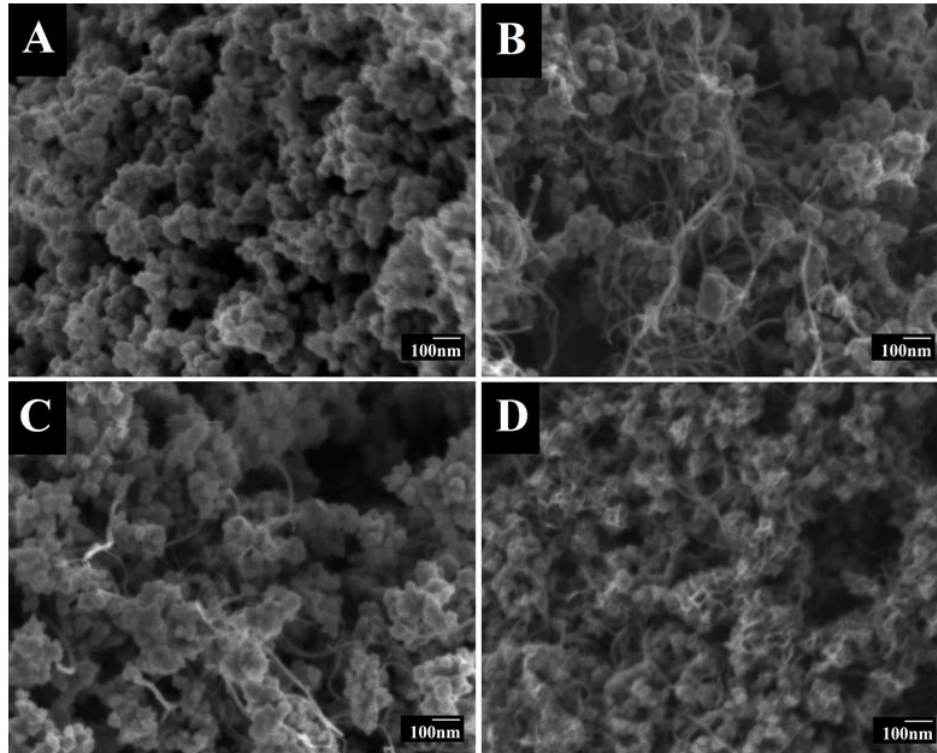


**Figure 9-10 SEM images of (A)  $\text{MnO}_2$  powder, (B)  $\text{MnO}_2$ -MWCNT composite prepared without dispersants, (C)  $\text{MnO}_2$ -MWCNT composite prepared using PHA and NB dispersants before electrochemical cycling, (D)  $\text{MnO}_2$ -MWCNT composite prepared using PHA and NB dispersants after 1000 cycles**

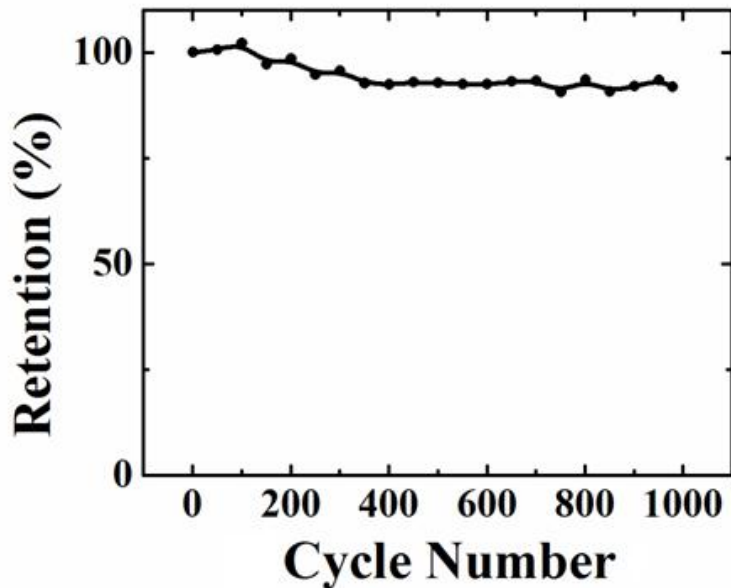


Figure 9-11 Capacitance retention versus cycle number at a scan rate of  $50 \text{ mV s}^{-1}$  for  $\text{MnO}_2$ -MWCNT electrodes, prepared using PHA and NB dispersants.

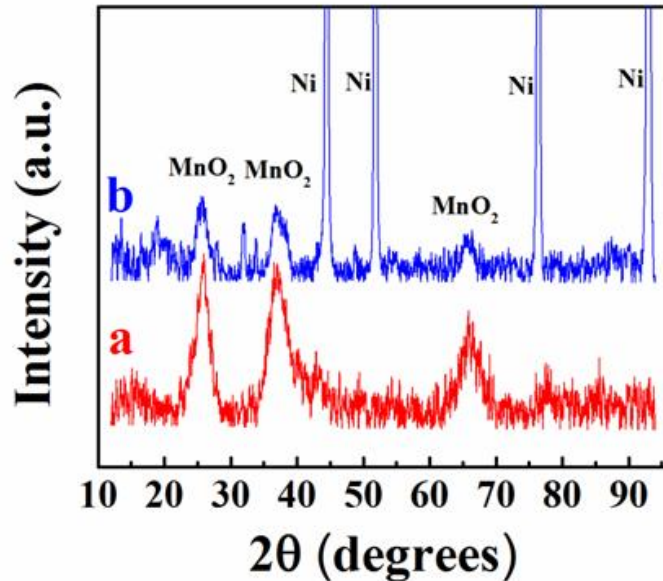


Figure 9-12 X-ray diffraction patterns of (a) as-prepared  $\text{MnO}_2$  powder and (b)  $\text{MnO}_2$ -MWCNT electrode, prepared using PHA and NB dispersants and Ni current collector, after 1000 cycles.

## 9.5 Electrochemical characterization of asymmetric device

The electrodes, prepared using PHA and NB, were used for the fabrication of asymmetric devices, containing MnO<sub>2</sub>-MWCNT positive electrodes and AC-CB negative electrodes.

The testing results for the coin cell asymmetric device, containing MnO<sub>2</sub>-MWCNT positive electrodes and AC-CB negative electrodes are presented in Figure 9-13. Nearly box shape CVs and nearly linear galvanostatic charge-discharge curves indicated good capacitive behavior in the voltage window of 1.6 V. The decrease in capacitance with increasing scan rate can result from diffusion limitations in pores of active materials. The asymmetric device showed relatively low impedance (Figure 9-11) and relaxation type dispersion of complex capacitance. The low frequency capacitance, calculated from the impedance data was comparable with capacitance, calculated from the CV data at low scan rates.

The device showed a capacitance retention of 82% after 5000 charge-discharge cycles (Figure 9-15). The supercapacitor devices were used for powering of LED bulbs (Figure 9-16). The results presented above indicated that considerable further advances in the development of asymmetric devices require improvement in the performance of the negative electrodes[37,38]. The capacitance and capacitance retention of the negative AC-CB electrodes must be increased in order to match the progress in the development of positive MnO<sub>2</sub>-MWCNT electrodes.

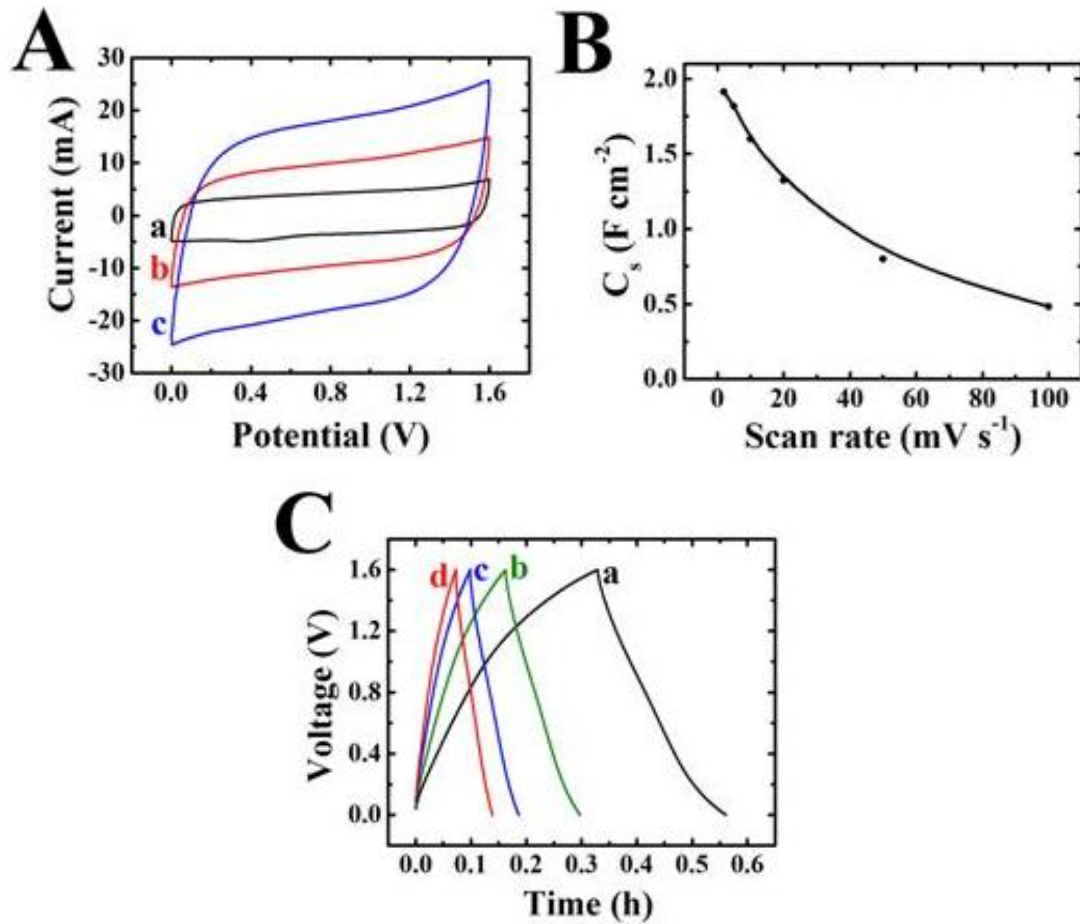


Figure 9-13 (A) CVs at scan rates of (a) 2, (b) 5 and (c) 10 mV s<sup>-1</sup>, (B) capacitance versus scan rate and (C) galvanostatic charge-discharge curves at currents at (a) 3, (b) 5, (c) 7.5 and (d) 10 mA for asymmetric coin cell capacitors, containing MnO<sub>2</sub>-MWCNT positive and AC-CB negative electrodes.

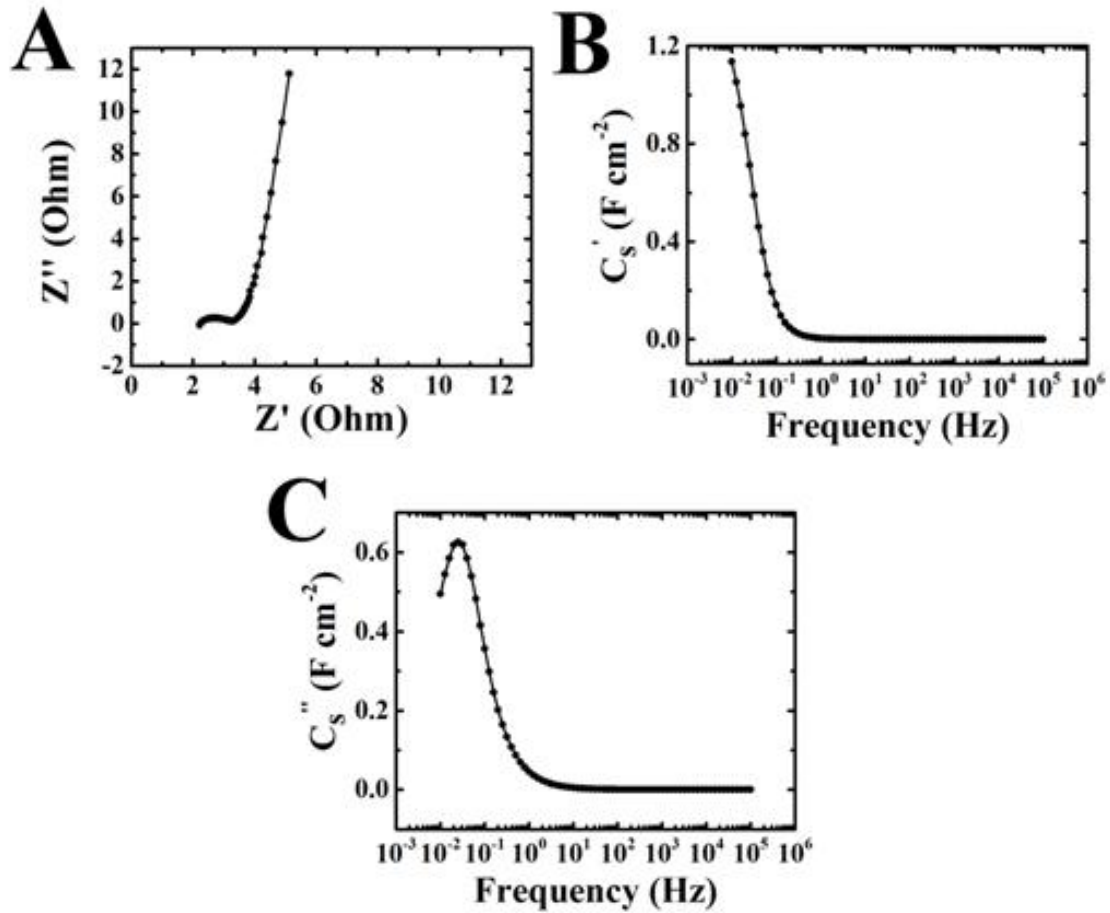
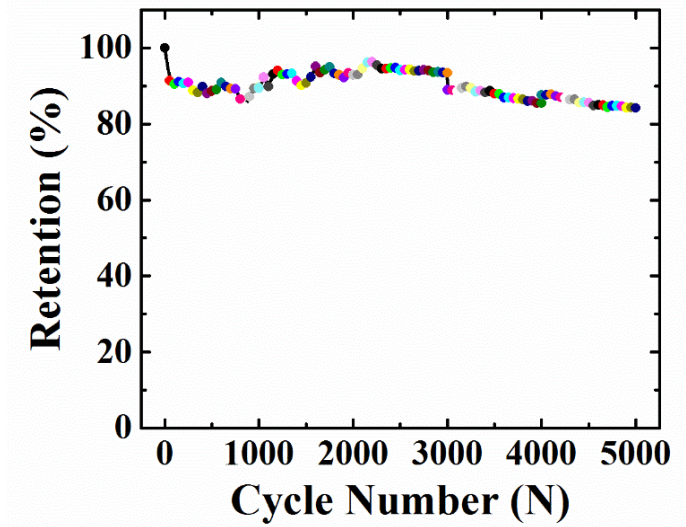


Figure 9-14 (A) Nyquist plot of complex impedance and (B,C) frequency dependences of components of complex capacitance: (B)  $C_s'$  and (C)  $C_s''$  for asymmetric coin cell capacitors, containing  $MnO_2$ -MWCNT positive and AC-CB negative electrodes.



**Figure 9-15** Capacitance retention versus cycle number at a scan rate of  $50 \text{ mV s}^{-1}$  for asymmetric capacitor cell containing  $\text{MnO}_2$ -MWCNT positive and AC-CB negative electrode.



**Figure 9-16** LED bulbs powered by supercapacitor devices.

## 9.6 Conclusion

MnO<sub>2</sub> was successfully dispersed in ethanol by using anionic PGR, PCA and PHA dispersants. The efficient dispersion was achieved at relatively low dispersant concentrations due to strong adsorption of the dispersants on the particle surface, which involved the polydentate bonding. We found the possibility of efficient dispersion of MWCNT in ethanol using AZA and NB, which imparted a negative charge to MWCNT. The electrostatic assembly method offers the benefit of improved mixing of MnO<sub>2</sub> and MWCNT. Various electrostatic assembly strategies based on the use of different anionic and cationic dispersants allowed the fabrication of electrodes with enhanced capacitance and improved capacitance retention at high charge–discharge rates and high active mass loadings. The highest capacitance of 2.39 F cm<sup>-2</sup> at a scan rate of 100 mV s<sup>-1</sup> was achieved using anionic PHA and cationic NB as dispersants for MnO<sub>2</sub> and MWCNT, respectively. The ability to achieve high areal capacitance at high charge–discharge rates is important for the development of efficient supercapacitor devices. The asymmetric devices, containing positive MnO<sub>2</sub>–MWCNT and negative AC–CB electrodes showed promising performance in a voltage window of 1.6 V.

## Reference:

- [1] Jiang, R., Huang, T., Tang, Y., Liu, J., Xue, L., Zhuang, J., and Yu, A., 2009, "Factors Influencing MnO<sub>2</sub>/Multi-Walled Carbon Nanotubes Composite's Electrochemical Performance as Supercapacitor Electrode," *Electrochimica Acta*, **54**(27), pp. 7173–7179.
- [2] Brousse, T., Toupin, M., and Belanger, D., 2004, "A Hybrid Activated Carbon-Manganese Dioxide Capacitor Using a Mild Aqueous Electrolyte," *J. Electrochem. Soc.*, **151**(4), pp. A614–A622.
- [3] Xia, H., and Huo, C., 2011, "Electrochemical Properties of MnO<sub>2</sub>/CNT Nanocomposite in Neutral Aqueous Electrolyte as Cathode Material for Asymmetric Supercapacitors," *Int. J. Smart Nano Mater.*, **2**(4), pp. 283–291.
- [4] Boccaccini, A. R., Cho, J., Roether, J. A., Thomas, B. J., Minay, E. J., and Shaffer, M. S., 2006, "Electrophoretic Deposition of Carbon Nanotubes," *Carbon*, **44**(15), pp. 3149–3160.
- [5] Casagrande, T., Lawson, G., Li, H., Wei, J., Adronov, A., and Zhitomirsky, I., 2008, "Electrodeposition of Composite Materials Containing Functionalized Carbon Nanotubes," *Mater. Chem. Phys.*, **111**(1), pp. 42–49.
- [6] Ata, M. S., Liu, Y., and Zhitomirsky, I., 2014, "A Review of New Methods of Surface Chemical Modification, Dispersion and Electrophoretic Deposition of Metal Oxide Particles," *Rsc Adv.*, **4**(43), pp. 22716–22732.
- [7] Pujari, S. P., Scheres, L., Marcelis, A., and Zuilhof, H., 2014, "Covalent Surface Modification of Oxide Surfaces," *Angew. Chem. Int. Ed.*, **53**(25), pp. 6322–6356.
- [8] Zhang, B., Kong, T., Xu, W., Su, R., Gao, Y., and Cheng, G., 2010, "Surface Functionalization of Zinc Oxide by Carboxyalkylphosphonic Acid Self-Assembled Monolayers," *Langmuir*, **26**(6), pp. 4514–4522.
- [9] Boissezon, R., Muller, J., Beaugeard, V., Monge, S., and Robin, J.-J., 2014, "Organophosphonates as Anchoring Agents onto Metal Oxide-Based Materials: Synthesis and Applications," *Rsc Adv.*, **4**(67), pp. 35690–35707.
- [10] Pawsey, S., Yach, K., and Reven, L., 2002, "Self-Assembly of Carboxyalkylphosphonic Acids on Metal Oxide Powders," *Langmuir*, **18**(13), pp. 5205–5212.

- [11] Kar, P., Pandey, A., Greer, J. J., and Shankar, K., 2012, "Ultrahigh Sensitivity Assays for Human Cardiac Troponin I Using TiO<sub>2</sub> Nanotube Arrays," *Lab. Chip*, **12**(4), pp. 821–828.
- [12] Kalska-Szostko, B., Rogowska, M., and Satuła, D., 2013, "Organophosphorous Functionalization of Magnetite Nanoparticles," *Colloids Surf. B Biointerfaces*, **111**, pp. 656–662.
- [13] Li, F., Zhong, H., Zhao, G., Wang, S., and Liu, G., 2016, "Adsorption of  $\alpha$ -Hydroxyoctyl Phosphonic Acid to Ilmenite/Water Interface and Its Application in Flotation," *Colloids Surf. Physicochem. Eng. Asp.*, **490**, pp. 67–73.
- [14] Schmitt Pauly, C., Genix, A.-C., G. Alauzun, J., Sztucki, M., Oberdisse, J., and Mutin, P. H., 2015, "Surface Modification of Alumina-Coated Silica Nanoparticles in Aqueous Sols with Phosphonic Acids and Impact on Nanoparticle Interactions," *Phys. Chem. Chem. Phys.*, **17**(29), pp. 19173–19182.
- [15] Thomas, G., Demoisson, F., Boudon, J., and Millot, N., 2016, "Efficient Functionalization of Magnetite Nanoparticles with Phosphonate Using a One-Step Continuous Hydrothermal Process," *Dalton Trans.*, **45**(26), pp. 10821–10829.
- [16] Cornard, J. P., and Lapouge, C., 2004, "Theoretical and Spectroscopic Investigations of a Complex of Al (III) with Caffeic Acid," *J. Phys. Chem. A*, **108**(20), pp. 4470–4478.
- [17] Ata, M. S., Zhu, G.-Z., Botton, G. A., and Zhitomirsky, I., 2014, "Electrophoretic Deposition of Manganese Dioxide Films Using New Dispersing Agents," *Adv. Appl. Ceram.*, **113**(1), pp. 22–27.
- [18] Chen, Z., and Naidu, R., 2004, "On-Column Complexation Capillary Electrophoretic Separation of Fe<sup>2+</sup> and Fe<sup>3+</sup> Using 2, 6-Pyridinedicarboxylic Acid Coupled with Large-Volume Sample Stacking," *J. Chromatogr. A*, **1023**(1), pp. 151–157.
- [19] Yenikaya, C., Poyraz, M., Sarı, M., Demirci, F., İlkimen, H., and Büyükgüngör, O., 2009, "Synthesis, Characterization and Biological Evaluation of a Novel Cu (II) Complex with the Mixed Ligands 2, 6-Pyridinedicarboxylic Acid and 2-Aminopyridine," *Polyhedron*, **28**(16), pp. 3526–3532.
- [20] Moghimi, A., Sharif, M. A., Shokrollahi, A., Shamsipur, M., and Aghabozorg, H., 2005, "A Novel Proton Transfer Compound Containing 2, 6-Pyridinedicarboxylic Acid and Creatinine and Its Zinc (II) Complex—Synthesis, Characterization, Crystal Structure, and Solution Studies," *Z. Für Anorg. Allg. Chem.*, **631**(5), pp. 902–908.

- [21] Griffith, D., Chopra, A., Müller-Bunz, H., and Marmion, C. J., 2008, "The Reduction of Platinum (IV) and Palladium (IV) Ions by 2, 6-Pyridinedihydroxamic Acid," *Dalton Trans.*, (48), pp. 6933–6939.
- [22] Hou, K.-L., Bai, F.-Y., Xing, Y.-H., Cao, Y.-Z., Wei, D.-M., and Niu, S.-Y., 2011, "A New Series Lanthanide-2, 6-Pyridinedicarboxylic Acid Complexes Containing Low Dimensionality: Synthesis, Structure and Photoluminescent Properties," *J. Inorg. Organomet. Polym. Mater.*, **21**(2), pp. 213–222.
- [23] Zhitomirsky, I., 2002, "Cathodic Electrodeposition of Ceramic and Organoceramic Materials. Fundamental Aspects," *Adv. Colloid Interface Sci.*, **97**(1–3), pp. 279–317.
- [24] Wu, K., and Zhitomirsky, I., 2011, "Electrophoretic Deposition of Ceramic Nanoparticles," *Int. J. Appl. Ceram. Technol.*, **8**(4), pp. 920–927.
- [25] Dobson, K. D., and McQuillan, A. J., 2000, "In Situ Infrared Spectroscopic Analysis of the Adsorption of Aromatic Carboxylic Acids to TiO<sub>2</sub>, ZrO<sub>2</sub>, Al<sub>2</sub>O<sub>3</sub>, and Ta<sub>2</sub>O<sub>5</sub> from Aqueous Solutions," *Spectrochim. Acta. A. Mol. Biomol. Spectrosc.*, **56**(3), pp. 557–565.
- [26] Jankovic, I. A., Saponjic, Z. V., Comor, M. I., and Nedeljkovic, J. M., 2009, "Surface Modification of Colloidal TiO<sub>2</sub> Nanoparticles with Bidentate Benzene Derivatives," *J. Phys. Chem. C*, **113**(29), pp. 12645–12652.
- [27] Wu, K., Wang, Y., and Zhitomirsky, I., 2010, "Electrophoretic Deposition of TiO<sub>2</sub> and Composite TiO<sub>2</sub>–MnO<sub>2</sub> Films Using Benzoic Acid and Phenolic Molecules as Charging Additives," *J. Colloid Interface Sci.*, **352**(2), pp. 371–378.
- [28] Sun, Y., Ata, M. S., and Zhitomirsky, I., 2012, "Electrophoretic Deposition of TiO<sub>2</sub> Nanoparticles Using Organic Dyes," *J. Colloid Interface Sci.*, **369**(1), pp. 395–401.
- [29] Yurdakul, Ş., and Yurdakul, M., 2007, "Vibrational Frequencies and Structural Determination of 2, 2'-Biquinoline," *J. Mol. Struct.*, **834**, pp. 555–560.
- [30] Shi, K., and Zhitomirsky, I., 2015, "Electrodeposition of Carbon Nanotubes Triggered by Cathodic and Anodic Reactions of Dispersants," *Mater. Manuf. Process.*, **30**(6), pp. 771–777.
- [31] Ata, M. S., and Zhitomirsky, I., 2015, "Colloidal Methods for the Fabrication of Carbon Nanotube–manganese Dioxide and Carbon Nanotube–polypyrrole Composites Using Bile Acids," *J. Colloid Interface Sci.*, **454**, pp. 27–34.

- [32] Pang, X., Imin, P., Zhitomirsky, I., Adronov, A., and others, 2010, "Amperometric Detection of Glucose Using a Conjugated Polyelectrolyte Complex with Single-Walled Carbon Nanotubes," *Macromolecules*, **43**(24), p. 10376.
- [33] Li, N., Yuan, R., Chai, Y., Chen, S., An, H., and Li, W., 2007, "New Antibody Immobilization Strategy Based on Gold Nanoparticles and Azure I/Multi-Walled Carbon Nanotube Composite Membranes for an Amperometric Enzyme Immunosensor," *J Phys Chem C*, **111**(24), p. 8443.
- [34] Du, P., Zhou, B., and Cai, C., 2008, "Development of an Amperometric Biosensor for Glucose Based on Electrocatalytic Reduction of Hydrogen Peroxide at the Single-Walled Carbon Nanotube/Nile Blue A Nanocomposite Modified Electrode," *J. Electroanal. Chem.*, **614**(1), pp. 149–156.
- [35] Kötzt, R., and Carlen, M., 2000, "Principles and Applications of Electrochemical Capacitors," *Electrochimica Acta*, **45**(15–16), pp. 2483–2498.
- [36] Wang, Y., Liu, Y., and Zhitomirsky, I., 2013, "Surface Modification of MnO<sub>2</sub> and Carbon Nanotubes Using Organic Dyes for Nanotechnology of Electrochemical Supercapacitors," *J. Mater. Chem. A*, **1**(40), pp. 12519–12526.
- [37] Pang, H., Zhang, Y.-Z., Run, Z., Lai, W.-Y., and Huang, W., 2015, "Amorphous Nickel Pyrophosphate Microstructures for High-Performance Flexible Solid-State Electrochemical Energy Storage Devices," *Nano Energy*, **17**, pp. 339–347.
- [38] Yan, Y., Li, B., Guo, W., Pang, H., and Xue, H., 2016, "Vanadium Based Materials as Electrode Materials for High Performance Supercapacitors," *J. Power Sources*, **329**, pp. 148–169.

## Chapter 10 EPD of $Mn_3O_4$ using CA and ClB

### 10.1 Introduction

Over the years,  $MnO_x$  has been studied intensively due to low cost of this naturally abundant and environmentally friendly material. Because of the potential applications in catalysis, magnetic devices, molecular adsorption, supercapacitors and batteries,  $MnO_x$  have been widely studied[1–3]. Based on the oxidation states of manganese (II, III or IV), different types of  $MnO_x$  ( $MnO$ ,  $Mn_2O_3$ , and  $Mn_3O_4$ ) are available.  $Mn_3O_4$  is mostly used as catalysts for removing CO[4] and  $NiO_x$ [5]. Additionally,  $Mn_3O_4$  with reduced particle size is expected to display good performance in magnetic applications[6]. The stable room temperature phase is hausmannite, which also exhibits electrochromic properties[7].

In this part of the thesis, we investigated hausmannite phase  $Mn_3O_4$ , prepared at 60°C. Preparation method has already been described in Chapter 4. Figure 10-1A shows that  $Mn_3O_4$  was prepared in the hausmannite phase. Based on the TEM images (Figure 10-2),  $Mn_3O_4$  particle size is around ~30nm.

Caffeic acid (CA) and celestine blue (ClB) are promising charging and dispersing agents for cathodic EPD of inorganic nanoparticles. Figure 10-2 shows structures of CA and ClB, which include a catechol ligand, containing aromatic ring and two OH groups adjacently bonded to the aromatic ring. The relatively large size of the ClB molecules, compared to that of CA, is beneficial for the electrosteric dispersion. Moreover, CA and ClB can be used for the dispersion and EPD of  $Mn_3O_4$  with advanced properties and fabrication of composites. The experimental results presented in this chapter showed good performance

of CIB as a dispersing agent for co-deposition of  $Mn_3O_4$ -MWCNT and deposition of composites, which were tested for the application in the supercapacitor electrodes.

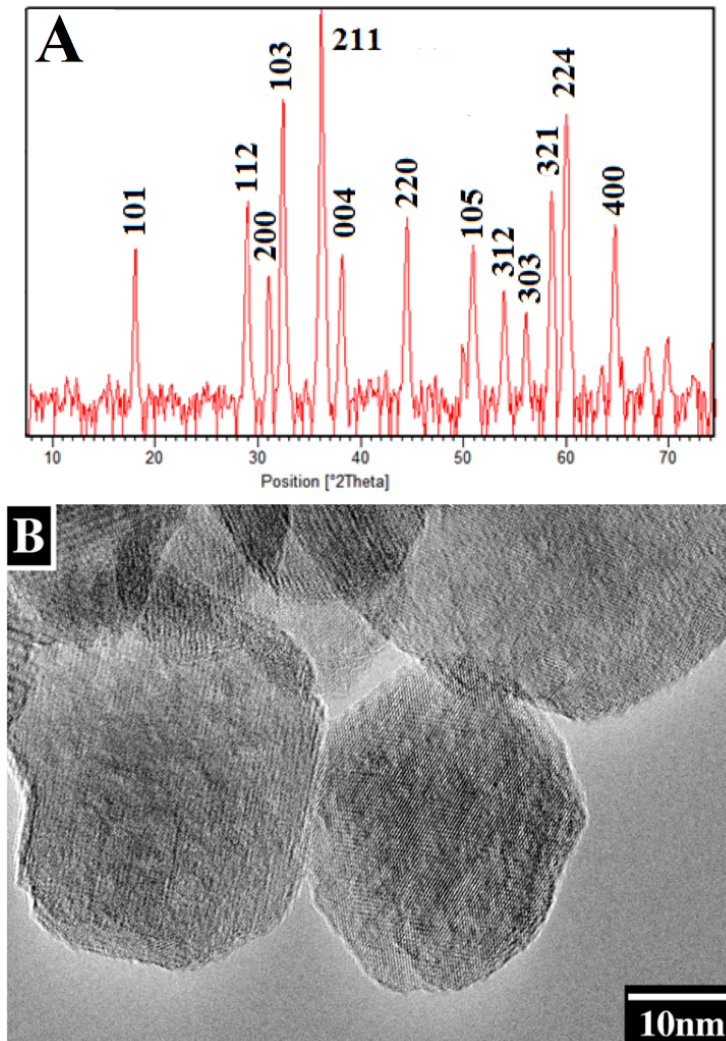


Figure 10-1 (A) XRD (B) TEM images of  $Mn_3O_4$  prepared at 60°C.

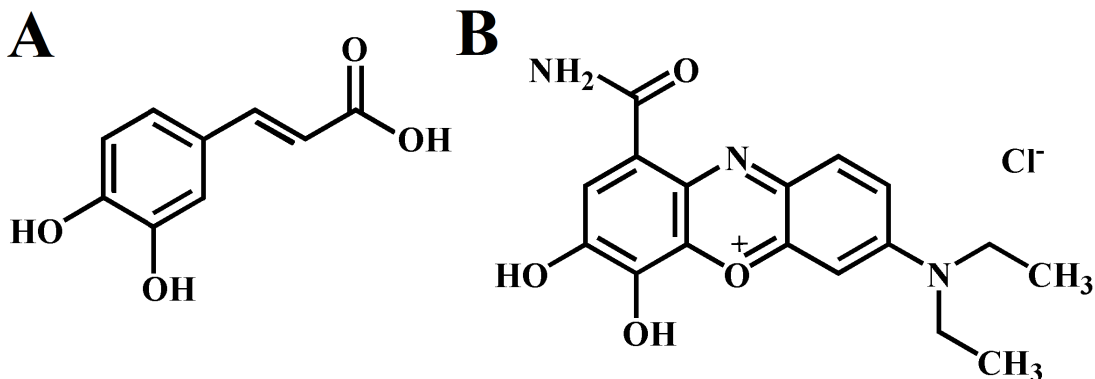
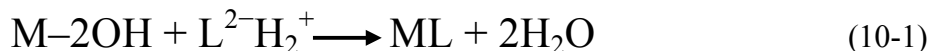


Figure 10-2 Chemical structure of (A) CA and (B) ClB

## 10.2 EPD of $Mn_3O_4$ using CA

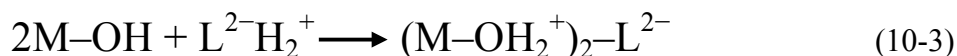
CA is important phenolic antioxidant, which is present in many plants and beverages[8]. It was found that CA can be used as an efficient green corrosion inhibitor for stainless steel[9]. Similar to DOPA, the structure of CA contains two OH groups bonded to adjacent carbon atoms of the aromatic ring (Figure 10-2). The anionic properties of CA are related to the dissociation of the carboxylic group (Figure 10-2). CA showed strong adsorption on inorganic surfaces, such as stainless steel[9],  $TiO_2$ [10,11], silica[12,13], zirconia[14] and  $MnO_2$ [14] in different solvents. The adsorption of CA on inorganic particles can involve phenolic and carboxylic (Figure 10-3) bonding sites[14]. Bidentate chelating bonding (Figure 10-3a) and bidentate bridging bonding (Figure 10-3b) mechanisms[15,16] were proposed for CA adsorption[14]. The adsorption can involve inner sphere (Figure 10-3b) or outer sphere bonding (Figure 10-3c), depending on the nature of the adsorbent material[17]. The following reaction stoichiometry was proposed[14] for bidentate chelating bonding[18,19], involving metal atoms (M), containing surface OH groups, and catechol ( $L^2-H_2^+$ ):



The bidentate bridging inner-sphere bonding[14] is based on the reaction[19,20]:



The outer sphere bonding66 is formed as follows[20,21]:



Other mechanisms[14] included monodentate bonding, involving one OH group, or mixed monodentate–bidentate bonding[16,22].

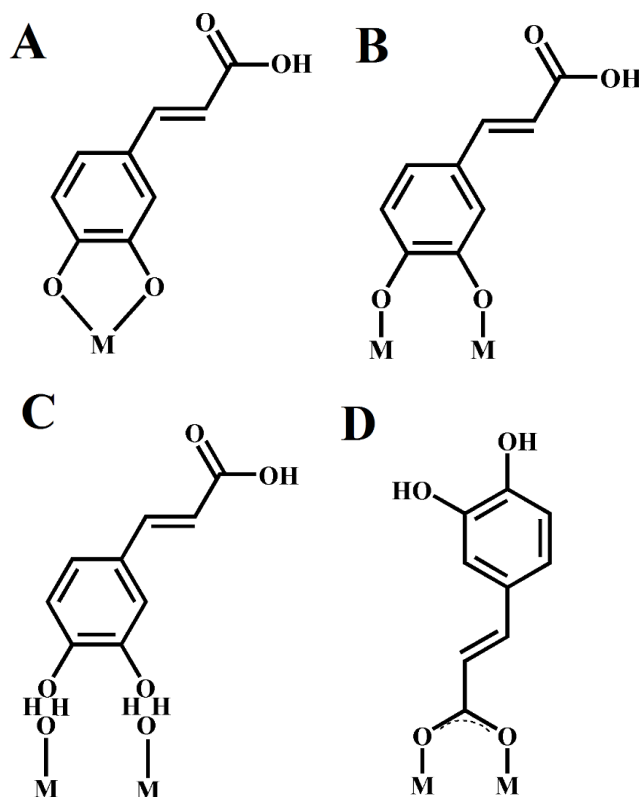


**Figure 10-3 Possible adsorption mechanisms of CA: (a) bidentate chelating bonding, (b) bidentate bridging bonding (inner sphere), (c) bidentate bridging bonding (outer sphere) of catechol group, (d) adsorption, involving a carboxylic group.**

The adsorption mechanism, involving a carboxylic group[23] is shown in Figure 10-3d. The investigation of benzoic and phthalic acids, which do not have OH groups bonded to the aromatic ring, provided evidence that carboxylic groups were involved in adsorption of the acids on zirconium, titanium and iron oxides[23,24]. Therefore, similar adsorption mechanism can be suggested for the adsorption of CA. Studies of the interactions of CA with different ions in aqueous solutions showed that the bonding mechanism depended on the nature of metal ions. Among the two possible coordination sites, the carboxylate group of CA showed greater complexing power toward Pb(II). However, Al(III) preferentially coordinated the catechol group of CA[25].

EPD of oxide materials provided important information related to CA adsorption mechanism.  $Mn_3O_4$  suspensions, containing CA, were investigated. The suspensions of  $Mn_3O_4$  in water was unstable, however the addition of CA, resulted in improved suspension stability. EPD from  $Mn_3O_4$  suspension, containing CA resulted in the formation of anodic deposits. The charge of the particles was governed by the competitive adsorption of dissociated anionic molecules and  $H^+$ . The preferred adsorption of anionic CA species resulted in the negative charge of the particles, which formed anodic deposits. The anodic deposition yield increased with increasing CA concentration (Figure 10-4) at low CA concentrations, showed a maximum at  $0.29 \text{ g L}^{-1}$  CA and then decreased. The deposit mass increased with increasing deposition time (Figure 10-5); therefore, the amount of material deposited can be varied.

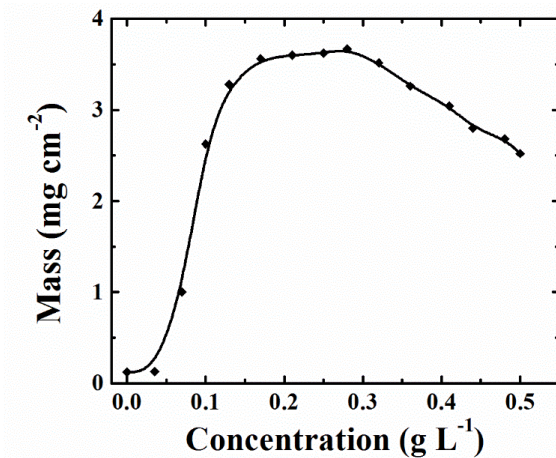


**Figure 10-4** Deposit mass versus CA concentration in 10 g L<sup>-1</sup> Mn<sub>3</sub>O<sub>4</sub> suspension at a deposition voltage 20 V and a deposition time 5 min.

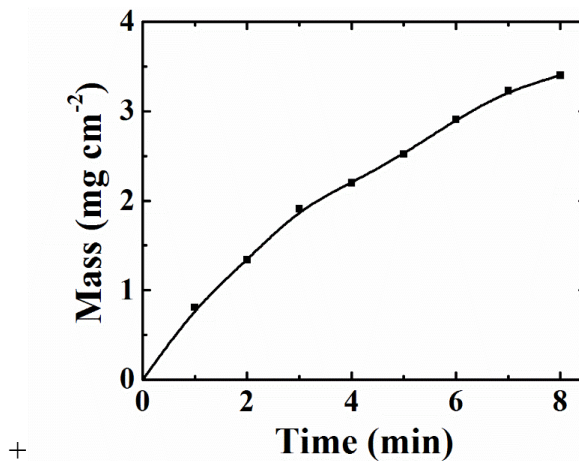


**Figure 10-5** Deposit mass versus deposition time for 10 g L<sup>-1</sup> Mn<sub>3</sub>O<sub>4</sub> suspension, containing 0.5 g L<sup>-1</sup> CA at a deposition voltage of 20 V.

### 10.3 EPD of Mn<sub>3</sub>O<sub>4</sub> using CIB

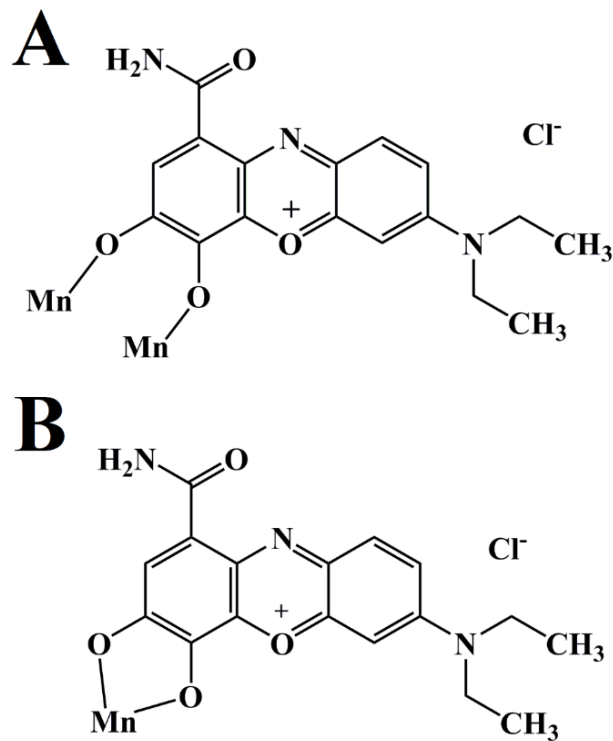
The larger size of the dyes, compared to that of mono-aromatic molecules (Figure 10-2A), is beneficial for electrosteric stabilization of nanoparticles in suspensions. Moreover, organic dyes have generated significant interest for the dispersion of carbon nanotubes and graphene. Therefore, organic dyes are promising co-dispersants for co-deposition of various materials.

Figure 10-2B shows a chemical structure of cationic CIB dye, which is under investigations for application in solar cells and sensors[26,27]. CIB belongs to the catechol family of materials. The positive charge of CIB makes this molecule important for application as a charging and dispersing agent for cathodic EPD of metal oxides. The larger size of CIB, compared to that of dopamine, is beneficial for the electrosteric dispersion. It is important to note that dopamine has no charge and must be protonated in acidic solutions for application in EPD. The dopamine is unstable in basic solutions due to self-polymerization. In contrast, the dissociation of CIB allows the formation of stable solutions of cationic CIB species.

The suspensions of  $Mn_3O_4$  particles in ethanol were unstable and showed rapid sedimentation after the ultrasonic agitation. It was found that adsorbed CIB provided improved suspension stability and imparted a positive charge to the particles. In fact, the suspensions of nanoparticles of  $Mn_3O_4$  containing  $0.5 \text{ g L}^{-1}$  CIB, were stable for more than 7 days. Cathodic deposits were obtained from the suspension, containing CIB, by EPD at a deposition voltage of 20 V.

Figure 10-7 shows the influence of CIB concentration on the deposition yield for  $Mn_3O_4$  suspension. Significant increase in the deposition yield was observed (Figure 10-7) with increasing CIB concentration in the range of 0–0.1  $\text{g L}^{-1}$  and then the deposition yield increased gradually at higher CIB concentrations. This indicated that the addition of CIB to the suspensions resulted in CIB adsorption on the oxide particles. Similar to DOPA, DA and other materials from the catechol family[28], the CIB adsorption involves bidentate bridging bonding (Figure 10-6A) or bidentate chelating bonding (Figure 10-6B). The adsorbed CIB provided suspension stability and imparted a positive charge to the particles for cathodic EPD. However, we cannot exclude the possibility that the suspensions also included free, non-adsorbed CIB. The high

deposition rate obtained at low CIB concentration indicated that CIB was efficiently adsorbed on the oxide particles and the amount of free CIB in the suspensions was very low. As pointed out above, a non-adsorbed dispersing agent is detrimental for the suspension stabilization. The addition of CIB to  $Mn_3O_4$  suspension resulted in rapid increase in the deposition rate in the range of 0-0.05 g L<sup>-1</sup> (Figure 10-7). At higher concentrations, the deposition yield increased and reached the maximum point between 0.2 and 0.3 g L<sup>-1</sup> then decreased slightly. The deposition yield increased with increasing time, indicating the formation of deposits of different mass (Figure 10-8). The decrease in the deposition rate with time is related to the decreasing electric field in the suspension due to the increasing voltage drop in the growing films. Figure 10-9 shows microstructure of a  $Mn_3O_4$  deposited using CIB as a dispersant and charging agent.



**Figure 10-6 Suggested adsorption mechanism of CIB, involving metal atoms M on a particle surface: (A) bidentate bridging bonding and (B) bidentate chelating bonding.**

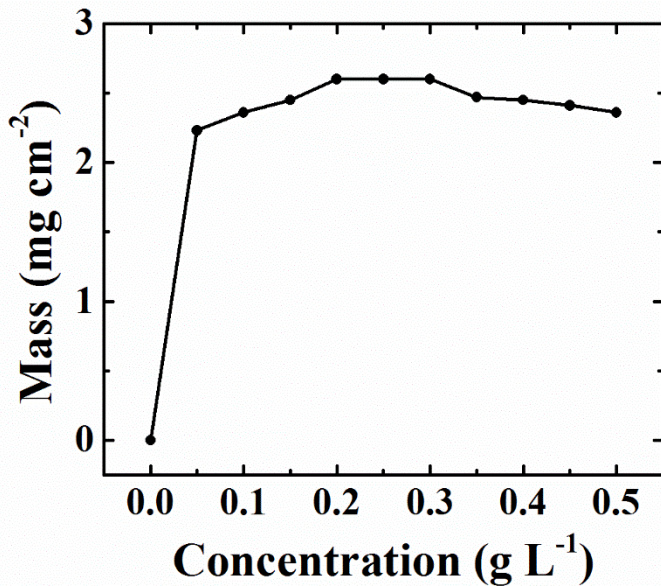


Figure 10-7 Deposit mass versus ClB concentration in 4 g L<sup>-1</sup> Mn<sub>3</sub>O<sub>4</sub> suspension at a deposition voltage 20 V and a deposition time 5 min.

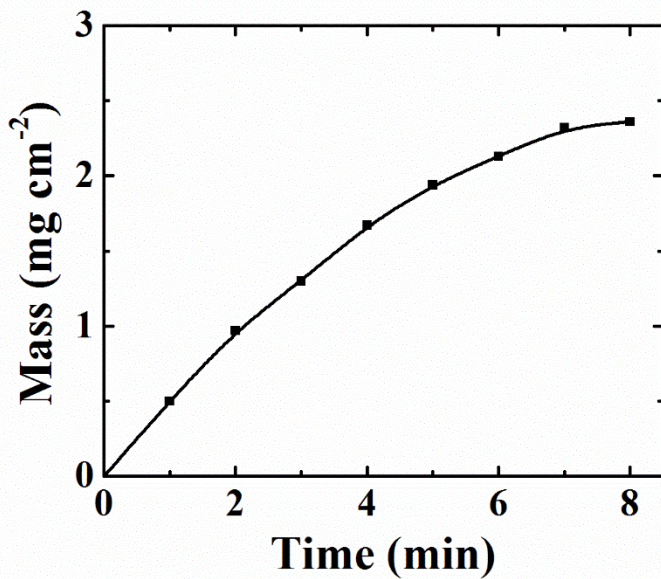
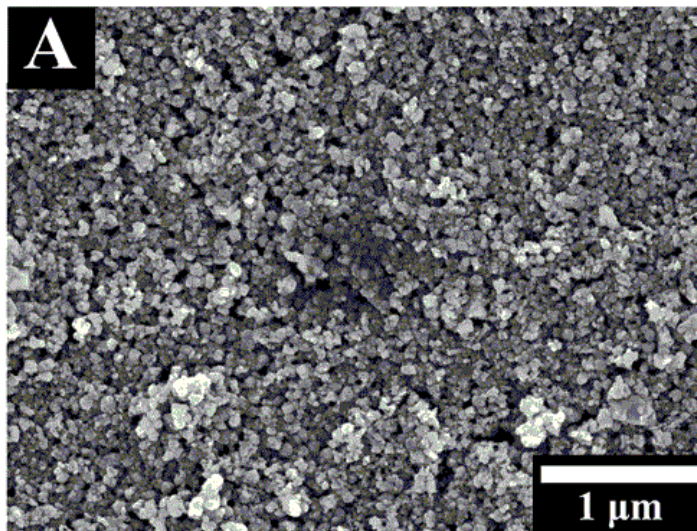


Figure 10-8 Deposit mass versus deposition time for 4 g L<sup>-1</sup> Mn<sub>3</sub>O<sub>4</sub> suspension, containing 0.5 g L<sup>-1</sup> ClB at a deposition voltage of 20 V.



**Figure 10-9 SEM images of films, prepared from  $4 \text{ g L}^{-1}$  suspensions of (A)  $\text{Mn}_3\text{O}_4$ , containing  $0.5 \text{ g L}^{-1}$  CIB at a deposition voltage of 20 V.**

Figure 10-10 shows the FTIR spectra of the  $\text{Mn}_3\text{O}_4$  deposits. The absorptions at  $1625 \text{ cm}^{-1}$ ,  $1567 \text{ cm}^{-1}$ ,  $1442 \text{ cm}^{-1}$  and  $1390 \text{ cm}^{-1}$  (Figure 10-10) were attributed to stretching vibrations of the aromatic ring  $\nu(\text{C}-\text{C})$  and  $\nu(\text{C}=\text{C})$ [23,28,29] of adsorbed CIB. The absorption at  $1344 \text{ cm}^{-1}$  was attributed to stretching  $\nu(\text{C}-\text{N})$  and  $\nu(\text{C}-\text{N})$  vibrations[30] of CIB. The broad absorptions in the UV-vis spectra at 622 nm (Figure10-10) were related to adsorbed CIB[31]. Therefore, the FTIR and UV-vis data confirmed that deposited ceramic particles contained adsorbed CIB.

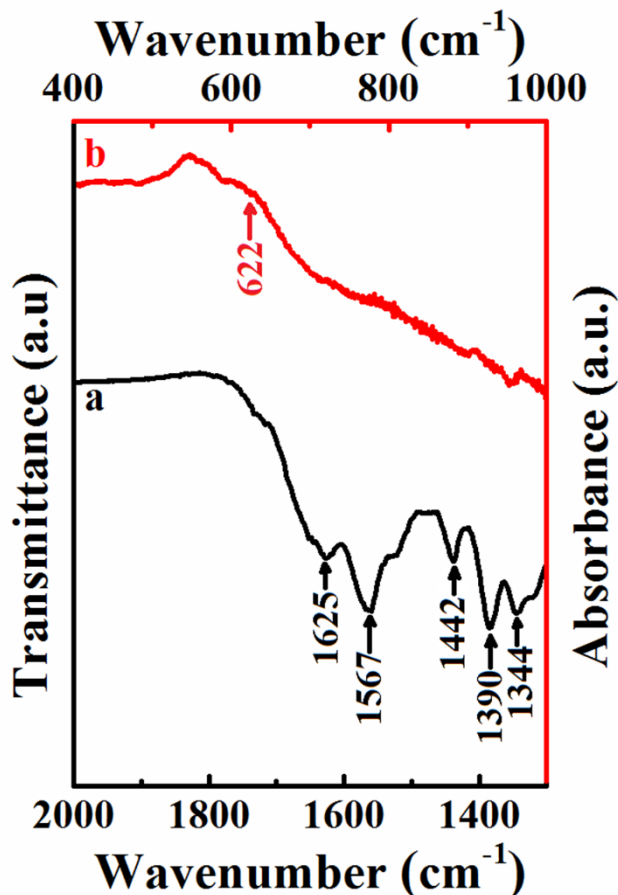
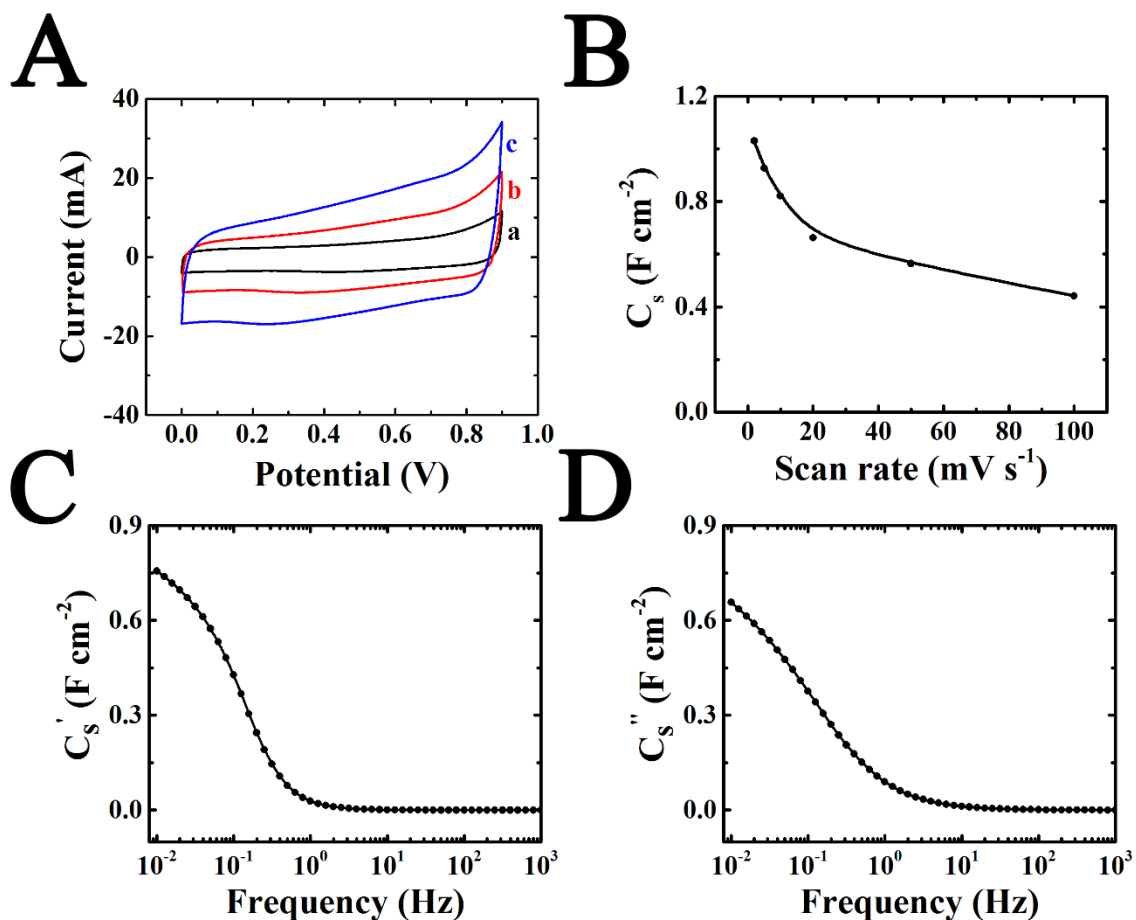


Figure 10-10 (a) FTIR and (b)UV-vis data for deposits, prepared from 4 g L<sup>-1</sup> suspensions of Mn<sub>3</sub>O<sub>4</sub>, containing 0.5 g L<sup>-1</sup> ClB at a deposition voltage of 20 V.

#### 10.4 Electrochemical characterization of Mn<sub>3</sub>O<sub>4</sub>-MWCNT composite electrodes prepared using ClB

The composite Mn<sub>3</sub>O<sub>4</sub>-MWCNT electrodes, prepared using ClB as a co-dispersant showed good electrochemical performance, as indicated by nearly box shape CV, presented in Figure 10-11A. The integral capacitances in the voltage window of 0.9 V were calculated from the CV data (Figure 10-11B). Relatively high specific capacitance of 1.02 F cm<sup>-2</sup> was obtained at a film mass of 40.8 mg cm<sup>-2</sup> and a scan rate of 2 mV s<sup>-1</sup>. The capacitance decreased with increasing scan rate due to the diffusion limitation in pores of the MnO<sub>2</sub>-

MWCNT composite. The capacitance retention at  $100 \text{ mV s}^{-1}$  was found to be 43% of the capacitance value at  $2 \text{ mV s}^{-1}$ . Figure 10-11(C, D) shows frequency dependences of components of differential capacitance, derived from the impedance data. The frequency dependences of capacitance showed a relaxation type dispersion[32], as indicated by the reduction of  $C_s'$  at frequencies above 100 mHz and corresponding relaxation maxima in  $C_s''$ .



**Figure 10-11 (A) CVs at scan rate (a) 2 (b) 5 and (c) 10  $\text{mV s}^{-1}$ , (B) specific capacitance versus scan rate, (C) real part  $C_s'$  and (D) imaginary part  $C_s''$  of complex areal capacitance  $C_s^* = C_s' - iC_s''$  versus frequency, calculated from the impedance data for the  $\text{MnO}_2$  electrodes, prepared using CIB as a dispersant and MWCNT (20 mass %) as conductive additive, using 0.5 M  $\text{Na}_2\text{SO}_4$  electrolyte.**

## 10.5 Conclusion

Anionic of CA and cationic of CIB molecules from the catechol family are promising charging and dispersing agents for EPD of  $Mn_3O_4$ . The molecules showed good adsorption on oxide particles due to interactions of their adjacent phenolic OH groups and COOH groups with metal atoms on the particle surface and allowed the fabrication of stable suspensions. The adsorption of new dispersing agents imparted important functional properties to oxide nanoparticles and allowed synthesis of non-agglomerated nanoparticles of controlled size. The use of CIB as a co-dispersant allowed for the fabrication of  $Mn_3O_4$ -MWCNT composites. Testing results showed promising performance of  $Mn_3O_4$ -MWCNT composites for applications in electrodes of electrochemical supercapacitors.

## References:

- [1] Fei, J. B., Cui, Y., Yan, X. H., Qi, W., Yang, Y., Wang, K. W., He, Q., and Li, J. B., 2008, "Controlled Preparation of  $MnO_2$  Hierarchical Hollow Nanostructures and Their Application in Water Treatment," *Adv. Mater.*, **20**(3), pp. 452–456.
- [2] Yang, Z., Zhang, Y., Zhang, W., Wang, X., Qian, Y., Wen, X., and Yang, S., 2006, "Nanorods of Manganese Oxides: Synthesis, Characterization and Catalytic Application," *J. Solid State Chem.*, **179**(3), pp. 679–684.
- [3] Fischer, A. E., Pettigrew, K. A., Rolison, D. R., Stroud, R. M., and Long, J. W., 2007, "Incorporation of Homogeneous, Nanoscale  $MnO_2$  within Ultraporous Carbon Structures via Self-Limiting Electroless Deposition: Implications for Electrochemical Capacitors," *Nano Lett.*, **7**(2), pp. 281–286.
- [4] Stobbe, E. R., De Boer, B. A., and Geus, J. W., 1999, "The Reduction and Oxidation Behaviour of Manganese Oxides," *Catal. Today*, **47**(1), pp. 161–167.

- [5] Zwinkels, M. F., Järvaas, S. G., Menon, P. G., and Griffin, T. A., 1993, "Catalytic Materials for High-Temperature Combustion," *Catal. Rev. Eng.*, **35**(3), pp. 319–358.
- [6] Vázquez-Olmos, A., Redón, R., Rodríguez-Gattorno, G., Mata-Zamora, M. E., Morales-Leal, F., Fernández-Osorio, A. L., and Saniger, J. M., 2005, "One-Step Synthesis of Mn<sub>3</sub>O<sub>4</sub> Nanoparticles: Structural and Magnetic Study," *J. Colloid Interface Sci.*, **291**(1), pp. 175–180.
- [7] Dubal, D. P., Dhawale, D. S., Salunkhe, R. R., Fulari, V. J., and Lokhande, C. D., 2010, "Chemical Synthesis and Characterization of Mn<sub>3</sub>O<sub>4</sub> Thin Films for Supercapacitor Application," *J. Alloys Compd.*, **497**(1), pp. 166–170.
- [8] Valero-Navarro, Á., Gómez-Romero, M., Fernández-Sánchez, J. F., Cormack, P. A. G., Segura-Carretero, A., and Fernández-Gutiérrez, A., 2011, "Synthesis of Caffeic Acid Molecularly Imprinted Polymer Microspheres and High-Performance Liquid Chromatography Evaluation of Their Sorption Properties," *J. Chromatogr. A*, **1218**(41), pp. 7289–7296.
- [9] de Souza, F. S., and Spinelli, A., 2009, "Caffeic Acid as a Green Corrosion Inhibitor for Mild Steel," *Corros. Sci.*, **51**(3), pp. 642–649.
- [10] Sun, Y., and Zhitomirsky, I., 2012, "Electrophoretic Deposition of Titanium Dioxide Using Organic Acids as Charging Additives," *Mater. Lett.*, **73**, pp. 190–193.
- [11] Barreto, W. J., Ando, R. A., Estevão, B. M., and Zanoni, K. P. da S., 2012, "Adsorption of Caffeic Acid on Titanium Dioxide: A Spectroscopic Study," *Spectrochim. Acta. A. Mol. Biomol. Spectrosc.*, **92**, pp. 16–20.
- [12] Dovbii, O. A., Kazakova, O. A., and Lipkovskaya, N. A., 2006, "The Effect of the Structure of Cinnamic Acid Derivatives on Their Interaction with Highly Dispersed Silica in Aqueous Medium," *Colloid J.*, **68**(6), pp. 707–712.
- [13] Pogorelyi, V. K., Kazakova, O. A., Barvinchenko, V. N., Smirnova, O. V., Pakhlov, E. M., and Gun'ko, V. M., 2007, "Adsorption of Cinnamic and Caffeic Acids on the Surface of Highly Dispersed Silica from Different Solvents," *Colloid J.*, **69**(2), pp. 203–211.
- [14] Wang, Y., and Zhitomirsky, I., 2012, "Bio-Inspired Catechol Chemistry for Electrophoretic Nanotechnology of Oxide Films," *J. Colloid Interface Sci.*, **380**(1), pp. 8–15.

- [15] Chen, Q., Jia, Y., Liu, S., Mogilevsky, G., Kleinhammes, A., and Wu, Y., 2008, "Molecules Immobilization in Titania Nanotubes: A Solid-State NMR and Computational Chemistry Study," *J. Phys. Chem. C*, **112**(44), pp. 17331–17335.
- [16] Ye, Q., Zhou, F., and Liu, W., 2011, "Bioinspired Catecholic Chemistry for Surface Modification," *Chem. Soc. Rev.*, **40**(7), pp. 4244–4258.
- [17] Gulley-Stahl, H., Hogan, P. A., Schmidt, W. L., Wall, S. J., Buhrlage, A., and Bullen, H. A., 2010, "Surface Complexation of Catechol to Metal Oxides: An ATR-FTIR, Adsorption, and Dissolution Study," *Environ. Sci. Technol.*, **44**(11), pp. 4116–4121.
- [18] Vasudevan, D., and Stone, A. T., 1998, "Adsorption of 4-Nitrocatechol, 4-Nitro-2-Aminophenol, and 4-Nitro-1,2-Phenylenediamine at the Metal (Hydr)Oxide/Water Interface: Effect of Metal (Hydr)Oxide Properties," *J. Colloid Interface Sci.*, **202**(1), pp. 1–19.
- [19] Vasudevan, D., and Stone, A. T., 1996, "Adsorption of Catechols, 2-Aminophenols, and 1,2-Phenylenediamines at the Metal (Hydr)Oxide/Water Interface: Effect of Ring Substituents on the Adsorption onto TiO<sub>2</sub>," *Environ. Sci. Technol.*, **30**(5), pp. 1604–1613.
- [20] Hwang, Y. S., and Lenhart, J. J., 2009, "Surface Complexation Modeling of Dual-Mode Adsorption of Organic Acids: Phthalic Acid Adsorption onto Hematite," *J. Colloid Interface Sci.*, **336**(1), pp. 200–207.
- [21] Klug, O., and Forsling, W., 1999, "A Spectroscopic Study of Phthalate Adsorption on  $\gamma$ -Aluminum Oxide," *Langmuir*, **15**(20), pp. 6961–6968.
- [22] Li, S.-C., Wang, J., Jacobson, P., Gong, X.-Q., Selloni, A., and Diebold, U., 2009, "Correlation between Bonding Geometry and Band Gap States at Organic–Inorganic Interfaces: Catechol on Rutile TiO<sub>2</sub>(110)," *J. Am. Chem. Soc.*, **131**(3), pp. 980–984.
- [23] Tunesi, S., and Anderson, M. A., 1992, "Surface Effects in Photochemistry: An in Situ Cylindrical Internal Reflection-Fourier Transform Infrared Investigation of the Effect of Ring Substituents on Chemisorption onto Titania Ceramic Membranes," *Langmuir*, **8**(2), pp. 487–495.
- [24] Dobson, K. D., and McQuillan, A. J., 2000, "In Situ Infrared Spectroscopic Analysis of the Adsorption of Aromatic Carboxylic Acids to TiO<sub>2</sub>, ZrO<sub>2</sub>, Al<sub>2</sub>O<sub>3</sub>, and Ta<sub>2</sub>O<sub>5</sub> from Aqueous Solutions," *Spectrochim. Acta. A. Mol. Biomol. Spectrosc.*, **56**(3), pp. 557–565.

- [25] Boilet, L., Cornard, J. P., and Lapouge, C., 2005, "Determination of the Chelating Site Preferentially Involved in the Complex of Lead(II) with Caffeic Acid: A Spectroscopic and Structural Study," *J. Phys. Chem. A*, **109**(9), pp. 1952–1960.
- [26] Noorbakhsh, A., and Salimi, A., 2009, "Amperometric Detection of Hydrogen Peroxide at Nano-Nickel Oxide/Thionine and Celestine Blue Nanocomposite-Modified Glassy Carbon Electrodes," *Electrochimica Acta*, **54**(26), pp. 6312–6321.
- [27] Yadav, S., and Lal, C., 2013, "Optimization of Performance Characteristics of a Mixed Dye Based Photogalvanic Cell for Efficient Solar Energy Conversion and Storage," *Energy Convers. Manag.*, **66**, pp. 271–276.
- [28] Janković, I. A., Šaponjić, Z. V., Čomor, M. I., and Nedeljković, J. M., 2009, "Surface Modification of Colloidal TiO<sub>2</sub> Nanoparticles with Bidentate Benzene Derivatives," *J. Phys. Chem. C*, **113**(29), pp. 12645–12652.
- [29] Mohammed-Ziegler, I., and Billes, F., 2002, "Vibrational Spectroscopic Calculations on Pyrogallol and Gallic Acid," *J. Mol. Struct. THEOCHEM*, **618**(3), pp. 259–265.
- [30] Çatıkkaş, B., Aktan, E., and Seferoğlu, Z., 2013, "DFT, FT-Raman, FTIR, NMR, and UV–Vis Studies of a Hetarylazo Indole Dye," *Int. J. Quantum Chem.*, **113**(5), pp. 683–689.
- [31] Yadav, S., and Lal, C., 2013, "Optimization of Performance Characteristics of a Mixed Dye Based Photogalvanic Cell for Efficient Solar Energy Conversion and Storage," *Energy Convers. Manag.*, **66**, pp. 271–276.
- [32] Shi, K., and Zhitomirsky, I., 2013, "Influence of Current Collector on Capacitive Behavior and Cycling Stability of Tiron Doped Polypyrrole Electrodes," *J. Power Sources*, **240**, pp. 42–49.

# **Chapter 11 Colloidal methods for the fabrication of Mn<sub>3</sub>O<sub>4</sub>-MWCNT electrodes with high areal capacitance**

## **11.1 Introduction**

Manganese oxides, such as MnO<sub>2</sub> and Mn<sub>3</sub>O<sub>4</sub> are under intensive investigation for charge storage applications in electrochemical supercapacitors and batteries[1–3]. The interest in manganese oxides for the development of supercapacitor electrodes is attributed to their high theoretical capacitance, nearly ideal capacitive charge-discharge behavior in a relatively large voltage window and low cost[4–6]. Many investigations were focused on the analysis of charge-discharge mechanisms and study of specific capacitance at different experimental conditions[7–10]. Relatively high gravimetric capacitance ( $C_m$ , F g<sup>-1</sup>) was achieved at low active mass loadings[5,10–14] in the range of 0.005-1 mg cm<sup>-2</sup>. Such active mass loadings usually result in relatively low ratios (<1-2%) of active material mass to the current collector mass. Significantly higher active mass loadings above 10 mg cm<sup>-2</sup> are necessary for practical applications[15]. However,  $C_m$  decreased drastically[16] with increasing mass of the active material, especially at high charge-discharge rates due to poor electrolyte access to the active material and low electronic conductivity. For practical applications, high  $C_m$  must be achieved at high mass loadings. The important parameter for the characterization of supercapacitor electrodes with high active mass loadings is areal capacitance ( $C_s$ , F cm<sup>-2</sup>).

Investigations[17–20] have shown that the specific capacitance does not correlate with the BET surface area, since some very small pores are inaccessible by the electrolyte. However, the preparation of non-agglomerated particles with small size is critical for the fabrication of advanced electrodes. The synthesis of nanoparticles in the presence of dispersing agents offers a way to reduce particle size and avoid agglomeration. Particles of  $\text{MnO}_2$  are usually prepared by the reduction of  $\text{KMnO}_4$  solutions[21,22]. However, the use of organic dispersion agents during synthesis presents difficulties, because  $\text{KMnO}_4$  is a strong oxidant, which reacts with organic dispersants. In contrast, the synthesis of  $\text{Mn}_3\text{O}_4$  can be achieved from  $\text{Mn}^{2+}$  salt solutions and various dispersants and colloidal strategies can be used for the control of particle size and morphology during  $\text{Mn}_3\text{O}_4$  preparation and fabrication of composite electrodes with advanced microstructures. Therefore,  $\text{Mn}_3\text{O}_4$  synthesis in the presence of organic dispersants is a promising strategy for the fabrication of  $\text{Mn}_3\text{O}_4$  electrodes with enhanced performance.

Electrochemical[23] and chemical[24] techniques can be used for the fabrication of  $\text{Mn}_3\text{O}_4$ . Recent studies showed that particle shape and growth rate during synthesis can be controlled by glucose adsorption[24]. It was demonstrated[25] that cationic polyelectrolytes, containing amino groups, such as chitosan and polyethylenimine, promoted room temperature crystallization of  $\text{Mn}_3\text{O}_4$  nanoparticles. Moreover, particle size can be varied by variation of the polymer concentration in the solutions[25]. Porous  $\text{Mn}_3\text{O}_4$  particles with high surface area were obtained for supercapacitor applications using a surfactant as a microstructure controlling agent[26]. In another investigation[27] tunable

microstructures were obtained using a block copolymer template (Pluronic F127) as a dispersant.

Nanostructured  $\text{Mn}_3\text{O}_4$  electrodes showed interesting activation phenomena, related to capacitance increase[5,23,28,29] during initial cycling with corresponding changes in the film morphology and oxidation of manganese ions to a higher oxidation state. Advanced  $\text{Mn}_3\text{O}_4$  based composites were developed[30–36], containing various conductive components, such as carbon nanotubes, graphene, graphite and  $\text{RuO}_2$ . The typical  $C_S$  values reported in the literature[7,37–40] for  $\text{Mn}_3\text{O}_4$  based electrodes were in the range of 0.02-0.6  $\text{F cm}^{-2}$ .

Despite the impressive progress achieved in the materials synthesis and microstructure design, further investigations are necessary for the preparation of  $\text{Mn}_3\text{O}_4$  based composites for advanced supercapacitor electrodes with high active mass loading. New strategies must be developed for the fabrication of well dispersed  $\text{Mn}_3\text{O}_4$  nanoparticles and their efficient mixing with carbon nanotubes in order to achieve high  $C_S$  and good capacitance retention at high charge-discharge rates.

The goal of this investigation was the development of efficient  $\text{Mn}_3\text{O}_4$ -multiwalled carbon nanotube (MWCNT) electrodes with high active mass loading and high areal capacitance. The approach was based on the use of poly(4-styrenesulfonic acid-*co*-maleic acid) sodium salt P(SSA-MA) as a dispersing agent for  $\text{Mn}_3\text{O}_4$  synthesis. The unique feature of P(SSA-MA) is that this polyelectrolyte exhibits strong adsorption on  $\text{Mn}_3\text{O}_4$  due to the bi-dentate bonding properties of the maleic acid monomers, which provide multiple bonding sites. The use of P(SSA-MA) during synthesis allowed the fabrication of non-agglomerated

nanoparticles, which were negatively charged and well dispersed. Another important finding was the possibility of efficient dispersion of MWCNT using small cationic dispersants, such as ethyl violet (EV) or pyronin Y (PY) dyes, which imparted a positive charge to MWCNT. It was found that the electrostatic heterocoagulation of the negatively charged  $\text{Mn}_3\text{O}_4$ , dispersed using P(SSA-MA), and positively charged MWCNT, dispersed using EV or PY, allowed good mixing of the individual components.

## **11.2 Morphology study of $\text{Mn}_3\text{O}_4$ using P(SSA-MA)**

Figure 11-1A shows a chemical structure of P(SSA-MA) used as a dispersant for  $\text{Mn}_3\text{O}_4$ . P(SSA-MA) is a co-polymer of 4-styrenesulfonic acid (SSA) and maleic acid (MA). The chemical structure of P(SSA-MA) offers many benefits for application of this polyelectrolyte as a dispersing agent for colloidal processing of oxide particles. A critical property of a dispersant is its adsorption on the particle surface, because a non-adsorbed ionic dispersant promotes particle coagulation[41]. It is important to note that typical dispersing agents contain a monodentate ligand, that only enables relatively weak adsorption on particles[41,42]. Recently, new strategies have emerged, based on the use of advanced dispersant molecules, which allow significantly stronger bi-dentate or tri-dentate bonding[41–43]. Further progress can be achieved by the use of polymers, containing special monomers, which provide chelating or bridging bonding and allow significantly stronger adsorption by creating multiple bonds with metal atoms on the particle surface.

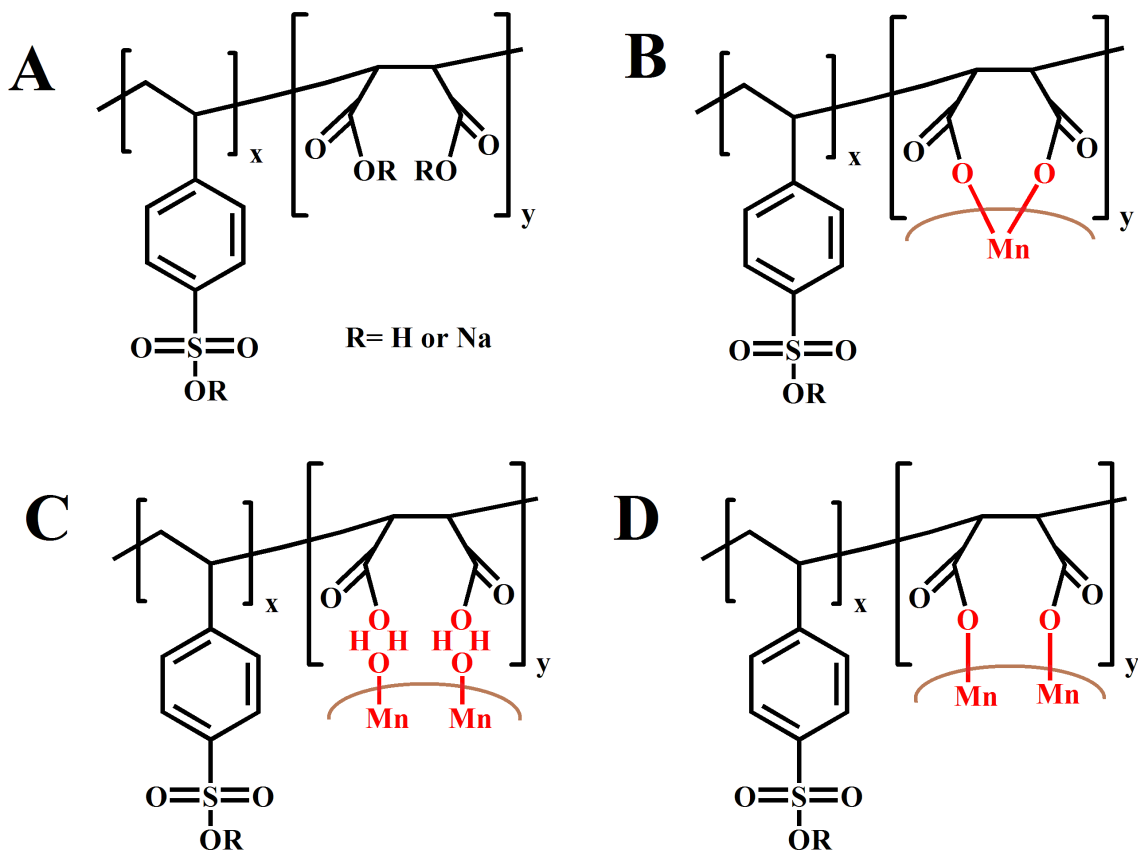


**Figure 11-1 (A) Chemical structure of P(SSA-MA) and (B-D) adsorption of P(SSA-MA) on  $Mn_3O_4$ , involving (B) complexation, (C) outer-sphere bonding and (D) inner-sphere bonding of Mn atoms on the particle surface by MA monomers.**

It is known[44] that organic molecules, containing carboxylic groups are highly reactive and adsorb on oxide surfaces through complexation or bridging bonding of surface metal atoms. Of particular interest is the adsorption of MA, involving bonding of two carboxylic groups in *cis*-configuration to metal atoms on the oxide particle surface[45]. The recent progress in the investigation of MA adsorption has generated the interest in the synthesis of polymaleic acid P(MA)[46] and co-polymers of MA, such as poly(acrylic acid-co-maleic acid) P(AA-MA)[47] and poly(styrene-alt-maleic acid) P(S-MA)[48], which were

used for the dispersion of  $\text{Al}_2\text{O}_3$ ,  $\text{BaTiO}_3$ ,  $\text{TiO}_2$ , hydroxyapatite and bioglass. The anchoring MA monomers play a vital role in the P(MA), P(AA-MA) and P(S-MA) adsorption on inorganic particles. Such polymers offer advantages, compared to MA molecules, because MA monomers of the polymer macromolecules provide multiple bonds with metal atoms on the particle surface, which allow strong adsorption. Moreover, the adsorbed polymer macromolecules allow for electrosteric dispersion. Therefore, it was expected that MA monomers of P(SSA-MA) will allow strong adsorption of this polymer on  $\text{Mn}_3\text{O}_4$  particles. Figure 11-1B shows adsorption of MA monomer of P(SSA-MA) on the particle surface, involving a complexation mechanism[48]. Taking into consideration other literature data[44,45] for MA molecules, the bridging outer-sphere (Figure 11-1C) and bridging inner-sphere (Figure 11-1D) mechanisms can also be suggested. Moreover, the adsorption of organic molecules can also involve a combination of different mechanisms[41,44,45].

It is important to note that the use of polymers, containing carboxylic groups, such as P(MA), P(AA-MA) and P(S-MA) for particle dispersion has some limitations due to their pH dependent solubility and pH-dependent charge. Therefore, such polymers can be used for dispersion of a limited number of materials. Moreover, the use of such polymers for particle synthesis by chemical precipitation methods presents difficulties due to significant pH variations during the synthesis procedure. In contrast, the SAA monomers (Fig.1A) of the P(SSA-MA) polymer offer the advantages of pH independent charge and solubility in a wide pH range. Therefore, P(SSA-MA) offers additional benefits for  $\text{Mn}_3\text{O}_4$  synthesis and dispersion.

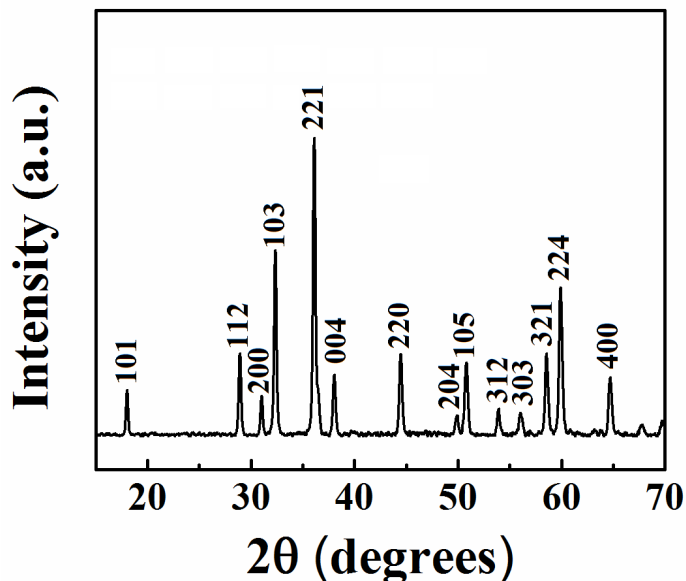


**Figure 11-2 X-ray diffraction pattern of  $Mn_3O_4$ .**

The XRD pattern of  $Mn_3O_4$  showed (Figure 11-2) diffraction peaks corresponding to the JCPDS file 24- 0734 (hausmanite). The analysis of the SEM images (Figure 11-3) of  $Mn_3O_4$  powder at different magnifications showed the formation of non-agglomerated nanoparticles with nearly spherical shape. The typical particle size was 40-50 nm. The sedimentation test of  $Mn_3O_4$  prepared without P(SSA-MA) showed rapid precipitation; however, the suspension prepared by  $Mn_3O_4$  containing P(SSA-MA) in water and mixed water ethanol (50% water) showed good stability for 5 months. The addition of P(SSA-MA) to both suspensions resulted in improved suspension stability. The improved suspension stability resulted from the adsorbed P(SSA-MA), which imparted a negative charge to the  $Mn_3O_4$  particles.

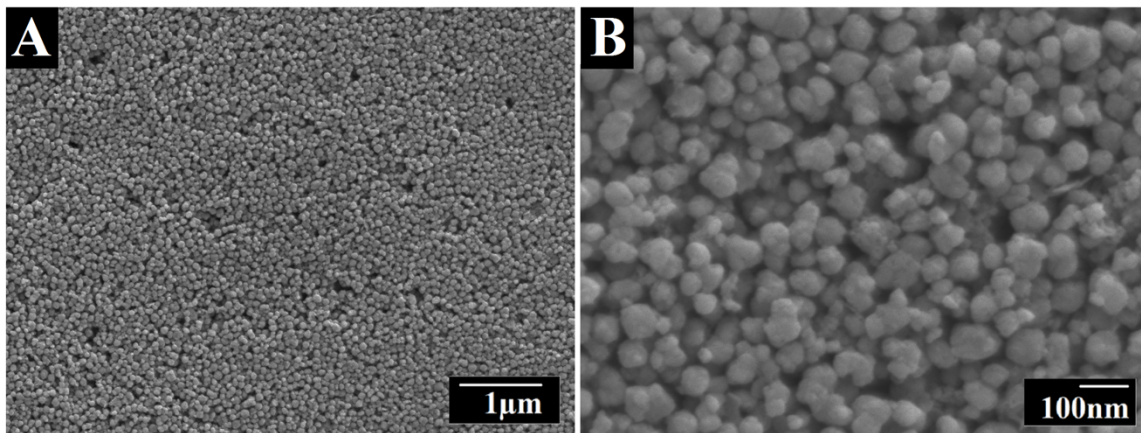


**Figure 11-3 SEM images of Mn<sub>3</sub>O<sub>4</sub> powder at different magnifications.**

Mn<sub>3</sub>O<sub>4</sub> particles must be mixed with conductive additives, such as MWCNT, in order to obtain composite electrode materials with enhanced conductivity. The efficient dispersion of MWCNT is critical for the electrode fabrication. Moreover, dispersed MWCNT must be well mixed with Mn<sub>3</sub>O<sub>4</sub> and efficiently dispersed in the Mn<sub>3</sub>O<sub>4</sub> matrix. Therefore, in this investigation, surface modification techniques have been explored in order to achieve efficient dispersion of MWCNT.

From the previous studies it becomes obvious that covalent functionalization techniques for MWCNT dispersion must be avoided, because such techniques result in degradation of MWCNT structure and properties[49]. The surface modification of MWCNT using small charged aromatic molecules is a promising approach to improving the MWCNT dispersion. Figure 11-4 shows chemical structures of the organic molecules, tested in this investigation. The aromatic structure of EV and PY was beneficial for their adsorption on MWCNT. The adsorption mechanism involved  $\pi$ - $\pi$  and hydrophobic interactions. The positive charge of the molecules facilitated electrostatic dispersion of MWCNT, containing adsorbed EV or

PY. Sedimentation tests showed good suspension stability of MWCNT, which were dispersed by the positively charged EV or PY. The electrostatic interaction of the positively charged  $\text{Mn}_3\text{O}_4$  and negatively charged MWCNT were used for their improved mixing, which allowed for enhanced electrochemical performance of the electrodes at high active mass loadings. Electrodes prepared using EV and PY were named as composite 1 and 2, respectively. Typical testing procedures (TP) involved 2, 3, 5, 10,10,10 cycles at scan rates of 2, 5, 10, 20, 50, 100  $\text{mV s}^{-1}$ , respectively. The capacitance was calculated from the CV data for the last cycle at each scan rate. EIS studies were performed before cycling and after each TP. After four TPs, only minor increase in capacitance, related to the electrode activation, was observed. After the last TP (TP4) the variation in capacitance was also investigated during 1000 cycles at a scan rate of 50  $\text{mV s}^{-1}$ .

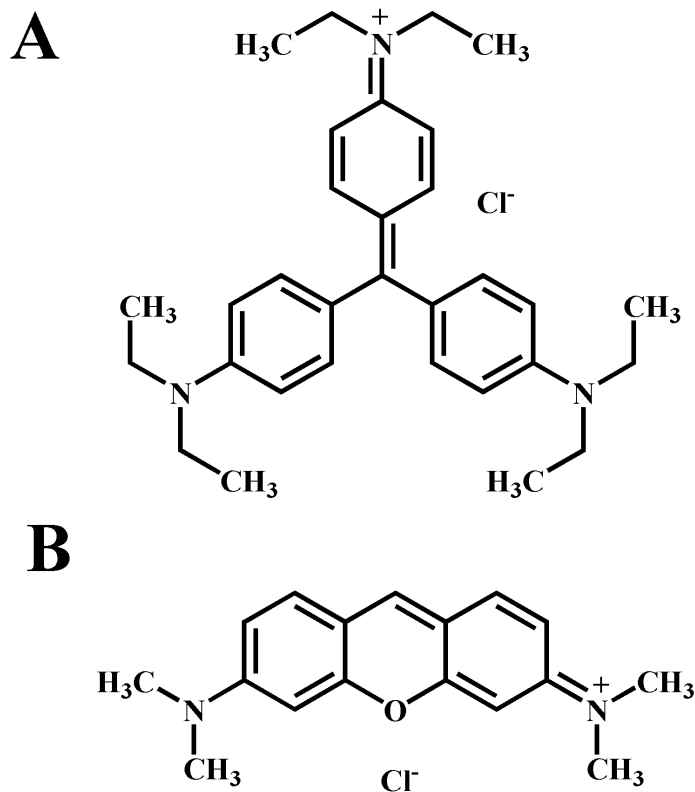
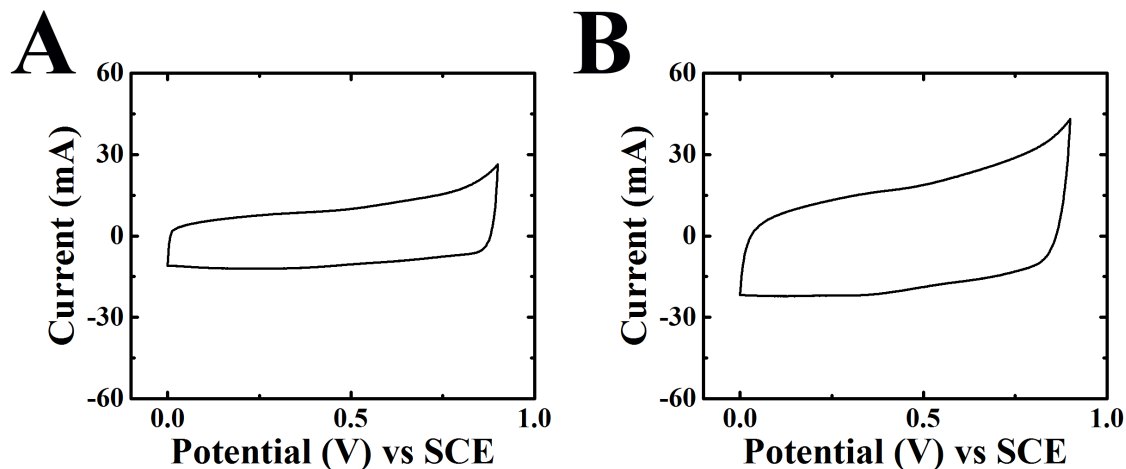


Figure 11-4 Chemical structure of (A) EV and (B) PY.

### 11.3 Electrochemical capacitive performance of Mn<sub>3</sub>O<sub>4</sub> using EV

Figure 11-5 shows CVs for composites 1 and 2, corresponding to the first cycle at a scan rate of 10 mV s<sup>-1</sup>. Nearly box shapes of the CVs indicated good electrochemical performance. However, the areas of the CVs increased during initial cycling. In order to study of the activation process, the capacitance data during TPs 1-4 were analyzed.



**Figure 11-5** CVs at a scan rate of  $10 \text{ mV s}^{-1}$  for as-prepared (A) composite 1 and (B) composite 2.

Figure 11-6 shows capacitance data for TPs 1-4 for the composite 1 and relatively high  $C_S$  above  $1 \text{ F cm}^{-2}$  was observed for TP1 at scan rates  $2\text{-}100 \text{ mV s}^{-1}$ . Cycling resulted in significant increase in capacitance. A capacitance of  $2.4 \text{ F cm}^{-2}$  was obtained at a scan rate of  $2 \text{ mV s}^{-1}$ . Moreover, remarkably high capacitance of  $2.1 \text{ F cm}^{-2}$  and high capacitance retention of 88% were observed at  $100 \text{ mV s}^{-1}$ . The EIS study before cycling showed relatively high resistance ( $Z'$ ) (Figure 11-7A). However, the resistance decreased drastically after the TP1. Moreover, cycling resulted in decrease in resistance after each TP (Figure 11-7B).

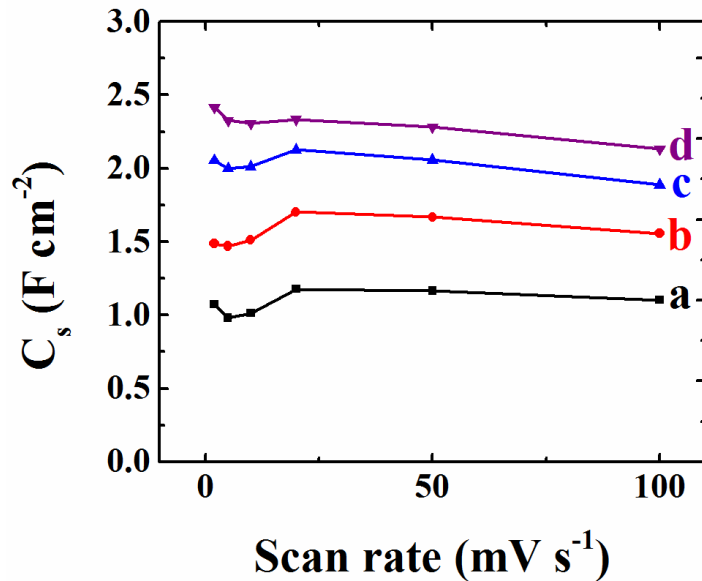


Figure 11-6 Specific capacitance versus scan rate for composite 1 for TPs: (a) 1, (b) 2, (c) 3, (d) 4.

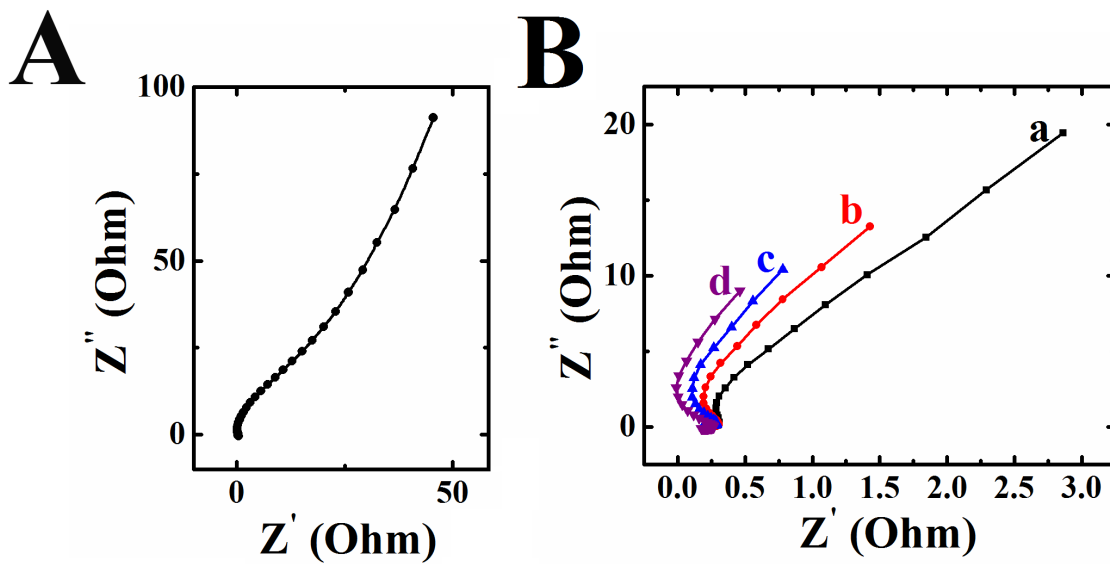
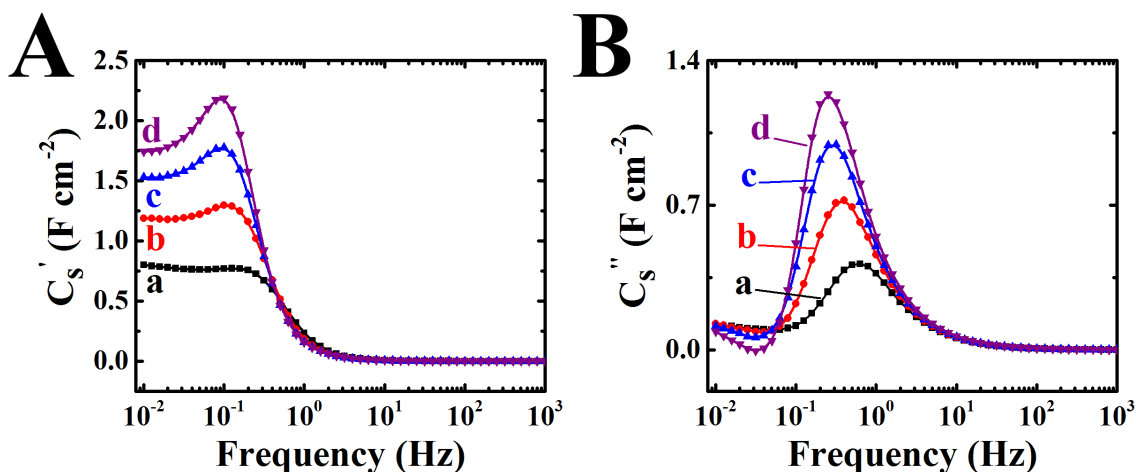


Figure 11-7 Nyquist plot of complex impedance for composite 1: (A) as prepared and (B) after TPs (a) 1, (b) 2, (c) 3 and (d) 4.

The capacitance was also calculated from impedance data after each TP and plotted versus frequency in Figure 11-8. The frequency dependences of capacitance showed a relaxation

type dispersion[50], as indicated by the reduction of  $C_s'$  at frequencies above 100 mHz and corresponding relaxation maxima in  $C_s''$ . The analysis if  $C_s'$  showed a continuously increase after each TP due to the activation process in agreement with the CV data.



**Figure 11-8** Frequency dependences of real ( $C_s'$ ) and imaginary ( $C_s''$ ) components of complex capacitance for composite 1, calculated from the impedance data, obtained after TPs (a) 1, (b) 2, (c) 3 and (d) 4.

The cycling at 50 mV s<sup>-1</sup> after TP4 showed capacitance increase of about 20% during 700 cycles and then capacitance decreased to the level of 110% of capacitance, corresponding to the cycle 1 (Figure 11-9A). The nearly box CV shape at 50 mV s<sup>-1</sup> (Figure 11-9B) indicated that good electrochemical performance can be achieved at high scan rates.

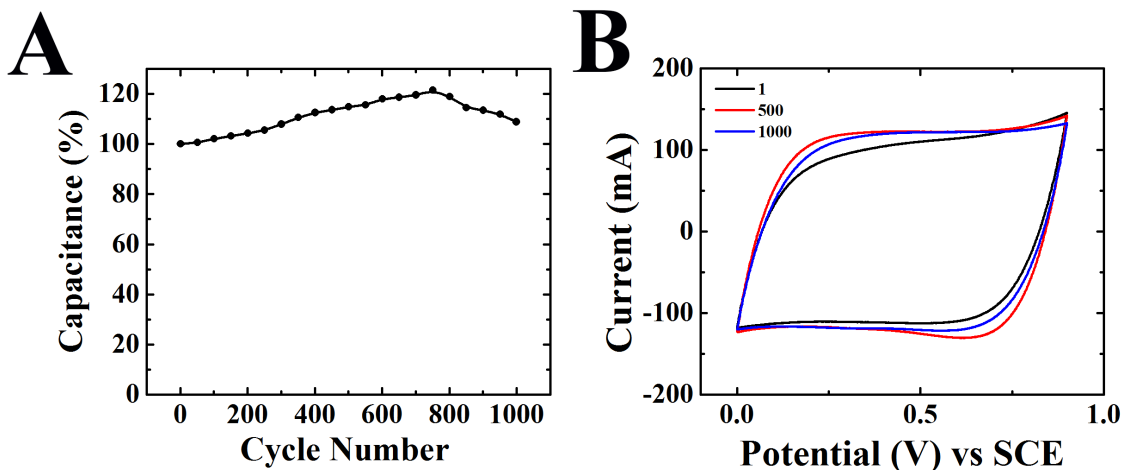


**Figure 11-9 (A) Capacitance variation with the cycle number at a scan rate of  $50 \text{ mV s}^{-1}$  for composite 1 after TP4 and (B) corresponding CV for cycles 1, 500 and 1000. The data in (A) is normalized by the capacitance calculated from the CV cycle 1.**

#### 11.4 Electrochemical capacitive performance of $\text{Mn}_3\text{O}_4$ using PY

The electrochemical testing of composite 2 showed capacitance increase after each TP (Figure 11-10). The highest capacitance of  $2.8 \text{ F cm}^{-2}$  was obtained at a scan rate of  $2 \text{ mV s}^{-1}$ . The capacitance retention at  $100 \text{ mV s}^{-1}$  was 64%. The comparison of the EIS data before cycling (Figure 11-11A) and after TP1 (Figure 11-11B(a)) showed significant reduction in resistance ( $Z'$ ). The resistance reduction was also observed after each TP (Figure 11-11B). The analysis of the frequency dependences of complex capacitance (Figure 11-12), calculated from the impedance data, also revealed significant changes, attributed to the activation process. The increase in the low frequency  $C_s'$  after each TP is in agreement with the CV data.

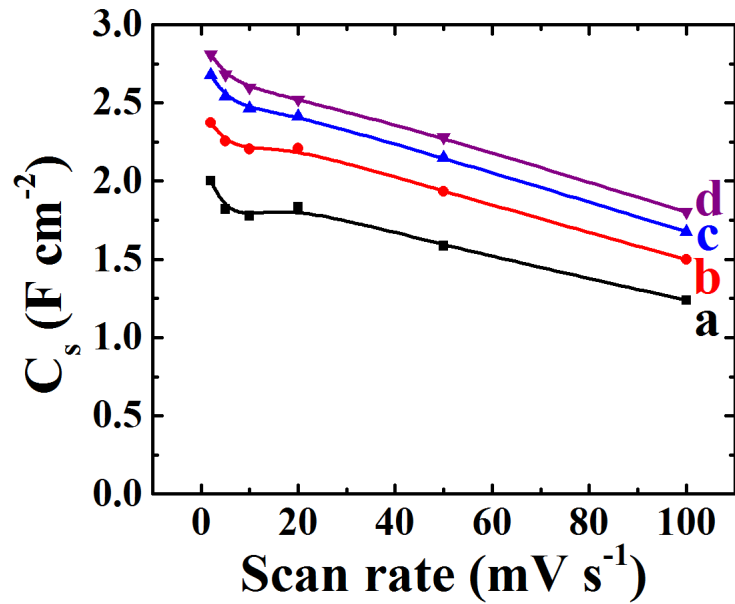


Figure 11-10 Specific capacitance versus scan rate for composite 2 for TPs: (a) 1, (b) 2, (c) 3, (d) 4.

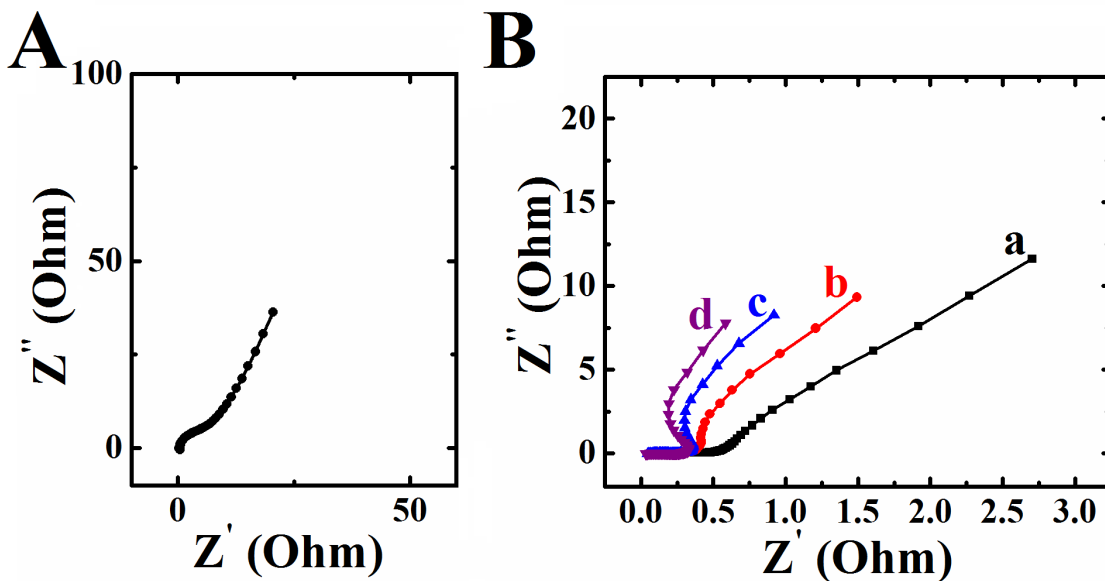


Figure 11-11 Nyquist plot of complex impedance for composite 2: (A) as prepared and (B) after TPs (a) 1, (b) 2, (c) 3 and (d) 4.

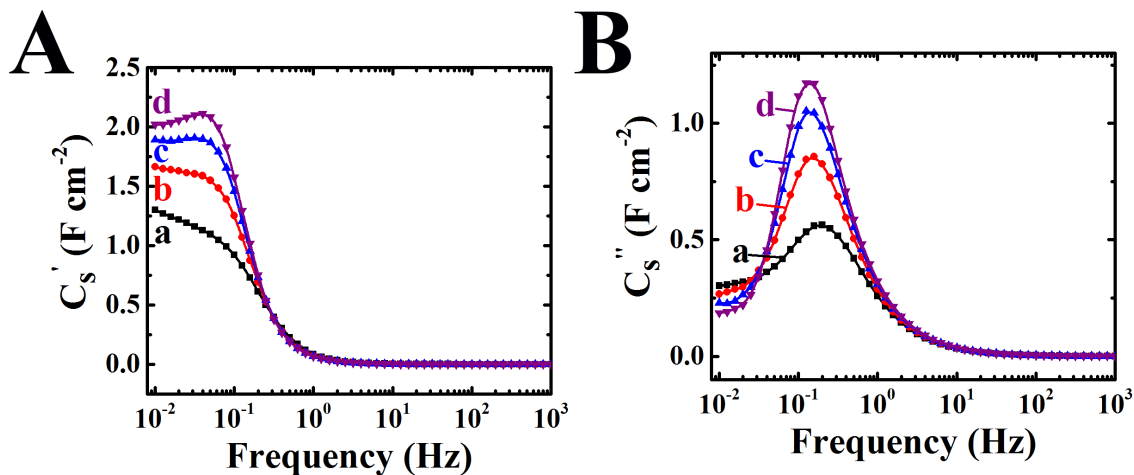


Figure 11-12 Frequency dependences of real ( $C'_s$ ) and imaginary ( $C''_s$ ) components of complex capacitance for composite 2, calculated from the impedance data, obtained after TPs (a) 1, (b) 2, (c) 3 and (d) 4.

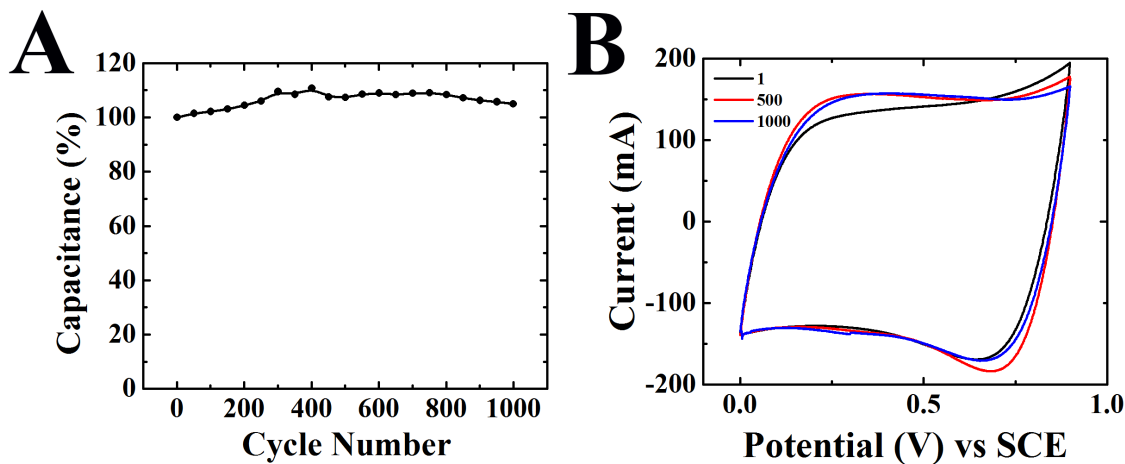


Figure 11-13 A) Capacitance variation with the cycle number at a scan rate of  $50 \text{ mV s}^{-1}$  for composite 2 after TP4 and (B) corresponding CV for cycles 1, 500 and 1000. The data in (A) is normalized by the capacitance calculated from the CV cycle 1.

The cycling at  $50 \text{ mV s}^{-1}$  showed an increase in  $C_S$  of about 10% during the first 400 cycles (Figure 11-13A) and then  $C_S$  gradually decreased. The  $C_S$  after 1000 cycles was 105% of

the capacitance, obtained for the cycle 1. The box shape CVs at  $50 \text{ mV s}^{-1}$  indicated good electrochemical performance at high scan rates (Figure 11-13B).

The results of this investigation indicated that good electrochemical performance can be achieved in the  $\text{Mn}_3\text{O}_4$  electrodes at relatively high active mass loadings of  $28.4 \text{ mg cm}^{-2}$  ( $\pm 3\%$ ), which meet the mass loading requirements for application in practical devices. The highest capacitance of  $2.8 \text{ F cm}^{-2}$  achieved for composite 2 exceeds significantly the literature data for  $\text{Mn}_3\text{O}_4$  electrodes[7,37–40], which were in the range of  $0.02\text{-}0.6 \text{ F cm}^{-2}$ . Of particular importance is high capacitance retention and high capacitance, achieved for the composite 1 at a scan rate of  $100 \text{ mV s}^{-1}$ . The capacitance of  $2.1 \text{ F cm}^{-2}$  achieved at  $100 \text{ mV s}^{-1}$  for composite 1 exceeds the capacitance of  $\text{MnO}_2$  electrodes ( $\sim 1 \text{ F cm}^{-2}$ ) obtained[16] at the same scan rate and mass loading of  $40 \text{ mg cm}^{-2}$ . The variation in capacitance of the electrodes during initial cycling correlates with literature data, which reported activation behavior of  $\text{Mn}_3\text{O}_4$ [5,23,28,29] due to the changes in the film morphology and oxidation of manganese ions to a higher oxidation state. Significant changes in resistance observed in this investigation indicate that microstructure changes in the bulk of the composite electrodes can be one of the dominant factors, contributing to the activation process. Further investigations, currently under way, are necessary for better understanding of the influence of the dye dispersant structure on the properties of the composites and the nature of the activation process.

## 11.5 Conclusion

The use of P(SSA-MA) facilitated the preparation of well-dispersed non-agglomerated  $\text{Mn}_3\text{O}_4$  nanoparticles. The dispersion strategy was based on the unique adsorption properties of P(SSA-MA), related to strong bidentate bonding of the MA monomers. The negative charge of the SSA monomers facilitated the electrosteric dispersion. The use of EV and PY dyes allowed the fabrication of stable suspensions of well-dispersed positively charged MWCNT. Efficient mixing of  $\text{Mn}_3\text{O}_4$  nanoparticles and MWCNT was achieved by the electrostatic heterocoagulation of the negatively charged  $\text{Mn}_3\text{O}_4$  nanoparticles and positively charged MWCNT. Building on the colloidal processing advantages offered by our approach, we have demonstrated the fabrication of  $\text{Mn}_3\text{O}_4$ -MWCNT electrodes with high active mass loading, which showed excellent capacitive performance. The high active mass loading meets the mass loading requirements for practical applications. The highest capacitance of  $2.8 \text{ F cm}^{-2}$  was obtained at a scan rate of  $2 \text{ mV s}^{-1}$  for the composites, prepared using PY. However, the composites, prepared using EV showed better capacitance retention and the capacitance of  $2.1 \text{ F cm}^{-2}$  was obtained at a scan rate of  $100 \text{ mV s}^{-1}$ . The composites showed activation behavior during cycling, which resulted in a capacitance increase and electrical resistance reduction. The results of this investigation pave the way for practical applications of  $\text{Mn}_3\text{O}_4$  in electrochemical supercapacitors.

## References:

- [1] Bose, V. C., and Biju, V., 2015, "Structure, Cation Valence States and Electrochemical Properties of Nanostructured  $Mn_3O_4$ ," *Mater. Sci. Semicond. Process.*, **35**, pp. 1–9.
- [2] Liu, C., Song, H., Zhang, C., Liu, Y., Zhang, C., Nan, X., and Cao, G., 2015, "Coherent  $Mn_3O_4$ -Carbon Nanocomposites with Enhanced Energy-Storage Capacitance," *Nano Res.*, **8**(10), pp. 3372–3383.
- [3] Li, Y., Ye, D., Liu, W., Shi, B., Guo, R., Pei, H., and Xie, J., 2017, "A Three-Dimensional Core-Shell Nanostructured Composite of Polypyrrole Wrapped  $MnO_2$ /Reduced Graphene Oxide/Carbon Nanotube for High Performance Lithium Ion Batteries," *J. Colloid Interface Sci.*, **493**, pp. 241–248.
- [4] Li, J., and Zhitomirsky, I., 2009, "Electrophoretic Deposition of Manganese Dioxide-carbon Nanotube Composites," *J. Mater. Process. Technol.*, **209**(7), pp. 3452–3459.
- [5] Wu, T.-H., Chu, Y.-H., Hu, C.-C., and Hardwick, L. J., 2013, "Criteria Appointing the Highest Acceptable Cell Voltage of Asymmetric Supercapacitors," *Electrochem. Commun.*, **27**, pp. 81–84.
- [6] Brousse, T., Toupin, M., Dugas, R., Athouël, L., Crosnier, O., and Bélanger, D., 2006, "Crystalline  $MnO_2$  as Possible Alternatives to Amorphous Compounds in Electrochemical Supercapacitors," *J. Electrochem. Soc.*, **153**(12), pp. A2171–A2180.
- [7] Li, X.-J., Song, Z., Zhao, Y., Wang, Y., Zhao, X.-C., Liang, M., Chu, W.-G., Jiang, P., and Liu, Y., 2016, "Vertically Porous Nickel Thin Film Supported  $Mn_3O_4$  for Enhanced Energy Storage Performance," *J. Colloid Interface Sci.*, **483**, pp. 17–25.
- [8] Brousse, T., Taberna, P.-L., Crosnier, O., Dugas, R., Guillemet, P., Scudeller, Y., Zhou, Y., Favier, F., Bélanger, D., and Simon, P., 2007, "Long-Term Cycling Behavior of Asymmetric Activated Carbon/ $MnO_2$  Aqueous Electrochemical Supercapacitor," *J. Power Sources*, **173**(1), pp. 633–641.
- [9] Athouël, L., Moser, F., Dugas, R., Crosnier, O., Bélanger, D., and Brousse, T., 2008, "Variation of the  $MnO_2$  Birnessite Structure upon Charge/Discharge in an Electrochemical Supercapacitor Electrode in Aqueous  $Na_2SO_4$  Electrolyte," *J. Phys. Chem. C*, **112**(18), pp. 7270–7277.
- [10] Simon, P., and Gogotsi, Y., 2008, "Materials for Electrochemical Capacitors," *Nat. Mater.*, **7**(11), pp. 845–854.

- [11] Pang, S.-C., Anderson, M. A., and Chapman, T. W., 2000, "Novel Electrode Materials for Thin-Film Ultracapacitors: Comparison of Electrochemical Properties of Sol-Gel-Derived and Electrodeposited Manganese Dioxide," *J. Electrochem. Soc.*, **147**(2), pp. 444–450.
- [12] Toupin, M., Brousse, T., and Bélanger, D., 2004, "Charge Storage Mechanism of MnO<sub>2</sub> Electrode Used in Aqueous Electrochemical Capacitor," *Chem. Mater.*, **16**(16), pp. 3184–3190.
- [13] Broughton, J. N., and Brett, M. J., 2004, "Investigation of Thin Sputtered Mn Films for Electrochemical Capacitors," *Electrochimica Acta*, **49**(25), pp. 4439–4446.
- [14] Nam, K.-W., and Kim, K.-B., 2006, "Manganese Oxide Film Electrodes Prepared by Electrostatic Spray Deposition for Electrochemical Capacitors," *J. Electrochem. Soc.*, **153**(1), pp. A81–A88.
- [15] Gogotsi, Y., and Simon, P., 2011, "True Performance Metrics in Electrochemical Energy Storage," *Science*, **334**(6058), pp. 917–918.
- [16] Wang, Y., Liu, Y., and Zhitomirsky, I., 2013, "Surface Modification of MnO<sub>2</sub> and Carbon Nanotubes Using Organic Dyes for Nanotechnology of Electrochemical Supercapacitors," *J. Mater. Chem. A*, **1**(40), pp. 12519–12526.
- [17] Dong, W., Sakamoto, J. S., and Dunn, B., 2003, "Electrochemical Properties of Vanadium Oxide Aerogels," *Sci. Technol. Adv. Mater.*, **4**(1), pp. 3–11.
- [18] Dong, W., Rolison, D. R., and Dunn, B., 2000, "Electrochemical Properties of High Surface Area Vanadium Oxide Aerogels," *Electrochem. Solid-State Lett.*, **3**(10), pp. 457–459.
- [19] Jeong, Y. U., and Manthiram, A., 2002, "Nanocrystalline Manganese Oxides for Electrochemical Capacitors with Neutral Electrolytes," *J. Electrochem. Soc.*, **149**(11), pp. A1419–A1422.
- [20] Reddy, R. N., and Reddy, R. G., 2003, "Sol-gel MnO<sub>2</sub> as an Electrode Material for Electrochemical Capacitors," *J. Power Sources*, **124**(1), pp. 330–337.
- [21] Cheong, M., and Zhitomirsky, I., 2009, "Electrophoretic Deposition of Manganese Oxide Films," *Surf. Eng.*, **25**(5), pp. 346–352.
- [22] Zhang, S. W., and Chen, G. Z., 2008, "Manganese Oxide Based Materials for Supercapacitors," *Energy Mater.*, **3**(3), pp. 186–200.
- [23] Nagarajan, N., Cheong, M., and Zhitomirsky, I., 2007, "Electrochemical Capacitance of MnO<sub>x</sub> Films," *Mater. Chem. Phys.*, **103**(1), pp. 47–53.

- [24] Wang, G., Ma, Z., Fan, Y., Shao, G., Kong, L., and Gao, W., 2015, "Preparation of Size-Selective  $\text{Mn}_3\text{O}_4$  Hexagonal Nanoplates with Superior Electrochemical Properties for Pseudocapacitors," *Phys. Chem. Chem. Phys.*, **17**(35), pp. 23017–23025.
- [25] Zhitomirsky, I., Cheong, M., and Wei, J., 2007, "The Cathodic Electrodeposition of Manganese Oxide Films for Electrochemical Supercapacitors," *JOM*, **59**(7), pp. 66–69.
- [26] Qiao, Y., Sun, Q., Xi, J., Cui, H., Tang, Y., and Wang, X., 2016, "A Modified Solvothermal Synthesis of Porous  $\text{Mn}_3\text{O}_4$  for Supercapacitor with Excellent Rate Capability and Long Cycle Life," *J. Alloys Compd.*, **660**, pp. 416–422.
- [27] Lee, Y.-F., Chang, K.-H., Hu, C.-C., and Chu, Y.-H., 2012, "Designing Tunable Microstructures of  $\text{Mn}_3\text{O}_4$  Nanoparticles by Using Surfactant-Assisted Dispersion," *J. Power Sources*, **206**, pp. 469–475.
- [28] Xia, H., Lai, M. O., and Lu, L., 2011, "Nanostructured Manganese Oxide Thin Films as Electrode Material for Supercapacitors," *JOM J. Miner. Met. Mater. Soc.*, **63**(1), pp. 54–59.
- [29] Dubal, D. P., Dhawale, D. S., Salunkhe, R. R., and Lokhande, C. D., 2010, "A Novel Chemical Synthesis of  $\text{Mn}_3\text{O}_4$  Thin Film and Its Stepwise Conversion into Birnessite  $\text{MnO}_2$  during Super Capacitive Studies," *J. Electroanal. Chem.*, **647**(1), pp. 60–65.
- [30] Wang, L., Li, Y., Han, Z., Chen, L., Qian, B., Jiang, X., Pinto, J., and Yang, G., 2013, "Composite Structure and Properties of  $\text{Mn}_3\text{O}_4$ /Graphene Oxide and  $\text{Mn}_3\text{O}_4$ /Graphene," *J. Mater. Chem. A*, **1**(29), pp. 8385–8397.
- [31] Ding, F., Zhang, N., Zhang, C., and Zhang, C., 2015, "The Tuning of Phase, Morphology and Performance of Graphene Oxide/Manganese Oxide for Supercapacitors," *Mater. Trans.*, **56**(11), pp. 1857–1862.
- [32] Wang, H., Li, Z., Yang, J., Li, Q., and Zhong, X., 2009, "A Novel Activated Mesocarbon microbead(aMCMB)/ $\text{Mn}_3\text{O}_4$  Composite for Electrochemical Capacitors in Organic Electrolyte," *J. Power Sources*, **194**(2), pp. 1218–1221.
- [33] Chen, C., and Ma, T., 2015, "Synthesis and Electrochemical Properties of Tube-like Nitrogen-Doped Graphene/Manganese Oxide Composite for Supercapacitors," *Micro Nano Lett.*, **10**(6), pp. 282–286.

- [34] Lee, H.-M., Jeong, G. H., Kang, D. W., Kim, S.-W., and Kim, C.-K., 2015, "Direct and Environmentally Benign Synthesis of Manganese Oxide/Graphene Composites from Graphite for Electrochemical Capacitors," *J. Power Sources*, **281**, pp. 44–48.
- [35] Cao, J., Wang, Y., Zhou, Y., Jia, D., Ouyang, J.-H., and Guo, L., 2012, "Performances of High Voltage Electrochemical Capacitor Using Ball-Milled Graphite/Mn<sub>3</sub>O<sub>4</sub> Composite Electrodes," *J. Electroanal. Chem.*, **682**, pp. 23–28.
- [36] Youn, D.-Y., Tuller, H. L., Hyun, T.-S., Choi, D.-K., and Kim, I.-D., 2011, "Facile Synthesis of Highly Conductive RuO<sub>2</sub>-Mn<sub>3</sub>O<sub>4</sub> Composite Nanofibers via Electrospinning and Their Electrochemical Properties," *J. Electrochem. Soc.*, **158**(8), pp. A970–A975.
- [37] Dubal, D. P., Dhawale, D. S., Salunkhe, R. R., Fulari, V. J., and Lokhande, C. D., 2010, "Chemical Synthesis and Characterization of Mn<sub>3</sub>O<sub>4</sub> Thin Films for Supercapacitor Application," *J. Alloys Compd.*, **497**(1), pp. 166–170.
- [38] Yadav, A. A., 2016, "Influence of Electrode Mass-Loading on the Properties of Spray Deposited Mn<sub>3</sub>O<sub>4</sub> Thin Films for Electrochemical Supercapacitors," *Thin Solid Films*, **608**, pp. 88–96.
- [39] A.V., R., and M.S., R. R., 2017, "Tunable Supercapacitance of Electrospun Mn<sub>3</sub>O<sub>4</sub> Beaded Chains via Charge- Discharge Cycling and Control Parameters," *Appl. Surf. Sci.*, **403**, pp. 601–611.
- [40] Hu, Y., Guan, C., Feng, G., Ke, Q., Huang, X., and Wang, J., 2015, "Flexible Asymmetric Supercapacitor Based on Structure-Optimized Mn<sub>3</sub>O<sub>4</sub>/Reduced Graphene Oxide Nanohybrid Paper with High Energy and Power Density," *Adv. Funct. Mater.*, **25**(47), pp. 7291–7299.
- [41] Ata, M. S., Liu, Y., and Zhitomirsky, I., 2014, "A Review of New Methods of Surface Chemical Modification, Dispersion and Electrophoretic Deposition of Metal Oxide Particles," *Rsc Adv.*, **4**(43), pp. 22716–22732.
- [42] Pujari, S. P., Scheres, L., Marcelis, A., and Zuilhof, H., 2014, "Covalent Surface Modification of Oxide Surfaces," *Angew. Chem. Int. Ed.*, **53**(25), pp. 6322–6356.
- [43] Thomas, G., Demoisson, F., Boudon, J., and Millot, N., 2016, "Efficient Functionalization of Magnetite Nanoparticles with Phosphonate Using a One-Step Continuous Hydrothermal Process," *Dalton Trans.*, **45**(26), pp. 10821–10829.
- [44] Hwang, Y. S., and Lenhart, J. J., 2008, "Adsorption of C4-Dicarboxylic Acids at the Hematite/Water Interface," *Langmuir*, **24**(24), pp. 13934–13943.

- [45] Lenhart, J. J., Heyler, R., Walton, E. M., and Mylon, S. E., 2010, "The Influence of Dicarboxylic Acid Structure on the Stability of Colloidal Hematite," *J. Colloid Interface Sci.*, **345**(2), pp. 556–560.
- [46] Mohanty, S., Das, B., and Dhara, S., 2013, "Poly(maleic Acid) – A Novel Dispersant for Aqueous Alumina Slurry," *J. Asian Ceram. Soc.*, **1**(2), pp. 184–190.
- [47] Zhao, J., Wang, X., Gui, Z., and Li, L., 2004, "Dispersion of Barium Titanate with Poly(acrylic Acid-Co-Maleic Acid) in Aqueous Media," *Ceram. Int.*, **30**(7), pp. 1985–1988.
- [48] Clifford, A., Luo, D., and Zhitomirsky, I., 2017, "Colloidal Strategies for Electrophoretic Deposition of Organic-Inorganic Composites for Biomedical Applications," *Colloids Surf. Physicochem. Eng. Asp.*, **516**, pp. 219–225.
- [49] Boccaccini, A. R., Cho, J., Roether, J. A., Thomas, B. J., Minay, E. J., and Shaffer, M. S., 2006, "Electrophoretic Deposition of Carbon Nanotubes," *Carbon*, **44**(15), pp. 3149–3160.
- [50] Shi, K., and Zhitomirsky, I., 2013, "Influence of Current Collector on Capacitive Behavior and Cycling Stability of Tiron Doped Polypyrrole Electrodes," *J. Power Sources*, **240**, pp. 42–49.

## Chapter 12 Conclusions

Several advancements in the ES technology have been achieved in this dissertation with main focus on the fabrication of composite materials for ESs electrodes and devices. The major achievements of this work can be summarized as-follows:

1. Nature-inspired strategies have been developed for the fabrication of MWCNT films and composites. It was found that bile acid dispersants provide outstanding colloidal stability of MWCNT, MnO<sub>2</sub>-MWCNT and PPy-MWCNT suspensions. The use of bile acids allowed high EPD yield due to pH dependent charge, binding and film forming properties of bile acid materials, containing anionic carboxylic groups. The analysis of experimental results provided an insight into the influence of molecular structure of dispersant and functional groups on dispersion of particles, MWCNT and microstructure of obtained composites.
2. Two different colloidal strategies have been utilized for the fabrication of electrodes of electrochemical supercapacitors. Composite MnO<sub>2</sub>-MWCNT films were obtained by anodic EPD using ChNa and DCNa as dispersants. In another strategy, good dispersion of MWCNT during Py polymerization was achieved using TChNa. The method allowed the formation of PPy coated MWCNT, which were utilized for the fabrication of electrodes with high active mass loading by a colloidal slurry impregnation method. The film and bulk electrodes, prepared by EPD and slurry impregnation methods, respectively, showed high capacitance and good capacitance retention at high charge-discharge rates.

3. Various organic additives, such as LPEI, PAH, FA and HA, were used for cathodic and anodic EPD of  $\text{MnO}_2$  and MWCNT. QCM was proved that deposition yield can be varied and controlled by variation of the deposition time and voltage. The analysis of FTIR data showed that the adsorption mechanism of the selected organic molecules on the oxide particles involved complexation or bridging of COOH and OH groups with Mn atoms on the particle surface.
4. We found that some of the dispersing agents have good film forming properties which allowed for EPD films from aqueous or water-ethanol solutions at various deposition voltages and concentrations of dispersants in the solutions. The discovery of dispersing agents with film forming properties opens the door to making advanced films and composites.
5. New dispersant molecules were investigated for applications as a charging, dispersing and film forming agents for the electrophoretic co-deposition of materials of different types, such as oxide nanoparticles of  $\text{MnO}_2$ , metal nanoparticles of Ni and Pd, MWCNT.
6. From the present study, it is evident that charge of inorganic particles in solutions of carboxyalkylphosphonic acids in ethanol is influenced by interactions of the acids with metal atoms on the particle surface. The strong interaction of phosphonate ligands of 3PHA and 16PHA with Mn atoms resulted in the formation of negatively charged  $\text{MnO}_2$  particles, which were dispersed in ethanol solutions and allowed for film formation by anodic EPD. The stronger steric repulsion effect of longer chained 16PHA allowed for improved dispersion and higher deposition

yield. The composite electrodes, prepared in presence of 3PHA showed better performance than 16PHA. The areal SCs of electrodes were achieved 3.75 and 2.95 F cm<sup>-2</sup> at scan rate of 2 mV s<sup>-1</sup> for 3PHA and 16PHA, respectively.

7. New strategies were developed based on electrostatic heterocoagulation in aqueous and non-aqueous suspensions. MnO<sub>2</sub> was successfully dispersed in ethanol by using anionic PGR, PCA and PHA dispersants. We found the possibility of efficient dispersion of MWCNT in ethanol using AZA and NB, which imparted a positive charge to MWCNT. The electrostatic assembly method offers the benefit of improved mixing of MnO<sub>2</sub> and MWCNT. Various electrostatic assembly strategies based on the use of different anionic and cationic dispersants allowed the fabrication of electrodes with enhanced capacitance and improved capacitance retention at high charge–discharge rates and high active mass loadings. The highest capacitance of 2.39 F cm<sup>-2</sup> at a scan rate of 100 mV s<sup>-1</sup> was achieved for MnO<sub>2</sub> and MWCNT, respectively. The ability to achieve high areal capacitance at high charge–discharge rates is important for the development of efficient supercapacitor devices. The asymmetric devices, containing positive MnO<sub>2</sub>–MWCNT and negative AC–CB electrodes showed promising performance in a voltage window of 1.6 V.
8. Anionic of CA and cationic of ClB molecules from the catechol family are promising charging and dispersing agents for EPD of Mn<sub>3</sub>O<sub>4</sub>. The use of ClB as a co-dispersant allowed for the fabrication of Mn<sub>3</sub>O<sub>4</sub>–MWCNT composites. Testing results showed promising performance of Mn<sub>3</sub>O<sub>4</sub>–MWCNT composites for applications in electrodes of electrochemical supercapacitors.

9. Finally, the use of P(SSA-MA) facilitated the preparation of well-dispersed non-agglomerated  $\text{Mn}_3\text{O}_4$  nanoparticles. The negative charge of the SSA monomers facilitated the electrosteric dispersion. The use of EV and PY dyes allowed the fabrication of stable suspensions of well-dispersed positively charged MWCNT. Efficient mixing of  $\text{Mn}_3\text{O}_4$  nanoparticles and MWCNT was achieved by the electrostatic heterocoagulation. Building on the colloidal processing advantages offered by our approach, we have demonstrated the fabrication of  $\text{Mn}_3\text{O}_4$ -MWCNT electrodes with high active mass loading, which showed excellent capacitive performance. The high active mass loading meets the mass loading requirements for practical applications. The highest capacitance of  $2.8 \text{ F cm}^{-2}$  was obtained at a scan rate of  $2 \text{ mV s}^{-1}$  for the composites, prepared using PY. However, the composites, prepared using EV showed better capacitance retention and the capacitance of  $2.1 \text{ F cm}^{-2}$  was obtained at a scan rate of  $100 \text{ mV s}^{-1}$ . The composites showed activation behavior during cycling, which resulted in a capacitance increase and electrical resistance reduction. The use of dispersing agents, such as individual molecules and polyelectrolytes is promising for further development of  $\text{Mn}_3\text{O}_4$  based electrodes. It is expected that further development of new colloidal strategies will result in enhanced performance of  $\text{Mn}_3\text{O}_4$  electrodes. The results of this investigation pave the way for practical applications of  $\text{Mn}_3\text{O}_4$  in electrochemical supercapacitors.

## **Future works**

This work solves many urgent problems, but it's also significant to give suggestions for the future works:

1. Development of negative electrodes with higher capacitance utilizing novel materials.
2. Investigation of complex metal oxides containing Mn for higher capacitance.
3. Development of  $\text{Mn}_3\text{O}_4$  syntheses with using novel surfactants to enhance its capacitive performance.
4. Development of slurry impregnation method for electrode preparations.